

# **Formation and evolution of star clusters and their host galaxies**

Diederik Kruijssen

© 2011 J. M. Diederik Kruijssen  
Alle rechten voorbehouden

ISBN 978 90 393 5576 3

Printed by Wöhrmann Print Service, Zutphen

Cover image by the author and Sophie Goldhagen. Contains several Hubble Space Telescope images (credit: Hubble Heritage Team; AURA/STScI/NASA).

# **Formation and evolution of star clusters and their host galaxies**

## **De vorming en ontwikkeling van sterrenhopen en hun moederstelsels**

(met een samenvatting in het Nederlands)

### **Proefschrift**

ter verkrijging van de graad van doctor aan de  
Universiteit Utrecht op gezag van de rector  
magnificus, prof. dr. G. J. van der Zwaan,  
ingevolge het besluit van het college voor  
promoties in het openbaar te verdedigen op

maandag 6 juni 2011 des middags te 12.45 uur

door

**Johan Marinus Diederik Kruijssen**

geboren op 4 mei 1985 te Nieuwegein

Promotoren: Prof. dr. H. J. G. L. M. Lamers  
Prof. dr. S. F. Portegies Zwart  
Prof. dr. V. Icke

This research has been supported by the Netherlands Organisation for Scientific Research (NWO). Additional support has come from the Leids Kerkhoven-Bosscha Fonds (LKBF).

*the Great Ocean of Truth is better perceived  
by taking a step back onto the dunes*  
— after Sir Isaac Newton

voor Sophie



# Contents

<b>1</b>	<b>Introduction</b>	<b>1</b>
1.1	Star formation . . . . .	2
1.2	Star cluster evolution . . . . .	4
1.3	Galaxy evolution . . . . .	7
1.4	This thesis . . . . .	9
	<b>Part A – The formation of star clusters</b>	<b>12</b>
<b>2</b>	<b>The dynamical state of stellar structure in star-forming regions</b>	<b>15</b>
2.1	Introduction . . . . .	15
2.2	Simulations and cluster selection . . . . .	17
2.3	Dynamical state of stellar subclusters . . . . .	21
2.4	Response to gas expulsion . . . . .	29
2.5	Summary and outlook . . . . .	35
2.A	Appendix: Independence of results on sink parameters . . . . .	38
	<b>Part B – The evolution of star clusters in their galactic environment</b>	<b>39</b>
<b>3</b>	<b>The photometric evolution of star clusters</b>	<b>43</b>
3.1	Introduction . . . . .	44
3.2	Cluster evolution . . . . .	46
3.3	Computation of photometric cluster evolution . . . . .	57
3.4	Photometric properties of clusters . . . . .	57
3.5	Application to globular clusters . . . . .	67
3.6	Discussion . . . . .	71
3.7	Conclusions . . . . .	76
3.A	Appendix: Outward motion of stellar remnants . . . . .	78
<b>4</b>	<b>Explaining the mass-to-light ratios of globular clusters</b>	<b>81</b>
4.1	Introduction . . . . .	81
4.2	Modeling method . . . . .	82
4.3	Applying the cluster models to observed clusters . . . . .	83
4.4	Discussion . . . . .	86

<b>5</b>	<b>On the reduced mass-to-light ratios of Galactic globular clusters</b>	<b>89</b>
5.1	Introduction . . . . .	90
5.2	Cluster evolution models and $M/L_V$ evolution . . . . .	94
5.3	Determining the dissolution timescale . . . . .	98
5.4	Predicted and observed mass-to-light ratios . . . . .	102
5.5	Observational verification . . . . .	109
5.6	Discussion and conclusions . . . . .	113
5.A	Appendix: Error analysis . . . . .	117
<b>6</b>	<b>On the interpretation of the globular cluster luminosity function</b>	<b>119</b>
6.1	Introduction . . . . .	119
6.2	Implications of a luminosity-dependent $M/L$ . . . . .	121
6.3	Models of the Galactic GC system . . . . .	122
6.4	Discussion . . . . .	125
<b>7</b>	<b>The evolution of the stellar mass function in star clusters</b>	<b>129</b>
7.1	Introduction . . . . .	130
7.2	The mass evolution of star clusters . . . . .	131
7.3	The evolution of the stellar mass function . . . . .	132
7.4	Comparison to $N$ -body simulations . . . . .	142
7.5	Star cluster evolution . . . . .	145
7.6	Discussion and applications . . . . .	155
	<b>Part C – The co-evolution of star clusters and galaxies</b>	<b>160</b>
<b>8</b>	<b>Star cluster populations in galaxy simulations</b>	<b>163</b>
8.1	Introduction . . . . .	164
8.2	Simulation code . . . . .	167
8.3	Summary of the model runs . . . . .	181
8.4	Isolated disc galaxies . . . . .	184
8.5	Galaxy mergers . . . . .	196
8.6	Discussion . . . . .	208
<b>9</b>	<b>The star cluster population in galaxy mergers</b>	<b>215</b>
9.1	Introduction . . . . .	215
9.2	Summary of the model . . . . .	216
9.3	Evolution of the star cluster population . . . . .	218
9.4	Discussion . . . . .	222
<b>10</b>	<b>Epilogue: The co-evolution of star clusters and galaxies in the Antennae system</b>	<b>225</b>
10.1	Introduction . . . . .	225
10.2	A model for the Antennae system . . . . .	227
10.3	Properties of the cluster population . . . . .	230
10.4	Emergent effects in galactic environments . . . . .	233



---

<b>Bibliography</b>	<b>237</b>
<b>Nederlandse samenvatting</b>	<b>251</b>
<b>List of publications</b>	<b>265</b>
<b>Dankwoord</b>	<b>267</b>
<b>Curriculum vitae</b>	<b>271</b>



---

# Chapter 1

## Introduction

Imagine encountering a stranger at night, in a dark and deserted field. There is hardly any Moon, but you can just see his scarred face as he approaches you. His shredded clothes are hanging from his skinny shoulders and he does not speak as he passes. A closer look at his mouth reveals several teeth are missing. The way he moves his left arm indicates a badly healed fracture that must have been menacing him for years. Just moments later, time freezes and everything stops moving, except you.

For some people, the discomfort of the situation might force them to run and leave this place. For others, the sight of the petrified world around them and the exceptional being that just passed may cause them to stand frozen themselves. Regardless of their response, everyone will wonder where the stranger came from, what caused his dreadful looks, and why he arrived in the first place. But he will never answer. Frozen as he stands, all you can rely on is the image of a man in a field, marked by his history.

In the skies, our stranger is not alone. For centuries, humanity has been delving deeper and deeper into a cosmos that appeared immobile at first sight, attempting to unravel its secrets and, in time, to understand the *causality* of things. The processes that shape the structure of the universe – the formation and evolution of stars, star clusters, and galaxies, all the way up to the scales of the cosmic web – tend to take place on time scales much longer than a human lifetime. Despite the continuous motion, this difference of time scales creates the illusion of a static cosmos. Observationally, astronomers have developed indirect means to detect motion, enabling them to discern kinematics that would otherwise go unnoticed. In terms of the interpretation and underlying theory of such observations, the digital revolution of the late twentieth century has left a spectacular imprint. State-of-the-art computer simulations provide a new level of freedom that allows astrophysicists to study idealised representations of the evolution of cosmic systems at any moment in time, in any configuration they prefer. The outcomes of such simulations can be used to trace a system back to its origin. Building from certain assumptions, we can now make the stranger move.

This work concerns the formation and evolution of star clusters in the context of their galactic environment. Our own Milky Way is surrounded by structures which are almost as old as the universe itself. These ‘globular clusters’ are the strangers we aim to understand – where did they come from, and what did they endure? What is the evolutionary history of

a population of star clusters, and how is it affected by the spectacular changes that its host galaxy may have experienced? A large fraction of all observed galaxies is interacting with other galaxies, often facing an inevitable coalescence into a single, larger galaxy. It seems obvious that the star cluster systems harboured by such galaxies are influenced in some way, but the nature of these effects should be quantified. In order to grasp the role of star cluster populations as tracers of a distant past, it is essential to understand their life from birth to death. In the following chapters, the formation and evolution of star clusters will be treated, going into the internal and external processes that influence their properties, up to the point where we can witness the *co*-evolution of star clusters and galaxies.

## 1.1 Star formation

The history of a star cluster begins in a giant molecular cloud (GMC) that becomes locally unstable to gravitational collapse (Jeans 1902), possibly induced by a density wave like a spiral arm or another (tidal) perturbation. During the contraction of the cloud, smaller structures become self-gravitating. The cloud fragments into collapsing clumps, which eventually reach densities high enough to ignite nuclear fusion. By that time, the cloud has formed (proto)stars, which continue to accrete gas until their energy output<sup>1</sup> inhibits further gas inflow and evacuates the star-forming region.

Protostars do not form in isolation. The turbulent fragmentation that occurs in a collapsing GMC produces a *population* of protostars (e.g. Bonnell et al. 1998, Bate et al. 2003, Bonnell et al. 2008). It depends on the efficiency of star formation and the density of the star-forming structure whether these protostars could potentially merge to form fewer, more massive stars (see Chapter 2 and Portegies Zwart et al. 1999, Gaburov et al. 2010). Observations of star-forming regions (see Fig. 1.1) reveal young stellar populations that are consistent with the fragmentation model – star formation produces groups of stars that are spatially associated. However, this does not necessarily indicate the birth of a star cluster. Recent observations of star-forming regions in the solar neighbourhood show that star formation takes place with a continuous range of stellar number densities (Bressert et al. 2010, also see Chapter 2), some of which are so low that the stellar associations disperse almost immediately.

Star formation ends when the remaining gas is expelled by stellar winds or supernovae<sup>2</sup>. Only then, the formation of a star cluster is finally definitive – whether the spatially associated stellar structure is disrupted by the change of the gravitational potential or remains as a bound (complex of) star cluster(s) is determined by its dynamical response to the expulsion of the remaining GMC gas. The disruption of gas-embedded star clusters by gas expulsion (Hills 1980, Elmegreen 1983) is called ‘infant mortality’ (Lada & Lada 2003) and has been thought to be the driving mechanism behind the relatively low fraction of star formation that produces bound clusters (Boily & Kroupa 2003a,b, Goodwin & Bastian 2006), which is about 3–20% (Lada & Lada 2003, Bastian 2008, Portegies Zwart et al. 2010). Claims of two separate

---

<sup>1</sup>Feedback in the form of radiation, stellar winds, or supernova ejecta.

<sup>2</sup>This termination of the star formation process implies that it is not efficient, i.e. not all gas is consumed in the star formation process. Indeed, typical ‘star formation efficiencies’ are of the order of a few percent on the scales of GMCs (McKee & Ostriker 2007).

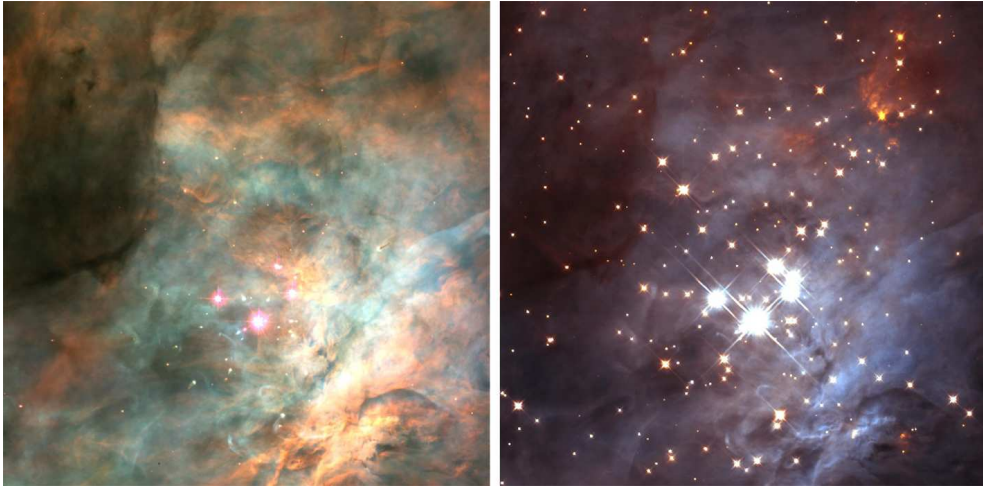


**Figure 1.1:** Hubble Space Telescope image of the Trapezium Cluster, located in the central part of the Orion Nebula (M42). *Left:* WFC2 optical image (credit: O’Dell & Wong; NASA). *Right:* NICMOS infrared image (credit: Luhman et al.; NASA). The clustered nature of the stellar structure is clearest in the infrared, which is less sensitive to extinction by the surrounding gas than optical light.

modes of star formation, yielding unbound field stars and clustered stars, have been refuted by the aforementioned discovery of a continuous range of stellar densities produced by the star formation process (Bressert et al. 2010). As we will explain in Chapter 2, the density above which the stellar structure remains bound throughout the process of gas expulsion is not constant and depends on the properties of the local environment. Consequently, the division of the star formation process in two distinct modes is not adequate, and clusters and field stars should be considered as the possible outcomes of a single star formation process.

The transition of gas-embedded structure to isolated bound star clusters poses a challenging observational problem. Visually, young stellar associations look very much alike and it can therefore be hard to assess which end up as bound structures. This touches an essential point: how is a star cluster defined? In a recent paper, Gieles & Portegies Zwart (2011) show that star clusters and associations can be reliably separated by comparing the age  $\tau$  of the stars with the crossing time ( $t_{\text{cr}} \propto \rho^{-1/2}$ , with  $\rho$  the density) of the stellar structure. Structures with stellar ages larger than their crossing times ( $\Pi \equiv \tau/t_{\text{cr}} > 1$ ) are star clusters. If the age is smaller than the crossing time ( $\Pi \equiv \tau/t_{\text{cr}} < 1$ ), the structure is an unbound association. This distinction is enhanced by the time evolution of star clusters and unbound associations – for star clusters,  $\Pi$  increases with time, while for unbound associations it decreases. In this work, the term ‘star cluster’ will refer to the bound product that remains after the star formation process ends and the remaining gas has been expelled.

As a result of the characteristics of the star formation process, star clusters are born with certain properties. Because the stars in a star cluster are generally formed from the same

GMC<sup>3</sup>, they share the same chemical composition. The short time scale on which star formation takes place implies that the stars also share the same ages – by the time that stellar structure can be identified as a star cluster, the age spread of the stars is much smaller than the age itself.

Not only the stars within a single cluster show similarities that reflect the imprint of their formation process, but also different star clusters in a population of clusters do. The distribution of stellar masses in young clusters ( $dn/dm$ , the ‘initial mass function’ or IMF) is largely universal (Bastian et al. 2010) and follows a segmented power law with a slope of  $-2.3$  at masses  $m > 0.5 M_{\odot}$  and a turnover at lower masses (Kroupa 2001). The main remaining debates in literature concern (1) the way in which real star clusters populate the massive end of this distribution, i.e. whether or not it is possible (from a probabilistic point of view) to form isolated O stars (Weidner et al. 2004, Bastian et al. 2010), (2) which underlying physics cause the characteristic mass of the distribution (e.g. Bonnell et al. 2006), and (3) whether the first generation of stars to populate the universe had a different IMF (e.g. Bromm & Larson 2004). For the star clusters that are considered in this work, the (approximate) universality of the stellar mass function is only violated due to cluster evolution, during the millions or billions of years following their formation until their eventual destruction.

## 1.2 Star cluster evolution

After the expulsion of the primordial gas, the evolution of star clusters and the stellar mass function is driven by a combination of internal and external processes. All of these processes yield a decrease of the star cluster mass, eventually leading to the destruction of a cluster. *Stellar evolution* removes the massive stars, which have the shortest lifetimes, and replaces them with stellar remnants, i.e. black holes, neutron stars or white dwarfs. This is the only destruction mechanism that is tied to a specific time scale – irrespective of the cluster mass, all clusters will have lost about 30% of their initial mass due to stellar evolution after 10 Gyr (Lamers et al. 2005a). Under the right circumstances<sup>4</sup>, the change of the gravitational potential due to the mass loss by stellar evolution can induce a secondary, dynamical loss of mass in the form of stars that were already moving at velocities close to the escape energy (Lamers et al. 2010). This additional mass loss is of the same order of magnitude as the mass loss due to stellar evolution itself. While the first-order effect of stellar evolution only removes the massive stars from a cluster, the escape probability of stars due to induced mass loss is largely independent of their mass, unless the cluster is mass-segregated (see below).

*Two-body relaxation* is the third internal disruption mechanism, but its implications are also influenced by external factors. It is dynamical in nature and does not act on a fixed time scale. Instead, the disruption rate due to two-body relaxation depends on the cluster mass

---

<sup>3</sup>There are certain exceptions to this rule, which is illustrated by the observation of multiple stellar populations in the colour-magnitude diagrams of intermediate-age star clusters in the Magellanic Clouds (e.g. Mackey & Broby Nielsen 2007, Mackey et al. 2008) and certain old globular clusters (e.g. Piotto et al. 2007). A possible explanation is that these subpopulations are the product of two star formation events at different ages or metallicities, where the second generation of stars possibly formed from the ejecta of the first generation (e.g. D’Ercole et al. 2008).

<sup>4</sup>This mainly depends on the density profile of the cluster and the effectiveness of the other disruption mechanisms.

and the tidal field in which a star cluster is situated. Two-body relaxation is the macroscopic term for the many individual encounters of the stars in a cluster, during which they exchange energy and evolve towards a state of energy equipartition (Spitzer 1987). The energy exchange affects the orbits of the stars, potentially moving them outside the Jacobi radius<sup>5</sup> at some point in time, which causes them to become unbound. The resulting rate at which mass is lost from the cluster is determined by the cluster mass – massive clusters lose a smaller fraction of their mass per unit time than low-mass clusters – and the tidal field strength – clusters orbiting an idealised galaxy with a smooth potential have higher disruption rates near the galactic centre than in the outskirts of a galaxy.

A secondary effect of two-body relaxation is mass segregation, i.e. the redistribution of stars such that the mean stellar mass decreases with radius. As a cluster evolves towards energy equipartition, to first order low-mass stars obtain higher velocities than massive stars, which causes them to move to larger radii. The massive stars sink towards the cluster centre (during which their velocity increases again) and stay there. The time scale on which mass segregation is reached decreases with stellar mass, i.e. massive stars segregate to the centre more quickly than low-mass stars move towards larger radii. The long-term effect of mass segregation is that low-mass stars have a higher probability to escape a cluster than massive stars. The mass function of stars in an *evolving* cluster is far from universal (Hénon 1969, Fukushige & Heggie 2000, Heggie & Hut 2003, Baumgardt & Makino 2003), because it is affected by cluster disruption. The rate at which it changes is set by environmental factors such as the tidal field as well as the mass of the cluster itself. This ‘low-mass star depletion’ or ‘preferential loss of low-mass stars’ also affects the integrated properties of clusters, such as their mass-to-light ratios (see Chapters 3–7).

The last disruption mechanism is related to episodic changes of the tidal field, which disrupt a star cluster by heating the kinematics of the stars (Spitzer 1958, Ostriker et al. 1972, Chernoff et al. 1986, Spitzer 1987, Gnedin & Ostriker 1997). These *tidal shocks* occur in nature when a cluster passes through a galaxy disc (a ‘disc shock’), moves through the pericentre of its orbit near the bulge of a galaxy (a ‘bulge shock’), encounters a GMC (Gieles et al. 2006b) or passes a spiral arm (Gieles et al. 2007a). Any process that changes the tidal field in which a cluster is situated causes a tidal shock and thereby contributes to the disruption of the cluster. The relative importance of the disruption rate due to tidal shocks changes with the environment. For globular clusters, which reside in the halo of large spiral and elliptical galaxies, it is known that disc and bulge shocks do not outweigh the disruption due to two-body relaxation (see Dinescu et al. 1999 and Chapter 5). However, tidal shocks do dominate the mass loss of open clusters that orbit in the discs of spiral galaxies (see Lamers et al. 2006 and Chapter 8). Although the energy injection occurs approximately uniformly throughout a cluster, the stars in the outskirts are typically closer to the escape energy than the stars residing in the cluster centre. Therefore, the mass function of the stars in a cluster can change due to tidal shocks, but only if the cluster is mass-segregated.

Summarising the different disruption mechanisms, it is evident that the long-term dynamical evolution of star clusters is largely governed by their galactic environment. When

---

<sup>5</sup>This is the radius of the zero-point in the gravitational potential, which separates the volume in which stars are bound to the cluster from the space where the stars become unbound due to the tidal field (see e.g. Fukushige & Heggie 2000, Portegies Zwart et al. 2010).



**Figure 1.2:** *Left:* optical image of the Pleiades (M45), an open cluster with an age of approximately  $10^8$  yr, taken with the Palomar 48-inch Schmidt telescope (credit: NASA/ESA/AURA/Caltech). *Right:* optical image of the globular cluster M80, which has an age of about  $10^{10}$  yr, taken with the Hubble Space Telescope/WFPC2 (credit: the Hubble Heritage Team; AURA/STScI/NASA).

considering populations of star clusters, either in different galaxies or in different parts of a single galaxy, it is important to recognise the imprints of the environment on the properties of the population. The initial age distribution of star clusters is given by the cluster formation history, while the mass spectrum of star clusters ( $dN/dM$ ) is initially characterised by a power law with index  $-2$  down to a lower mass limit of about  $50 M_{\odot}$  (Lada & Lada 2003, Portegies Zwart et al. 2010). After some  $10^8$  years of dynamical evolution, these distributions have changed. Because star clusters are disrupted as time progresses, the actual age distribution of star clusters deviates from the cluster formation history that defines its initial form – at older ages, there is an increasing deficit of clusters, up to the point where none are left and all have been disrupted (e.g. Hunter et al. 2003, Smith et al. 2007). The mass distribution of clusters evolves in a similar way. All disrupted clusters lose mass, but the relative fraction of their mass that is lost per unit time increases as fewer stars remain (Lamers et al. 2005a). In other words, the mass loss rate of a star cluster escalates. The absolute mass loss rate may decrease, but the relative mass loss rate increases. As a result, disruption causes the initial cluster mass spectrum to flatten at the low-mass end (Elmegreen & Efremov 1997, Vesperini 2001, Boutloukos & Lamers 2003, Lamers et al. 2005a, Larsen 2009).

The dynamical evolution of star clusters has a pronounced impact on the observed properties of cluster populations, primarily so in older systems. Within the Milky Way, these imprints have given rise to the classical distinction between open and globular clusters (see Fig. 1.2), which differ in terms of their ages, masses, metallicities and spatial configurations. Open clusters reside in the disc of the Milky Way, are typically young ( $\tau < 10^9$  yr), low-mass ( $M < 10^4 M_{\odot}$ ) and metal-rich ( $Z \sim Z_{\odot}$ ). Globular clusters, on the other hand, are found in the Milky Way halo, have ages comparable to the age of the universe<sup>6</sup> ( $\tau \sim 12$  Gyr), are mas-

---

<sup>6</sup>A ‘Hubble time’.



sive ( $M \sim 10^5 M_{\odot}$ ), and contain little metals ( $Z \sim 0.05 Z_{\odot}$ ). Of these two populations, the youngest should be expected to best reflect the initial properties of a population of star clusters. Indeed, the mass distribution of open clusters in different age ranges can be described by a power law with index close to  $-2$  (Portegies Zwart et al. 2010), while the mass function of globular clusters is depleted at the faint or low-mass end (Harris 1996). Over the past decade, the origin of the globular cluster mass function has been extensively debated in literature. Most studies consider a dynamical origin (Elmegreen & Efremov 1997, Vesperini 1998, Fall & Zhang 2001, Vesperini & Zepf 2003), but other works have argued that the conditions in the early universe could have been such that the initial mass spectrum of star clusters differed from its current form (Harris & Pudritz 1994, Parmentier & Gilmore 2007).

Given the ages of globular clusters, it is not surprising that their properties differ so strongly from those of open clusters. Not only is a Hubble time of dynamical evolution bound to have a lasting impact on a population of star clusters, but the environmental conditions under which globular clusters formed and evolved must also have changed widely. An understanding of how the characteristics of star cluster populations change with time, under a variety of conditions, will provide insight in the cluster populations that may result after several gigayears of cluster formation and evolution. In turn, this approach can be reversed to use (globular) cluster populations to trace the cosmic conditions throughout their history.

### 1.3 Galaxy evolution

Processes on galactic scales influence the properties of a star cluster population. The presence or absence of spiral arms, the GMC number density, and the star formation rate all impact the formation and destruction of star clusters in isolated galaxies. In the more irregular environments of interacting galaxies and dwarf galaxy accretion, large-scale processes such as tidal stripping and violent relaxation continuously redistribute stars and star clusters. These processes are capable of dominating the macroscopic evolution of star cluster populations.

Some of the main interests of modern astrophysics concern the formation and evolution of galaxies, and their hierarchical assembly through merging (e.g. Sanders & Mirabel 1996, Conselice et al. 2003). In the current picture of hierarchical cosmology (White & Rees 1978), galaxy mergers play a fundamental role. In the early universe, the first dwarf galaxies condensed from small fluctuations that deviated from an otherwise almost homogeneous distribution of matter. As the gravitational contraction of the first structures continued, these galaxies accreted gas and collided with other galaxies, coalescing to form larger and more massive systems. This hierarchical build-up of galaxies has continued up to the present day (McConnachie et al. 2009), producing a wide variety of galaxies. Some of the early dwarf galaxies are still present, but in other cases the hierarchical assembly of mass has created gas-rich spiral galaxies or giant elliptical galaxies, in which gas is absent. The cosmological environment of a galaxy determines how much gas it can accrete or whether it can merge with other galaxies. As a result, the galaxy population has emerged as an excellent tool to test cosmological models (e.g. Kauffmann et al. 1993, Somerville & Primack 1999, Bell et al. 2005). By connecting the evolution of star clusters to that of their host galaxies, hierarchical cosmology and star cluster populations become associated as well.

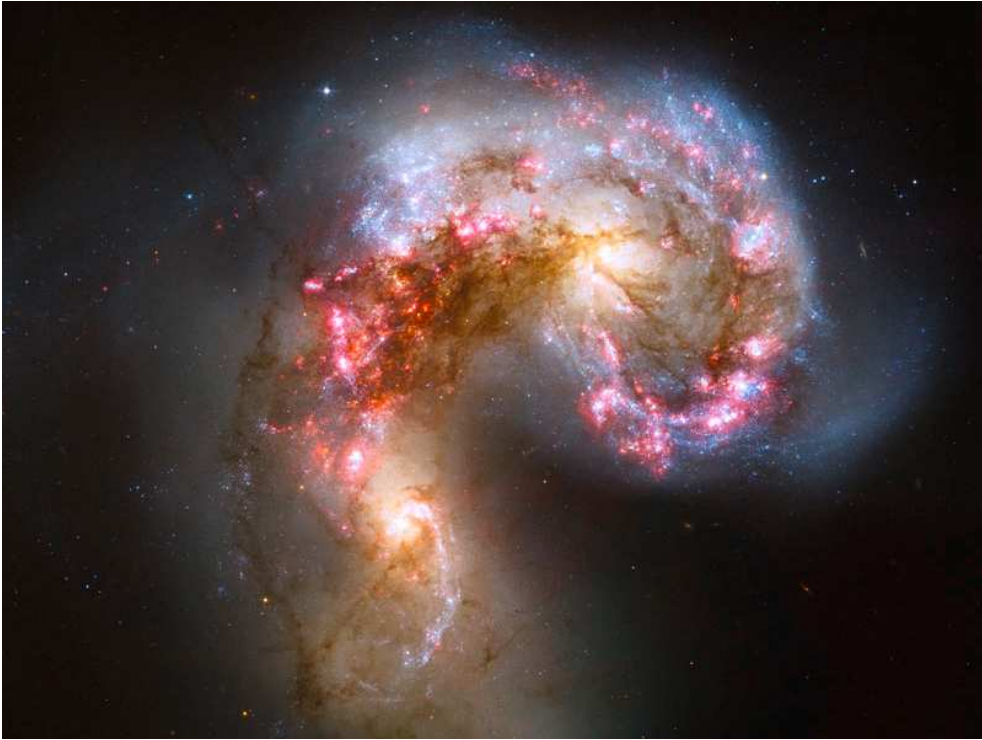


**Figure 1.3:** Optical image of the Antennae galaxies (NGC 4038/9), taken with the Hubble Space Telescope/ACS/WFC (credit: Whitmore et al.; the Hubble Heritage Team; AURA/STScI/NASA/ESA). The blue dots and clumpy structure represent (complexes of) young star clusters, which are formed at an increased rate due to the interaction between both galaxies. The orange regions are the bulges of the galaxies, the pink haze surrounding the clusters represents the gas, and the brown filamentary structure reflects the distribution of dust.

In isolated galaxies, the formation of stars and star clusters is governed by the density structure of the interstellar medium (ISM) and internal perturbations that may trigger the gravitational collapse of GMCs, which signifies the onset of star formation. On a global scale, the star formation rate density<sup>7</sup> is set by the gas density through the Schmidt-Kennicutt law (Schmidt 1959, Kennicutt 1998b). The density of star formation is higher in dense regions than in sparse ones. The clumpiness of the ISM in disc-like galaxies is known to have evolved strongly over the course of a Hubble time. Massive and dense clumps dominated the morphology of these galaxies at redshifts of  $z \sim 2$  (Elmegreen & Elmegreen 2005), which as a result have been put forward as the possible formation sites of the metal-rich part of the globular cluster population (Shapiro et al. 2010).

The range of possible origins of globular clusters is not restricted to the dense clumps

---

<sup>7</sup>The star formation rate per unit area or volume.

of isolated disc galaxies. Interacting and merging galaxies exhibit spectacular amounts of star and cluster formation in relatively small volumes. When two disc galaxies interact and merge, the tidal torques that are exerted on the galaxy discs yield an inflow of the gas towards the centres of the galaxies, where the high density fuels a burst of star formation, potentially up to  $100 M_{\odot} \text{ yr}^{-1}$  (Hernquist 1989, Mihos & Hernquist 1996). A certain fraction of this star formation will result in bound star clusters (Holtzman et al. 1992, Schweizer et al. 1996, Whitmore et al. 1999), of which the most massive ones could be the progenitors of globular clusters that populate the halos of spiral and giant elliptical galaxies (see Ashman & Zepf 1992 and Chapter 9). In the nearby universe, galaxy mergers such as the ‘Antennae’ galaxies (NGC 4038/9, see Fig. 1.3) are well known for their extremely rich populations of young, massive clusters. It is hard to imagine a better example of how the galactic (and cosmological) environment can affect a star cluster population. Not only do the starbursts change the appearance of these merging disc galaxies by consuming (almost) all of the gas and eventually leaving a ‘dead’ giant elliptical galaxy, but they also produce the beacons that may remain visible for billions of years after the collision has ended. It is one of the main aims of the final part of this work to find out which star clusters can survive such galaxy interactions, and how they are affected by these drastic events.

## 1.4 This thesis

This work concerns the formation and evolution of (populations of) star clusters in the context of their galactic environment. It covers the internal dynamics of stellar clusters during their formation and subsequent evolution, and also connects their evolution to galaxy-scale events such as mergers. The key question that will be asked throughout is how star clusters dynamically respond to their environment, and what the macroscopic implications are for a population of star clusters. The first part of this work treats the formation of stellar subclusters and their response to gas expulsion – the first stage of what could potentially become a (population of) star cluster(s). The second part discusses the internal dynamics of star clusters, the effect cluster disruption has on their photometric properties, and what the implications are for the characteristics of (globular) cluster populations. In the third and final part, the different ingredients are combined to assess the evolution of star cluster populations in simulations of (interacting) galaxies. This is the part in which the properties of star cluster populations and the evolutionary histories of their host galaxies are connected.

### Part A – The formation of star clusters

**Chapter 2** During the turbulent fragmentation of GMCs, accreting protostars interact and form small groups. These stellar subclusters are the seeds for the hierarchical formation of actual star clusters. This chapter addresses the dynamics of subclusters in hydrodynamical simulations of star formation, in order to investigate their response to gas expulsion and the fraction of star formation that results in bound clusters. When ignoring the gravitational potential of the gas, we find that the subclusters evolve towards a state of virial equilibrium before the onset of gas expulsion. This surprising result is caused by the fact that the subclus-

ters are gas-poor on spatial scales corresponding to their half-mass radii, with gas fractions below 10%. Due to their low gas fractions, the subcluster radii hardly change upon gas expulsion. By scaling the units of the simulation, we estimate the mass and length scales on which actual star clusters could become gas-poor before gas expulsion. We propose that the disruption of clusters during the transition from a gas-embedded to a gas-rid state is not always due to gas expulsion (infant mortality), but also due to the tidal shocking of clusters by the surrounding GMCs (the ‘cruel cradle effect’).

## **Part B – The evolution of star clusters in their galactic environment**

**Chapter 3** The photometric properties of star clusters are influenced by the IMF, their metallicities, the retention of stellar remnants, and the evolution of the mass function due to cluster disruption, which generally leads to low-mass star depletion (also see Chapter 7). In this chapter, we present semi-analytic star cluster models in which these effects are included. Low-mass star depletion is approximated to first order by increasing the lower mass limit of the stellar mass spectrum as a cluster loses mass. We compute the evolution of star clusters for a range of initial masses and disruption rates, and synthesise their broad-band photometric properties by using stellar evolutionary isochrones. It is found that the choice of IMF affects the mass and mass-to-light ratio evolution of clusters, the choice of metallicity influences their magnitude, colour and mass-to-light ratio evolution, the inclusion of stellar remnants alters their mass and mass-to-light ratio evolution, and accounting for low-mass star depletion impacts their magnitude and mass-to-light ratio evolution. When considering a population of clusters, low-mass (faint) clusters have typically experienced more disruption than massive clusters. As a result, we find that the mass-to-light ratio of clusters increases with cluster luminosity and mass. A comparison with the properties of Galactic globular clusters gives good results, provided that low-mass star depletion and the retention of stellar remnants are accounted for.

**Chapter 4** The mass-to-light ratios of globular clusters are too low for their respective metallicities when comparing them with simple stellar population models. We apply the models from Chapter 3 to samples of globular clusters in the Milky Way, Centaurus A, M31, and the Large Magellanic Cloud. We characterise evolutionary tracks and cluster isochrones in the mass vs. mass-to-light ratio plane, and compare the model predictions to the distribution of observed globular clusters in this plane. The models are found to be consistent with the observed masses and mass-to-light ratios for a physically acceptable range of disruption rates. Without accounting for low-mass star depletion, only 39% of all clusters lie within one standard deviation of their expected mass-to-light ratios. With our new models, this percentage increases to 92%.

**Chapter 5** Of all known Galactic globular clusters, a subset of 24 has known orbits and mass-to-light ratios. Assuming a fixed orbit over their lifetimes, we model the disruption history of these clusters to predict the mass-to-light ratio they should have according to our models from Chapter 3. The disruption rates we derive for the globular cluster orbits lie in the same range as those needed in Chapter 4. Out of the 24 globular clusters in the sample under

consideration, 12 clusters have observed mass-to-light ratios that are within one standard deviation of the predicted ones. For about half of the discrepant clusters, the difference arises because their central and global mass-to-light ratios are not similar. Our models predict global mass-to-light ratios, while the observations are biased to the stars inside the half-mass radius. This leads to dissimilarities for clusters with high mass segregation and a long disruption time. They can be excluded by imposing limits on the derived disruption rates and observed King parameters. For the thus obtained sample of clusters, the predicted and observed mass-to-light ratios are about 78% of the value they would have had without low-mass star depletion. This depletion of low-mass stars should be present in observations of the stellar mass function in globular clusters, which we confirm by considering the set of clusters for which the data is available. We end the chapter by identifying targets for an observational campaign aimed at constructing the stellar mass functions of globular clusters.

**Chapter 6** The mass function of dissolving globular clusters becomes depleted in low-mass stars, which have high mass-to-light ratios. Therefore, the cluster mass-to-light ratio decreases with respect to clusters with a stellar mass function that still follows the shape of the IMF. Statistically speaking, low-mass clusters have lost more stars than massive clusters. This implies that for a fixed age, the mass-to-light ratio increases with cluster mass and luminosity. We apply this trend to the conversion of the peaked globular cluster luminosity function to a cluster mass function. The observed luminosity function is consistent with an exponentially truncated power law initial cluster mass function, provided that the mass loss rate of the clusters depends on their mass. The slope of the globular cluster mass function at masses below the peak is 0.7 when accounting for the effects of low-mass star depletion, and 1.0 when these effects are ignored. These results hold for a single relation between luminosity and mass-to-light ratio, but also for a population of globular clusters with different orbits (and disruption rates), for which this ‘relation’ is more of a trend with substantial scatter.

**Chapter 7** The change of the stellar mass function in dissolving star clusters is caused by two-body relaxation. In this chapter, a simple physical model is derived from the principles of two-body encounters and energy considerations. The evolution of the stellar mass function is determined by the disruption rate, the masses and retention fraction of stellar remnants, and the IMF. The escape probability is typically highest at stellar masses around 15–20% of the maximum stellar mass in a cluster. After about 400 Myr, stellar evolution has decreased this mass to such an extent that stars of the lowest masses have the highest escape probability. Low-mass star depletion is inhibited by the retention of massive stellar remnants, such as black holes, which efficiently eject stars with masses similar to those of white dwarfs and neutron stars. As a result, the cluster mass constituted by the different remnant types is also affected by the dynamical evolution of the mass function. A comparison of the predicted mass function slopes to those of Galactic globular clusters gives excellent agreement.

## **Part C – The co-evolution of star clusters and galaxies**

**Chapter 8** The formation and evolution of star clusters is governed by the local environment. In isolated galaxies and galaxy mergers, the environments of star clusters should

be expected to vary widely in time and space. To address the possible emergent properties of the cluster population that could arise in a complex environment, we present  $N$ -body/hydrodynamic simulations of galaxies in which a semi-analytic model for the star cluster population is included. The model includes star formation, feedback, stellar evolution, and star cluster disruption by two-body relaxation and tidal shocks. We validate the model by comparing it to the results from  $N$ -body simulations of dissolving star clusters. The evolution of selected individual clusters shows that their evolution is dominated by the variation of their environment in time and space. In isolated disc galaxies, the disruption rate decreases with cluster age, due to clusters escaping their dense formation sites ('cluster migration') and the preferential disruption of clusters residing in dense environments ('natural selection'). These mechanisms exemplify the emergent properties of star cluster populations in complex environments. In galaxy mergers, such effects are even more prevalent. The evolutionary histories of individual clusters in a galaxy merger are completely determined by their orbits and the corresponding changes of the environment. Clusters that escape into the stellar halo survive the merger, while those clusters that stay near the central starbursts have very short lifetimes. This form of natural selection has a lasting impact on the star cluster population of a merger remnant.

**Chapter 9** Galaxy mergers are famous for their high star formation rates and large numbers of clusters. However, it is also known that dense environments and changes in the tidal field can efficiently destroy clusters. We apply the model from Chapter 8 to assess the evolution of the cluster population during a merger. It is found that the tidal shocks that occur during a merger are strong enough to destroy clusters at such a rate that destruction dominates over the formation of clusters. The number of clusters increases only for the subset of massive and young clusters that is easily detected in observations. The preferential destruction of low-mass clusters causes the power law initial cluster mass function to evolve into a peaked form. Just after the merger, the peak mass is about  $10^{2.5} M_{\odot}$ , which subsequently evolves to higher masses. This suggests that globular cluster systems could be the natural consequence of the large starbursts and the corresponding cluster disruption that took place in the early universe.

**Chapter 10** The model of Chapter 8 is applied to the case of the Antennae galaxies (see Fig. 1.3), which is a textbook example of how the changing galactic environment can affect the population of star clusters. It is found that the observed and predicted distributions of cluster ages and masses are in excellent agreement. Moreover, their characteristics suggest that the mechanisms of cluster migration and natural selection (see Chapter 8), and the resulting decrease of the disruption rate with cluster age are important for ages below  $\tau \sim 150$  Myr. This is verified by considering the mean ambient gas density of the clusters as a function of age, which is also found to decrease until ages of about  $\tau \sim 150$  Myr. We discuss the results in the context of Chapter 2 and the cruel cradle effect, and conclude the chapter by discussing how the Antennae galaxies illustrate the necessity of accounting for variations of the environment when modelling cluster populations.

# **Part A – The formation of star clusters**





---

# Chapter 2

## The dynamical state of stellar structure in star-forming regions

J. M. Diederik Kruijssen, Thomas Maschberger, Nickolas Moeckel,  
Cathie J. Clarke, Nate Bastian and Ian A. Bonnell  
*Monthly Notices of the Royal Astronomical Society*, submitted (2011)

**Abstract** The fraction of star formation that results in bound star clusters is influenced by the density spectrum in which stars are formed and by the response of the stellar structure to gas expulsion. We analyse hydrodynamical simulations of turbulent fragmentation in star-forming regions to assess the dynamical properties of the resulting population of stars and (sub)clusters. Stellar subclusters are identified using a minimum spanning tree algorithm. When considering only the gravitational potential of the stars and ignoring the gas, we find that the identified subclusters are close to virial equilibrium (the typical virial ratio  $Q_{\text{vir}} \approx 0.59$ , where virial equilibrium would be  $Q_{\text{vir}} \sim 0.5$ ). This virial state is a consequence of the low gas fractions within the subclusters, caused by gas accretion and the accretion-induced shrinkage of the subclusters. Because the subclusters are gas-poor, up to a length scale of 0.1–0.2 pc at the end of the simulation, they are only weakly affected by gas expulsion. The fraction of subclusters that reaches the high density required to evolve to a gas-poor state increases with the density of the star-forming region. We extend this argument to star cluster scales, and suggest that the absence of gas indicates that the early disruption of star clusters due to gas expulsion (infant mortality) plays a smaller role than anticipated, and is potentially restricted to star-forming regions with low ambient gas densities. We propose that in *dense* star-forming regions, the tidal shocking of young star clusters by the surrounding gas clouds could be responsible for the early disruption. This ‘cruel cradle effect’ would work in addition to disruption by gas expulsion. We suggest possible methods to quantify the relative contributions of both mechanisms.

### 2.1 Introduction

Over the past years, the implications of clustered star formation have touched a range of astrophysical disciplines, from the scales of the star formation process itself (see the review by

McKee & Ostriker 2007) to the fundamental properties of young star clusters (e.g. McMillan et al. 2007, Allison et al. 2009a, Moeckel & Bonnell 2009), or possibly even the global stellar mass assembly of galaxies (see e.g. Pflamm-Altenburg et al. 2007, Bastian et al. 2010). While it seems evident that most stars form in a clustered setting (e.g. Parker & Goodwin 2007), estimations of the exact fraction are hampered by the substantial dissociation of stellar structure that occurs during (but is not necessarily related to) the transition from the gas-embedded phase to classical, gas-poor star clusters (Lada & Lada 2003, Portegies Zwart et al. 2010). The traditional interpretation that most, if not all stars form in clusters, with gas expulsion leading to their early disruption ('infant mortality', see Lada & Lada 2003, Bastian & Goodwin 2006, Goodwin & Bastian 2006) has recently been challenged by observational studies suggesting that stars form with a continuous distribution of densities, of which only the high-density tail eventually leads to bound stellar clusters (Bressert et al. 2010, Gieles & Portegies Zwart 2011).

Current advancements in numerical calculations of turbulent fragmentation in star-forming regions enable the study of clustered star formation in increasing detail (e.g. Bonnell et al. 1998, Klessen & Burkert 2000, Bate et al. 2003, Bonnell et al. 2008). However, theoretical investigations of the response of stellar structure to gas expulsion are still largely based on the assumption of either a static gas potential or initial equilibrium between the stars and gas (e.g. Tutukov 1978, Adams 2000, Geyer & Burkert 2001, Boily & Kroupa 2003a,b, Baumgardt & Kroupa 2007, Parmentier et al. 2008), which need not apply to star-forming regions in nature. A more realistic setting was recently explored by Offner et al. (2009), who find that the velocity dispersions of the stars in hydrodynamic simulations of star formation are smaller than that of the gas by about a factor of 5, suggesting that the assumption of equilibrium between both components indeed does not hold. The response of star clusters to gas expulsion has also been investigated by Moeckel & Bate (2010), who consider  $N$ -body simulations of star clusters using initial conditions from hydrodynamic simulations, and by Moeckel & Clarke (2010), who address the dynamical evolution of star clusters under the condition of ongoing gas accretion. They propose that the disruptive effect of gas expulsion is limited by the way in which gas and stars are redistributed by the accretion-induced shrinkage of clusters.

The hydrodynamical calculations of Bonnell et al. (2008) cover the hierarchical formation of several stellar (sub)clusters, which have been identified and analysed by Maschberger et al. (2010). The simulation is very suitable for investigating the properties of the (sub)cluster population due to the relatively large range of mass scales of the modelled structure (see Sect. 2.2). In this paper, we analyse the simulations reported in Bonnell et al. (2008) to probe the response of gas-embedded stellar structure to gas expulsion. We consider the dynamical state of the stars while ignoring the gas, which is equivalent to observing the stellar structure under the condition of instantaneous gas expulsion at any time in the simulation.

This paper starts with a discussion of the setup of the simulations, the subcluster identification algorithm, and the characteristics of the stellar structure in Sect. 2.2. An analysis of the dynamical state of the subclusters follows in Sect. 2.3, which covers quantities such as the virial ratio, bound mass fraction and gas content. The response of the clusters to gas expulsion and an extension to the length scales of actual star clusters is considered in Sect. 2.4. The paper is concluded with a summary and an outlook in Sect. 2.5, where we discuss the possible dependence of the results on the initial conditions of the simulations and the input

physics, and suggest ways in which our analysis could be improved and extended.

## 2.2 Simulations and cluster selection

In this work, we analyse the hydrodynamical/ $N$ -body simulations of Bonnell et al. (2003) and Bonnell et al. (2008), extending the analysis of Maschberger et al. (2010) and Maschberger & Clarke (2011). These smoothed particle hydrodynamics (SPH) simulations follow the evolution of a initially marginally unbound, homogeneous gas sphere of  $10^3 M_\odot$  with a diameter of 1 pc (Bonnell et al. 2003), and a cylinder of  $3 \times 10$  pc that contains  $10^4 M_\odot$  gas, bound in the upper part and unbound in the lower (Bonnell et al. 2008). Initial turbulent motions are modelled with an initially divergence-free random Gaussian velocity field with a power spectrum  $P(k) \propto k^{-4}$ . The gas is kept at a temperature of 10 K, staying isothermal throughout the  $10^3 M_\odot$  simulation. In the  $10^4 M_\odot$  simulation, the gas follows a modified Larson-type equation of state (Larson 2005) comprised of three barotropic equations of state:

$$P = k\rho^\gamma, \quad (2.1)$$

with  $P$  the pressure,  $\rho$  the density, and where

$$\begin{aligned} \gamma &= 0.75; & \rho &\leq \rho_1 \\ \gamma &= 1.0; & \rho_1 < \rho &\leq \rho_2 \\ \gamma &= 1.4; & \rho_2 < \rho &\leq \rho_3 \\ \gamma &= 1.0; & \rho &> \rho_3, \end{aligned} \quad (2.2)$$

and  $\rho_1 = 5.5 \times 10^{-19} \text{ g cm}^{-3}$ ,  $\rho_2 = 5.5 \times 10^{-15} \text{ g cm}^{-3}$ ,  $\rho_3 = 2 \times 10^{-13} \text{ g cm}^{-3}$ .

Star formation is modelled via sink particles, which are formed if the densest gas particle and its  $\sim 50$  neighbours are gravitationally bound (the critical density is  $1.5 \times 10^{-15} \text{ g cm}^{-3}$  for the  $10^3 M_\odot$  simulation, and  $6.8 \times 10^{-14} \text{ g cm}^{-3}$  for the  $10^4 M_\odot$  simulation). The mass resolutions of the sink particles are  $\sim 0.1 M_\odot$  and  $0.0167 M_\odot$ , respectively. Accretion onto sink particles occurs if SPH particles move within the sink radius (200 AU for both simulations) and are gravitationally bound, or if SPH particles move within the accretion radius (40 AU for both simulations). Gravitational forces between sink particles are softened at smoothing lengths of 160 AU ( $10^3 M_\odot$ ) and 40 AU ( $10^4 M_\odot$ ).

Under the influence of gravity, the initially smooth gas distributions quickly form filaments in which the sink particles are formed. The sink particles themselves group together in subclusters that merge into larger structures, leading to the formation of one ‘star cluster’ in the  $10^3 M_\odot$  simulation and about three ‘star clusters’ in the  $10^4 M_\odot$  simulation. Throughout this paper, we will focus on the  $10^4 M_\odot$  simulation, which contains about ten times more subclusters than the  $10^3 M_\odot$  simulation, and therefore enables us to consider a *population* of subclusters rather than a select set of examples. We also ran our analyses for the  $10^3 M_\odot$  simulation, which gave results that are consistent with those from the  $10^4 M_\odot$  simulation.

For the identification of the subclusters, we employ a minimum spanning tree (MST) based clustering technique, which has been used in the context of young star forming regions (e.g. Maschberger et al. 2010, Kirk & Myers 2011). The MST, which has the advantageous

property of not imposing any geometrical symmetry on the data set, has also been used to quantify the amount of substructure (e.g. Cartwright & Whitworth 2004, Schmeja et al. 2008, Maschberger et al. 2010) and mass segregation (e.g. Allison et al. 2009a,b, Maschberger et al. 2010, Parker et al. 2011 – see Moeckel & Bonnell 2009 and Maschberger & Clarke 2011 for alternative methods) in star forming regions. The MST is a concept from graph theory, which represents the unique connection of all points of a data set, so that there are no closed loops (a ‘tree’), and so that the total length of all edges between the points is minimal. Typically, two separated groups of points are connected with one single, long edge, whereas the points within the groups have short edges. By simply removing edges that are longer than a chosen break distance the tree can be split in subtrees, which connect the points of the subclusters in the data set (further information on MST based clustering techniques can be found in Zahn 1971). To avoid spurious detections, we require that a subcluster contains a minimum number of 12 stars.

The MST technique utilises one free parameter, which is the break distance. Automated methods to determine the break distance are ill-suited for the analysis of the simulations due to the highly varying properties of the stellar distribution. We therefore choose a break distance of  $d_{\text{break}} = 0.035$  pc, which gives subclusters that are comparable to those identified by the human eye, although they do not include the stellar haloes surrounding them. This break distance is larger than the choice of Maschberger et al. (2010), but leads to comparable clusters because we analyse the stellar structure in three spatial dimensions and not in projection. Because the choice of a single break distance could introduce an artificial length scale into the analysis (Bastian et al. 2007), we have also performed our calculations for a set of other break distances in the range  $d_{\text{break}} = 0.020\text{--}0.100$  pc, of which the results are used when discussing the implications and applicability of our findings in Sects. 2.4 and 2.5.

An example of the results of the subcluster identification method can be seen in Fig. 2.1, which shows the spatial distribution of sink particles and subclusters at the end of the  $10^4 M_{\odot}$  simulation at  $t = 0.641$  Myr, some 0.3 Myr after the onset of star formation. At this point in the simulation, after one free-fall time, about 60% of all stellar mass is constituted by subclusters. The spatial distribution shown in Fig. 2.1 is the result of a complex tree of hierarchical merging of small subclusters (Maschberger et al. 2010). This process is still ongoing at the end of the simulation, which is illustrated by the close proximity of the subclusters towards the right in the plane of Fig. 2.1.

Following Casertano & Hut (1985), we use the projected distance to the  $N$ th nearest neighbour to determine the surface density distribution of the sink particles. For a rank number  $N$ , the local surface density at the locations of each of the sink particles is  $\Sigma_{\text{sink}} = (N - 1)/(\pi D_N^2)$ , with  $D_N$  the projected distance to the  $N$ th nearest neighbour in the x-y plane. The resulting distribution of surface densities for  $N = 7$  is shown in Fig. 2.2, which includes all sink particles at the end of the simulation ( $t = 0.641$  Myr), as well as those from a snapshot at  $t = 0.442$  Myr, not too long after the onset of star formation (also see Fig. 2.3). The difference between the surface density distributions at both times shows that the stellar structure in the simulation typically evolves towards higher densities, even though the density range spanned by the sink particles does not change much. As should be expected, the high end of the surface density distribution is occupied by the sink particles that are residing in subclusters (shaded area), reaching densities of more than  $10^5$  stars per  $\text{pc}^2$ . These surface densities

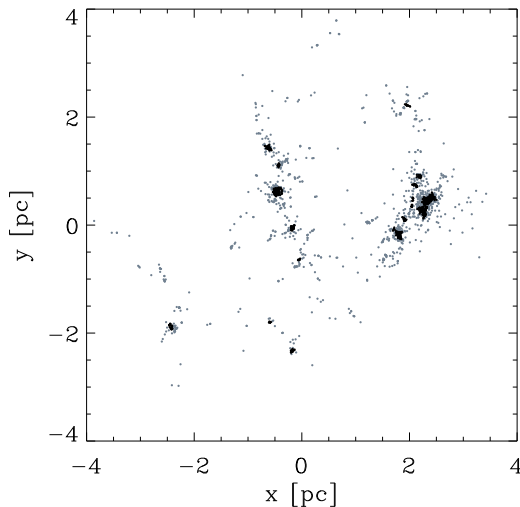


**Figure 2.1:** Spatial distribution of sink particles that are present at the end of the  $10^4 M_{\odot}$  simulation ( $t = 0.641$  Myr), projected on the x-y plane. Black particles constitute subclusters, and dark grey particles belong to the field population. Since the spatial extent of the simulation in the z-direction is larger than in the x-y plane, some of the apparent clustering is the result of the projection.

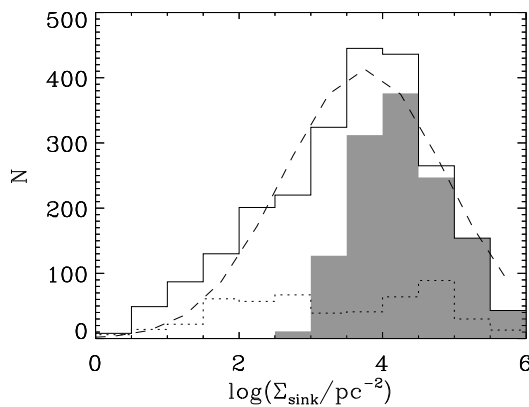


**Figure 2.2:** Surface density distributions of sink particles. The solid histogram includes all sink particles present at the end of the simulation ( $t = 0.641$  Myr), with the shaded histogram marking the subset of particles that belong to subclusters. The dashed curve represents a lognormal fit to the distribution with a peak at  $\log(\Sigma_{\text{sink}}) = 3.75$  and a dispersion of  $\sigma_{\log \Sigma} = 1.13$ . For comparison, the dotted histogram denotes the surface density distribution of sink particles at  $t = 0.442$  Myr.

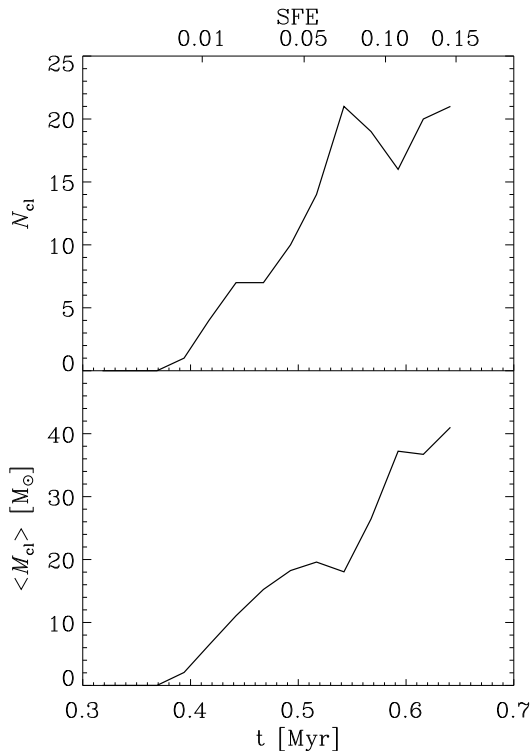


**Figure 2.3:** *Top:* time evolution of the number of subclusters. *Bottom:* time evolution of the mean subcluster mass. The star formation efficiency (SFE) of the entire simulation is indicated along the top axis.

are several orders of magnitude higher than those observed in nearby ( $< 500$  pc) star-forming regions by Bressert et al. (2010), which is not surprising for three reasons. Firstly, crowding obstructs the observation of the densest parts of star-forming regions, which are therefore not included in their sample. Secondly, we consider a population of *subclusters* in a region that would be identified as only one or two actual star clusters in their analysis. Lastly, the high densities that are achieved in the simulation are likely the result of the initial conditions. Nonetheless, the surface densities do compare well to the high-density region in the Orion Nebula cluster (ONC;  $\Sigma \geq 10^3 \text{ pc}^{-2}$ , Hillenbrand & Hartmann 1998, Bressert et al. 2010), although the system under consideration here is about one order of magnitude younger than the ONC.

The subcluster assembly history is considered in Fig. 2.3, which shows how the number of subclusters and the mean subcluster mass evolve as a function of time and star formation efficiency (SFE, the fraction of gas that has been converted to stars). The number of subclusters initially increases until it reaches a maximum, which occurs when the formation of new

concentrations of sink particles is neutralised by the hierarchical merging of other subclusters. This is nicely illustrated by the mean stellar subcluster mass, which steeply increases around  $t = 0.55\text{--}0.60$  Myr, when the merging of new-formed subclusters causes the number of clusters to decrease. The mean mass keeps increasing until the end of the simulation due to the ongoing accretion of gas and small subclusters onto sink particles and the merging of small subclusters with a few massive ones. This mass increase would eventually be halted on time scales much longer than the duration of the simulation, when the available gas reservoir is depleted or, more likely, when the further inflow of gas is obstructed by feedback from supernovae and stellar winds (neither of which are included in the simulation).

## 2.3 Dynamical state of stellar subclusters

Whether or not a gas-embedded stellar structure survives gas expulsion depends on its dynamical state. Excluding the gas from the dynamical analysis is equivalent to observing the stellar structure at the moment of instantaneous gas removal. This represents the extreme case of gas expulsion, since a more gradual expulsion could allow a subcluster to (adiabatically) respond to the potential change and thereby retain a larger number of stars. As a result, the analysis of the dynamical state of solely the stellar component in simulations of star formation provides a lower limit to the retention of stellar structure upon gas removal.

### 2.3.1 Dynamical quantities

We have followed the evolution of several (dynamical) properties of the identified subclusters over the course of the simulation of Bonnell et al. (2008), such as the stellar mass, the stellar half-mass radius<sup>1</sup>, the fraction of the subcluster mass that is bound, and the virial ratio. The properties of the stellar component are supplemented with information on the gas, including the gas mass fractions within the subclusters.

The gravitational boundedness and virial ratio of subclusters are fundamental measures for their dynamical state. Both quantities are based on the potential energy and internal kinetic energy of a subcluster. For a sink particle  $i$ , the potential energy  $V_i$  is defined as

$$V_i = - \sum_{j \neq i} \frac{Gm_i m_j}{r_{ij}}, \quad (2.3)$$

where  $m_i$  and  $m_j$  are the sink particle masses and  $r_{ij}$  their mutual distance. The kinetic energy  $T_i$  of a sink particle is

$$T_i = \frac{1}{2} m_i |\mathbf{v}_i - \mathbf{v}_{\text{cl}}|^2, \quad (2.4)$$

where  $\mathbf{v}_i$  and  $\mathbf{v}_{\text{cl}}$  are the respective velocity vectors of the sink particle and the centre of mass of the subcluster. A particle is gravitationally bound if  $T_i + V_i < 0$ . We define the virial ratio

---

<sup>1</sup>The subclusters have predominantly small elongations (Maschberger et al. 2010, Fig. 10), which enables the use of a half-mass radius.

$Q_{\text{vir}}$  as

$$Q_{\text{vir}} = -\frac{2 \sum_i T_i}{\sum_i V_i}. \quad (2.5)$$

The factor 2 reflects the correction for counting the potential energy twice for each particle pair when combining Eqs. 2.3 and 2.5. A subcluster is in virial equilibrium if  $Q_{\text{vir}} \sim 0.5$  and gravitationally bound if  $Q_{\text{vir}} < 1$ . Supervirial subclusters have  $Q_{\text{vir}} > 0.5$ , while subvirial subclusters have  $Q_{\text{vir}} < 0.5$ .

It is possible that a single, dynamically hard binary, triple or multiple system dominates the energy of a subcluster. We correct for this by searching the sink particle list for binaries<sup>2</sup> and replacing them with a single centre of mass particle. We repeat this step two more times, thereby correcting for triples and higher-order multiple systems. During the last iteration, the kinetic and potential energies of the subclusters generally remain unchanged, which indicates that a correction for higher order multiples is not required. We quantify the effect of binaries on the observables of interest below.

In previous studies, the SFE has been identified as a key parameter which determines the survival chances of stellar clusters upon gas expulsion (e.g. Goodwin & Bastian 2006). However, a more fundamental critical factor is the dynamical state of the stars when the gas is removed. The *effective* SFE,  $\text{eSFE} = 1/2 Q_{\text{vir}}$ , was therefore introduced as a measure for the survival probability of stellar structure at the moment of instantaneous gas expulsion (e.g. Verschueren 1990, Goodwin 2009). If the gas and stars were in virial equilibrium before gas expulsion, the eSFE is equivalent to the actual SFE. If they were not in virial equilibrium, the eSFE no longer reflects the actual SFE. In that case, the survival chance of stellar clusters is not related to the actual SFE, but is solely determined by their dynamical state. The eSFE is naturally higher in the identified subclusters than in the simulation as a whole.

### 2.3.2 Virial ratio

As star formation progresses, the population of subclusters grows in terms of its total mass. The hierarchical merging of the subclusters inhibits the increase of their number and causes it to level off towards the end of the simulation, when the formation of new subclusters is balanced by their accretion onto more massive ones (see Fig. 2.3 and Maschberger et al. 2010). Another consequence of this hierarchical buildup is that the properties of the subcluster population as a whole is not a direct representation of the evolution of individual subclusters, but also include ‘emergent’ properties of the population due to the interactions between the subclusters. This is also relevant when considering the mean virial ratio of the subclusters as a function of time. Individual subclusters can be formed either subvirially or supervirially with respect to the total potential, and would eventually virialise with the total potential if kept in isolation. Deviations from this trend occur when subclusters merge or accrete smaller stellar aggregates, which temporarily increases the virial ratio of the merger product due to the relative velocity of the progenitors. Another thing to keep in mind is that we only include

---

<sup>2</sup>Binaries are selected by identifying a most bound partner for each sink particle. If it exists and the semimajor axis is smaller than 1000 AU, it is considered a binary.



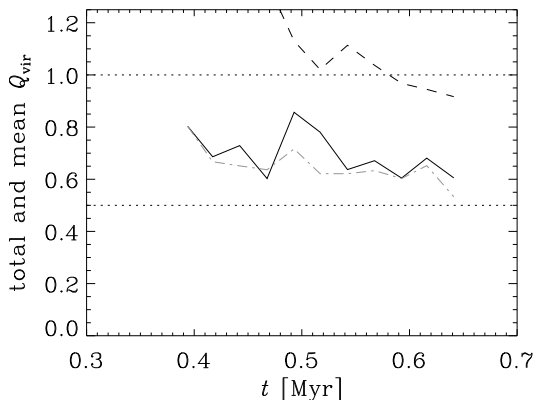


**Figure 2.4:** Time evolution of the mean virial ratio of the stellar subclusters (black solid line), of the mean virial ratio weighted by subcluster mass (grey dash-dotted line), and of the total virial ratio of all sink particles in the simulation (dashed line). The horizontal dotted lines indicate the marginally gravitationally bound case ( $Q_{\text{vir}} < 1$ ) and the virialised case ( $Q_{\text{vir}} = 0.5$ ). After  $t = 0.5$  Myr, about 40–60% of the stars resides in subclusters.

the stars in our dynamical analysis, implying that the obtained virial ratio is always higher than its actual value by an amount that depends on the gas fraction. This affects the mean virial ratio of the population of subclusters, in which there is a continuous formation of new, gas-rich subclusters, which are typically still supervirial and only reach  $Q_{\text{vir}} = 0.5$  after some further evolution.

Despite the complex setting of hierarchical star formation, the evolution of the mean virial ratio can be used as a first indication of how the dynamical state of the subcluster population evolves over time. This is shown in Fig. 2.4, which also includes the time evolution of the virial ratio of the entire simulation. As indicated earlier, we ignore the contribution of the gas to the gravitational potential, in order to assess the dynamical state of the stellar structure under the assumption of instantaneous gas removal. Even without accounting for the gas potential, the population of subclusters evolves to a near-virialised state on a time scale of only a few tenths of a Myr. This would suggest that the subclusters are typically gas-poor on length scales corresponding to their half-mass radii. The difference between the mean virial ratio and the mean virial ratio weighted by subcluster mass in Fig. 2.4 indicates that more massive subclusters are typically somewhat closer to virial equilibrium than low-mass subclusters. This is more of a trend than a relation: a simple linear regression of the virial ratio and subcluster mass  $M$  yields a best fit of  $Q_{\text{vir}} = 0.86 - 0.16 \log M$ , but with scatter larger than the fitted slope. Lastly, it is also shown by Fig. 2.4 that the entire stellar population in the simulation does not reach virial equilibrium, but does become marginally bound. This occurs because the simulation as a whole has a higher gas fraction than the subclusters (see Sect. 2.3.3), which illustrates that the SFE depends on the location and length scale on which

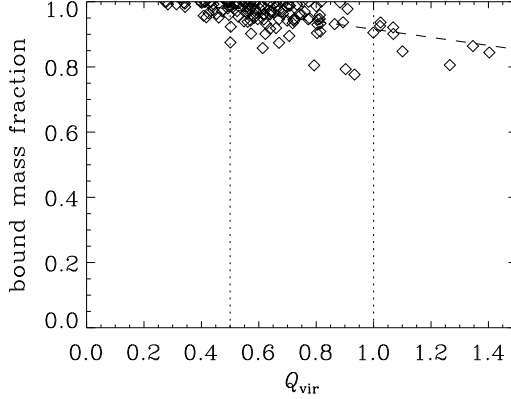


**Figure 2.5:** Dependence of the bound mass fraction (ratio of the total mass of the bound sink particles to the subcluster mass) on the virial ratio for the subclusters from all snapshots of the simulation. Each symbol represents a subcluster. The dashed line represents a linear fit to the data. Like in Fig. 2.4, the dotted lines indicate the marginally gravitationally bound case ( $Q_{\text{vir}} < 1$ ) and the virialised case ( $Q_{\text{vir}} = 0.5$ ).

it is computed. The dynamical state of the entire simulation also bears some traces of the initial conditions, covering a cylinder that contains a bound upper half and an unbound lower half (see Sect. 2.2).

The virial ratios of individual subclusters do not show notable correlations with subcluster mass or half-mass radius<sup>3</sup>. Instead, they depend more strongly on the recent mass evolution of the subclusters. The virial ratio temporarily increases whenever the subcluster mass increases, be it due to the merging with other subclusters or by individual sink particles moving inside the MST break distance. When sink particles move more than a break distance away and the subcluster mass decreases, the virial ratio decreases as well. Both are natural consequences of the inclusion or exclusion of transient substructure in the identification of the subclusters. The same dependence is found when using different MST break distances to identify the subclusters: larger break distances yield more extended subclusters and consequently the mean virial ratio is higher. When set to extreme values ( $d_{\text{break}} > 0.050$  pc), close passages of subclusters are incorrectly picked up as merger products, causing a spurious increase of the virial ratio. For the largest break distance used in our analysis ( $d_{\text{break}} = 0.100$  pc), these fluctuations can yield mean virial ratios briefly hitting  $\langle Q_{\text{vir}} \rangle = 1$ , in clear contrast with the result from Fig. 2.4.

The quantity that most strongly correlates with the virial ratio is the bound mass fraction of the subclusters, i.e. the fraction of their mass that is bound even without accounting for the potential of the gas (see the definition in Sect. 2.3.1, a sink particle is bound if  $T_i +$

<sup>3</sup>Except for the unbound subclusters ( $Q_{\text{vir}} > 1$ ), which are generally small ( $r_h < 0.04$  pc) and low-mass ( $M < 30 M_{\odot}$ ).

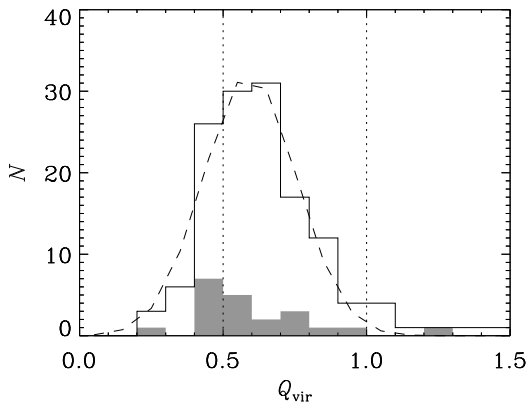


**Figure 2.6:** Histogram of the virial ratios of the subclusters from all snapshots of the simulation (solid line). The shaded histogram represents the set of subclusters from the last snapshot at  $t = 0.641$  Myr. The dashed line is a Gaussian fit to the data for all snapshots, with mean value  $Q_{\text{vir}} = 0.59$  and standard deviation  $\sigma_Q = 0.16$ . The vertical dotted lines again indicate the marginally gravitationally bound case ( $Q_{\text{vir}} < 1$ ) and the virialised case ( $Q_{\text{vir}} = 0.5$ ).

$V_i < 0$ ). It is shown in Fig. 2.5 that subclusters with high virial ratios tend to have lower bound mass fractions, albeit with substantial scatter. This is not surprising, because the virial ratio is efficiently increased by fast, unbound sink particles that are included by the MST algorithm but would be left out with a physically motivated identification. For larger break distances, the correlation between bound mass fraction and virial ratio is stronger, due to the erroneous identification of kinematically hot structure as subclusters. Nonetheless, most subclusters contain only very few unbound stars, with typical bound mass fractions of 0.95. Figure 2.5 also confirms that most subclusters are close to virial equilibrium, which was already suggested by the evolution of the mean virial ratio in Fig. 2.4. For further illustration, Fig. 2.6 shows the distribution of the virial ratios of the subclusters from all snapshots, as well as those from the last snapshot, which are shown as the shaded region. Only 8% of the subclusters are unbound when excluding the gas, while 25% remains subvirial. When considering the subclusters from all snapshots, a Gaussian fit to the distribution of virial ratios gives a mean of  $Q_{\text{vir}} = 0.59$  and a standard deviation of  $\sigma_Q = 0.16$ . As in Fig. 2.4, the gradual decrease of the mean virial ratio towards  $Q_{\text{vir}} = 0.5$  is also visible in Fig. 2.6. A comparison of the two histograms shows that the subclusters in the last snapshot are closer to being virialised than the population of subclusters from all snapshots. These virial ratios imply that the eSFE is close to unity, i.e. the majority of subclusters will not be strongly affected by gas expulsion (see Sect. 2.4).

Replacing hard binaries and higher order multiples by their centre of mass particles is essential to obtain a reliable picture of the subcluster dynamics. The disruption of the subclusters during gas expulsion is controlled by the dynamical state of the binary centres of

mass rather than the binaries themselves. If we would not correct for binaries or higher order multiples, the measures for the dynamical state of the subclusters would fluctuate with the orbital phase of a few tightly bound and eccentric binaries.

The bound mass fraction of the subclusters is not strongly affected by the presence of binaries (unbound sink particles are generally single), but because binaries are in virial equilibrium<sup>4</sup> or slightly subvirial, the mean virial ratio of the subclusters from all snapshots is decreased by 0.1–0.2 if it is not corrected for multiples. About two thirds of this difference is due to binaries, while the remaining third is accounted for by triples and quadruples. This shift of the virial ratio means that without correcting for binaries, the subclusters could be incorrectly interpreted as being slightly subvirial<sup>5</sup> ( $Q_{\text{vir}} \sim 0.45\text{--}0.50$ ), and the entire simulation would be close to virialised ( $Q_{\text{vir}} \sim 0.60\text{--}0.65$ ) instead of the marginally bound state that is shown in Fig. 2.4. With respect to the binary-corrected results from Fig. 2.4, this rather modest difference arises because the finite gravitational smoothing length used in the simulation inhibits the formation of very hard binaries. Nonetheless, the correction for binaries improves the accuracy of our analysis, and therefore all results shown in this paper are corrected for binaries and higher order multiple systems.

### 2.3.3 Gas content

The key question is *why* the subclusters are so close to virial equilibrium when neglecting the gas potential. An obvious answer would be that the subclusters are generally gas-poor, which would imply that they are hardly affected by the gas potential in the first place. To assess the gas potential and its time evolution, we have analysed the distribution of the gas in two snapshots of the simulation, at times  $t_1 = 0.442$  Myr (when star formation is ongoing) and  $t_2 = 0.641$  Myr (the last snapshot of the simulation, after one free-fall time; also see Fig. 2.3). For each of the identified subclusters in these snapshots, we calculate the fraction of the total mass within the stellar half-mass radius of the stellar distribution that is constituted by gas. The distribution of these gas fractions is shown in Fig. 2.7, which confirms that the subclusters are indeed gas-poor on their typical length scales, with gas fractions of  $\langle f_{\text{gas}} \rangle = 0\text{--}0.2$ . Because the simulation does not include feedback, this means that the accretion of gas onto the sink particles can keep up with the overall gas inflow towards the subclusters. Another mechanism that naturally leads to gas-poor subclusters is their accretion-driven shrinking (Bonnell et al. 1998, Moeckel & Bate 2010, Moeckel & Clarke 2010), which increases the density contrast between the subclusters and the surrounding gas.

Gas accretion and the time evolution of the structural properties of the population of subclusters both further decrease the gas fraction as time progresses. This evolution is illustrated by comparing the data of the two snapshots in Fig. 2.7, corresponding to times  $t_1 = 0.442$  Myr and  $t_2 = 0.641$  Myr. During the enclosed time interval, the mean gas fraction of all detected subclusters decreases by 0.63 dex, from  $\langle f_{\text{gas}}(t_1) \rangle = 0.238$  to  $\langle f_{\text{gas}}(t_2) \rangle = 0.056$ . The mean

---

<sup>4</sup>Instantaneously, this only holds for binaries on circular orbits. Binaries on eccentric orbits exhibit a variation of the virial ratio, with a subvirial state near apocentre and a supervirial state near pericentre. When considering the time-averaged virial ratio, eccentric binaries are in virial equilibrium. However, because the phase velocity is lowest near apocentre, a sampled population of randomly oriented binaries will typically be slightly subvirial.

<sup>5</sup>As in all of Sect. 2.3.2, this statement excludes the gravitational potential of the gas.

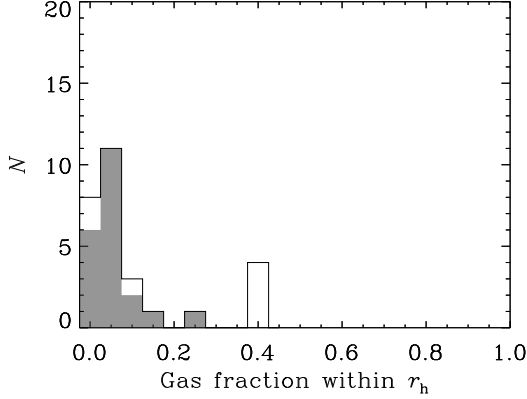


**Figure 2.7:** Histogram of the gas fraction within the stellar half-mass radius  $r_h$  of each subcluster from the two snapshots at  $t_1 = 0.442$  Myr and  $t_2 = 0.641$  Myr (solid line). The shaded histogram only shows the gas fractions for the last snapshot at  $t = 0.641$  Myr.

half-mass radius of the subclusters decreases from  $\langle r_h(t_1) \rangle = 0.020$  pc to  $\langle r_h(t_2) \rangle = 0.013$  pc, which is a decrease of 0.18 dex. Even though the shrinking of subclusters is a second order effect caused by gas accretion, it is interesting to ask which of both mechanisms contributes most to the decrease of the gas fraction. Is it mainly driven by the increasing mean stellar density of the subclusters or by the ongoing gas accretion onto the sink particles?

To assess the relative contributions to gas depletion by accretion and subcluster shrinking, we consider the spatial distribution of the sink particles and the gas. Due to the relatively small numbers of stars in individual subclusters, it is best to examine the mean density profiles of the populations of subclusters in the two snapshots at  $t_1$  and  $t_2$ . Such a combination of the different density profiles decreases the influence of low-number statistics on the result. In Fig. 2.8, we show the subcluster mass-weighted, mean cumulative mass distributions of gas, sink particles, and both combined. The distributions represent the enclosed mass fractions  $\mu$ , normalised to the sum of the subcluster mass  $M_{cl}$  and the enclosed gas mass within three stellar half-mass radii  $M_{gas}$ :

$$\mu_i(\xi) \equiv \frac{M_i(\xi)}{M_{cl} + M_{gas}}, \quad (2.6)$$

with  $i = \{\text{stars, gas, all}\}$  and  $M_i(\xi)$  the enclosed mass at  $\xi \equiv r/r_h$ , which is the radial distance in units of the stellar half-mass radius. The mean distributions shown in Fig. 2.8 are weighted by subcluster mass to emphasise those subclusters with better statistics. A first comparison of both panels in Fig. 2.8 shows that the gas fraction indeed decreases between  $t_1$  and  $t_2$ . The contribution to this decrease by subcluster shrinking can be estimated by a simple thought experiment, in which the gas distribution is kept fixed and the distribution of stellar mass is compressed by the appropriate amount. In the top panel of Fig. 2.8, the half-mass radii

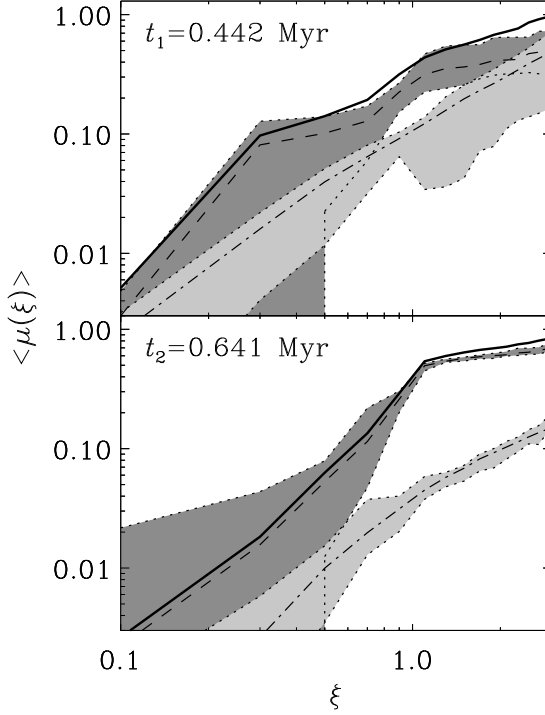


**Figure 2.8:** Subcluster mass-weighted, mean cumulative mass fractions  $\langle \mu(\xi) \rangle$  (see Eq. 2.6) of sink particles (dashed line), gas particles (dash-dotted line) and the sum of both (solid line), as a function of the radial distance in units of the half mass radius ( $\xi \equiv r/r_h$ ). *Top:* mean cumulative distributions for the subclusters present at  $t_1 = 0.442$  Myr. *Bottom:* mean cumulative distributions for the subclusters present at  $t_2 = 0.641$  Myr. The shaded areas enclosed by the dotted lines mark the 16th and 84th percentiles and illustrate the typical spread of the enclosed mass fractions of sink particles (dark grey) and gas (light grey).

$\langle r_h(t_1) \rangle$  and  $\langle r_h(t_2) \rangle$  correspond to  $\xi = 1$  and  $\xi = 0.66$ , between which the enclosed gas mass differs by 0.26 dex. In other words, if the gas distribution was held fixed and the stellar distribution was shrunk appropriately, then the gas fraction within the new half-mass radius would have declined by 0.26 dex. This is a probe for the decrease of the gas fraction that is solely caused by the shrinking of the subclusters. Comparing it with the actual decrease of the mean gas fraction between  $t_1$  and  $t_2$  of 0.63 dex, we see that it covers about half of the decrease, with the remaining 0.37 dex covered by gas accretion itself – not only by adding to the mass in stars, but also by decreasing the gas mass. We conclude that the evacuation of the gas due to ongoing gas accretion is about equally important for the gas depletion as the shrinking of the subclusters.

Apart from enabling a quantitative comparison of the effect of gas accretion and cluster

shrinking, Fig. 2.8 also demonstrates the spatial variation of the gas fraction in the subclusters. At early times, the gas is still prevalent in the outskirts of the subclusters, contributing 20–60% of the enclosed mass at  $\xi = 3$ . At the end of the simulation this gas has mostly vanished, leaving only a few percent of the mass within the stellar half-mass radius as gas, and typically 20% at  $\xi = 3$ . It is interesting to note that the relative increase of the enclosed gas mass fraction with respect to the enclosed sink particle mass fraction only occurs at radii where the latter flattens, i.e. the subclusters only become gas-rich at radii where very little stellar mass is present. The influence of the gas on the subcluster dynamics is therefore best evaluated at radii smaller than where the flattening of  $\mu_{\text{stars}}$  occurs. At  $t_1$ , the ratio between the enclosed stellar mass and gas mass just before the flattening is about 4:1, while at  $t_2$  it has increased to 11:1. This suggests that if feedback starts at a time  $t > t_2$ , the resulting gas expulsion will not strongly affect the subcluster dynamics, and that their virialised state (see Sect. 2.3.2) will be largely retained.

## 2.4 Response to gas expulsion

Motivated by the low gas fractions found in Sect. 2.3, we now address the response of the subclusters to gas expulsion in more detail.

### 2.4.1 The expansion of subclusters

The long-term response of the subclusters to gas expulsion can be evaluated by once again omitting the gas from the simulations and considering only the identified stellar subclusters and their evolution towards virial equilibrium. Given a certain virial ratio and bound mass fraction, does a subcluster expand or shrink after gas removal? We combine the data from the simulations with a simple energy argument similar to Hills (1980) to estimate how the subcluster masses and half-mass radii evolve after the expulsion of the gas. It is insightful to consider the system at two key moments.

- (1) *The time of instantaneous gas removal*, which is equivalent to the current system in the simulations while omitting the gas. This can be done for each snapshot, thereby providing a larger sample of subclusters than when only the last snapshot were to be considered. Of course, including subclusters from different snapshots implies a correspondingly extended range of moments of gas expulsion.
- (2) *The time at which each subcluster attains virial equilibrium*. These times are different for each cluster per definition, but by considering the subclusters at their respective times of virialisation the long-term impact of gas removal is most clearly isolated and identified.

The evolution of the subclusters between these two moments can be quantified by evaluating the conservation of energy. For any subcluster, we can express the kinetic energy as

$$T = \frac{1}{2} M_{\text{cl}} \langle v^2 \rangle \equiv -VQ_{\text{vir}} \approx \frac{GM_{\text{cl}}^2}{2r_v} Q_{\text{vir}}, \quad (2.7)$$

where  $r_v$  is the virial radius, and  $\langle v^2 \rangle$  denotes the mean square velocity, which as a result can be written as

$$\langle v^2 \rangle = Q_{\text{vir}} \frac{GM_{\text{cl}}}{r_v}. \quad (2.8)$$

The total energy at the moment of instantaneous gas removal thus becomes

$$E_1 = (Q_{\text{vir},1} - 1) \frac{GM_{\text{cl},1}^2}{2r_{v,1}}, \quad (2.9)$$

where the relevant quantities have been marked with subscript ‘1’ to indicate the moment of gas expulsion.

Given a deviation from virial equilibrium, a subcluster will respond by changing its radius and/or mass. As can be verified from Fig. 2.5, most subclusters contain a certain number of unbound sink particles, which were either previously retained by the gas potential, or are randomly passing the subcluster close enough to be included by the cluster identification algorithm. These unbound sink particles will escape the subcluster upon gas expulsion and take away some of the kinetic energy. We now consider a second moment in time, at which the gas-rich subcluster has reached virial equilibrium ( $Q_{\text{vir},2} = 0.5$ ) and the unbound sink particles have successfully escaped. At this time, energy conservation dictates

$$E_1 = E_2 + E_{\text{esc}} = -\frac{GM_{\text{cl},2}^2}{4r_{v,2}} + (M_{\text{cl},1} - M_{\text{cl},2}) \frac{\beta \langle v_2^2 \rangle}{2}, \quad (2.10)$$

where  $E_2$  is the total energy of the (virialised) subcluster,  $E_{\text{esc}}$  is the total energy of the escaped stars, and the relevant quantities have been marked with subscript ‘2’ to indicate the moment of virialisation. The parameter  $\beta$  denotes the surplus energy per unit mass of the escaped stars after they clear the potential of the subcluster, in units of its mean square velocity. The values of  $\beta$  can be estimated from the simulation by computing  $(T_i + V_i)/(GM_{\text{cl},2}m_i/2r_{v,1})$  for each of the unbound sink particles<sup>6</sup>. For this, we use the relation between the virial and half-mass radius corresponding to a Plummer (1911) potential, which is given by  $r_v = 1.3r_h$  (e.g. Heggie & Hut 2003). The escaping sink particles are the tail of an approximately Maxwellian velocity distribution of the sink particles in the subcluster, and consequently the distribution of  $\beta$  declines exponentially as  $f(\beta) \propto \exp(-\beta/\beta_0)$ , with  $\beta_0$  around unity. The mean of such a distribution equals  $\beta_0$  per definition, which illustrates that unbound stars typically retain velocities similar to the mean square velocity in the subcluster after they escape.

Combining Eqs. 2.8 and 2.10, one obtains an expression for the evolution of the gas-rich subcluster as it approaches virial equilibrium, which relates the half-mass radii, masses, initial virial ratio and  $\beta$ . It is given by

$$\frac{r_{h,2}}{r_{h,1}} \approx \frac{r_{v,2}}{r_{v,1}} = \frac{1}{1 - Q_{\text{vir},1}} \left[ \frac{1 + \beta}{2} \left( \frac{M_{\text{cl},2}}{M_{\text{cl},1}} \right)^2 - \frac{\beta}{2} \frac{M_{\text{cl},2}}{M_{\text{cl},1}} \right], \quad (2.11)$$

<sup>6</sup>The denominator holds a slightly modified form of the mean square velocity  $\langle v_2^2 \rangle$  (see Eq. 2.8) and assumes that the virial radius does not change much between gas expulsion and virialisation (i.e.  $r_{v,1} \approx r_{v,2}$ ). This is required since  $r_{v,2}$  is not available in the simulation. The assumption will be verified below.



where  $r_{h,2}$  is the only unknown and all other variables given by the simulation. For  $\beta = 0$ , i.e. all escaping stars are only marginally unbound, the expression returns the basic result that when unbound stars escape from a virialised system ( $Q_{\text{vir},1} = 0.5$ ), it contracts to regain virial equilibrium<sup>7</sup>. Inserting typical values of  $\beta = 1$  (see above),  $Q_{\text{vir},1} = 0.59$  and  $M_{\text{cl},2}/M_{\text{cl},1} = 0.95$  (see Sect. 2.3.2) in Eq. 2.11 yields  $r_{h,2}/r_{h,1} = 1.04$ , which justifies the earlier assumption that the radius does not change much between instantaneous gas removal and virialisation (see footnote 6). This minor expansion is driven by the slightly supervirial state of the subclusters, and inhibited by the escape of unbound stars, which have velocities larger than the escape velocity.

As discussed in Sect. 2.3.2, the virial ratios of the subclusters give an indication of their survival fraction after gas removal. Out of all 140 subclusters identified in the simulation, only 10 have virial ratios  $Q_{\text{vir}} > 1$  and are therefore unbound. In the last snapshot of the simulation, only one of the 21 subclusters will disperse after the removal of the gas<sup>8</sup>. As a result, typically 90–95% of all the identified subclusters survive gas expulsion. The fate of these survivors depends on whether they expand, and how their environment affects them. Expanded subclusters with lower densities are more susceptible to disruption by tidal shocks. The evolution of the half-mass radii after gas expulsion can be considered in more detail by evaluating Eq. 2.11 for each of the subclusters in the simulation. This enables a comparison of the distribution of half-mass radii of the current subclusters (at the moment of instantaneous gas removal) with the distribution of their half-mass radii when they have reached virial equilibrium, which is shown in Fig. 2.9. The distribution of half-mass radii changes remarkably little after gas removal, as the means of the lognormal functions that are fitted to both distributions differ by 0.035 dex. This implies  $r_{h,2}/r_{h,1} = 1.08$ , very similar to the earlier, simple estimate of  $r_{h,2}/r_{h,1} = 1.04$ . The subclusters in the last snapshot experience roughly 1.5 times this expansion after gas removal, which is of the same order of magnitude as the expansion of the other subclusters. The relative stability of the half-mass radii indicates that the subclusters themselves do not become more susceptible to tidal perturbations due to their expansion following gas expulsion.

## 2.4.2 The cluster formation efficiency

The instantaneous gas removal discussed in this paper is an extreme form of the more gradual expulsion occurring in nature. As a result, the described weak effect of gas expulsion should be even weaker in real subclusters. It seems that gas expulsion plays a negligible role on the length scales of the compact stellar aggregates in star-forming regions. However, the regions between subclusters may still be gas-dominated, implying that feedback could prevent the further merging of subclusters and thereby inhibit their hierarchical growth.

---

<sup>7</sup>This situation, in which the naturally unbound component of a system escapes, should not be confused with the response of a virialised system to mass loss due to stellar evolution, when energy is injected into the system to unbind mass. In such a case, the surplus energy of the escaping mass is supplied by the energy injection and not by the dynamical system itself, which therefore mainly loses potential energy. This does not apply to the case under consideration in Eq. 2.11, where no energy is injected and the unbound stars take away more kinetic energy than potential energy.

<sup>8</sup>These unbound subclusters are typically low-mass, compact systems, and are often newly formed or have just experienced a subcluster merger.

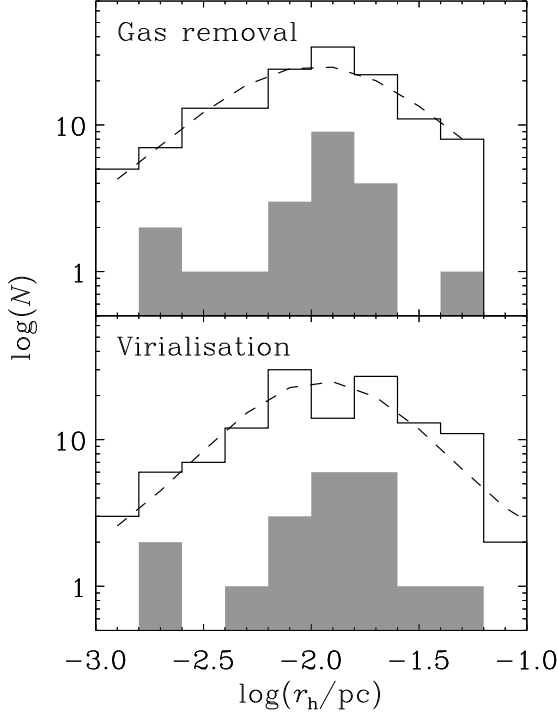


**Figure 2.9:** Histogram of the stellar half-mass radii of the subclusters from all snapshots (solid line). The shaded histogram represents the set of subclusters from the last snapshot at  $t = 0.641$  Myr. *Top:* for the simulated radii, representing the moment of instantaneous gas removal. *Bottom:* for analytically computed radii, reflecting the subclusters at a later moment, when they have reached virial equilibrium. The dashed lines are lognormal fits to the data for the subclusters from all snapshots, with mean values  $\log(r_h/\text{pc}) = \{-1.98, -1.95\}$  and standard deviations  $\sigma_{\log r} = \{0.73, 0.61\}$  for the top and bottom panel, respectively, with median half-mass radii  $\log(r_h/\text{pc}) = \{-1.96, -1.91\}$ .

The length scale on which the subclusters will have merged and have become gas-poor depends on the moment at which feedback starts. For the MST break distance and corresponding length scale that is used in most of this paper, the subclusters are gas-poor irrespective of time. However, there should be a break distance at which a notable time-evolution of the gas fraction appears. By comparing the subcluster gas fractions for different break distances, we find that at the end of the simulation (after one free-fall time), the subclusters have become gas-poor ( $\langle f_{\text{gas}} \rangle < 0.1$ ) on a length scale of about 0.1–0.2 pc. This length scale will increase further with the number of free-fall times that are completed before the onset of feedback. In turn, this increases the spatial extent over which the subclusters are allowed to merge before gas expulsion, which implies that the most massive bound structure is inversely related to the free-fall time.

The free-fall time is related to the density as  $t_{\text{ff}} \propto \rho^{-1/2}$ , which implies that the time of the onset of feedback  $t_{\text{fb}}$  is associated with a density  $\rho_{\text{fb}}$  that has a free-fall time equal to  $t_{\text{fb}}$ . For a given density spectrum of subclusters (see e.g. Bressert et al. 2010), only those subclusters with densities  $\rho \gg \rho_{\text{fb}} \propto t_{\text{fb}}^{-2}$  have the opportunity to undergo the collapse and shrinkage that we find in the simulations. The CFE increases with the fraction of subclusters that forms in these density peaks. As subclusters merge, accrete gas and shrink, the density of the stellar structure further increases (see Sect. 2.3). Each free-fall time, more subclusters evolve into the density regime where  $\rho \gg \rho_{\text{fb}}$ , also on larger length scales. This means that the length scales on which star-forming regions produce virialised stellar systems that are insensitive to gas expulsion are larger in dense sites of star formation than in sparse ones. The resulting dense clusters are also less susceptible to disruptive tidal effects from their environment, which potentially further increases their survival chances. As a result, the CFE should increase with density. Through the Schmidt-Kennicutt law (Schmidt 1959, Kennicutt 1998b), this suggests a relation between the CFE and the star formation rate per unit volume  $\rho_{\text{SFR}}$  or per unit surface area  $\Sigma_{\text{SFR}}$ . Indeed, first observational indications for such a relation have been found by Larsen & Richtler (2000), Larsen (2004), and recently also by Goddard et al. (2010), who obtain  $\text{CFE} \propto \Sigma_{\text{SFR}}^{0.24}$ . A relation between the CFE and the star formation rate density would also be consistent with the high cluster formation efficiencies that are found in starburst galaxies (e.g. Zepf et al. 1999). However, dense star-forming regions are generally also more disruptive to clustered structure due to the higher frequency and amplitude of tidal shocks (Lamers et al. 2005b, Kruijssen et al. 2011c). This implies that a relation between the CFE and the ambient density would be weakened or could even be cancelled (also see Sect 2.4.3).

### 2.4.3 Infant mortality and the ‘cruel cradle effect’

It is often said that most stars form in stellar clusters. The concept of ‘infant mortality’ (Lada & Lada 2003), i.e. the rapid dispersal of stellar structure following the change of the gravitational potential due to gas expulsion, has been put forward in the literature to explain the observed rapid, mass-independent decline of the number of stellar clusters between ages of a few Myr and several tens of Myr (e.g. Bastian & Goodwin 2006). Because the majority of stars has been thought to form in clusters, infant mortality was also held responsible for the low number of clusters per unit field star mass. However, recent (observational) evidence is pointing towards a picture in which star clusters are the dense end of a continuous density spectrum of star formation (see Fig. 2.2 and Bressert et al. 2010, Gieles & Portegies Zwart 2011). This view challenges the need for infant mortality in the early disruption of stellar structure.

The results presented in this paper show that stellar substructure can evolve towards a virialised state before the gas is removed. This occurs because the dynamics of the stars and the gas are decoupled (also see Offner et al. 2009), as the accretion of gas onto the stars together with the subcluster shrinkage can compensate the overall gas inflow onto the subclusters. In time, this causes the subclusters to become gas-poor, thereby diminishing the disruptive effect of gas expulsion. It depends on the length and mass scales on which the gas is evacuated whether this result can be extended from subclusters to actual star clusters.

Towards the end of the simulation, after about 0.3 Myr of star formation, the subclusters have a mean mass of  $40 M_{\odot}$  and are gas-poor on length scales of 0.1–0.2 pc. As a very crude first-order estimate, one can re-scale the units of the simulation to have the subclusters match the typical properties of young star clusters<sup>9</sup>. By multiplying the mass unit by a factor of 25 and the length unit by a factor of 5, we re-scale the mean cluster mass to  $10^3 M_{\odot}$ , and the length scale on which the stellar structure will be gas-poor to 0.5–1 pc. By scaling the time unit accordingly, we see that such gas depletion is reached on a time scale of 0.8 Myr, which is of the same order as the expected  $t_{\text{fb}}$  due to stellar winds and ionisation feedback. This order-of-magnitude estimate is of course far from conclusive, but it does show the relevance of pursuing this problem further.

If clusters reach a relatively gas-poor state before the onset of feedback, the influence of gas expulsion on the dynamical state of the clusters will be smaller than previously expected. Rather than leading to the disruption of clusters (‘infant mortality’), the different spatial distributions of gas and stars imply that gas expulsion could leave clusters marginally affected, unbinding only a certain fraction of their stars (e.g. Moeckel & Bate 2010). This is in clear contrast with earlier (theoretical) approaches in literature (e.g. Boily & Kroupa 2003a,b, Bastian & Goodwin 2006, Goodwin & Bastian 2006, Baumgardt & Kroupa 2007, Parmentier et al. 2008), which assumed a model where the gas and stars are in equilibrium during gas expulsion. Clearly, this is not the case in the simulation of Bonnell et al. (2008).

Because the density of the stellar structure determines whether or not gas expulsion affects the survival chances of star clusters, a continuous density spectrum of young stellar structure as in Bressert et al. (2010) and Fig. 2.2 naturally leads to the situation in which the dispersed part of the new-born stellar structure is affected by gas expulsion, while the other, dense and clustered part is not. However, this does not imply that the survival chances of these clusters are necessarily higher. Recent papers have argued that the disruption of star clusters due to tidal shocks from the natal environment could be substantial (Elmegreen & Hunter 2010, Kruijssen et al. 2011c, Kruijssen & Bastian 2011). Although the disruption rate due to tidal shocks decreases with cluster density, sufficiently strong<sup>10</sup> shocks could still disrupt dense clusters. Such shocks could be prevalent in dense star-forming regions. As clusters move out of their primordial environment, the typical ambient gas density decreases (Elmegreen & Hunter 2010, Kruijssen et al. 2011c), which lessens the disruptive effect of tidal shocks. Observationally, this mechanism affects the star cluster population in a way that is very similar to infant mortality: the fact that young clusters are more efficiently disrupted than older clusters gives rise to a strong decline of the number of clusters with age at young ages. This decline acts on the age scale corresponding to the time it takes to migrate out of the star-forming region. Rather than being an internal effect, like infant mortality is, the primordial disruption by tidal shocks is driven by the state of the environment in which the clusters are born. We will therefore refer to this mechanism as the ‘cruel cradle effect’.

It will be interesting to quantify what the relative contributions of gas expulsion and the cruel cradle effect are to the early disruption of young stellar clusters. It is likely that both effects coexist, and that the relative importance changes with the environment. It was explained

---

<sup>9</sup>The simulations are scale-free except for the sink particle radius and accretion radius mentioned in Sect. 2.2. For the scaling used in this example, these respective radii are  $10^3$  AU and 200 AU.

<sup>10</sup>The strength of a tidal shock corresponds to the amount of energy it injects into the cluster.

in Sect. 2.4.2 that the fraction of clusters that is affected by gas expulsion decreases with the ambient density of the star-forming region. The cruel cradle effect shows the opposite dependence, as the disruptive effect of tidal shocks increases with the ambient gas density. It would therefore not be unlikely that gas expulsion and the cruel cradle effect each dominate a different side of the gas density spectrum of star-forming regions. Their relative strength would then determine the relation between the CFE and the ambient gas density.

## 2.5 Summary and outlook

In this paper, we have assessed the dynamical state of stellar structure in star-forming regions and its response to gas expulsion by analysing the properties of the stellar structure in the SPH/sink particle simulations of Bonnell et al. (2003, 2008). Subclusters have been identified using a minimum spanning tree algorithm (MST, following Maschberger et al. 2010), and binaries have been replaced by their centre-of-mass particles when computing the global dynamical properties of the subclusters. We have also discussed the long-term implications of gas expulsion for the properties of star cluster populations. The main results are as follows.

- (1) The surface density distribution of sink particles follows an approximately lognormal distribution similar to that observed by Bressert et al. (2010). However, the surface density corresponding to the peak of the distribution is several orders of magnitudes higher than the observed one, because the subclusters considered in our study are part of a region that would represent only one or two clusters in the observations. The high-density end of the distribution is occupied by sink particles belonging to the subclusters that are identified with the MST.
- (2) When excluding the potential of the gas from the dynamical analysis and only considering the sink particles, we find that the simulation as a whole becomes marginally bound after one free-fall time, and the population of individual subclusters is close to virial equilibrium. The mean value of a Gaussian fit to the distribution of virial ratios from all snapshots is  $Q_{\text{vir}} = 0.59$ , where virial equilibrium would imply  $Q_{\text{vir}} = 0.5$ . The mean virial ratio of the population slowly decreases with time, from  $Q_{\text{vir}} = 0.70\text{--}0.80$  early on to  $Q_{\text{vir}} = 0.55\text{--}0.60$  towards the end of the simulation.
- (3) The virialisation of the subclusters occurs due to their low gas fractions. We consider the spatial distributions of gas and sink particles at two characteristic moments during the simulation ( $t_1 = 0.442$  Myr and  $t_2 = 0.641$  Myr, reflecting the system early on and after one free-fall time), and find that the mean gas fraction within the stellar half-mass radii of the subclusters decreases by 0.63 dex during the enclosed time interval, from  $\langle f_{\text{gas}}(t_1) \rangle = 0.238$  to  $\langle f_{\text{gas}}(t_2) \rangle = 0.056$ . By comparing the density profiles of gas and sink particles, we conclude that this decrease is caused by gas accretion and subcluster shrinkage to approximately the same degree.
- (4) Because the subclusters are relatively gas-poor, they are only weakly affected by gas expulsion and the subsequent evolution towards virial equilibrium. According to our analytical estimate, they expand by an average factor of 1.08 after gas removal. The

length scale on which the subclusters are gas-poor ( $\langle f_{\text{gas}} \rangle < 0.1$ ) is about 0.1 pc at the end of the simulation. By scaling up the units of the simulation from subcluster to star cluster scales, we find that after about 0.8 Myr of star formation, star clusters with a mean mass of  $10^3 M_{\odot}$  would be gas-poor on a length scale of 0.5–1 pc.

- (5) Only those (sub)clusters with densities much larger than the density that is associated with a free-fall time equal to the gas expulsion time can exhibit the shrinkage and accretion that causes them to become gas poor. The fraction of clusters that reaches the required density to become insensitive to gas expulsion before the onset of feedback therefore increases with ambient gas density. This suggests a relation between the cluster formation efficiency (CFE) and the ambient gas or star formation rate density, with a larger fraction of star formation resulting in bound clusters in dense regions.
- (6) A possible relation between the CFE and the ambient gas density is affected by a second mechanism. In dense regions, the survival chances of stellar structure are not determined by gas expulsion or ‘infant mortality’, but by the disruptive effect of tidal shocks from the surrounding gas (Elmegreen & Hunter 2010, Kruijssen et al. 2011c). This disruption of young clusters by their environment is titled the ‘cruel cradle effect’ and is suggested to take over the disruptive role of gas expulsion in dense star-forming regions. The strength and relative contributions of infant mortality and the cruel cradle effect as a function of ambient gas density will be the decisive factor to assess the relation between the CFE and the ambient gas density. This needs to be quantified in future studies, because the time scale covered by the simulation is too short to include the disruption of subclusters due to the cruel cradle effect.

Throughout the paper, we have mentioned directions in which further research should be undertaken to verify and expand our conclusions. It is essential to check to what extent these results depend on the properties of the simulations we analysed, such as their initial conditions and input physics. The three chief concerns would be whether the results are affected by (1) the turbulence spectrum and initial setup of the simulation, (2) the inclusion or exclusion of feedback and magnetic fields, (3) the choice of sink particle radius.

- (1) The turbulence spectrum and overall boundedness of the simulation primarily influence the time evolution of the overall star formation efficiency (McKee & Ostriker 2007, Dale & Bonnell 2008), and will only impact the evolution of subclusters if the inflow of gas becomes too high to be compensated by accretion and subcluster shrinkage. Judging the relative ease at which the subclusters in the current simulation become gas-poor, it is unlikely that the situation of a saturating gas inflow would take place. However, a dynamical analysis of a larger set of simulations will be needed to obtain a conclusive picture, also to include the formation of stars and subclusters in environments with lower densities.
- (2) Feedback from accreting sink particles would inhibit the inflow of the gas, which in turn would lead to a lower gas fraction within the subclusters. There have been several efforts in literature to quantify the effect of (positive or negative) feedback on the star formation process, which generally consider effects on the length scales of the giant

molecular clouds in which the star formation takes place (see e.g. McKee & Ostriker 2007). While global effects could influence the gas-poor state of the (sub)clusters, the nature of feedback is such that it evacuates the gas on stellar scales, which would therefore should not lead to a fundamentally different conclusion than made in this paper. Magnetic fields could slow down the accretion process. If this decrease of the accretion rate would be smaller in the outskirts of the subclusters than within the stellar half-mass radius, it would increase the gas fractions and virial ratios of the stellar component. Therefore, the influence of magnetic fields on our results will need to be investigated.

- (3) If the accretion and/or sink radii of the sink particles were comparable to the typical interstellar separation, the gas-poor nature of the subclusters would be a trivial result of a high ‘filling factor’ of the subclusters by the sink particles, as the volume where the gas could reside without being accreted would be too small to achieve a stable configuration. We have addressed this to first order by computing the accretion and sink volumes taken up by sink particles and dividing it by the enclosed volume. This was done for each sink particle while taking the nearest neighbour<sup>11</sup>, and also by calculating a mean radial ‘filling factor’ profile for each subcluster, analogous to Fig. 2.8. Both methods returned low filling factors, with typical values of  $10^{-2}$  for the sink radius and  $10^{-4}$  for the accretion radius. In other words, less than 1% of the volume inside the subclusters is taken up by the sink particles. In order to assess to which extent this allows us to neglect spurious accretion, we ran a set of simple test simulations with different accretion and sink particle radii. These tests show that the gas accretion rate is hardly affected by the accretion and sink radii, which validates our results. The details of the tests are given in the Appendix Sect. 2.A.

Ideally, the next step would be to perform the same type of calculation as in Bonnell et al. (2008) for different initial conditions, including descriptions for radiative and mechanical feedback, potentially accounting for magnetic fields, and varying the sink particle radius. The dynamical analysis of such simulations would provide a good verification of our conclusions, and would improve the current understanding of the dependence on initial conditions and input physics.

The order-of-magnitude extension of our results from subcluster to actual star cluster scales should be investigated further. With the continuously improving computational facilities, it will be possible to simulate systems on the scales needed to cover the formation of star clusters. The key ingredients of such an effort will be larger particle numbers and smaller sink particle radii. Additionally, infrared or spectroscopic observations can be used to verify the length scales on which star-forming regions are gas-poor prior to the onset of feedback. The current and upcoming generation of telescopes will provide excellent opportunities for this.

If gas expulsion indeed only weakly affects the survival chances of stellar structure, it will need to be verified in which regimes infant mortality still plays a role. In order to understand the relation between the CFE and the local environment, the relative contributions to early

---

<sup>11</sup>We used the particle list that was corrected for multiples, implying that bound neighbours were ignored.

star cluster disruption of infant mortality and the cruel cradle effect will need to be quantified. The kinematic signatures of both effects should differ and would therefore be measurable in the velocity maps of young disrupted clusters. Possible ways in which this could be done observationally include searching for young clusters that are currently going through gas expulsion and mapping the radial velocities of the stars, or tracing the velocity dispersion profiles of young, gas-poor clusters in dense regions. To aid this effort, the differences between the kinematic signatures of energy injection into a star cluster by gas expulsion or tidal shocks have to be established theoretically. The combination of these approaches should provide a conclusive picture of the mechanisms that determine which fraction of star formation results in bound star clusters.

**Acknowledgements** This research is supported by the Leids Kerkhoven-Bosscha Fonds (LKBF) and the Netherlands Organisation for Scientific Research (NWO), grant 021.001.038. JMDK acknowledges the kind hospitality of the Institute of Astronomy in Cambridge, where a large part of this work took place.

## 2.A Appendix: Independence of results on sink parameters

In this appendix we verify that the resolution of the SPH simulation is not playing an important role in the evolution of the stellar-to-gas mass ratio of the subclusters. We accomplish this via a series of controlled, idealised tests in which a cluster of 10 sink particles accretes from an envelope of gas. The total mass of the system is 1, divided equally between the sinks and the gas. The sinks are initially of equal mass, thus each has mass 0.05. They are placed randomly in a Plummer model of virial radius  $r_{\text{sinks}} = 1$ , and we use the same initial configuration of the stars in each test. The median nearest neighbour separation of the sinks is 0.43. The gas is likewise in a Plummer sphere spatially, although with a larger radius than the sinks. The gas has zero initial kinetic energy and minimal thermal support, so that the gas falls onto the sink cluster and is accreted. We run two sets of tests, one in which the gas sphere's virial radius is ten times  $r_{\text{sinks}}$ , i.e.  $r_{\text{gas}} = 10$ , and one in which  $r_{\text{gas}} = 3$ .

The two numerical scales we are concerned with are the accretion radius of the sinks  $r_{\text{acc}}$ , and the smoothing length of the gas particles. For the sink radii, we use the set  $r_{\text{acc}} = \{0.125, 0.0625, 0.03125\}$ . The middle value yields approximately the ratio of the neighbour distance to the accretion radius seen in the clusters in the simulation. The smoothing length of the gas is determined by the number of gas particles. To roughly match the simulated value, suppose the sinks have masses  $1 M_{\odot}$ . The total gas mass is then  $10 M_{\odot}$ , and  $5 \times 10^4$  gas particles approximates the resolution of the large-scale simulation. We run the 0.0625 accretion radius cases with four times more and fewer gas particles, i.e.  $2 \times 10^5$  and  $1.25 \times 10^4$ .

In Fig. 2.10 we show the gas mass as a function of time for the test runs. In the top panel we show the results for the case with  $r_{\text{gas}} = 3$ . Time is measured dimensionlessly where we have taken the gravitational constant  $G = 1$ ; the crossing time of the sink cluster is  $\sim 2$ . In this setup, the gas free-fall time is  $\sim 6$  and the gas accretes quickly compared to the time for the  $N$ -body dynamics to dissolve the small- $N$  sink system. The agreement between all the test runs is excellent. The bottom panel shows the  $r_{\text{gas}} = 10$  cases, and the gas falls



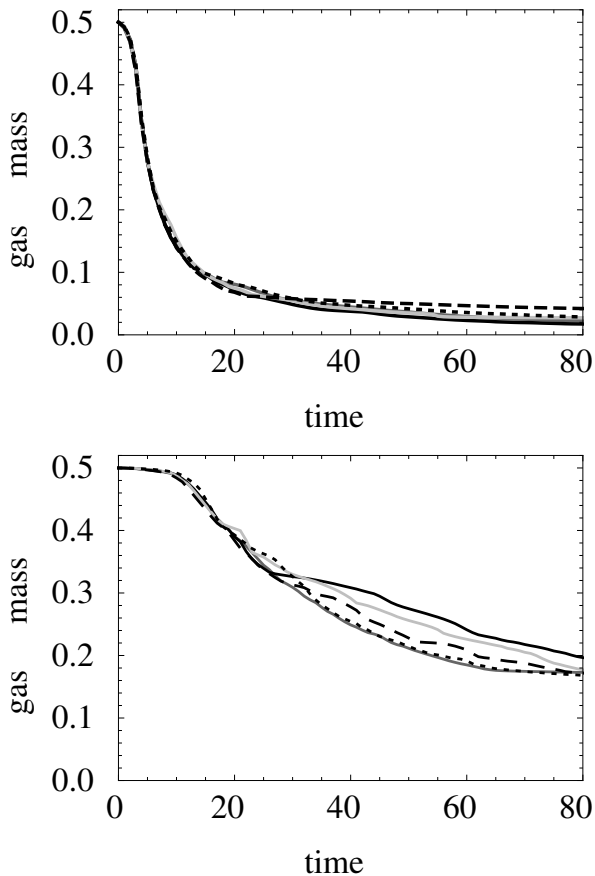


**Figure 2.10:** Remaining gas mass as a function of time for our tests of the SPH simulation sink parameters. Top panel: the runs with  $r_{\text{gas}} = 3r_{\text{sinks}}$ ; bottom panel, the runs with  $r_{\text{gas}} = 10r_{\text{sinks}}$ . Grey lines have  $r_{\text{acc}} = 0.125$ , black lines have  $r_{\text{acc}} = 0.0625$ , and light grey lines have  $r_{\text{acc}} = 0.03125$ . Solid lines have  $5 \times 10^4$  gas particles. The dashed lines have  $2 \times 10^5$  particles, and the dotted lines have  $1.25 \times 10^4$  particles.

onto the sink system over a longer time scale, with a free-fall time  $\sim 35$ . At early times the agreement is quite good, with some disagreement between the runs appearing after  $t \sim 20$ . We attribute this to the fact that at this point the  $N$ -body dynamics of the different runs have set the clusters on clearly divergent paths; recall that the gravitational smoothing length of the sinks is proportional to their sink radius. By  $t = 80$  the cluster of sinks has effectively dissolved. We conclude that gas accretion time scale is not greatly affected by the choices of the sink radius.



# **Part B – The dynamical evolution of star clusters in their galactic environment**



# Chapter 3

---

## The photometric evolution of star clusters and the preferential loss of low-mass bodies – with an application to globular clusters\*

J. M. Diederik Kruijssen and Henny J. G. L. M. Lamers  
*Astronomy & Astrophysics*, v. 490, p. 151–171 (2008)<sup>†</sup>

**Abstract** To obtain an accurate description of broad-band photometric star cluster evolution, certain effects should be accounted for. Energy equipartition leads to mass segregation and the preferential loss of low-mass stars, while stellar remnants severely influence cluster mass-to-light ratios. Moreover, the stellar initial mass function and cluster metallicity affect photometry as well. Due to the continuous production of stellar remnants, their impact on cluster photometry is strongest for old systems like globular clusters. This, in combination with their low metallicities, evidence for mass segregation, and a possibly deviating stellar initial mass function, makes globular clusters interesting test cases for cluster models. In this chapter we describe cluster models that include the effects of the preferential loss of low-mass stars, stellar remnants, choice of initial mass function and metallicity. The photometric evolution of clusters is predicted, and the results are applied to Galactic globular clusters. The cluster models presented in this chapter represent an analytical description of the evolution of the underlying stellar mass function due to stellar evolution and dynamical cluster dissolution. Stellar remnants are included by using initial-remnant mass relations, while cluster photometry is computed from the Padova 1999 isochrones. Our study shows that the preferential loss of low-mass stars strongly affects cluster magnitude, colour and mass-to-light ratio evolution, as it increases cluster magnitudes and strongly decreases mass-to-light ratios. The effects of stellar remnants are prominent in the evolution of cluster mass, magnitude and mass-to-light ratio, while variations of the initial mass function induce similar, but smaller changes. Metallicity plays an important role for cluster magnitude, colour and mass-to-light ratio evolution. The different effects can be clearly separated with our models. We apply the models

---

\*The models presented in this chapter are publicly available in electronic form at the CDS via anonymous ftp to <http://cdsweb.u-strasbg.fr/> (130.79.128.5) or via <http://cdsweb.u-strasbg.fr/cgi-bin/qcat?J/A+A/>.

<sup>†</sup>Reproduced with permission © ESO.

to the Galactic globular cluster population. Its properties like the magnitude, colour and mass-to-light ratio ranges are well reproduced with our models, provided that the preferential loss of low-mass stars and stellar remnants are included. We also show that the mass-to-light ratios of clusters of similar ages and metallicities cannot be assumed to be constant for all cluster luminosities. Instead, mass-to-light ratio increases with cluster luminosity and mass. These models underline the importance of more detailed cluster models when considering cluster photometry. By including the preferential loss of low-mass stars and the presence of stellar remnants, the magnitude, colour and mass-to-light ratio ranges of modelled globular clusters are significantly altered. With the analytic framework provided in this chapter, observed cluster properties can be interpreted in a more complete perspective.

### 3.1 Introduction

In recent studies, the photometric evolution of star clusters has been extensively treated from various approaches (e.g. Anders & Fritze-v. Alvensleben 2003, Lamers et al. 2006, von Hippel et al. 2006, Fagiolini et al. 2007). Because cluster photometry is used for a broad range of applications, like age-dating galaxies and tracking their formation history, it is crucial to obtain an accurate description of the photometric evolution of clusters. While *Simple Stellar Population* (SSP) models (e.g. Leitherer et al. 1999, Bruzual & Charlot 2003, Anders & Fritze-v. Alvensleben 2003, Maraston 2005) only consider the changing photometric properties due to stellar evolution, other models that also use the dynamical input of  $N$ -body simulations can predict the photometric evolution of clusters under a wider variety of conditions (e.g. Lamers et al. 2006, Fagiolini et al. 2007, Borch et al. 2007). In reality, not only stellar evolution but also the dynamical interaction of a cluster with its environment causes it to lose stars (e.g. Baumgardt & Makino 2003). This process, which is called dissolution, occurs due to internal two-body relaxation and external effects like tidal perturbation, spiral arm passages or encounters with Giant Molecular Clouds (e.g. Baumgardt & Makino 2003, Gieles et al. 2006b, 2007a). It can change the shape of the stellar mass function, and will also affect photometric cluster evolution. This is the case as a cluster evolves towards energy equipartition, causing it to preferentially lose low-mass stars (e.g. Portegies Zwart et al. 2001, Baumgardt & Makino 2003, Hurley et al. 2005).

The physical driving force of the preferential loss of low-mass bodies is subject to debate. On the one hand, energy equipartition between the bodies constituting a cluster increases the velocities of low-mass objects and thereby gives rise to the preferential loss of low-mass stars. On the other hand, it has been proposed that mass segregation, a phenomenon in which due to energy equipartition the more massive stars sink towards the cluster centre and low-mass objects move outwards, leads to the same effect since bodies in the cluster outskirts are more loosely bound than objects in the cluster centre and are thus more easily lost (e.g. Leon et al. 2000, Portegies Zwart et al. 2001, Lamers et al. 2006). This line of reasoning is not compatible with King (1966), where it is shown that the escape rate of stars from a cluster does not vary with radius. In that scenario, the preferential loss of low-mass stars and mass segregation are both the effects of energy equipartition, but do not necessarily share any causal connection (e.g. de la Fuente Marcos 2000). Regardless of its specific nature, in the remainder of this chapter we consider energy equipartition to be the fundamental cause of the preferential

loss of low-mass stars: either directly, via mass segregation, or a combination of the two. In any case, mass segregation can serve as an indicator for clusters that have undergone a strong preferential loss of low-mass stars (e.g. Portegies Zwart et al. 2001, Baumgardt & Makino 2003) and will therefore be used in that respect.

There have been many observations of Galactic open and globular clusters in which evidence of mass segregation was found (e.g. Anderson & King 1996, Hillenbrand & Hartmann 1998, Zoccali et al. 1998, Albrow et al. 2002, Richer et al. 2004, Koch et al. 2004, Pasquali et al. 2004). These clusters can be expected to exhibit non-canonical photometric evolution. Furthermore, for a number of clusters overall mass-to-light ratios are observed that strongly deviate from the mean value presented in McLaughlin (2000) (e.g. Baumgardt et al. 2003b, van de Ven et al. 2006), which suggests a range of scenarios for photometric cluster evolution. This, in combination with the high mass-to-light ratio *in the centre* of some globular clusters (e.g. Pasquali et al. 2004, van den Bosch et al. 2006) and the consequent invocation of intermediate mass black holes (IMBHs) (e.g. Portegies Zwart & McMillan 2002, Gürkan et al. 2004), asks for a cluster model that can explain the observed range of mass-to-light ratios. While some studies suggest IMBHs to explain the high mass-to-light ratio in the centres of globular clusters (e.g. Gebhardt et al. 2005, Noyola et al. 2006), others show that these are not required and central concentrations of stellar remnants also provide a solution (e.g. Baumgardt et al. 2003a,b, Hurley 2007). Therefore, it is important to investigate to what extent either model can be used to explain the observed range of mass-to-light ratios, colours and magnitudes. A model describing cluster mass-to-light ratios may also be able to provide insight in the connection between globular clusters and ultra-compact dwarf galaxies (UCDs), the latter having a different mass-to-light ratio range than globular clusters (e.g. Haşegan et al. 2005, Evstigneeva et al. 2007, Rejkuba et al. 2007, Mieske & Kroupa 2008).

In this chapter we present cluster models that are based on stellar isochrones like all SSP models, but analytically incorporate dynamical effects on cluster photometry by following the results from  $N$ -body simulations (Baumgardt & Makino 2003). The resulting speed and applicability to a large parameter space makes it very suitable for studying the effect of a range of parameters on cluster evolution. We show how photometric properties of clusters like their magnitude, colour and overall mass-to-light ratio are affected by the preferential loss of low-mass stars, the inclusion of stellar remnants, the stellar initial mass function (IMF) and metallicity.

The structure of the chapter is as follows. Our cluster evolution models are presented in Sect. 3.2. In Sect. 3.2.2 it is shown how stellar evolution affects the cluster content, including the production of stellar remnants. We derive the equations describing dynamical effects of cluster evolution on a multi-component powerlaw IMF (e.g. Kroupa 2001) in Sect. 3.2.3. The effects of the preferential loss of low-mass stars and the dynamical loss of remnants are included. In that section, we also provide the final set of equations to describe cluster evolution with our models. The computation of photometric evolution is treated in Sect. 3.3. The results are presented in Sect. 3.4, where also the influences of the preferential loss of low-mass stars, stellar remnants, IMF and metallicity are investigated, and the results are compared to previous studies. In Sect 3.5, the models are applied to Galactic globular clusters. Section 3.6 contains a discussion of the results, while our conclusions are provided in Sect. 3.7.

## 3.2 Cluster evolution

In this section we describe cluster evolution: first we formulate the stellar mass function in the cluster, secondly we describe cluster mass loss due to stellar evolution, and thirdly cluster mass loss due to dissolution. We include the effects of the preferential loss of low-mass stars and stellar remnants. The models presented here represent the cluster evolution part of our new cluster population synthesis code SPACE<sup>1</sup>, which is a fast code to predict observables like age, mass and magnitude distributions of clusters for a range of galactic conditions.

### 3.2.1 The stellar mass function

Stars in a cluster are distributed according to a mass function, for which we assume a general expression for a multi-component powerlaw mass function, which is a function of time:

$$N_s(t, m_s)dm_s = C(t)\eta(m_s)m_s^{-\beta(m_s)}dm_s, \quad (3.1)$$

for  $m_{\min}(t) < m_s < m_{\max}(t)$ , where  $N_s(t, m_s)$  represents the number of stars per  $M_\odot$  at age  $t$ ,  $C(t)$  is the (time-dependent) normalisation of the mass function,  $\eta(m_s)$  is introduced to preserve continuity at the stellar mass where the slope  $\beta(m_s)$  changes, and  $m_s$  denotes stellar mass in  $M_\odot$ . Setting  $t = 0$  gives the *initial* mass function (IMF):  $N_s(0, m_s)$ . For a Salpeter IMF, we have constant values  $\eta(m_s) = 1$  and  $\beta(m_s) = 2.35$  with  $m_{\min,i} \approx 0.1 M_\odot$ , while a Kroupa IMF is described by

$$\beta(m_s) = \begin{cases} \beta_1 = 1.3 & \text{for } 0.08 M_\odot \leq m_s < 0.50 M_\odot, \\ \beta_2 = 2.3 & \text{for } 0.50 M_\odot \leq m_s, \end{cases} \quad (3.2)$$

with initial minimum stellar mass  $m_{\min,i} = 0.08 M_\odot$  and  $\eta(m_s \geq 0.50 M_\odot) = 2\eta(m_s < 0.50 M_\odot)$ .

After cluster formation, clusters *lose* mass due to stellar evolution and dissolution<sup>2</sup>. This section provides a description of how both mechanisms affect the stellar mass function and cluster content. Clusters with and without the preferential loss of low-mass stars are treated.

### 3.2.2 Stellar evolution

The total mass loss due to stellar evolution and dissolution can be written as

$$\frac{dM_{\text{cl}}^{\text{tot}}}{dt} = \left( \frac{dM_{\text{cl}}^{\text{tot}}}{dt} \right)_{\text{ev}} + \left( \frac{dM_{\text{cl}}^{\text{tot}}}{dt} \right)_{\text{dis}}. \quad (3.3)$$

In this section we describe the mass loss due to stellar evolution. We separate cluster mass into its two constituents: the mass in stars, or the luminous mass  $M_{\text{cl}}^{\text{lum}}(t)$ , and the mass in stellar remnants  $M_{\text{cl}}^{\text{sr}}(t)$ . The total mass  $M_{\text{cl}}^{\text{tot}}(t)$  is then obtained from

$$M_{\text{cl}}^{\text{tot}}(t) = M_{\text{cl}}^{\text{lum}}(t) + M_{\text{cl}}^{\text{sr}}(t). \quad (3.4)$$

<sup>1</sup>This is an acronym for Stellar Population Age Computing Environment.

<sup>2</sup>As shown by Mieske & Baumgardt (2007), the capture of stars by clusters is ineffective.



## Luminous mass

The first right-hand term of Eq. 3.3 can be expressed in terms of a mass fraction  $\mu_{\text{ev}}^{\text{tot}}(t) \equiv M_{\text{cl}}^{\text{tot}}(t)/M_{\text{cl},i}$  that is still present in the cluster if stellar evolution were the only mass loss mechanism<sup>3</sup>:

$$\left(\frac{dM_{\text{cl}}^{\text{tot}}}{dt}\right)_{\text{ev}} = \frac{d\mu_{\text{ev}}^{\text{tot}}(t)}{dt} M_{\text{cl},i} \frac{C(t)}{C(0)}, \quad (3.5)$$

where the fraction  $C(t)/C(0)$  is included to correct the mass loss for a possible changing mass function normalisation due to dissolution (which will be described in Sect. 3.2.3). Consequently, the mass fraction lost due to stellar evolution is defined by  $q_{\text{ev}}^{\text{tot}}(t) \equiv 1 - \mu_{\text{ev}}^{\text{tot}}(t)$ . The remaining total mass fraction  $\mu_{\text{ev}}^{\text{tot}}(t)$  is the sum of the luminous mass fraction  $\mu_{\text{ev}}^{\text{lum}}(t)$  and the stellar remnant (sr) mass fraction  $\mu_{\text{ev}}^{\text{sr}}(t)$ :

$$\mu_{\text{ev}}^{\text{tot}}(t) = \mu_{\text{ev}}^{\text{lum}}(t) + \mu_{\text{ev}}^{\text{sr}}(t). \quad (3.6)$$

Lamers et al. (2005a) have shown that for luminous cluster mass,  $q_{\text{ev}}^{\text{lum}}(t) \equiv 1 - \mu_{\text{ev}}^{\text{lum}}(t)$  can be approximated as

$$\log q_{\text{ev}}^{\text{lum}} = (\log t - a_{\text{ev}})^{b_{\text{ev}}} + c_{\text{ev}}, \quad (3.7)$$

for  $\log t > a_{\text{ev}}$ , and where  $a_{\text{ev}}$ ,  $b_{\text{ev}}$  and  $c_{\text{ev}}$  are constants determined by the IMF and metallicity of the cluster. We use the Padova 1999 isochrones (Bertelli et al. 1994, AGB treatment as in Girardi et al. 2000) to determine the maximum stellar mass  $m_{\text{max}}(t)$  that is still present in the cluster at time  $t$ . This also provides the initial maximum stellar mass  $m_{\text{max},i}$ , which is taken to be the maximum mass at the youngest isochrone ( $\log t = 6.6$ ). After assuming an IMF, i.e.  $N_s(0, m_s)$ , we can write the remaining mass fraction of luminous mass as

$$\mu_{\text{ev}}^{\text{lum}}(t) = \frac{\int_{m_{\text{min},i}}^{m_{\text{max}}(t)} m_s N_s(0, m_s) dm_s}{M_{\text{cl},i}}, \quad (3.8)$$

from which exact values for  $q_{\text{ev}}^{\text{lum}}(t) \equiv 1 - \mu_{\text{ev}}^{\text{lum}}(t)$  can be determined. The resulting fitting constants  $a_{\text{ev}}$ ,  $b_{\text{ev}}$  and  $c_{\text{ev}}$  are summarised in the top half of Table 3.1<sup>4</sup>. The method assumes the instantaneous removal of stars and ignores mass loss by stellar winds, but this assumption is legitimate since massive stars hardly contribute to overall cluster mass and low-mass stars only suffer significant mass loss during the last 10% of their lifetime. In order to determine  $\mu_{\text{ev}}^{\text{tot}}(t)$  and evaluate Eq. 3.5 also  $\mu_{\text{ev}}^{\text{sr}}(t)$  is required, which will be discussed separately in Sect. 3.2.2.

Since in the present study the stellar content of clusters is considered, we will be evolving the stellar mass function of a cluster (and thereby indirectly the cluster mass) rather than evaluating cluster mass itself. Therefore, we will use  $m_{\text{max}}(t)$  from the isochrones instead of Eq. 3.5 to incorporate stellar evolution. The time evolution of  $m_{\text{max}}(t)$  is shown in the left-hand panel of Fig. 3.1 for metallicities  $Z = \{0.0004, 0.004, 0.02\}$ .

<sup>3</sup>If cluster mass also decreases due to dissolution, then the mass loss would be larger, see Sect. 3.2.3.

<sup>4</sup>Values for the case of a Salpeter IMF are also provided by Lamers et al. (2005a), but these are based on an older version of the *GALEV* models (Schulz et al. 2002, Anders & Fritze-v. Alvensleben 2003).

Luminous cluster mass ( $q_{\text{ev}}^{\text{lum}}$ )							
		Salpeter IMF			Kroupa IMF		
$Z$	$m_{\text{max},i}$	$a_{\text{ev}}$	$b_{\text{ev}}$	$c_{\text{ev}}$	$a_{\text{ev}}$	$b_{\text{ev}}$	$c_{\text{ev}}$
0.0004	68.5101	6.83	0.316	-1.824	6.84	0.298	-1.648
0.0040	69.8779	6.80	0.313	-1.844	6.80	0.295	-1.667
0.0080	71.6802	6.76	0.309	-1.853	6.77	0.291	-1.674
0.0200	68.1211	6.70	0.308	-1.872	6.71	0.290	-1.691
0.0500	49.4481	6.63	0.314	-1.897	6.65	0.297	-1.714
Total cluster mass ( $q_{\text{ev}}^{\text{tot}}$ )							
		Salpeter IMF			Kroupa IMF		
$Z$	$m_{\text{max},i}$	$a_{\text{ev}}$	$b_{\text{ev}}$	$c_{\text{ev}}$	$a_{\text{ev}}$	$b_{\text{ev}}$	$c_{\text{ev}}$
0.0004	68.5101	6.93	0.271	-1.855	6.93	0.255	-1.682
0.0040	69.8779	6.89	0.271	-1.872	6.90	0.256	-1.696
0.0080	71.6802	6.88	0.265	-1.877	6.88	0.250	-1.701
0.0200	68.1211	6.82	0.263	-1.893	6.83	0.248	-1.716
0.0500	49.4481	6.78	0.263	-1.908	6.79	0.249	-1.731

**Table 3.1:** *Top:* Fitting values for  $a_{\text{ev}}$ ,  $b_{\text{ev}}$  and  $c_{\text{ev}}$  for the *luminous* fractional cluster mass decrease due to stellar evolution  $q_{\text{ev}}^{\text{lum}}(t)$  using the Padova 1999 isochrones (see text) at five different metallicities for Salpeter ( $0.1 M_{\odot} < m_s < m_{\text{max},i}$ ) and Kroupa ( $0.08 M_{\odot} < m_s < m_{\text{max},i}$ ) IMFs. The values of the initial maximum stellar mass  $m_{\text{max},i}$  correspond to the maximum masses at the youngest isochrones ( $\log t = 6.6$ ). The maximum difference between the fits and the exact  $q_{\text{ev}}^{\text{lum}}(t)$  curves is 3% after 19 Gyr. *Bottom:* Same as above, but for *total* fractional cluster mass decrease due to stellar evolution, accounting for stellar remnants. The maximum difference between the fits and the exact  $q_{\text{ev}}^{\text{tot}}(t)$  curves is less than 10% after 19 Gyr.

### Stellar remnants

Stellar remnants can constitute a large fraction of the total cluster mass<sup>5</sup>. Especially during the later stages of cluster lifetime, the cluster content is likely to be dominated by remnants. As will be shown in Sect. 3.4 several observables can be significantly affected, making it essential to include remnants when studying cluster evolution.

The distinction between total and luminous cluster mass can be made by writing  $M_{\text{cl}}^{\text{tot}} = M_{\text{cl}}^{\text{lum}} + M_{\text{cl}}^{\text{sr}}$ , where  $M_{\text{cl}}^{\text{sr}}$  denotes the part of the total cluster mass constituted by stellar remnants. The evolution of dark cluster mass can be expressed as

$$\frac{dM_{\text{cl}}^{\text{sr}}}{dt} = \left( \frac{dM_{\text{cl}}^{\text{sr}}}{dt} \right)_{\text{ev}} + \left( \frac{dM_{\text{cl}}^{\text{sr}}}{dt} \right)_{\text{dis}}, \quad (3.9)$$

where at the right-hand side the first (positive) term describes the production of remnants due to stellar evolution, and the second (negative) term represents remnant loss due to dis-

<sup>5</sup>If stellar mass-dependent cluster dissolution is omitted, after 12 Gyr stellar remnants constitute about 30% of the total cluster mass. Within this fraction, the summed mass ratios of black holes, neutron stars and white dwarfs are 1:3.5:9. These ratios change when mass-dependent dissolution is included.

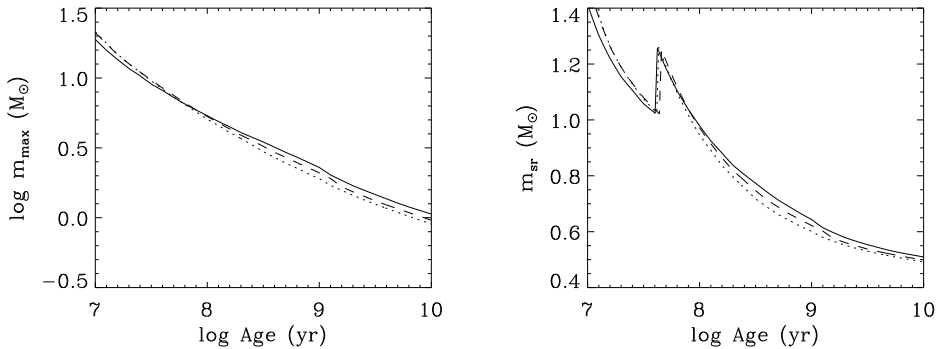


**Figure 3.1:** *Left:* Maximum stellar mass  $m_{\max}(t)$  as a function of age for  $Z = \{0.0004, 0.004, 0.02\}$  (dotted, dashed and solid lines, respectively). *Right:* Produced stellar remnant mass  $m_{\text{sr}}(t)$  as a function of age for  $Z = \{0.0004, 0.004, 0.02\}$  (dotted, dashed and solid lines, respectively). The peak corresponds to the transition from neutron star production to white dwarf production, i.e. the lifetime of an  $8 M_{\odot}$  star.

solution. Stellar evolution removes stars at the high-mass end of the mass function. Stellar remnant production can be included by assuming an initial-remnant mass relation and leaving a remnant mass  $m_{\text{sr}}$  upon such removal.

From Kalirai et al. (2008), for white dwarfs ( $m_s < 8 M_{\odot}$ ) this relation is given by

$$m_{\text{sr}} = 0.109 m_s + 0.394 M_{\odot}, \quad (3.10)$$

with  $m_{\text{sr}}$  the remnant mass and  $m_s$  the stellar mass, where  $m_s$  is equal to the initial stellar mass in our models since instantaneous death is assumed. For  $m_s < 0.45 M_{\odot}$ , Eq. 3.10 is not valid since the remnant mass then exceeds the progenitor mass. However, this does not cause any problems because it only occurs for ages *much* larger than the Hubble time.

For neutron stars ( $8 M_{\odot} \leq m_s < 30 M_{\odot}$ ), the initial-remnant mass relation is taken to be (Nomoto et al. 1988):

$$m_{\text{sr}} = 3.63636 \times 10^{-2} (m_s - 8 M_{\odot}) + 1.02 M_{\odot}. \quad (3.11)$$

Stars with masses  $m_s \geq 30 M_{\odot}$  result in a black hole and since no definitive models for black hole formation exist, the corresponding remnant mass is assumed to be

$$m_{\text{sr}} = 8 M_{\odot}. \quad (3.12)$$

This value is in agreement with dynamical masses obtained from X-ray binary observations (e.g. Casares 2007). When the above initial-remnant mass relation is linked to the maximum stellar mass  $m_{\max}(t)$ , the remnant mass  $m_{\text{sr}}(t)$  that is produced at time  $t$  can be obtained. This varies with metallicity; for  $Z = \{0.0004, 0.004, 0.02\}$  examples are shown in the right-hand panel of Fig. 3.1.

We can now compute the total cluster mass fraction in stellar remnants  $\mu_{\text{ev}}^{\text{sr}}(t)$  by integrating the remnant masses  $m_{\text{sr}}$  over the mass function for the mass range of all stars that have ended their lives:

$$\mu_{\text{ev}}^{\text{sr}}(t) = \frac{\int_{m_{\text{max}}(t)}^{m_{\text{max},i}} m_{\text{sr}}(m_s) N_s(0, m_s) dm_s}{M_{\text{cl},i}}, \quad (3.13)$$

with  $N_s(0, m_s)$  the initial form of Eq. 3.1. The total remaining mass fraction  $\mu_{\text{ev}}^{\text{tot}}(t)$  is obtained by adding this to the mass fraction in luminous mass (see Eq. 3.6). Similarly to  $q_{\text{ev}}^{\text{lum}}$ , we provide fitting constants as in Eq. 3.7 for  $q_{\text{ev}}^{\text{tot}} \equiv 1 - \mu_{\text{ev}}^{\text{tot}}$  in the bottom half of Table 3.1. Again, we will not use these fits in the remainder of this study, since the stellar content of clusters is treated. Instead, the initial-remnant relations from Eqs. 3.10—3.12 are used. Nonetheless, Table 3.1 is provided for convenience.

Given the expression for  $\mu_{\text{ev}}^{\text{sr}}(t)$ , the remnant production per unit time (first right-hand term of Eq. 3.9) can now be determined. By multiplying the time derivative of  $\mu_{\text{ev}}^{\text{sr}}(t)$  with initial cluster mass and correcting the normalisation of the stellar mass function for a possible decrease due to dissolution, this fraction can be translated into the time derivative of non-luminous cluster mass

$$\left( \frac{dM_{\text{cl}}^{\text{sr}}}{dt} \right)_{\text{ev}} = \frac{d\mu_{\text{ev}}^{\text{sr}}(t)}{dt} M_{\text{cl},i} \frac{C(t)}{C(0)}, \quad (3.14)$$

which is similar to the expression derived for the total cluster mass evolution due to stellar evolution (Eq. 3.5).

The above approach does not account for kick velocities that are obtained by neutron stars and black holes upon their creation. The implications for integrated cluster properties are discussed in Sect. 3.6.1, point (3).

### 3.2.3 Dissolution

The effect of dissolution on the stellar mass function differs for clusters with or without the preferential loss of low-mass stars. In clusters that have reached energy equipartition, the low-mass objects tend to reside in the outer regions, while the most massive bodies are generally located near the cluster centre, and the cluster preferentially loses low-mass objects. In clusters without the preferential loss of low-mass stars, bodies<sup>6</sup> of different masses are lost with almost equal probabilities. Both cases are treated in this section.

The dynamical mass loss (second right-hand term of Eq. 3.3) can be expressed as

$$\left( \frac{dM_{\text{cl}}^{\text{tot}}}{dt} \right)_{\text{dis}} = -\frac{M_{\text{cl}}^{\text{tot}}}{\tau_{\text{dis}}} = -\frac{M_{\text{cl}}^{\text{tot}}}{t_0 M_{\text{cl}}^{\text{tot}\gamma}} = -\frac{M_{\text{cl}}^{\text{tot}1-\gamma}}{t_0}, \quad (3.15)$$

where  $\tau_{\text{dis}}$  is the dissolution timescale. In empirical studies it was shown to be related to present cluster mass as  $\tau_{\text{dis}} = t_0 (M_{\text{cl}}/M_{\odot})^{\gamma}$  by Boutloukos & Lamers (2003) and Lamers et al. (2005a). Boutloukos & Lamers (2003) found  $\gamma = 0.62 \pm 0.06$ , the same value as derived

<sup>6</sup>‘Bodies’ denotes either stars or stellar remnants.

by Gieles et al. (2004) for the  $N$ -body simulations of clusters in tidal fields by Baumgardt & Makino (2003). Please note that  $M_{\text{cl}}^{\text{tot}}$  represents the total cluster mass and thus includes stars as well as their remnants.

The rapidity of the exponential mass decrease in Eq. 3.15 is set by the dissolution timescale parameter  $t_0$ , which is essentially the dissolution timescale for a hypothetical  $1 M_{\odot}$  cluster. Because the total disruption time  $t_{\text{dis}}^{\text{total}}$  of a cluster is determined by dynamical dissolution *and* stellar evolution and thus depends on the adopted IMF and on metallicity, we prefer the use of  $t_0$  over  $t_{\text{dis}}^{\text{total}}$  to characterise the strength of dissolution alone. Throughout this chapter we will give the typical total disruption times associated with used values of the dissolution timescale  $t_0$ .

### Mass loss from clusters without the preferential loss of low-mass stars: the ‘canonical mode’

Cluster mass evolution can be computed numerically from its time derivatives due to stellar evolution and dissolution (Eqs. 3.5 and 3.15). For a more detailed and more accurate description of cluster evolution we turn to its stellar content. We distinguish between stellar mass-independent dissolution (‘canonical mode’) and the preferential loss of low mass stars (‘preferential mode’). When considering mass loss in the canonical mode, i.e. the evolution of the stellar mass function of a cluster without the preferential loss of low-mass stars, the influence of mass loss due to stellar evolution and dissolution is twofold. Stellar evolution decreases the maximum stellar mass  $m_{\text{max}}(t)$ , while dissolution decreases the normalisation factor of the mass function  $C(t)$  (see Eq. 3.1) because stellar masses are randomly distributed throughout the cluster and thus all bodies have approximately similar probabilities of being ejected.

The normalisation of the mass function  $C(t)$  is directly proportional to luminous cluster mass  $M_{\text{cl}}^{\text{lum}}(t)$  because the latter is obtained by integrating the mass function (Eq. 3.1) over stellar mass. We define a parameter  $f_{\text{pref}}(t)$  to describe the fraction of mass loss occurring in preferential mode (see Sect. 3.2.3) and a fraction  $f_{\text{sr}}(t)$  of the mass loss to occur in the form of stellar remnants. This implies that the factor  $1 - f_{\text{pref}}(t)$  denotes the fraction of mass loss that occurs in the canonical mode, while the factor  $1 - f_{\text{sr}}(t)$  represents the fraction of mass loss that takes place in the form of luminous mass (i.e. not in stellar remnants). For mass loss in the canonical mode, i.e. without the preferential loss of low-mass stars, we have  $f_{\text{pref}}(t) = 0$ . Then the time derivative of luminous cluster mass from a cluster in the canonical mode, i.e. without the preferential loss of low-mass stars, is written as

$$\left( \frac{dM_{\text{cl}}^{\text{lum}}}{dt} \right)_{\text{dis}}^{\text{can}} = [1 - f_{\text{pref}}(t)][1 - f_{\text{sr}}(t)] \left( \frac{dM_{\text{cl}}^{\text{tot}}}{dt} \right)_{\text{dis}} = \frac{M_{\text{cl}}^{\text{lum}}}{C(t)} \frac{dC}{dt}, \quad (3.16)$$

where  $C \propto M_{\text{cl}}^{\text{lum}}$  and thus  $d \ln C / dt = d \ln M_{\text{cl}}^{\text{lum}} / dt$  leads to the last equality, and the label ‘can’ indicates we are dealing with mass loss in the canonical mode. Substituting the total mass derivative from Eq. 3.15 yields after rearranging

$$\frac{dC}{dt} = -[1 - f_{\text{pref}}(t)][1 - f_{\text{sr}}(t)] \frac{M_{\text{cl}}^{\text{tot}1-\gamma}}{t_0 M_{\text{cl}}^{\text{lum}}} C(t). \quad (3.17)$$

In the canonical mode, the influence of mass loss on the stellar mass function is completely described by this expression. If either the cluster only loses stars of the lowest masses ( $f_{\text{pref}}(t) = 1$ ) or all mass is lost in the form of stellar remnants ( $f_{\text{sr}}(t) = 1$ ), we have constant normalisation  $C(t)$  and mass loss affects the cluster content in different ways (see below and Sect. 3.2.3).

To include the loss of stellar remnants, we specify the expression for the fraction of mass loss that occurs in the form of remnants  $f_{\text{sr}}(t)$ . For mass loss in the canonical mode the spatial distribution of bodies is random. This implies that the fraction of the total mass lost due to dissolution that is lost in the form of remnants is equal to the ratio of remnant mass to total cluster mass

$$f_{\text{sr}}(t) = M_{\text{cl}}^{\text{sr}}(t)/M_{\text{cl}}^{\text{tot}}(t). \quad (3.18)$$

We can use this parameter to describe how the cluster mass in stellar remnants changes due to dissolution (the second right-hand term of Eq. 3.9):

$$\left(\frac{dM_{\text{cl}}^{\text{sr}}}{dt}\right)_{\text{dis}}^{\text{can}} = [1 - f_{\text{pref}}(t)]f_{\text{sr}}(t) \left(\frac{dM_{\text{cl}}^{\text{tot}}}{dt}\right)_{\text{dis}} = -[1 - f_{\text{pref}}(t)]f_{\text{sr}}(t)\frac{M_{\text{cl}}^{\text{tot}1-\gamma}}{t_0}, \quad (3.19)$$

where we use the description of the total mass loss derivative due to dissolution from Eq. 3.15. Again, the factor  $1 - f_{\text{pref}}(t)$  represents the fraction of mass loss that takes place in the canonical mode, while the factor  $f_{\text{sr}}(t)$  denotes the fraction of mass loss that occurs in the form of stellar remnants. This expression completely describes the influence of mass loss in the canonical mode on the total cluster mass in stellar remnants.

### Mass loss from clusters including the preferential loss of low-mass stars: the ‘preferential mode’

From  $N$ -body simulations, it is shown by Baumgardt & Makino (2003) how energy equipartition affects the evolution of the stellar mass function. From their study it is evident that most clusters exhibit the preferential loss of low-mass stars, making it a very important mechanism when considering cluster evolution. In Lamers et al. (2006), analytical models for the evolution of the mass function are presented which are based on these simulations. In their models, dissolution no longer induces a uniform effect on the mass function by decreasing its normalisation. Instead, preferentially low-mass stars are removed. This can be approximated by a gradual increase in the lower mass limit of the stars present in the cluster  $m_{\text{min}}(t)$  (Lamers et al. 2006). By using this description, the *slope* of the mass function remains unchanged as the loss of low-mass stars is incorporated by increasing the lower mass limit. This is done in such a way that the mean stellar mass is always comparable to the mean stellar mass in the  $N$ -body simulations by Baumgardt & Makino (2003), in which the shape of the mass function *does* change due to the preferential loss of low-mass stars.

To describe mass loss in the preferential mode, i.e. mass loss including the preferential loss of low-mass stars, we use the parameter  $f_{\text{pref}}(t)$  that represents the fraction of cluster mass loss that occurs in preferential mode at time  $t$ . The formulation allows for intermediate cases of energy equipartition, since  $f_{\text{pref}}(t)$  can have any value between 0 and 1. The  $N$ -body simulations by Baumgardt & Makino (2003) suggest a rapid transition from a random

ejection of bodies to the preferential loss of low-mass stars, resulting in almost a step function for  $f_{\text{pref}}(t)$ . For a cluster that initially does not preferentially lose low-mass stars but reaches complete energy equipartition at  $t = t_{\text{pref}}$  we can then write

$$f_{\text{pref}}(t) = \begin{cases} 0 & \text{for } t < t_{\text{pref}} \\ 1 & \text{for } t \geq t_{\text{pref}}. \end{cases} \quad (3.20)$$

However, because complete energy equipartition ( $f_{\text{pref}}(t) = 1$ ) is unlikely to occur (see the discussion in Sect. 3.4), we will probably have  $f_{\text{pref}}(t) < 1$  for  $t \geq t_{\text{pref}}$ .

By explicitly integrating stellar mass over the mass function (Eq. 3.1), the luminous cluster mass is obtained. Because in the preferential mode dissolution only affects the minimum stellar mass, we can write for the time derivative of luminous cluster mass:

$$\left( \frac{dM_{\text{cl}}^{\text{lum}}}{dt} \right)_{\text{dis}}^{\text{pref}} = f_{\text{pref}}(t)[1 - f_{\text{sr}}^{\text{pref}}(t)] \left( \frac{dM_{\text{cl}}^{\text{tot}}}{dt} \right)_{\text{dis}} = -\frac{C(t)\eta(m_{\text{min}})}{2 - \beta(m_{\text{min}})} \frac{d}{dt} m_{\text{min}}^{2 - \beta(m_{\text{min}})}, \quad (3.21)$$

for  $\beta(m_{\text{min}}) \neq 2$  and

$$\left( \frac{dM_{\text{cl}}^{\text{lum}}}{dt} \right)_{\text{dis}}^{\text{pref}} = f_{\text{pref}}(t)[1 - f_{\text{sr}}^{\text{pref}}(t)] \left( \frac{dM_{\text{cl}}^{\text{tot}}}{dt} \right)_{\text{dis}} = -C(t)\eta(m_{\text{min}}) \frac{d}{dt} \ln(m_{\text{min}}), \quad (3.22)$$

if  $\beta(m_{\text{min}}) = 2$ , where  $\beta(m_{\text{min}})$  is the slope of the stellar mass function (see Eq. 3.1) and the label ‘pref’ indicates we are dealing with mass loss in the preferential mode. The fraction of mass loss occurring in the preferential mode is represented by the factor  $f_{\text{pref}}(t)$ , while the factor  $1 - f_{\text{sr}}^{\text{pref}}(t)$  denotes the fraction of mass loss in the preferential mode occurring in the form of luminous mass (i.e. not in the form of remnants, see below for more details). Again, we substitute the total mass derivative (Eq. 3.15), which yields a differential equation describing the effect of the preferential loss of low-mass stars. After rearranging the terms, mass loss in the preferential mode thus results in an evolution of the lower mass limit  $m_{\text{min}}(t)$ :

$$\frac{dm_{\text{min}}}{dt} = f_{\text{pref}}(t)[1 - f_{\text{sr}}^{\text{pref}}(t)] \frac{M_{\text{cl}}^{\text{tot}1-\gamma} m_{\text{min}}(t)^{\beta(m_{\text{min}})-1}}{C(t)\eta(m_{\text{min}})t_0}, \quad (3.23)$$

for all values of  $\beta(m_{\text{min}})$ . If a cluster is has not reached energy equipartition ( $f_{\text{pref}}(t) = 0$ ), mass loss is independent of stellar mass. In that case, the time derivative  $dm_{\text{min}}/dt = 0$  and we thus have constant  $m_{\text{min}}(t)$ .

We now describe stellar remnant loss from clusters that have reached energy equipartition. If a cluster is completely mass-segregated, remnants are produced in the cluster centre and only become available for dissolution if remnants are the least massive bodies in the cluster. Therefore, the fraction of mass loss taking place in the form of stellar remnants that is used here  $f_{\text{sr}}^{\text{pref}}(t)$  differs from the expression for canonical mass loss (Eq. 3.18).

From Fig. 3.1 we know that the produced remnant mass nearly always decreases with time, while  $m_{\text{min}}(t)$  is a monotonously increasing function of  $t$ . This implies that there is a time  $t_{\text{sr}}$  at which  $m_{\text{min}}(t)$  increases to a value larger than the smallest stellar remnant mass

$m_{\text{sr}}(t)^7$ . For all  $t \geq t_{\text{sr}}$  mass can be lost in the form of remnants<sup>8</sup>. For these values of  $t$ , all remnant masses  $m_{\text{sr}}(t) \leq m_{\text{sr}} \leq m_{\text{min}}(t)$  are considered to be immediately available for dissolution (see the Appendix Sect. 3.A for a justification of this assumption). Consequently, they are immediately *lost* by dissolution, because they are the least massive bodies in the cluster.

The fraction of mass loss occurring in the form of stellar remnants is different for clusters with and without the preferential loss of low-mass stars. Therefore, we define a separate parameter  $f_{\text{sr}}^{\text{pref}}(t)$  for the fraction of mass loss in the form of remnants if the cluster preferentially loses low-mass bodies. The time derivative of dark cluster mass (the second right-hand term in Eq. 3.9) thus becomes:

$$\left(\frac{dM_{\text{cl}}^{\text{sr}}}{dt}\right)_{\text{dis}}^{\text{pref}} = f_{\text{pref}}(t)f_{\text{sr}}^{\text{pref}}(t)\left(\frac{dM_{\text{cl}}^{\text{tot}}}{dt}\right)_{\text{dis}} = -f_{\text{pref}}(t)f_{\text{sr}}^{\text{pref}}(t)\frac{M_{\text{cl}}^{\text{tot}1-\gamma}}{t_0}, \quad (3.24)$$

which is nearly the same expression as Eq. 3.19 that is valid in the canonical mode. The fraction of mass loss occurring in the preferential mode is again represented by the factor  $f_{\text{pref}}(t)$ . We have yet to specify the fraction of mass loss in the form of remnants for a the preferential loss of low-mass stars  $f_{\text{sr}}^{\text{pref}}(t)$ . If we consider a certain time interval  $dt$ , there are two possibilities: either the remnant mass available for dissolution ( $M_{\text{cl}}^{\text{sr,dis}}$ , which is the total mass of all remnants with masses smaller than the lowest stellar mass present at time  $t$ ) is so large that all mass loss during the interval  $dt$  can be accounted for by removing remnants *only*, or luminous mass has to be lost as well. In the former case, the minimum stellar mass  $m_{\text{min}}(t)$  is not reached before the end of the time interval  $dt$  while losing the lowest mass bodies (i.e. remnants) and all mass loss takes place in the form of stellar remnants. For the latter case,  $m_{\text{min}}(t)$  is reached during the interval  $dt$ , and the fraction of mass loss to occur in the form of remnants is then described by the ratio of the available remnant mass and the total mass loss during the time interval  $dt$ . This implies

$$f_{\text{sr}}^{\text{pref}}(t) = \min \left[ 1, -M_{\text{cl}}^{\text{sr,dis}} / \frac{dM_{\text{cl}}^{\text{tot}}}{dt} dt \right], \quad (3.25)$$

where the denominator of the second term between brackets can be obtained from the expression for cluster mass loss due to dissolution (Eq. 3.15) and the numerator is computed numerically from

$$M_{\text{cl}}^{\text{sr,dis}}(t) = \int_{m_{\text{max}}(t)}^{m_{\text{s}}^{\text{min,sr}}(t)} m_{\text{sr}}(m_{\text{s}})N_{\text{s}}(t, m_{\text{s}})dm_{\text{s}} - \int_0^t f_{\text{pref}}(t')f_{\text{sr}}^{\text{pref}}(t')\frac{M_{\text{cl}}^{\text{tot}}(t')^{1-\gamma}}{t_0}dt'. \quad (3.26)$$

<sup>7</sup>Incidentally, because the produced stellar remnant mass nearly always decreases with time, the smallest remnant mass at time  $t$  is the stellar remnant mass that is produced at that time.

<sup>8</sup>Strictly spoken, this merely holds for  $m_{\text{min}}(t)$  that intersect  $m_{\text{sr}}(t)$  only once. From Fig. 3.1 we see that at the transition from neutron star production to white dwarf production there is a possibility for curves of  $m_{\text{min}}(t)$  to increase to a value larger than  $m_{\text{sr}}(t)$ , before briefly being overtaken again due to the change of produced remnant type. In that case,  $m_{\text{min}}(t)$  intersects  $m_{\text{sr}}(t)$  three times. However, the slope of  $m_{\text{min}}(t)$  is typically very steep compared to  $m_{\text{sr}}(t)$ , and thus only a very small fraction of all cluster initial masses will pass through the described fluctuation over a negligible timespan. Therefore, we can indeed assume that for all  $t \geq t_{\text{sr}}$  mass can be lost in the form of stellar remnants.



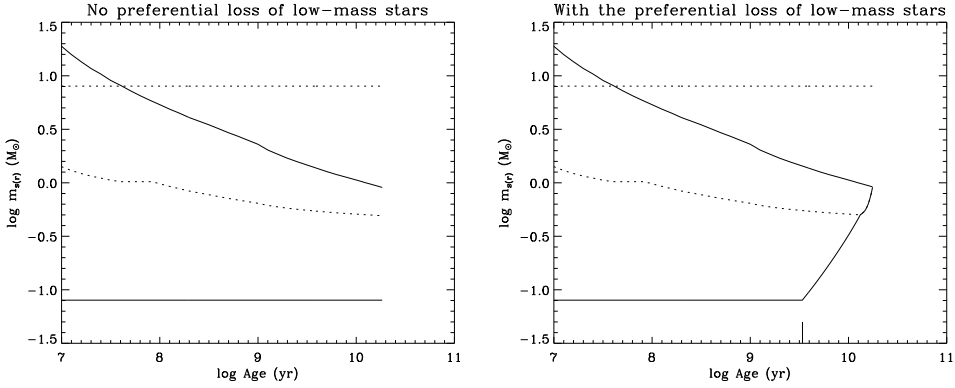


**Figure 3.2:** *Left:* Evolution of minimum and maximum masses of stars (solid) and stellar remnants (dotted) in a cluster with  $M_{\text{cl},i} = 10^6 M_{\odot}$ ,  $t_0 = 3$  Myr and without the preferential loss of low-mass stars. *Right:* Same as left, but including the preferential loss of low-mass stars. The tickmark at  $\log t \approx 9.5$  indicates the onset of the preferential mode (see Sect. 3.4.1).

The first right-hand term denotes the total produced remnant mass that is available for a given *present* mass function  $N_s(t, m_s)$  and increases with time. The upper integration limit of the integral  $m_s^{\text{min},\text{sr}}(t)$  represents the initial stellar mass corresponding to remnants with mass equal to  $m_{\text{min}}(t)$ <sup>9</sup> and the mass function is thus integrated for produced remnant masses  $m_{\text{sr}}(t) \leq m_{\text{min}}(t)$ . By introducing the second right-hand term in Eq. 3.26, we subtract the part of the produced remnant mass that has already been lost by dissolution. This integral follows from the time derivative of non-luminous cluster mass (Eq. 3.24) and describes all remnant mass that was lost in the preferential mode. Using the present mass function in the first right-hand term of Eq. 3.26 assumes that any change in the normalisation of the stellar mass function has a proportional effect on total remnant mass. The normalisation only changes for mass loss in the canonical mode (i.e. mass loss from clusters without the preferential loss of low-mass stars), for which dissolution is stellar mass-independent. Hence, if the normalisation of the stellar mass function were to change, the total mass in remnants would be affected accordingly, thereby justifying the above assumption.

### 3.2.4 Total cluster evolution

The description of cluster evolution from Sects. 3.2.1 to 3.2.3 includes stellar evolution and four modes of mass loss: luminous mass loss and stellar remnant loss from clusters without the preferential loss of low-mass stars, and luminous mass loss and stellar remnant loss from clusters that have reached energy equipartition and do preferentially lose low-mass stars. In this section the derived expressions are combined.

The evolution of the stellar mass function is completely described by (1) the time derivative of its normalisation factor  $C(t)$  (Eq. 3.17) that describes the general decrease of the mass

<sup>9</sup>These are the most massive remnants that are available for dissolution.

function, (2) the time derivative of the minimum stellar mass  $m_{\min}(t)$  (Eq. 3.23) that describes the loss of low-mass stars, and (3)  $m_{\max}(t)$  that describes the loss of high-mass stars due to stellar evolution. When combining these equations, the luminous cluster mass follows from

$$M_{\text{cl}}^{\text{lum}}(t) = \int_{m_{\min}(t)}^{m_{\max}(t)} m_s N_s(t, m_s) dm_s, \quad (3.27)$$

with  $N_s(t, m_s)$  the stellar mass function from Eq. 3.1.

Similarly, the expressions describing stellar remnant loss for clusters with and without the preferential loss of low-mass stars (Eqs. 3.19 and 3.24) can be combined with the expression representing remnant production (Eq. 3.14) to write

$$\frac{dM_{\text{cl}}^{\text{sr}}}{dt} = \frac{d\mu_{\text{ev}}^{\text{sr}}(t)}{dt} M_{\text{cl},i} \frac{C(t)}{C(0)} - \{ [1 - f_{\text{pref}}(t)] f_{\text{sr}}(t) + f_{\text{pref}}(t) f_{\text{sr}}^{\text{pref}}(t) \} \frac{M_{\text{cl}}^{\text{tot}1-\gamma}}{t_0}, \quad (3.28)$$

with  $\mu_{\text{ev}}^{\text{sr}}(t)$  from Eq. 3.13. The first right-hand term denotes the production of stellar remnants, while the second represents the loss of stellar remnants in the canonical mode (represented by the factor  $[1 - f_{\text{pref}}(t)] f_{\text{sr}}(t)$ ) and in the preferential mode (represented by the factor  $f_{\text{pref}}(t) f_{\text{sr}}^{\text{pref}}(t)$ ). This equation can be integrated for the total remnant mass in the cluster  $M_{\text{cl}}^{\text{sr}}(t)$ . Finally, addition of the total remnant mass to the luminous cluster mass from Eq. 3.27 yields the total cluster mass as formulated in Eq. 3.4.

The above set of equations can be solved numerically and represents a range of models that describe the complete evolution of cluster content for clusters with and without the preferential loss of low-mass stars. A simple recursive integration scheme is used. As a criterion for total cluster disruption, we use a lower luminous cluster mass limit  $M_{\text{cl}}^{\text{lum}} = 100 M_{\odot}$ , though other values can be adopted if necessary.

We now briefly illustrate the time evolution of the mass ranges of stars and remnants in a  $10^6 M_{\odot}$  cluster. These are shown in Fig. 3.2 for models with and without the preferential loss of low-mass stars. Solid lines describe the upper and lower mass limits of the stars in the cluster, while the minimum and maximum masses of stellar remnants are represented by dotted curves. The left panel shows the evolution without the preferential loss of low-mass stars, while for the right panel it is included.

Without the preferential loss of low-mass stars, the minimum stellar mass is constant since mass loss occurs by removing stars of all masses and thus by decreasing the normalisation of the mass functions of stars and remnants. Stellar evolution causes the maximum stellar mass to decrease. The maximum remnant mass remains constant at the maximum remnant mass that was produced in the cluster. On the other hand, the minimum remnant mass decreases as remnants of lower masses are produced. Until total cluster disruption, bodies from a broad mass range can be retained. The cluster is completely disrupted when the normalisation constant  $C(t)$  approaches zero.

When including the preferential loss of low-mass stars, the minimum stellar mass starts to increase as soon as mass loss occurs in the preferential mode. The maximum stellar and remnant masses exhibit the same behaviour as for clusters without the preferential loss of low-mass stars. Initially, the same holds for the minimum remnant mass. However, when the minimum remnant mass reaches the minimum stellar mass, the lowest mass bodies in the

cluster are stars and remnants. This leads to a combined evolution of the lower mass limits of both. The cluster is completely disrupted when the stellar mass limits meet.

### 3.3 Computation of photometric cluster evolution

Cluster photometry is computed from the Padova 1999 isochrones, that are described in Bertelli et al. (1994) and are based on spectral energy distributions from Kurucz (1992), but use a treatment of AGB stars as in Girardi et al. (2000). The photometry computation is accomplished by direct integration of luminosities over the stellar mass function for a given age and initial cluster mass. This approach allows for greater flexibility when including the preferential loss of low-mass stars, since the evolving mass function is explicitly included in the computation. If existing SSP models had been adopted, this would not have been the case because such models only include fading by stellar evolution for a fixed mass function.

For a cluster of arbitrary age  $t$  and initial mass  $M_{\text{cl},i}$ , the stellar luminosities of the two isochrones at ages  $t_i$ ,  $i = \{1, 2\}$  closest to  $t$  are integrated over the computed mass functions at these ages, with  $t_1 < t$  and  $t_2 > t$ . This results in total cluster luminosities  $L_{\text{cl},\lambda}(t_i, M_{\text{cl},i})$  for passband  $\lambda$ . These luminosities are then interpolated to obtain  $L_{\text{cl},\lambda}(t, M_{\text{cl},i})$  and converted to absolute magnitudes.

For existing SSP models, which only account for the effect of stellar evolution and therefore do not treat clusters near their total disruption, the above procedure suffices to determine photometric cluster evolution. However, if  $t_1 < t < t_{\text{dis}} < t_2$  the cluster is disrupted before  $t_2$  and there are no stars left at  $t_2$ . This leads to inadequate luminosity computations if the above interpolation is used. In that case the stellar mass function of the cluster at age  $t$  is adopted for both ages  $t_1$  and  $t_2$  and the mass range is shifted to fit the appropriate maximum stellar masses at these ages. After integrating the resulting two mass functions, we obtain two luminosities  $L_{\text{cl},\lambda}(t_i, M_{\text{cl},i})$  for each passband. Interpolation then yields  $L_{\text{cl},\lambda}(t, M_{\text{cl},i})$ . The described method does not accurately reproduce the luminosity contribution of the lowest stellar masses because the mass function is shifted to fit to  $M_{\text{max}}(t_1, t_2)$ . However, this leaves the resulting magnitude almost completely unaffected since the high-mass end of the mass function completely dominates cluster photometry.

Contrary to some existing SSP models like *GALEV*, no gas emission is included in our photometric models. Line emission is only important for clusters that contain massive stars that emit ionising photons. This implies that our photometry can be considered to be accurate for ages  $t \gtrsim 8$  Myr for solar metallicity and  $t \gtrsim 20$  Myr if  $Z = 0.0004$  (Anders & Fritzev. Alvensleben 2003).

### 3.4 Photometric properties of clusters

In this section we apply the models described in Sects. 3.2 to 3.3 to investigate the effects of the preferential loss of low-mass stars, stellar remnants, IMF and metallicity on the mass, magnitude, colour and mass-to-light ratio evolution of clusters. We computed our models for cases with and without the preferential loss of low-mass stars, with and without stellar remnants, Salpeter and Kroupa IMFs, and metallicities  $Z = \{0.0004, 0.004, 0.008, 0.02, 0.05\}$ .

Moreover, we considered initial cluster masses  $M_{\text{cl},i}$  in the range  $10^2$ — $10^7 M_\odot$  and dissolution timescales  $t_0$  of 0.1—100 Myr<sup>10</sup>. As a result, cluster evolution for total disruption times  $t_{\text{dis}}^{\text{total}} > 10$  Myr has been computed for cluster ages between 10 Myr and 19 Gyr (the upper age limit of the stellar isochrones). Models for a broad range of parameters are publicly available in electronic form at the CDS, while predictions for specific models can be made by the first author upon request. The most important results of our models are discussed in this section.

### 3.4.1 The effects of model components

Accounting for the preferential loss of low-mass stars and including the mass of stellar remnants both have their effects in the framework of our models. In this section these effects are considered.

#### The effects of the preferential loss of low-mass stars

The preferential loss of low-mass stars induced by energy equipartition and possibly also mass segregation (see Sect. 3.1) can be expected to have a significant effect on the magnitude and colour evolution of clusters (Lamers et al. 2006), but also on their mass and mass-to-light ratio. Complete energy equipartition ( $f_{\text{pref}}(t) = 1$ ) implies that *only* bodies of the lowest masses are lost, an implication that does not seem likely to be in accordance with reality for two reasons. First of all, external perturbations are not strictly confined to the very outer radius of a cluster due to internal cluster dynamics. Therefore, dynamical mass loss is not confined to the very outer layer of the cluster, which results in the loss of stars or remnants with masses above  $m_{\text{min}}(t)$ . Secondly, complete energy equipartition may not be reached by a cluster (Baumgardt & Makino 2003), inducing only a partial preferential loss of low-mass stars. Therefore, we tuned the evolution of  $m_{\text{min}}(t)$  in our complete models to the  $N$ -body simulations by Baumgardt & Makino (2003) so that their mean stellar mass evolution is similar. This allows us to determine a step function form for  $f_{\text{pref}}(t)$  that leads to a mean mass evolution that corresponds best to its counterpart in the  $N$ -body simulations. This analysis results in

$$f_{\text{pref}}(t) = \begin{cases} 0.0 & \text{for } t < t_{\text{pref}}, \\ 0.4 & \text{for } t \geq t_{\text{pref}}, \end{cases} \quad (3.29)$$

with  $t_{\text{pref}} = 0.2t_{\text{dis}}^{\text{total}}$ . A more gradual evolution would follow the simulations somewhat better, but a step function serves as a good approximation (see Lamers et al. (2006) and Sect. 3.6).

The assumption of constant  $t_{\text{pref}}/t_{\text{dis}}^{\text{total}} = 0.2$  serves as a typical timescale after which the preferential loss of low-mass stars can become important. It can be justified by considering the mass-dependences of  $t_{\text{pref}}$  and  $t_{\text{dis}}^{\text{total}}$ . The total disruption time scales with cluster mass

<sup>10</sup>This is the typical dissolution timescale range (e.g. Lamers et al. 2005b), corresponding to  $t_{\text{dis}}^{\text{total}} \approx 10^8$ — $10^{11}$  yr for a  $10^5 M_\odot$  cluster. It can be easily checked by considering that the total disruption time is of the order of  $t_{\text{dis}}^{\text{total}} \sim t_0(M_{\text{cl},i}/M_\odot)^\gamma$ . Throughout this section  $t_0 = 3$  Myr will be used, which is the mean value of this range and is the typical timescale for clusters in the solar neighbourhood. This value is typical of tidally dissolving globular clusters on circular orbits at 3 kpc from the Galactic centre, or clusters on eccentric ( $e = 0.7$ ) orbits with an apogalactic distance of 8.5 kpc (Baumgardt & Makino 2003).

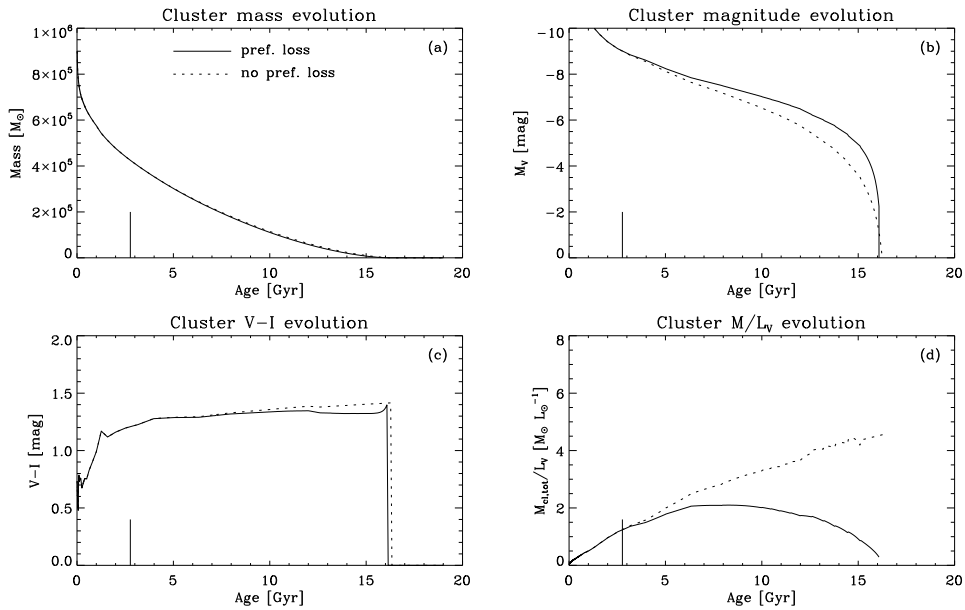


**Figure 3.3:** Effect of the preferential loss of low-mass stars on (a) total cluster mass, (b) V-band magnitude, (c)  $V - I$  and (d)  $M/L_V$  evolution for clusters with initial mass  $M_{\text{cl},i} = 10^6 M_{\odot}$ , no stellar remnants, a dissolution timescale  $t_0 = 3 \text{ Myr}$  ( $t_{\text{dis}}^{\text{total}} = 16\text{--}16.5 \text{ Gyr}$ ), metallicity  $Z = 0.02$ , and a Kroupa IMF. Solid curves denote cluster evolution when the preferential loss of low-mass stars is included, while clusters without the preferential loss of low-mass stars are represented by dotted lines. The onset of the preferential mode  $t_{\text{pref}}$  is denoted by a vertical line.

similarly to the dissolution timescale, i.e.  $t_{\text{dis}}^{\text{total}} \propto M^{0.62}$ . On the other hand,  $t_{\text{pref}}$  can be expected to scale with the half-mass relaxation time  $t_{\text{rh}}$ , i.e.  $t_{\text{pref}} \propto M^{0.5} r_{\text{h}}^{1.5}$ . If we adopt a mean mass-radius relation  $r_{\text{h}} \propto M^{0.10 \pm 0.03}$  (Larsen 2004), this leads to  $t_{\text{pref}} \propto M^{0.65}$ , which is comparable to the mass-dependence of the total disruption time. We also considered models with  $t_{\text{pref}} = t_{\text{rh}}$ , assuming the same mass-radius relation, which indeed yields values for  $t_{\text{pref}}$  that are similar to  $0.2 t_{\text{dis}}^{\text{total}}$ .

Furthermore, we do not consider primordial mass segregation ( $t_{\text{pref}} = 0$ ) for the model runs that are presented in this section. However, from other model runs where we did set  $t_{\text{pref}} = 0$  we know that the effects of the preferential loss of low-mass stars on cluster observables are about 10% stronger for primordial mass segregation than for the described results. Of course,  $t_{\text{pref}}$  can always be adapted to describe different forms of mass segregation.

The formulation in Eq. 3.29 implies that after  $t_{\text{pref}}$  dynamical mass loss simultaneously occurs in both modes. Hereafter, any reference to the ‘preferential loss of low-mass stars’ implies the use of this prescription for  $f_{\text{pref}}$  in our models. The value of  $f_{\text{pref}}(t \geq t_{\text{pref}})$  is different from the one presented by Lamers et al. (2006) because they did not compare its value to  $N$ -body simulations: only  $t_{\text{pref}}$  was treated in that study.

In Fig. 3.3 the effect of the preferential loss of low-mass stars on the total cluster mass  $M_{\text{cl}}^{\text{tot}}$ , V-band magnitude,  $V - I$  and mass-to-light ratio ( $M/L_V$ ) evolution is shown for clusters with initial mass  $M_{\text{cl},i} = 10^6 M_{\odot}$ , no inclusion of stellar remnants (i.e. all remnants are immediately removed), a dissolution timescale  $t_0 = 3$  Myr, metallicity  $Z = 0.02$ , and a Kroupa IMF. This leads to a total disruption time of  $t_{\text{dis}}^{\text{total}} \approx 16$  Gyr. For cluster evolution without the preferential loss of low-mass stars, some expected trends are immediately evident: mass and magnitude decrease with time, while  $M/L_V$  increases and the cluster becomes redder.

As can be observed when comparing the curves in Fig. 3.3, including the preferential loss of low-mass stars has several implications for the cluster evolution computed with our models.

- (1) *The total disruption time of a cluster including the preferential loss of low-mass stars hardly changes but is slightly smaller than for a cluster for which it is omitted.* This is the result of our model assumptions, as the preferential loss of low-mass bodies causes a larger number of massive stars to be retained in the cluster. The corresponding shorter lifetimes induce an increase in the cluster mass loss by stellar evolution. The enhanced decrease of total cluster mass consequently leads to a smaller total disruption time. However, this effect does not include the possible decrease of the total disruption time due to quicker two-body relaxation in clusters with enhanced mean stellar masses. Note that the decrease of total disruption time is of order  $\sim 1\%$ , which is best visible in the panel displaying colour evolution.
- (2) *As soon as the preferential loss of low-mass stars starts, i.e.  $f_{\text{pref}}(t) > 0$ , the cluster stays much brighter than for mass loss in the canonical mode.* Because the luminosity per unit mass is much higher for massive stars, a cluster that preferentially loses low-mass stars will be more luminous than a cluster of the same mass that does not. The change in the V-band magnitude induced by the preferential loss of low-mass stars peaks at about  $0.9 t_{\text{dis}}^{\text{total}}$  and is at most 1.5 mag.
- (3) *The colour evolution of clusters is affected by the preferential loss of low-mass stars in two ways. After the onset of energy equipartition, Fig. 3.3(c) shows that these clusters are bluer than clusters without the preferential loss of low-mass stars, while just before total disruption reddening can be observed.* At first, the bottom end of the main sequence, which is being lost due to the preferential loss of low-mass stars, is redder than the average colour of the cluster. Due to the removal of its red constituents, such a cluster will appear bluer than a cluster without the preferential loss of low-mass stars. However, as stars are lost and  $m_{\text{min}}(t)$  moves up the main sequence the colours of the stars that are ejected become increasingly blue. Cluster colour is then dominated by red giants and the ejected stars are bluer than the average cluster colour. Before total disruption, this induces a reddening of clusters exhibiting the preferential loss of low-mass stars. The ages at which these changes occur depend on cluster  $t_{\text{dis}}^{\text{total}}$ . For model runs with different  $t_{\text{dis}}^{\text{total}}$  (either by varying initial cluster mass  $M_{\text{cl},i}$  or dissolution timescale  $t_0$ ), we find that clusters including the preferential loss of low-mass stars always become slightly bluer from about  $0.4 t_{\text{dis}}^{\text{total}}$  on. However, the reddening is stronger and

occurs at a smaller fraction of  $t_{\text{dis}}^{\text{total}}$  for clusters with smaller total disruption times. This tendency is caused by massive red giants, which are redder and more luminous than low-mass giants. For smaller total disruption times, the reddening causes clusters in the preferential mode to become much redder than clusters losing mass in the canonical mode during the last few percent of their lifetime. This effect is also present for the initial conditions used here if stellar remnants are included (see Fig. 3.4).

- (4) As can be observed in Fig. 3.3(d), *the preferential loss of low-mass stars leads to a much smaller mass-to-light ratio than for clusters losing mass in the canonical mode.* Considering points (1) and (2), this is not surprising. A higher luminosity and slightly smaller mass together imply a decrease in  $M/L_V$ . The magnitude of the induced decrease is comparable to the change in cluster V-band luminosity, which follows from the magnitude change to be about a factor six.

In their study, Lamers et al. (2006) obtained magnitude evolution curves that are much more weakly affected by the preferential loss of low-mass stars than is shown in Fig. 3.3. In the present chapter, cluster photometries are directly computed from the changing stellar mass function, which is a more direct method than the one used in Lamers et al. (2006)<sup>11</sup>. Therefore, our computation of cluster evolution provides an update to their results. Furthermore, they found that clusters including the preferential loss of low-mass stars are bluer for  $0.4 < t/t_{\text{dis}}^{\text{total}} < 0.8$  and redder for  $t \geq 0.8 t_{\text{dis}}^{\text{total}}$ . Our extended study of the parameter space shows that especially the value of 0.8 depends on the total disruption time of the cluster.

The effect of the preferential loss of low-mass stars is clearly visible in *magnitude, colour* and  $M/L_V$  *evolution* of clusters. Especially cluster magnitude and  $M/L_V$  are significantly affected. This implies that when considering either observable, it is very important to determine whether the cluster exhibits the preferential loss of low-mass stars or not, for example by checking whether it is mass-segregated. In order to obtain an appropriate interpretation of cluster colour, it has to be determined how close to total disruption the cluster is.

### The effects of stellar remnants

The inclusion of stellar remnants follows the description presented in Sects. 3.2.2 and 3.2.3. In our models, it implies that part of the mass is retained upon the death of a star and clusters thus lose mass due to stellar evolution at a slower rate. It can be expected to affect cluster mass evolution, because a significant fraction of cluster mass can be constituted by remnants. Clearly, the mass-to-light ratio will then be altered as well. To assess the effect of stellar remnants on cluster evolution, our model results are shown in Fig. 3.4 for clusters with initial mass  $M_{\text{cl},i} = 10^6 M_{\odot}$ , with and without the preferential loss of low-mass stars, a dissolution timescale  $t_0 = 3$  Myr ( $t_{\text{dis}}^{\text{total}} = 16\text{--}18.5$  Gyr), metallicity  $Z = 0.02$  and a Kroupa IMF.

We observe the following changes in our models due to the inclusion of stellar remnants.

- (1) Because the net mass loss due to stellar evolution is smaller if stellar remnants are retained in the cluster after the death of their progenitors, *the total cluster mass is higher*

---

<sup>11</sup>Lamers et al. (2006) calculated magnitudes by using the photometry of stellar mass-truncated GALEV models.

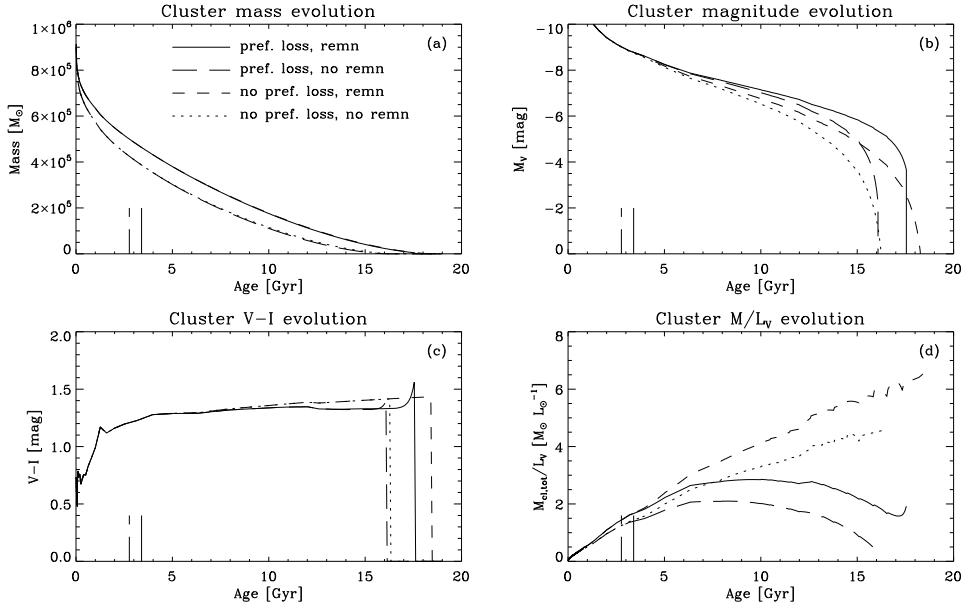


**Figure 3.4:** Effect of stellar remnants on (a) total cluster mass, (b) V-band magnitude, (c)  $V - I$  and (d)  $M/L_V$  evolution for clusters with initial mass  $M_{\text{cl},i} = 10^6 M_{\odot}$ , a dissolution timescale  $t_0 = 3$  Myr ( $t_{\text{dis}}^{\text{total}} = 16\text{--}18.5$  Gyr), metallicity  $Z = 0.02$ , and a Kroupa IMF. Solid curves denote the evolution for clusters including the preferential loss of low-mass stars with stellar remnants, long-dashed curves without stellar remnants. For clusters without the preferential loss of low-mass stars, short-dashed curves represent the case in which remnants are included and dotted curves represent the result without stellar remnants. The onset of the preferential mode  $t_{\text{pref}}$  is marked by vertical lines in the linestyles of the corresponding model runs.

than in the non-remnant case at any time. The immediate consequence is that the models predict a larger total disruption time. For clusters including the preferential mode, which more easily keep their remnants (see Sect. 3.2.3 and point (3)), this effect is smaller than for clusters without the preferential loss of low-mass stars, because the death criterion of clusters in our simulations ( $M_{\text{cl}}^{\text{lum}} < 100 M_{\odot}$ ) only depends on luminous cluster mass. Retaining remnants implies that mass loss due to dissolution more strongly affects luminous cluster mass, causing a cluster that exhibits the preferential loss of low-mass stars to satisfy the death criterion of our models earlier than expected for its total mass. However, though this weakens the lifetime-increasing effect of keeping stellar remnants, it never dominates.

- (2) For clusters without the preferential loss of low-mass stars, where the fraction of mass lost in the form of remnants is simply equal to the remnant mass fraction, the inclusion of remnants leads to a higher luminosity. Increasing luminosity by including remnants might be counter-intuitive. However, when including stellar remnants part of the clus-



ter mass loss by dissolution is in the form of remnants instead of luminous stars. This implies that the average luminosity of bodies that are lost by dissolution is smaller than in the case without remnants, leading to a smaller luminosity decrease. Though less explicitly, the same effect is present in clusters including the preferential loss of low-mass stars since low-mass stars hardly contribute to the total cluster luminosity. Moreover, the lifetime-extending effect of remnants also implies that (luminous) mass is lost at a slower pace. We conclude that *the cluster luminosity decrease due to dissolution becomes smaller if stellar remnants are included.*

- (3) The mass-to-light ratio evolution shows a very clear effect of stellar remnants as *for both mass loss modes the  $M/L_V$  curves are much higher if remnants are included.* This means that the relative increase of cluster mass due to remnants is larger than the corresponding relative increase of cluster magnitude that was discussed at point (2). The former is a direct consequence of adding remnants, while the latter is an induced effect: the average  $M/L_V$  of all bodies in a cluster is higher per definition if dark mass is added. Furthermore, *for clusters with the preferential loss of low-mass stars that also includes stellar remnants, the mass-to-light ratio shows an increase during the final part of cluster evolution.* This can be attributed to the preservation of remnants in clusters losing mass in the preferential mode, which is due to the fact that remnants can only be lost from these clusters if  $m_{sr} < m_{min}(t)$ .

Because remnant production or loss does not directly alter the colour composition of luminous cluster content, colour evolution is hardly affected by the inclusion of remnants.

We find that the inclusion of stellar remnants strongly affects the *mass, magnitude* and  *$M/L_V$  evolution* of clusters. This is because part of the cluster mass loss occurs in the form of remnants rather than luminous stars. The extent of the differences (up to 30% at  $t = 0.5t_{dis}^{total}$  and increasing afterwards) suggests that a proper treatment of remnants should be included in any cluster model.

### 3.4.2 The effects of the stellar IMF

As discussed in Sect. 3.2.3, our models can be calculated for any multi-component power law IMF. Different IMFs are likely to exhibit a tendency to higher or lower stellar masses with respect to one another. For the Kroupa and Salpeter IMFs, the consequences of this effect are investigated here. As mentioned in Sect. 3.2, the lower mass limit is taken to be  $m_{min,i} = 0.08 M_{\odot}$  for a Kroupa IMF and  $m_{min,i} = 0.1 M_{\odot}$  for a Salpeter IMF. Since a Salpeter IMF has a slightly steeper slope than a Kroupa IMF, and the latter features a bend at  $0.5 M_{\odot}$ , the Salpeter IMF has a lower mean stellar mass. Figure 3.5 displays our results for both IMFs in the case of clusters with initial mass  $M_{cl,i} = 10^6 M_{\odot}$ , with and without the preferential loss of low-mass stars, with stellar remnants, a dissolution timescale  $t_0 = 3$  Myr ( $t_{dis}^{total} = 17.5$ –21 Gyr) and metallicity  $Z = 0.02$ .

The initial mass function affects the resulting cluster evolution in the following ways.

- (1) *Total cluster mass stays higher for clusters with a Salpeter IMF.* Consequently, their total disruption times are increased as well. Since it has a slightly steeper slope, the

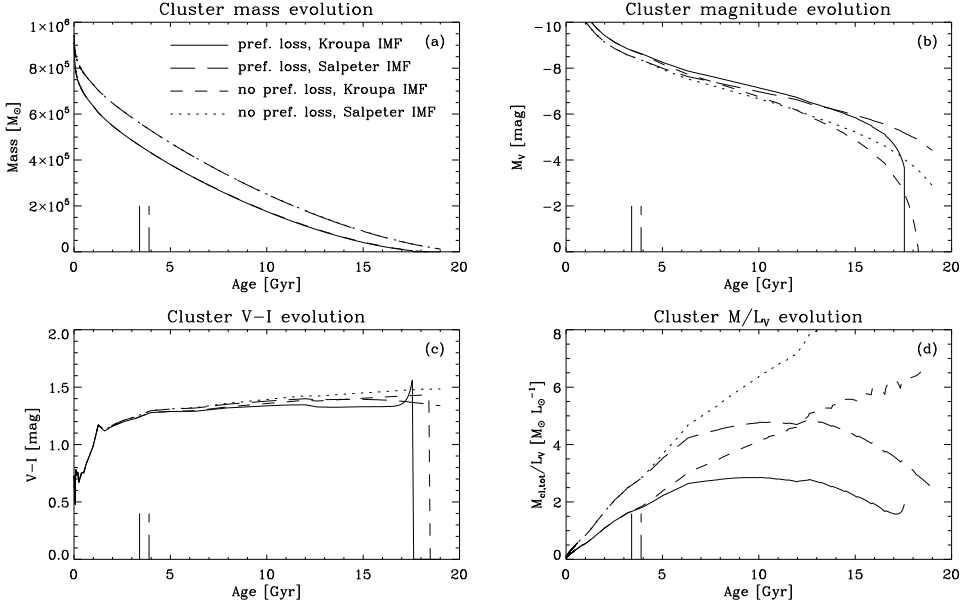


**Figure 3.5:** Effect of initial mass function on (a) total cluster mass, (b)  $V$ -band magnitude, (c)  $V - I$  and (d)  $M/L_V$  evolution for clusters with initial mass  $M_{\text{cl},i} = 10^6 M_{\odot}$ , including stellar remnants, a dissolution timescale  $t_0 = 3$  Myr ( $t_{\text{dis}}^{\text{total}} = 17\text{--}21$  Gyr) and metallicity  $Z = 0.02$ . For a Kroupa IMF, solid curves denote the evolution for clusters including the preferential loss of low-mass stars, short-dashed lines for clusters with canonical mass loss. Clusters with a Salpeter IMF are represented by long-dashed lines when the preferential loss of low-mass stars is included and dotted lines describe the case where it is omitted. The onset of the preferential mode  $t_{\text{pref}}$  is marked by vertical lines in the linestyles of the corresponding model runs.

mass loss due to stellar evolution is smaller than for a Kroupa IMF. The resulting higher cluster mass leads to dissolution acting on a longer timescale, thereby also contributing to an extended lifetime of the cluster. In this case, the example model clusters with a Salpeter IMF survive beyond the maximum age spanned by the models.

- (2) Because it favours stars of higher masses, a Kroupa IMF leads to clusters that are initially slightly brighter than for a Salpeter IMF. However, the mass decrease due to stellar evolution is also stronger for a Kroupa IMF, causing its cluster mass to be lower than for a Salpeter IMF. As a result, the luminosities of clusters with a Salpeter IMF overtake those with a Kroupa IMF later on. Though still very weak, the transition is best visible when comparing the curves corresponding to clusters with mass loss in the preferential mode in Fig. 3.5(b). For these, the transition occurs at about  $0.7 t_{\text{dis}}^{\text{total}}$ . From model runs with other total disruption times, we observe that this fraction of  $t_{\text{dis}}^{\text{total}}$  is not constant. It significantly increases for smaller  $t_{\text{dis}}^{\text{total}}$ , with  $M_V$  of a Salpeter IMF always being fainter than that of a Kroupa IMF for  $t_{\text{dis}}^{\text{total}} \lesssim 500$  Myr.

- (3) *Clusters with a Kroupa IMF are slightly bluer than those with a Salpeter IMF.* However, this effect is too small to be observable in real clusters. It can be understood by considering the relatively larger contribution of massive (blue) stars in evolved clusters with a Kroupa IMF. Had the Salpeter examples been disrupted within the model age range, the characteristic reddening just before total disruption would have been visible for that IMF as well.
- (4) The higher masses of clusters with a Salpeter IMF and their generally lower luminosities that were described at point (2) together lead to *higher mass-to-light ratios for clusters evolving from a Salpeter IMF.* Again, for clusters including the preferential loss of low-mass stars, the final  $M/L_V$  increase upon total disruption would also be visible for the Salpeter IMF if it would have been completely disrupted within the model age range.

Although specifically applied to the Kroupa and Salpeter IMFs, qualitatively the results of the above analysis hold for any two mass functions of which one has a different mean mass than the other. Quantitatively, there will still be variations depending on the specific IMF.

Because the underlying stellar IMF in a cluster determines its future mass loss due to stellar evolution, it strongly affects the *total disruption time* and *mass-to-light ratio*. Any treatment of these two observables requires an accurate description of the IMF.

### 3.4.3 The effects of metallicity

To investigate the influence of metallicity on our results, we consider  $Z = \{0.0004, 0.004, 0.02\}$  in Fig. 3.6. Model results are shown for clusters with initial mass  $M_{\text{cl},i} = 10^6 M_{\odot}$ , with and without the preferential loss of low-mass stars, including stellar remnants, a dissolution timescale  $t_0 = 3 \text{ Myr}$  ( $t_{\text{dis}}^{\text{total}} = 17\text{--}18.5 \text{ Gyr}$ ) and a Kroupa IMF.

The effects of metallicity on the results are as follows.

- (1) We see that *total cluster mass is hardly affected by metallicity at any time.* It marginally increases with  $Z$ , which is caused by more rapid stellar evolution for low metallicities (e.g. Hurley et al. 2000, 2004). Consequently, the total disruption time also slightly increases with metallicity, which is best observed in the  $M_V$  and  $V - I$  panels. Nevertheless, the effect is small, less than 10% of the total lifetime. This is in excellent agreement with the results from Hurley et al. (2004).
- (2) *Low- $Z$  clusters are brighter than high- $Z$  clusters.* This is due to a general luminosity decrease of stars with metallicity (e.g. Girardi et al. 2000, Hurley et al. 2004). The difference is observed for clusters with and without the preferential loss of low-mass stars, and is typically more than one  $V$ -band magnitude.
- (3) The colour evolution shows a uniform trend with  $Z$ . *Clusters with high metallicity are much redder than clusters with low metallicity.* This is the result of stellar atmospheres and stellar evolution (e.g. Hurley et al. 2000). For high ages, the  $V - I$  value is more or less constant for each metallicity, underlining its value as metallicity probe for globular clusters when considering broadband colours (e.g. Maraston 2005). The  $V - I$  shift

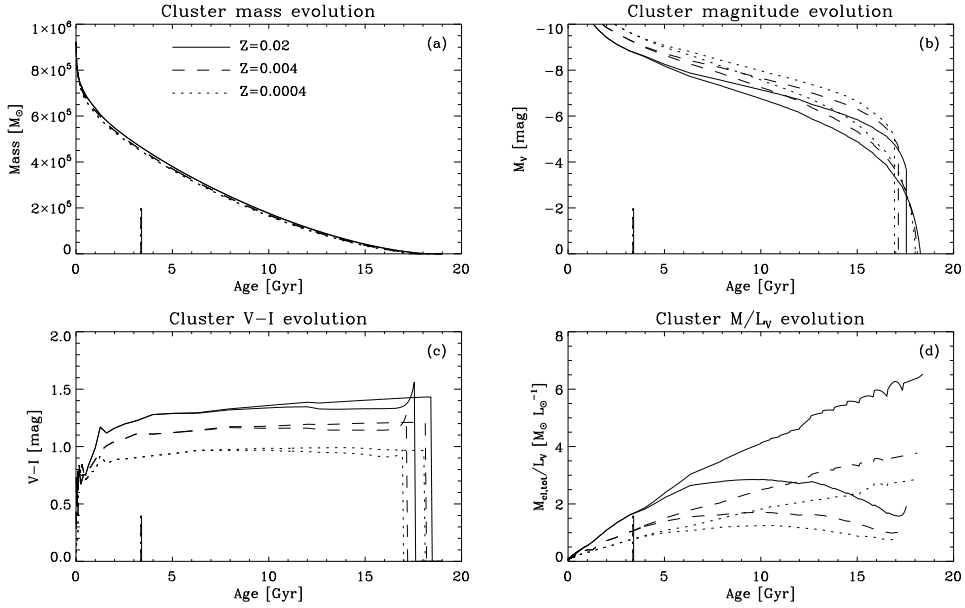


**Figure 3.6:** Effect of metallicity on (a) total cluster mass, (b)  $V$ -band magnitude, (c)  $V - I$  and (d)  $M/L_V$  evolution for clusters with initial mass  $M_{\text{cl},i} = 10^6 M_{\odot}$ , including stellar remnants, a dissolution timescale  $t_0 = 3$  Myr ( $t_{\text{dis}}^{\text{total}} = 17\text{--}18.5$  Gyr) and a Kroupa IMF. Solid curves denote the evolution for  $Z = 0.02$ , dashed curves for  $Z = 0.004$ , and dotted ones for  $Z = 0.0004$ . Results with and without the preferential loss of low-mass stars show effects as presented in Fig. 3.3 and described in Sect. 3.4.1 and are therefore represented by the same linestyles. The onset of the preferential mode  $t_{\text{pref}}$  is marked by vertical lines in the linestyles of the corresponding model runs.

between  $Z = 0.0004$  and  $Z = 0.02$  is about 0.5 mag, but varies for colours at other wavelengths. This is in accordance with the fact that clusters of different metallicities move on clearly distinguishable paths in colour-colour diagrams (e.g. Bruzual & Charlot 2003).

- (4) The higher luminosity of low-metallicity stars and the consequently slightly enhanced mass loss by stellar evolution induce a common effect on cluster mass-to-light ratios. From Fig. 3.6(d) we see that  $M/L_V$  *strongly increases with metallicity*. The effect is strong enough to move the  $M/L_V$  evolution of a  $Z = 0.0004$  cluster with canonical mass loss through the  $M/L_V$  range of a cluster that does include the preferential loss of low-mass stars at  $Z = 0.02$ . This apparent degeneracy is lifted by taking cluster colours into account (see point (3)).

Whenever cluster *magnitude*, *colour* and *mass-to-light ratio* evolution are considered, cluster metallicity plays an important role. They are all strongly affected by the adopted metallicity. For globular cluster populations this implies that a range of colours and mass-to-light ratios

can be covered by a metallicity spread of the population or internal cluster processes like self-enrichment.

In Lamers et al. (2005a), an expression is provided for the total disruption time  $t_{\text{dis}}^{\text{total}}$  as a function of  $t_0$ ,  $M_{\text{cl},i}$  and  $\gamma$ . In this study, we find that  $t_{\text{dis}}^{\text{total}}$  depends on the inclusion of the preferential loss of low-mass stars, stellar remnants, IMF and metallicity. Therefore, values for  $t_{\text{dis}}^{\text{total}}$  are best obtained by integrating the models presented in this chapter. Regardless, the expression from Lamers et al. (2005a) can still be used to estimate  $t_{\text{dis}}^{\text{total}}$  with approximately 20% accuracy.

## 3.5 Application to globular clusters

The results presented in Sect. 3.4 cover a wide range of masses, magnitudes, colours and mass-to-light ratios. As a first indication, it is relevant to check whether the properties of Galactic globular clusters can be reproduced in our models. For this purpose, the results have to be considered at ages  $t \approx 12$  Gyr. From Harris (1996) the  $M_V$  range is found to be  $M_V = -1.60$  (Pal 1) to  $M_V = -10.29$  ( $\omega$ Cen). For the Solar neighbourhood value of the dissolution timescale in the case of  $e = 0.7$  orbits  $t_0 = 3 \text{ Myr}^{12}$ , we find that this range can be covered at  $t = 12$  Gyr for any metallicity  $Z \leq 0.02$  if the maximum *initial* cluster mass equals  $M_{\text{cl}}^{\text{max}} = 10^7 M_{\odot}$ . For longer dissolution timescales (i.e. larger galactocentric radii) the observed magnitude range can be covered with even smaller maximum initial cluster masses. Please note that the dissolution timescale depends on the tidal field strength and that it therefore varies for different globular cluster orbits. This implies that it is not possible to impose limits on the properties of the complete globular cluster population (like their maximum initial masses) from an analysis in which this variation is not incorporated.

### 3.5.1 The mass-to-light ratio

Galactic globular cluster mass-to-light ratios are found to be  $M/L_V = 1.45 \pm 0.1 M_{\odot} L_{\odot}^{-1}$  (McLaughlin 2000). SSP models, in which only stellar evolution is included and dynamical effects are neglected, predict a *minimum* value of  $M/L_V \approx 2 M_{\odot} L_{\odot}^{-1}$  at  $t = 12$  Gyr, requiring the minimum metallicity of our models  $Z = 0.0004$  (see Fig. 3.6). This further complicates explaining the observed mass-to-light ratios, since globular cluster metallicities are typically  $Z = 0.0004$ – $0.014$  (VanDalfsen & Harris 2004). Dynamical effects are thus needed to explain the even smaller mass-to-light ratio of Galactic globular clusters. If the preferential loss of low-mass stars is included, cluster mass-to-light ratio curves do span the correct part of  $M/L_V$  space, ranging down to  $M/L_V < 1 M_{\odot} L_{\odot}^{-1}$  (see also Kruijssen 2008). From Fig. 3.4 we see that accounting for stellar remnants yields an *increase* up to  $1 M_{\odot} L_{\odot}^{-1}$  relative to model clusters without stellar remnants, obviously implying that they should be included for accurate interpretations of globular cluster observations. If globular clusters are populated using a Salpeter IMF rather than a Kroupa IMF, this effect is nearly doubled (see Fig. 3.5). From Fig. 3.6(d) we find that cluster models at high metallicities do not reproduce the low observed  $M/L_V = 1.45 \pm 0.1 M_{\odot} L_{\odot}^{-1}$ . Thus, metal-poor clusters including the preferential

---

<sup>12</sup>See Sect. 3.4.1.

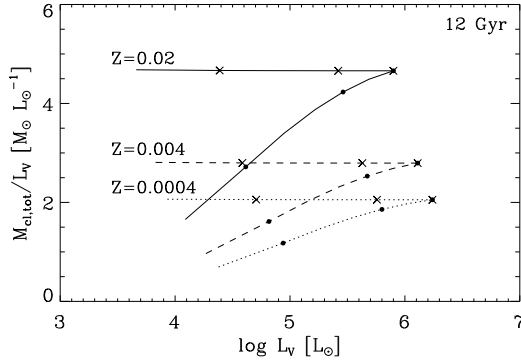


**Figure 3.7:** Effect of the preferential loss of low-mass stars on the relation between mass-to-light ratio and luminosity at an age of  $t = 12$  Gyr. Metallicities  $Z = \{0.0004, 0.004, 0.02\}$  are denoted by dotted, dashed and solid curves, respectively. Horizontal lines represent clusters without the preferential loss of low-mass stars, while inclined curves show the relation if it is included. The models are computed for initial masses between  $10^2 M_\odot$  and  $10^7 M_\odot$ , a Kroupa IMF, dissolution timescale  $t_0 = 3$  Myr and including stellar remnants. On each curve, clusters with (from left to right) *initial* masses  $\log M_{cl,i} = \{6, 6.5, 7\}$  are marked with crosses (canonical mode) and dots (preferential mode). The present day mass can be derived from the luminosity and mass-to-light ratio.

loss of low-mass stars with a Kroupa IMF<sup>13</sup> are required to reach the low average mass-to-light ratio. If these conditions are met, the moderately flat  $M/L_V$  evolution curves show that a more or less constant time-average is not surprising.

Some globular clusters have mass-to-light ratios that are much higher than the mean value of  $M/L_V = 1.45 \pm 0.1 M_\odot L_\odot^{-1}$ . An example is  $\omega$ Cen ( $M/L_V = 2.5 M_\odot L_\odot^{-1}$ , see van de Ven et al. 2006), which is also the most massive Galactic globular cluster<sup>14</sup>, with  $M_{cl}^{\omega\text{Cen}} = 2.5 \times 10^6 M_\odot$  (van de Ven et al. 2006). Since a high mass implies a large relaxation time, this could agree with the view that  $\omega$ Cen has not yet reached energy equipartition.

Another important implication of our analysis of mass-to-light ratio evolution is that globular clusters of comparable ages can *not* be assumed to have constant  $M/L_V$  for different cluster luminosities at fixed metallicity. For a given age, the mass-to-light ratio can strongly ( $\sim 0.6$  dex) depend on the dynamical state of the cluster (see Fig. 3.3(d)), and thus on cluster mass and luminosity. The variation of  $M/L_V$  with luminosity when including mass loss in the preferential mode is illustrated in Fig. 3.7. Models are shown of clusters with and without the preferential loss of low-mass stars, metallicities  $Z = \{0.0004, 0.004, 0.02\}$  (dotted, dashed and solid curves, respectively), age  $t = 12$  Gyr, a maximum cluster mass of  $10^7 M_\odot$ , a Kroupa IMF, dissolution timescale  $t_0 = 3$  Myr and including stellar remnants. The horizontal lines denote the constant mass-to-light ratios predicted if the preferential loss of low-mass

<sup>13</sup>Or any other IMF that slightly favours massive stars with respect to a Salpeter IMF.

<sup>14</sup>In fact,  $\omega$ Cen is not a normal globular cluster since there are strong indications that it could be a stripped dwarf galaxy (e.g. Ijeta & Makino 2004).

stars is ignored, while the inclined curves show the relation between  $M/L_V$  and luminosity if it is accounted for.

Since more luminous clusters are also more massive, the onset of mass loss in the preferential mode occurs later on for these clusters, implying that its effects are weaker for massive clusters at any age. Because the preferential loss of low-mass stars decreases the mass-to-light ratio, this decrease is thus smaller for clusters of higher masses, leading to a mass-to-light ratio that increases with cluster mass and  $L_V$  as in Fig. 3.7. Observational evidence of this effect for the same quantitative range has been found for Galactic and extragalactic globular clusters (e.g. Mandushev et al. 1991, Rejkuba et al. 2007, Kruijssen 2008). If cluster masses are determined using a fixed  $M/L_V$ , thereby not accounting for the effects of the preferential loss of low-mass stars, these masses can be strongly *overestimated* by as much as 0.6 dex. Because the error is larger for lower masses, the slope of the inferred cluster mass function will be *underestimated* (i.e. a negative slope will be steeper) if the preferential loss of low-mass stars is ignored.

It is straightforward to derive a quantitative estimate for the effect on the inferred (powerlaw) cluster mass function. Let us consider clusters with ‘true’ mass  $M$  that are exhibiting the preferential loss of low-mass stars and are thus in the regime that is inconsistent with canonical cluster models. If we now use a powerlaw with index  $A$  to reasonably approximate the mass-to-light ratio increase with luminosity from Fig. 3.7, i.e.  $M/L \propto L^A$  for  $\log L \lesssim 5.5$  depending on metallicity, then the ratio of the photometrically inferred mass  $M_{\text{SSP}}$  for which constant  $M_{\text{SSP}}/L$  is assumed to its true mass  $M$  scales as  $M_{\text{SSP}}/M \propto L^{-A}$ . This is equivalent to using a powerlaw with index  $B = A/(1 + A)$  to approximate the mass-to-light ratio increase with *true mass*, i.e.  $M/L \propto M^B$ , leading to  $M_{\text{SSP}}/M \propto M^{-B}$ . Then, for a ‘true’ slope of the cluster mass function  $-\alpha$ , its *photometrically inferred* slope  $-\alpha_{\text{SSP}}$  using constant mass-to-light ratios is given by

$$-\alpha_{\text{SSP}} = -\alpha - \alpha A + A = (-\alpha + B)/(1 - B). \quad (3.30)$$

From Fig. 3.7 we find that typically  $A \sim 0.27$  (and thus  $B \sim 0.21$ ), implying that for  $\alpha = 2$  we find  $\alpha_{\text{SSP}} \sim 2.27$ . The deviation increases with the age of the cluster sample (here we used  $t = 12$  Gyr, while for  $t = 3$  Gyr  $\alpha_{\text{SSP}} \sim 2.23$ ) and the above approach assumes a constant dissolution timescale for the cluster sample. For (more realistic) varying dissolution timescales, the deviation will typically be between 50% and 100% of the presented value. This is still significant and should thus be accounted for when studying the cluster mass function of old cluster samples.

The variation of  $M/L_V$  with luminosity is crucial for cluster masses inferred from luminosities, which can be incorrectly determined by 0.6 dex. Because of increasing evidence that more globular clusters are preferentially losing low-mass stars and might have evolved to a mass-segregated state than previously thought (e.g. De Marchi et al. 2007), this effect should always be considered when studying globular clusters.

### 3.5.2 Colours of globular clusters

The typical colour range of Galactic globular clusters is 0.75—1.1 in  $V - I$  (Smith et al. 2007). From Fig. 3.6(c) we can conclude that this range is covered by varying metallicity in

our models. Obviously, IMF variations might slightly affect the colour range as well, with top-heavy IMF showing a tendency to bluer colours (see Fig. 3.5(c)). However, this effect is only significant for strongly deviating IMFs. Still, from all figures in Sect. 3.4 we still see that colours are affected by the preferential loss of low-mass stars and the colour range is increased. Figure 3.6(c) illustrates that if mass loss in the preferential mode would be ignored, uncertainties up to 0.2 mag (0.1 mag up and down) should be included for computed cluster colours at a any fixed age and metallicity. This happens to be the same colour spread at fixed metallicity as found by Smith et al. (2007) in their colour-metallicity relation.

### 3.5.3 Ultra-compact dwarf galaxies

We see that including the preferential loss of low-mass stars and stellar remnants allows for a more extensive analysis of globular clusters and affects their reproduced property ranges. It is evident that globular clusters or more massive globular cluster-like objects with very high mass-to-light ratios (with regard to their metallicities) cannot have experienced significant mass loss in the preferential mode unless their  $M/L_V$  is increased by a strongly differing IMF or by agents unaccounted for by our models, for instance by intermediate mass black holes, modified gravity or dark matter. Hence, if indications for the preferential loss of low-mass stars (such as mass segregation or a bottom-depleted mass function) are found for such objects, they points to these causes for the high observed  $M/L_V$ . For objects with masses  $M > 10^7 M_\odot$  this is unlikely to occur, since their relaxation times are of the order of a Hubble time or larger.

If there is a present day globular cluster mass above which no clusters have yet reached energy equipartition, any objects above that mass will have high mass-to-light ratios with respect to clusters below that mass. This is found for UCDs, of which the  $M/L_V$ -range is typically  $2\text{--}10 M_\odot L_\odot^{-1}$  (e.g. Mieske & Kroupa 2008). Pending the role of dark matter these galaxies could be regarded a natural continuation of the mass spectrum beyond globular clusters. Indications for such a continuation are found by Wehner & Harris (2007) for UCD candidates in NGC 3311. As is clear from Fig. 3.5(d), our models without the preferential loss of low-mass stars produce mass-to-light ratios similar to UCDs if a Salpeter IMF is assumed (in agreement with Hilker et al. 2007), while the canonical Kroupa IMF cannot reproduce the range that is typical to UCDs (as is also found by Mieske et al. 2008). Nonetheless, any possible connection between globular clusters and UCDs would be smoothed by metallicity spreads and the possible influence of dark matter, making it a challenge to be directly observed.

Contrary to low-mass UCDs, more massive examples have not reached energy equipartition within a Hubble time due to their long relaxation times. However, this would lead to constant mass-to-light ratios at high masses, while Rejkuba et al. (2007) have shown that the trend of increasing  $M/L_V$  with mass is even stronger for UCDs than it is for globular clusters.



## 3.6 Discussion

We have described models to calculate the evolution of star clusters including the preferential loss of low-mass stars and stellar remnants. Furthermore, they have been used to investigate the influence of these model components, as well as of the IMF and metallicity on cluster evolution. In this section we discuss the assumptions that were made, their influence on the results and the applicability of our models. We also indicate how the models can be improved.

### 3.6.1 Influence of assumptions

The models presented in this study are based on the following assumptions.

- (1) We adopt the Padova 1999 stellar evolution models (Bertelli et al. 1994, AGB treatment as in Girardi et al. 2000) to compute photometry, determine stellar lifetimes and describe the consequent cluster mass loss due to stellar evolution. For the *mass evolution* of all stars we assume constant stellar masses until their instantaneous deaths. Only very massive stars experience strong mass loss during a significant part of their lives, but these stars hardly contribute to the total cluster mass. Low-mass stars with  $m_s \lesssim 8 M_\odot$  only suffer significant mass loss during the last 10% of their lives. Therefore, instantaneous death is a reasonable assumption when calculating cluster mass. *The photometric properties of stars are not affected* by our assumption of instantaneous death, since stellar photometry as described in the Padova models includes the photometric effects of stellar mass loss. The Padova isochrones include a description of AGB evolution, which is very important since AGB stars dominate the photometric evolution of stars after about 100 Myr.
- (2) If stellar remnants are included, upon its death a star is replaced by a body with mass determined by the initial-remnant mass relation. For white dwarfs, the relation from Kalirai et al. (2008) is assumed, while neutron star and black hole masses are based on studies by Nomoto et al. (1988) and Casares (2007), respectively. Our resulting initial-remnant mass relation for the full stellar mass range is independent of metallicity. However, generally a metallicity dependence is found for both white dwarf (e.g. Kalirai et al. 2005, Meng et al. 2008) and neutron star masses (e.g. Hurley et al. 2000). Remnants formed at high metallicities are generally less massive than those formed at low metallicities. The difference between  $Z = 0.0004$  and  $Z = 0.02$  is typically  $\sim 10\%$ , which implies that the speed of the increase of non-luminous cluster mass  $M_{\text{cl}}^{\text{sr}}$  due to stellar remnant production would be enhanced by 10% at low metallicities. For Fig. 3.6, which shows the effect of metallicity on our results, this would have some small consequences. Assuming a remnant to total cluster mass fraction  $M_{\text{cl}}^{\text{sr}}/M_{\text{cl}}^{\text{tot}} \approx 0.5$ , the slope of total cluster mass evolution (Fig. 3.6(a)) would be increased (i.e. become less steep) by a few percent at low metallicities, extending the total disruption time by a comparable but slightly lower percentage due to the  $M_{\text{cl}}^{\text{tot}\gamma}$  mass dependence of the dissolution timescale. Moreover, curves describing  $M/L_V$  cluster evolution (Fig. 3.6(d)) would exhibit metallicity effects that are smaller by a few percent. Overall, these corrections are not sufficiently large to have a significant effect on our results.

- (3) We assume all remnant bodies to be initially bound to the cluster. In reality, supernovae may induce kick velocities on their remnant black holes and neutron stars (e.g. Portegies Zwart et al. 1997). A fraction of these remnants will have velocities larger than the escape velocity. Typical escape velocities of globular clusters are  $\sim 30 \text{ km s}^{-1}$  (McLaughlin & van der Marel 2005), while in some cases kick velocities of several hundreds  $\text{km s}^{-1}$  are observed (e.g. Lyne & Lorimer 1994). This would imply that it would not be possible to retain all black holes and neutron stars in globular clusters, but nonetheless high numbers of neutron stars are observed in real globular clusters (Camilo et al. 2000). Pfahl et al. (2002) suggest that low kick velocities are obtained if neutron stars are formed in long-period and low-eccentricity high-mass X-ray binary (HMXB) systems. In that case, the retained neutron star fraction would be four times higher than expected for commonly observed ‘fast’ neutron stars. Because of the lack of any definitive answer to the black hole and neutron star retention problem, and for the sake of model simplicity, we ignore kick velocities. In Fig. 3.8 we show the effect of including or excluding all black holes and neutron stars from our models. The panel is identical to that of Fig. 3.4, however curves representing model runs without stellar remnants are now replaced by ones which include white dwarfs *only* and for which all black holes and neutron stars have been removed. The effect is negligibly small (e.g.  $\lesssim 10\%$  in all observables) because the total remnant mass is generally dominated by white dwarfs at ages  $\gtrsim 100 \text{ Myr}$ . In reality, the effect will be even smaller since a number of black holes and neutron stars have velocities smaller than the escape velocity and are thus retained in the cluster.
- (4) Binaries are only partially incorporated in our models. Dynamically, they are included since our models are fitted to the collisional  $N$ -body simulations by Baumgardt & Makino (2003). However, these do not include a primordial binary population. Photometrically, binaries are not accounted for, because our model clusters are populated using single-star isochrones. As a result, we have no mechanism in which white dwarfs can evolve towards neutron stars due to mass transfer. If we had, it would increase the total remnant mass by a very small amount proportional to the fraction of white dwarfs undergoing mass transfer in a binary system.
- (5) The preferential loss of low-mass stars is included by monotonously increasing the minimum stellar mass  $m_{\min}(t)$  of the bound stars in the cluster. As is discussed in Sect. 3.4.1, this is an approximation to the true evolution of the stellar mass function. The  $N$ -body simulations by Baumgardt & Makino (2003) show that the slope of the IMF below a certain pivot-point mass  $m_s^{\text{biv}}$  increases<sup>15</sup>, thus exhibiting the preferential loss of low-mass stars. The maximum stellar mass  $m_{\max}(t)$  is reduced by stellar evolution. Together, these effects narrow the mass function. In Fig. 3.9, our model mass and bolometric mass-to-light ratio evolution are compared to Baumgardt & Makino (2003). The mass evolution shows good agreement, with a small offset at intermediate age that can be attributed to the different stellar evolution prescriptions of both models

---

<sup>15</sup>Because the slope is negative this means that it becomes *less negative* and eventually more and more positive.

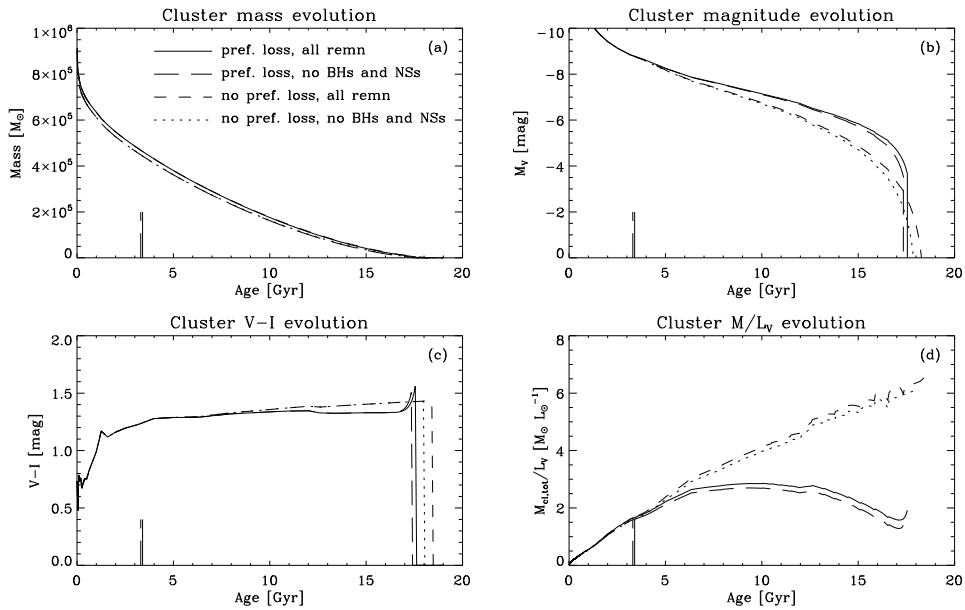


**Figure 3.8:** Effect of neutron star ejection on (a) total cluster mass, (b)  $V$ -band magnitude, (c)  $V-I$  and (d)  $M/L_V$  evolution for clusters with initial mass  $M_{\text{cli}} = 10^6 M_{\odot}$ , including all other stellar remnants, a dissolution timescale  $t_0 = 3$  Myr ( $t_{\text{dis}}^{\text{total}} = 17\text{--}18.5$  Gyr), metallicity  $Z = 0.02$  and a Kroupa IMF. Similar to Fig. 3.4, solid curves denote the evolution for clusters including the preferential loss of low-mass stars with all neutron stars and black holes retained, long-dashed curves for clusters without these massive remnants. For clusters without the preferential loss of low-mass stars, short-dashed curves represent the case in which neutron stars and black holes are included and dotted curves represent the result where these remnants are removed upon their formation. The onset of the preferential mode  $t_{\text{pref}}$  is marked by vertical lines in the linestyles of the corresponding model runs.

(Padova 1999 for the present work and Hurley et al. (2000) for Baumgardt & Makino (2003)). Consequently, both models also differ in metallicity, as the value used by Baumgardt & Makino (2003) is unavailable in the Padova isochrones. The difference in mass evolution is fully accounted for by these differences.

The bolometric mass-to-light ratio evolution is very similar to our model including the preferential loss of low-mass stars for the largest part of cluster lifetime. A strong difference between our approach and the  $N$ -body simulations only arises in cluster photometry and remnant loss close to total cluster disruption, when  $m_{\text{min}}(t)$  and  $m_{\text{max}}(t)$  nearly meet. In that case, model clusters only retain their giant branch, because increasing  $m_{\text{min}}(t)$  first removes the main sequence before giants are lost. This leads to luminosities that are overestimated close to total disruption. Moreover, this could cause real clusters to retain more remnants close to total disruption than is computed in our models. Consequently, the true mass-to-light ratio of clusters near total disruption

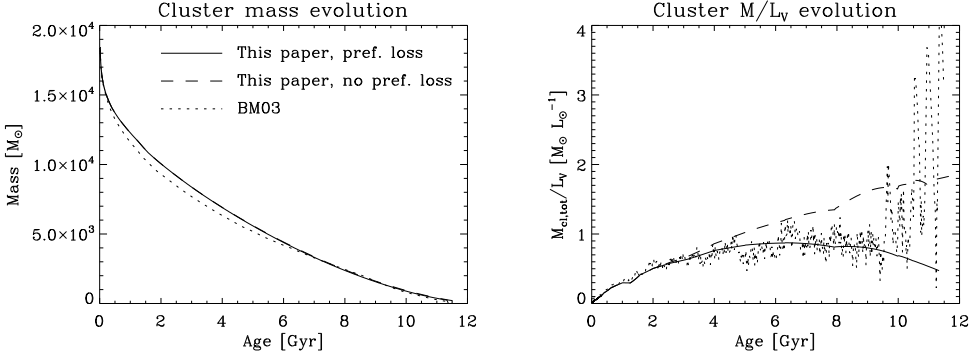


**Figure 3.9:** Comparison of the mass (left) and bolometric mass-to-light ratio evolution (right) from two of our models with and without the preferential loss of low-mass stars ( $M_{cl,i} = 18407.6 M_{\odot}$ , with remnants,  $t_0 = 22.5$  Myr ( $t_{dis}^{total} \sim 11.5$  Gyr),  $Z = 0.004$  and a Kroupa IMF between  $0.1 M_{\odot}$  and  $15 M_{\odot}$ ) to the results from Baumgardt & Makino (2003) (same initial mass,  $W_0 = 5$ ,  $R_{gc} = 8.5$  kpc, circular orbit,  $Z = 0.001$  and a Kroupa IMF between  $0.1 M_{\odot}$  and  $15 M_{\odot}$ ).

would be larger than shown in this study. This is important in the last  $\sim 15\%$  of total cluster lifetime (see Fig. 3.9), during which the mass-to-light ratio evolution can be expected to have a positive slope due to the retain of stellar remnants rather than the computed negative one. Therefore, the slight upturn near total disruption induced by the inclusion of remnants that was shown in Fig. 3.4(d) can be expected to be much stronger in reality. Even a slight upturn does not appear in Fig. 3.9 because the IMF used by Baumgardt & Makino (2003) is truncated at  $15 M_{\odot}$ , implying that there is no production of black holes, which are needed for the upturn to occur in models where the preferential loss of low-mass bodies is represented by an increasing lower mass limit.

However, it is important to note that  $t = 0.85 t_{dis}^{total}$  in Fig. 3.9 is also the point from where on the  $N$ -body simulations are strongly affected by statistical noise. As the number of stars in the cluster decreases and it starts to be dominated by both high- and low-luminosity objects (giants and massive remnants) the imprint of statistics on especially the mass-to-light ratio is enhanced. Consequently, it is very difficult to accurately describe the mass-to-light ratio evolution in the very last part of cluster lifetime, as such predictions are scatter-dominated and are thus not very likely to apply to any specific real cluster.

The fractional range near total cluster disruption for which our models do not follow the mass-to-light ratio rise from Baumgardt & Makino (2003) increases with the total disruption time of a cluster, with 15% being the typical value for a  $t_{dis}^{total}$  of about a Hubble time. Shorter lived clusters are covered for by our models for a larger part of their lifetime, while for very long-lived clusters still at least 70% of their lifetime is covered. The vast majority of globular clusters is presently in the range where they can

be treated with our models.

- (6) We adopt a step-function form for  $f_{\text{pref}}(t)$  to describe the fraction of the cluster mass loss occurring in the form of low-mass stars if the cluster has (partially) reached energy equipartition. In the increasing minimum stellar mass approximation, a step-function requires the form of Eq. 3.29 to most accurately reproduce the  $N$ -body simulations by Baumgardt & Makino (2003). However, cluster magnitude evolution will be better reproduced if a smooth function of  $t$  is formulated. Nonetheless, this is not likely to lead to an exact or better representation of Baumgardt & Makino (2003) due to the fundamentally different approach of including the preferential loss of low-mass stars. Instead, in a future study we will incorporate an improved description of the changing mass function due to the loss of low-mass stars to account for the effect of the preferential loss of low-mass stars (see Sect. 3.6.2).
- (7) Stellar remnants with masses smaller than the minimum stellar mass in the cluster, i.e.  $m_{\text{sr}} < m_{\text{min}}(t)$  are immediately available for dissolution. If the escape rate of bodies is not constant with cluster radius, this ignores the outward transport of remnants from their birth location (for a mass-segregated cluster this is considered to be in the cluster centre) to the cluster outskirts on the half-mass relaxation timescale  $t_{\text{rh}}$ . Because generally  $t_{\text{rh}} < t_{\text{dis}}^{\text{total}} - t$  except close to total cluster disruption (see the Appendix Sect. 3.A), this is a reasonable approach. In the exceptional case where  $t_{\text{rh}} > t_{\text{dis}}^{\text{total}} - t$ , remnant loss is halted since the cluster is disrupted on a shorter timescale than  $t_{\text{rh}}$ .
- (8) The speed of cluster dissolution is assumed to be independent of cluster radius. Gieles & Baumgardt (2008) have shown that this is a reasonable assumption for most tidally dissolving clusters, especially for large- $N$  systems like globular clusters.

### 3.6.2 Applicability and future studies

Because this study is based on collisional  $N$ -body simulations that confirm the existence of the preferential loss of low-mass stars and the retain of stellar remnants, the predicted effects will be present in real clusters. It is shown that these phenomena, but also IMF and metallicity variations can have unique effects on either the mass, magnitude, colour and mass-to-light ratio evolution of clusters. Therefore, the effects of the preferential loss of low-mass stars, stellar remnants, IMF and metallicity can be expected to be observable and interpretable. Clusters of all ages between 10 Myr and 19 Gyr can be treated with our models. Near total cluster disruption the results are affected by our formulation of the preferential loss of low-mass stars, in which red giants are the very last bodies to be lost near total cluster disruption. As a result, the cluster magnitude is overestimated and the mass-to-light ratio is underestimated during the last  $\sim 15\%$  of cluster lifetime. Therefore, photometry-related observables have to be used with caution near total cluster disruption (see Sect. 3.6.1).

The metallicity dependence of stellar remnant mass and an improved description of the preferential loss of low-mass stars are to be included in future studies. This will provide more accurate descriptions of non-luminous cluster mass, and cluster photometry and mass-to-light ratio close to total disruption. A new set of evolutionary synthesis models with a

time-dependent stellar mass function, based on  $N$ -body simulations will soon be available (Anders et al. 2009). Moreover, we have made a quantitative comparison of our models to a number of globular cluster systems, and have assessed unexplained features of the mass-to-light ratio distribution (Kruijssen 2008). A paper in which the individual properties of Galactic globular clusters, like their orbital parameters and metallicities, are used to explain their mass-to-light ratios is in preparation (Kruijssen & Mieske 2009).

### 3.7 Conclusions

We have treated the influence of the preferential loss of low-mass stars, stellar IMF, metallicity and the inclusion of stellar remnants on cluster mass, magnitude, colour and mass-to-light ratio evolution. We presented analytical models that describe the evolution of cluster content and photometry, based on stellar evolution from the Padova 1999 isochrones and on simplified dynamical dissolution models as first presented in Lamers et al. (2005a). The latter, in turn, is based on the  $N$ -body simulations by Baumgardt & Makino (2003).

The models represent the cluster evolution part of our new cluster population synthesis code SPACE. We considered Kroupa and Salpeter IMFs and metallicities in the range  $Z = 0.0004$ – $0.05$ . The obtained data are publicly available in electronic form at the CDS. The results from our models are as follows.

- (1) *The preferential loss of low-mass stars* slightly decreases the total disruption time of a cluster by a few percent. However, the most significant changes are effected in cluster photometry. The effect of fading is decreased as clusters including mass loss in the preferential mode can stay more than 1.5 V-band magnitudes brighter than clusters losing mass in the canonical mode, because most of the dynamical mass loss occurs in the form of low-mass stars that contribute little to cluster luminosity. Initially, clusters exhibiting the preferential loss of low-mass stars are bluer than standard ones, but they become redder during the last  $\sim 10\%$  of cluster lifetime. The cluster mass-to-light ratio is severely decreased due to the preferential loss of low-mass stars. The decrease typically ranges from  $2$ – $4 M_{\odot} L_{\odot}^{-1}$  (i.e. up to 0.6 dex) near total cluster disruption for total disruption times  $t_{\text{dis}}^{\text{total}} > 12$  Gyr. If the upturn of the  $M/L_V$  evolution that is much more prominent in Baumgardt & Makino (2003) than in our models (see Sect. 3.6.1, point (5)) is accounted for, this range of  $M/L_V$  decrease is at most  $0.5 M_{\odot} L_{\odot}^{-1}$  smaller.
- (2) Including the mass of *stellar remnants* obviously yields an increase in the total cluster mass and consequently also in total disruption time with respect to cluster evolution without remnants. The extended lifespan also implies that cluster luminosity less rapidly decreases. The mass-to-light ratio is enhanced by almost  $2 M_{\odot} L_{\odot}^{-1}$  at its maximum, close to total disruption.
- (3) We compared the evolution of clusters with *Salpeter and Kroupa IMFs*, which can be considered to favour high stellar masses (Kroupa, or a ‘top-oriented’ IMF) or low masses (Salpeter, or a ‘bottom-oriented’ IMF) alternatives due to the bend in the Kroupa IMF and a slight slope difference. As can be expected, clusters with a bottom-oriented

IMF retain more mass due to stellar evolution, which eventually causes these clusters to become brighter than clusters with a top-oriented IMF. However, they start out being slightly fainter since a top-oriented IMF favours massive stars and is thus brighter than a bottom-oriented one. Similarly, clusters with a top-oriented IMF are bluer and have smaller mass-to-light ratios than clusters with a bottom-oriented IMF. For the Kroupa and Salpeter IMFs, the latter change can amount up to several  $M_{\odot} L_{\odot}^{-1}$ .

- (4) *Metallicity* variations hardly influence the total mass evolution of clusters. In accordance with stellar studies (Hurley et al. 2004) low-metallicity clusters are brighter and also much bluer than high-metallicity ones. Consequently, the mass-to-light ratio is a strongly increasing function of metallicity.
- (5) When applying our results to *Galactic globular clusters*, it is evident that the preferential loss of low-mass stars is required to explain their low observed *mass-to-light ratios*, especially if stellar remnants are accounted for. Low metallicity is insufficient to serve as an explanation. Another important implication of our study is that the mass-to-light ratio can *not* be assumed to be constant over varying luminosity, as it is strongly affected by the dynamical history of clusters.
- (6) The fact that clusters of high masses may not have reached energy equipartition yet suggests that the effects of the preferential loss of low-mass stars disappear with increasing cluster mass. Because clusters exhibiting the preferential loss of low-mass stars have much lower mass-to-light ratios than clusters that lose their mass in the canonical mode, clusters with high masses would then have much higher mass-to-light ratios than ones with lower masses. This effect may have been found by Rejkuba et al. (2007). The above interpretation and its application to the observations of Rejkuba et al. (2007) is treated more extensively in Kruijssen (2008).
- (7) The typical *colour range of globular clusters* is covered by our models. When considering the colour-metallicity relation as reported by Smith et al. (2007), from an order-of-magnitude comparison we suggest that the observed colour scatter at fixed metallicity could be the effect of the preferential loss of low-mass stars.
- (8) Only when adopting a Salpeter IMF down to  $m_{\min,i} = 0.1 M_{\odot}$ , the mass-to-light ratios of UCDs are reproduced by our models. While UCDs could represent a natural continuation of the trend of increasing mass-to-light ratio with (globular) cluster mass (Rejkuba et al. 2007), this is not expected to be of a dynamical nature, since more massive UCDs are not expected to have reached energy equipartition within a Hubble time.

The retain of remnants and the existence of the preferential loss of low-mass stars are found in  $N$ -body simulations of clusters and in observations, while metallicity and IMF variations are observed among real clusters. Therefore the effects described in this chapter should be considered when observing clusters, and observed cluster properties have to be interpreted very carefully<sup>16</sup>.

---

<sup>16</sup>Predictions for specific models can be made by the first author upon request.

**Acknowledgements** We thank the International Space Science Institute (ISSI) in Bern, Switzerland, for hosting a star cluster workshop where part of this project was carried out. We are grateful to Holger Baumgardt for comments on this chapter and for kindly providing the data from Baumgardt & Makino (2003). We also thank Mark Gieles, Marina Rejkuba, Steffen Mieske, Dean McLaughlin, Reinier Zeldenrust and Peter Anders for valuable discussions, comments and suggestions. The anonymous referee is acknowledged for constructive comments that strongly improved the manuscript. This work is supported by the Netherlands Organisation for Scientific Research (NWO), grant number 021.001.038.

### 3.A Appendix: Outward motion of stellar remnants

In this study it is assumed that when stellar remnants are the lowest mass bodies in a cluster that preferentially loses low-mass stars they are immediately available for dissolution. In mass-segregated clusters, remnants are created in the cluster centre, where the most massive stars reside. Because bodies are only lost from the cluster if they cross the tidal radius, this leads to a delay compared to remnants that would be produced at all radii unless the escape rate from the cluster is independent of radius as proposed by King (1966). In this Appendix we show that the delay can be neglected even if the escape rate varies throughout the cluster.

If the lowest mass bodies in the cluster are stellar remnants, these will move outwards on a half-mass relaxation timescale  $t_{\text{th}}$  (e.g. Spitzer 1987, Heggie & Hut 2003, Ch. 14). Our description of remnant loss ignores any delay caused by the motion of remnants from the cluster centre to its outskirts. Therefore it implicitly assumes  $t_{\text{th}} \ll t_{\text{dis}}^{\text{total}} - t$ , where the latter term represents the remaining lifetime of the cluster. To compare the two terms, we define  $\chi = (t_{\text{dis}}^{\text{total}} - t)/t_{\text{th}}$ . If  $\chi > 1$ , remnants are able to reach the tidal radius before total cluster disruption; for  $\chi < 1$ , the cluster is completely disrupted before such equilibrium can be reached.

In Fig. 3.10,  $\log \chi$  is shown for initial cluster masses between  $10^2$  and  $10^7 M_{\odot}$ , with a dissolution timescale of  $t_0 = 3$  Myr, metallicity  $Z = 0.02$ , a Kroupa IMF and complete energy equipartition ( $f_{\text{pref}}(t) = 1$ ) after  $t = 0.2t_{\text{dis}}^{\text{total}}$ . When a cluster reaches energy equipartition, there is a rapid drop in  $t_{\text{th}}$  because the mean mass in the cluster centre increases. This is reflected in a sudden increase of  $\log \chi$  with age for any specific initial mass. This can be observed in Fig. 3.10 at the dashed curve, which represents the onset of the preferential mode  $t_{\text{pref}}$  (see Sect. 3.4.1) for the entire initial mass range. From Fig. 3.10 and model runs for other choices of dissolution timescale, metallicity and IMF, we can conclude that after  $t_{\text{pref}}$ ,  $\chi \gtrsim 3$  for all parameter sets relevant to globular clusters, and still  $\chi \gtrsim 1.4$  for clusters with initial masses  $M_{\text{cl},i} < 10^3 M_{\odot}$  and extremely rapid cluster dissolution ( $t_0 = 0.3$  Myr). For massive clusters, we typically have  $\chi \sim 10$  for  $t > t_{\text{pref}}$ , implying that the immediate availability of remnants is a legitimate approximation.

Only during the very last few Myrs before total cluster disruption a cluster can have  $\chi < 1$  because the numerator (*remaining* cluster lifetime) approaches zero more rapidly than the denominator ( $t_{\text{th}}$ ). Remnants that are produced during that brief phase cannot be lost in the preferential mode. If just before total disruption  $\chi < 1$ , the lower integration limit  $m_{\text{max}}(t)$  in Eq. 3.26, that determines the total remnant mass available for dissolution, should be replaced



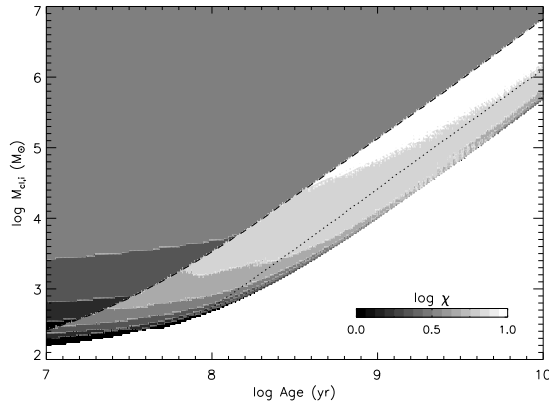


**Figure 3.10:** Logarithm of the ratio of remaining cluster lifetime and the half-mass relaxation timescale,  $(t_{\text{dis}}^{\text{total}} - t)/t_{\text{th}} \equiv \chi$ , as a function of cluster age  $t$  and initial cluster mass  $M_{\text{cl},i}$ . The dashed line represents the onset of the preferential mode  $t_{\text{pref}}$  for a cluster of corresponding y-axis initial mass, and the dotted line denotes the time from which on remnants are lost from such a cluster ( $t_{\text{sr}}$ , see Sec. 3.2.3 for details). For the displayed model run we used a dissolution timescale of  $t_0 = 3$  Myr, metallicity  $Z = 0.02$ , a Kroupa IMF and complete energy equipartition for  $t \geq 0.2t_{\text{dis}}^{\text{total}}$ .

by  $m_{\text{max}}(t_\chi)$ , with  $t_\chi$  the time at which  $\chi$  decreases below unity<sup>17</sup>.

As we have shown, for other parts of cluster evolution the assumption of the immediate loss of remnants with masses  $m_{\text{sr}}(t) \leq m_{\text{sr}} \leq m_{\text{min}}(t)$  is reasonable. Note that for clusters including the preferential loss of low-mass stars with  $t \geq t_{\text{pref}}$ , typically  $t_{\text{th}}$  is not only very small compared to the remaining cluster lifetime, but also ( $\lesssim 10\%$ ) compared to its age.

<sup>17</sup>To determine  $\chi$ , the total disruption time  $t_{\text{dis}}^{\text{total}}$  has to be known before having integrated cluster properties over (and thus having obtained-) the entire cluster lifetime. This is alleviated by estimating  $t_{\text{dis}}^{\text{total}}$  using straightforward integration of Eq. 3.3 at the very start of the computation.



---

# Chapter 4

## Explaining the mass-to-light ratios of globular clusters

J. M. Diederik Kruijssen

*Astronomy & Astrophysics*, v. 486, p. L21–L24 (2008)<sup>†</sup>

**Abstract** The majority of observed mass-to-light ratios of globular clusters are too low to be explained by ‘canonical’ cluster models, in which dynamical effects are not accounted for. Moreover, these models do not reproduce a recently reported trend of increasing  $M/L$  with cluster mass, but instead predict mass-to-light ratios that are independent of cluster mass for a fixed age and metallicity. This study aims to explain the  $M/L$  of globular clusters in four galaxies by including stellar evolution, stellar remnants, and the preferential loss of low-mass stars due to energy equipartition. Analytical cluster models are applied that account for stellar evolution and dynamical cluster dissolution to samples of globular clusters in Cen A, the Milky Way, M31 and the LMC. The models include stellar remnants and cover metallicities in the range  $Z = 0.0004$ – $0.05$ . Both the low observed mass-to-light ratios and the trend of increasing  $M/L$  with cluster mass can be reproduced by including the preferential loss of low-mass stars, assuming reasonable values for the dissolution timescale. This leads to a mass-dependent  $M/L$  evolution and increases the explained percentage of the observations from 39% to 92%. This study shows that the hitherto unexplained discrepancy between observations and models of the mass-to-light ratios of globular clusters can be explained by dynamical effects, provided that the globular clusters exhibiting low  $M/L$  have dissolution timescales within the ranges assumed in this chapter. Furthermore, it substantiates that  $M/L$  cannot be assumed to be constant with mass at fixed age and metallicity.

### 4.1 Introduction

The mass-to-light ratios of globular clusters (GCs) have been given a lot of attention recently (e.g. McLaughlin & van der Marel 2005, Rejkuba et al. 2007, Mieske & Kroupa 2008,

---

<sup>†</sup>Reproduced with permission © ESO.

Dabringhausen et al. 2008). Rejkuba et al. (2007) have observed an  $M/L$  trend with cluster mass above a certain cluster mass, as more massive clusters appear to have higher  $M/L$  than low-mass clusters (see also Mandushev et al. 1991). This is an observation contrary to fundamental plane studies of GCs (e.g. McLaughlin 2000) and also in strong disagreement with the constant  $M/L$  for fixed age that is commonly assumed in observational and theoretical GC studies (e.g. Harris et al. 2006, Mora et al. 2007, Bekki et al. 2007). Moreover, for Galactic GCs McLaughlin (2000) find  $M/L_V = 1.45 M_\odot L_\odot^{-1}$ , whereas Simple Stellar Population models (e.g. Bruzual & Charlot 2003, Anders & Fritze-v. Alvensleben 2003) predict significantly higher values of  $M/L_V = 2\text{--}4 M_\odot L_\odot^{-1}$  for typical GC metallicities. Given the important role of GCs in galactic astronomy, it is essential to explain these apparent contradictions.

In numerical and analytical studies of dynamical effects in clusters (e.g. Baumgardt & Makino 2003, Lamers et al. 2006, Kruijssen & Lamers 2008) it has become clear that the dynamical evolution of clusters strongly affects cluster luminosity, colour and mass-to-light ratio. In Kruijssen & Lamers (2008, hereafter KL08) it is shown how the evolution of these observables changes due to dynamical effects such as the preferential loss of low-mass stars and the retain of stellar remnants, but also due to the stellar initial mass function and metallicity. It is shown that  $M/L$  cannot be assumed to be constant for a fixed age and metallicity, but instead depends on cluster mass when dynamical effects are accounted for.

In this chapter, the analytical cluster models from KL08 are applied to explain the observations of GCs in several galaxies from Rejkuba et al. (2007) and Mieske et al. (2008). In Sect. 4.2 I first summarise the models presented in KL08, which is applied to the observations in Sect. 4.3. In Sect. 4.3.1 the effect of metallicity and the cluster dissolution timescale on cluster evolution in the  $\{M, M/L_V\}$ -plane is investigated. The observations are discussed in Sect. 4.3.2 and are compared to the models in Sect. 4.3.3. A discussion of the results and the conclusions are presented in Sect. 4.4.

## 4.2 Modeling method

In this study, analytic cluster models are used that incorporate the effects of stellar evolution, stellar remnant production, cluster dissolution and energy equipartition. They are summarised here and are treated in more detail in KL08.

In the models, clusters gradually lose mass due to stellar evolution and dissolution. The total cluster mass evolution is described by  $dM_{cl}/dt = (dM_{cl}/dt)_{ev} + (dM_{cl}/dt)_{dis}$ , with the first term denoting stellar evolution and the second representing dissolution. Taking into account the formation of stellar remnants and the mass-dependent loss of stars by dissolution, this provides a description of the changing mass function and cluster mass in remnants.

Stellar evolution is included by using the Padova 1999 isochrones<sup>1</sup>. It removes the most massive stars from the cluster and increases the dark cluster mass by turning stars into remnants, which is included by assuming an initial-remnant mass relation. A Kroupa (2001) IMF is assumed.

---

<sup>1</sup>These isochrones are based on Bertelli et al. (1994), but use the AGB treatment as in Girardi et al. (2000).

Cluster dissolution represents the dynamical cluster mass loss due to stars passing the tidal radius. This mass loss acts on a dissolution timescale  $\tau_{\text{dis}}$ :

$$\left(\frac{dM_{\text{cl}}(t)}{dt}\right)_{\text{dis}} = -\frac{M_{\text{cl}}(t)}{\tau_{\text{dis}}} = -\frac{M_{\text{cl}}(t)^{1-\gamma}}{t_0}, \quad (4.1)$$

where  $\tau_{\text{dis}}$  is related to the present day cluster mass  $M_{\text{cl}}(t)$  as  $\tau_{\text{dis}} = t_0 M_{\text{cl}}(t)^\gamma$  (Lamers et al. 2005a), leading to the second equality in Eq. 4.1. The characteristic timescale  $t_0$  depends on the environment and determines the strength of dissolution. For example, in the case of tidal dissolution  $t_0$  depends on tidal field strength and thus on galactocentric radius and galaxy mass. Typical values are  $t_0 = 10^5\text{--}10^8$  yr (e.g. Lamers et al. 2005b), translating into a total disruption time  $t_{\text{dis}}^{\text{total}} \approx 10^8\text{--}10^{11}$  yr for a  $10^5 M_\odot$  cluster. From  $N$ -body simulations of tidal dissolution (Lamers et al. 2005b) and observations (Boutloukos & Lamers 2003, Gieles et al. 2005), the exponent  $\gamma$  is found to be  $\gamma \approx 0.62$ .

The effect of dissolution on the mass function depends on the dynamical state of the cluster. If it has reached energy equipartition, i.e. after core collapse, the cluster becomes mass-segregated and low-mass stars are preferentially lost. This occurs at about 20% of the total cluster lifetime (Baumgardt & Makino 2003). For clusters without equipartition, bodies of all masses are lost with similar probabilities.

Cluster photometry is computed by integrating the stellar mass function over the stellar isochrones, yielding cluster magnitude evolution  $M_\lambda(t, M_{\text{cl},i})$  for a passband  $\lambda$  and a cluster with initial mass  $M_{\text{cl},i}$ .

### 4.3 Applying the cluster models to observed clusters

In this section I present the evolution of clusters in the  $\{M, M/L_V\}$ -plane, and apply this to explain the  $\{M, M/L_V\}$  distribution observed in real clusters.

#### 4.3.1 Cluster evolution in the mass- $M/L_V$ plane

In ‘canonical’ Simple Stellar Population (SSP) models, clusters only evolve due to stellar evolution, and therefore their mass-to-light ratios do not change due to dynamical effects. As the most massive stars (with low  $M/L_V$ ) gradually disappear, in these models  $M/L_V$  is a monotonously increasing function of time that is constant for any set of clusters at a single age and metallicity. However, this is only correct if cluster dissolution occurs independently of stellar mass and the shape of the stellar mass function is preserved, i.e. there is *no* preferential loss of low-mass stars.

Contrary to clusters from SSP models, in reality clusters do preferentially lose low-mass stars (e.g. Hillenbrand & Hartmann 1998, Albrow et al. 2002, Baumgardt & Makino 2003). KL08 have shown that this strongly affects the  $M/L$  evolution of clusters due to the preferential loss of low-mass stars (having high  $M/L$ ), and that consequently  $M/L$  cannot be assumed to be constant for clusters of a given age.

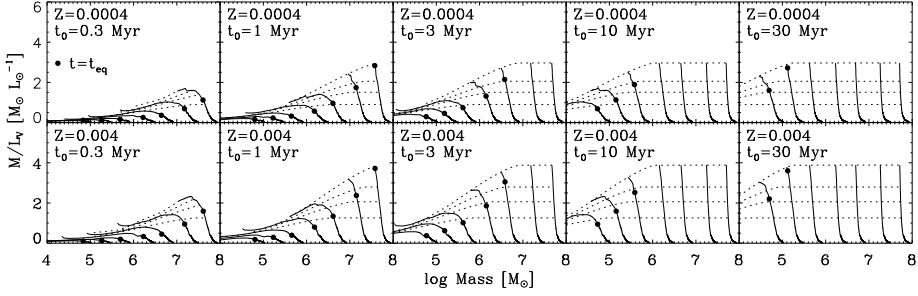


**Figure 4.1:** Cluster evolution in the  $\{M, M/L_V\}$ -plane for metallicities  $Z = \{0.0004, 0.004\}$  ( $[\text{Fe}/\text{H}] = \{-1.7, -0.7\}$ ) and dissolution timescales  $t_0 = \{0.3, 1, 3, 10, 30\}$  Myr. Solid lines represent evolutionary tracks for initial masses in the range  $M_{\text{cl},i} = 10^5\text{--}10^8 M_\odot$  with 0.5-dex intervals, while the dotted curves denote cluster isochrones at ages  $t = \{4, 8, 12, 19\}$  Gyr. Dots denote the onset of the preferential loss of low-mass stars for each evolutionary track.

In order to explain the appearance of clusters in the  $\{M, M/L_V\}$ -plane, I first compute the model cluster evolutionary tracks for different metallicities and dissolution timescales. The results are shown in Fig. 4.1.

Initially, model clusters are not in equipartition and they evolve to lower masses and *increasing*  $M/L_V$  (due to the death of massive stars), moving up and to the left in Fig. 4.1. From the moment they reach mass segregation, happening earlier for low-mass clusters due to quicker relaxation (Baumgardt & Makino 2003), they preferentially lose low-mass stars, which have high  $M/L$ . This *decreases* the cluster  $M/L$  and explains the maximum in the cluster evolution curves for lower initial masses. Along the cluster isochrones of constant age (dotted lines in Fig. 4.1),  $M/L_V$  increases with mass, since at any age low-mass clusters have spent more time in energy equipartition and thus have retained more massive (i.e. low- $M/L$ ) stars compared to massive clusters. The cluster isochrones flatten at the highest masses, since these clusters have yet to reach equipartition, leaving them at constant  $M/L$ .

Within a galaxy, its GCs generally have similar ages (e.g. Vandenberg et al. 1990). Observations of GC systems should thus approximately follow cluster isochrones in the  $\{M, M/L_V\}$ -plane. Therefore, the isochrones are used in Fig. 4.1 to probe the influence of metallicity and dissolution timescale on the expected GC distribution. Increasing metallicity leads to a higher maximum  $M/L$ , and thus also to steeper isochrones. Increasing the dissolution timescale shifts the entire isochrone to the left: for long dissolution timescales, it takes more time to reach equipartition and therefore only clusters of the lowest masses have preferentially lost low-mass stars. The dissolution timescale thus sets the location of the ‘knee’ in the isochrones, which is the cluster mass at which they flatten due to the absence of equipartition. This can be used to determine the dissolution timescale range of an observed GC system.

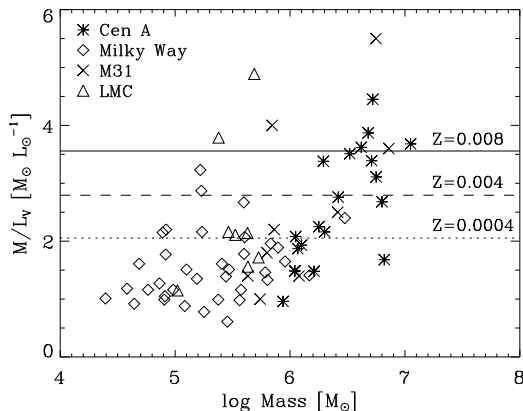


**Figure 4.2:** Mass-to-light ratio versus mass for globular clusters in different galaxies. The Cen A data is from Mieske et al. (2008), all other data is taken from Rejkuba et al. (2007). The canonical (mass-independent) models are overplotted as solid, dashed and dotted lines for  $Z = \{0.0004, 0.004, 0.008\}$ , respectively.

### 4.3.2 Observations of globular cluster mass-to-light ratios

In Rejkuba et al. (2007, Fig. 9) the (dynamical-)  $\{M, M/L_V\}$ -plane is presented for GCs in several host galaxies. In Fig. 4.2, I show their  $\{M, M/L_V\}$ -plane for GCs from Cen A, the Milky Way, M31, and the Large Magellanic Cloud (LMC). For the Cen A data, aperture corrections as in Hilker et al. (2007) have been computed for the cluster masses and  $M/L_V$  (Mieske et al. 2008). The  $M/L_V$  values for mass-independent cluster models (the ‘canonical’ models from KL08) are overplotted, and fail to reproduce a large part of the data. When considering the metallicities and errors of the data (not shown in Fig. 4.2), only 39% of the observed GCs can be covered within their  $1-\sigma$  errors if the canonical models are used<sup>2</sup>.

Although the data show quite some scatter, there are indications for a trend of increasing  $M/L_V$  with mass, such as the lack of low- $M/L$  clusters for  $\log M > 6.3$ . I argue that this is the same behaviour as can be observed in the cluster isochrones including the preferential loss of low-mass stars in Fig. 4.1, implying that the increase of  $M/L_V$  with mass corresponds to a decreasing effect of energy equipartition.

### 4.3.3 Explaining the mass-to-light ratios of globular clusters

Figure 4.3 compares the model cluster isochrones ( $t = 12$  Gyr) to the GC data for Cen A, the Milky Way, M31 and the LMC. The different colours represent three metallicities, and coloured model lines belong to data points of the same colour.

<sup>2</sup>SSP models (e.g. Bruzual & Charlot 2003, Anders & Fritze-v. Alvensleben 2003) all predict  $M/L = 2 - 4 M_\odot L_\odot^{-1}$  for GC metallicities, a Kroupa IMF and  $t = 12$  Gyr, comparable to the ‘canonical’ models used here.

Galaxy	$t_0$ range (Myr)		
	$Z = 0.0004$	$Z = 0.004$	$Z = 0.008$
Cen A	$\leq 5$ —5	$\leq 1$ —2	<b>0.2</b> —2
M31	$\leq 1$ —10	$\leq 0.5$ —2	
MW	<b>1</b> —20	<b>0.7</b> —8	<b>0.6</b> —0.6
LMC	$\leq 3$ —20		

**Table 4.1:** Required dissolution timescale ranges for globular clusters of three metallicities in four studied galaxies, as derived from the cluster samples. Due to possible incompleteness at low masses and high  $M/L$  (see Fig. 4.3), all upper limits represent minimum values and lower limits often represent maxima. Limits that do not suffer from incompleteness are shown in boldface.

For any galaxy and metallicity, the data cover an area in the  $\{M, M/L_V\}$ -plane that can be spanned by two model curves of different dissolution timescales. Left curves denote upper limits, while right curves represent lower limits for the dissolution timescale ranges in which clusters are observed. These limits are chosen as such that they encompass the data points. Contrary to the sparse coverage of the data by the canonical models (see Fig. 4.2), it is shown in Fig. 4.3 that 92% of the data can be explained within their  $1\text{-}\sigma$  errors by using the new models (KL08) that account for dynamical effects. The remaining 8% has too high  $M/L$  to be explained by stellar population models, unless their observed ages or metallicities are underestimated.

The minimum and maximum dissolution timescales that are required to explain the observations are summarised in Table 4.1. All values fall within the physically reasonable range of  $10^5$ — $10^8$  yr (Lamers et al. 2005b). For each galaxy, a broad range of dissolution timescales is required to explain the observed range of  $M/L$ . This is not surprising, since the observed clusters are located at various galactocentric radii and thus experience different tidal dissolution strengths. Regardless of this spread, there is a clear trend of decreasing required dissolution timescale with metallicity. This is likely to be related to the radial metallicity gradient observed in galaxies (first established by Searle 1971), with metal-rich clusters at small galactocentric radii and thus at short dissolution timescales. Another trend is that of decreasing required dissolution timescale with galaxy mass. Again, this is not surprising, as more massive galaxies can have stronger tidal fields and thus give rise to more rapid cluster dissolution.

## 4.4 Discussion

In this chapter, I have shown that the hitherto unexplained discrepancy between observations and models of the mass-to-light ratios of globular clusters can be explained by dynamical effects. The preferential loss of low-mass stars due to energy equipartition gives rise to  $M/L$  evolution that depends on cluster mass, contrary to what is assumed in canonical cluster models. This is confirmed by the application of models that include dynamical effects to the GC populations of Cen A, the Milky Way, M31 and the LMC.



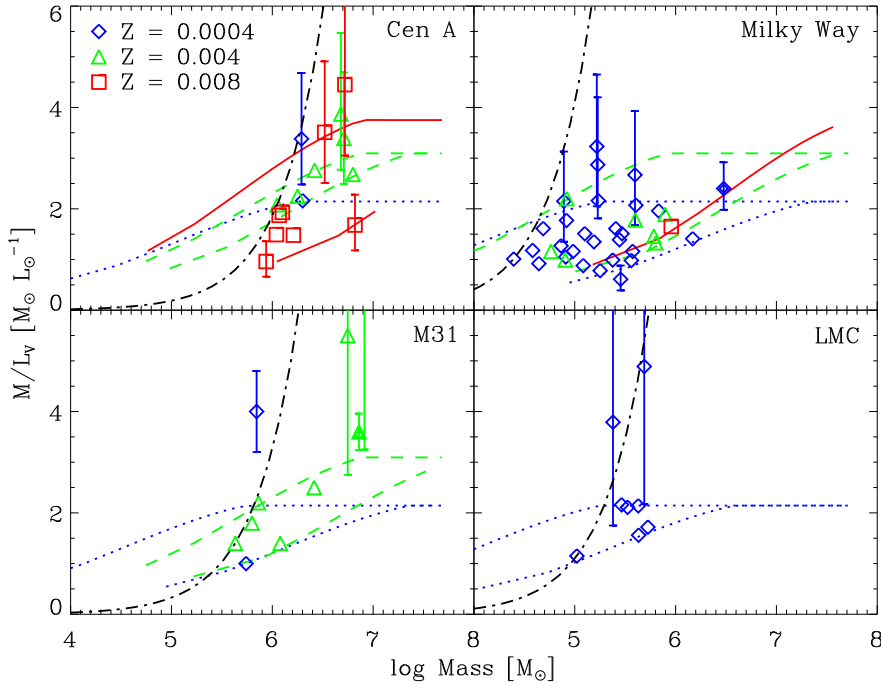


**Figure 4.3:** Comparison of  $t = 12$  Gyr model cluster isochrones in the  $\{M, M/L_V\}$ -plane to globular clusters in four different galaxies. Clusters with metallicities  $Z = \{0.0004, 0.004, 0.008\}$  are denoted with blue diamonds, green triangles, and red squares, respectively. Model curves for these metallicities are shown in the same colours, with dotted, dashed and solid lines, respectively. In all cases an age of  $t = 12$  Gyr is assumed. For each galaxy, a dash-dotted line of constant luminosity represents the faintest cluster that is covered by the models, illustrating that the samples are magnitude-limited. Metallicities are from Beasley et al. (2008, Cen A), Harris (1996, Milky Way), Dubath & Grillmair (1997, M31) and Mackey & Gilmore (2004, LMC). To prevent crowding, error bars are only shown for clusters that fall outside the range covered by the models.

Without the preferential loss of low-mass stars, current stellar population models cannot explain mass-to-light ratios below  $2 M_\odot L_\odot^{-1}$  for metallicity  $Z = 0.0004$  and below  $2.8 M_\odot L_\odot^{-1}$  for  $Z = 0.004$ . As becomes clear from Fig. 4.3, this would leave half of the cluster sample in Cen A and most of the Milky Way sample unexplained. Accounting for the effects of energy equipartition increases the explained percentage of the observations from 39% to 92%.

The dissolution timescales required to explain the observed GC samples lie within the physically reasonable range of  $t_0 = 10^5$ – $10^8$  yr. Observed trends of decreasing dissolution timescale with galaxy mass and metallicity are as expected when considering the strength of

tidal dissolution and the radial metallicity gradient in galaxies.

The dependence of  $M/L$  on cluster mass (and thus on luminosity) implies that photometrically derived masses using canonical models may be strongly overestimated (KL08). The results presented here underline the importance of accounting for dynamical effects when modeling clusters or interpreting observations of (globular) clusters.

**Acknowledgements** I am very grateful to Marina Rejkuba for kindly providing me with an electronic version of the data presented in Rejkuba et al. (2007) and Mieske et al. (2008). I also thank Steffen Mieske, Mark Gieles and the anonymous referee for constructive comments, and Henny Lamers for encouragement, advice and suggestions. This work is supported by the Netherlands Organisation for Scientific Research (NWO), grant number 021.001.038.

# Chapter 5

---

## Dissolution is the solution: on the reduced mass-to-light ratios of Galactic globular clusters

J. M. Diederik Kruijssen and Steffen Mieske  
*Astronomy & Astrophysics*, v. 500, p. 785–799 (2009)<sup>†</sup>

**Abstract** The observed dynamical mass-to-light ( $M/L$ ) ratios of globular clusters (GCs) are systematically lower than the value expected from ‘canonical’ simple stellar population models, which do not account for dynamical effects such as the preferential loss of low-mass stars due to energy equipartition. It has recently been shown that low-mass star depletion can qualitatively explain this discrepancy for globular clusters in several galaxies. To verify whether low-mass star depletion is indeed the driving mechanism behind the  $M/L$  decrease, we aim to predict the  $M/L_V$  ratios of individual GCs for which orbital parameters and dynamical V-band mass-to-light ratios  $M/L_V$  are known. There is a sample of 24 Galactic GCs for which this is possible. We used the SPACE cluster models, which include dynamical dissolution, low-mass star depletion, stellar evolution, stellar remnants, and various metallicities. We derived the dissolution timescales due to two-body relaxation and disc shocking from the orbital parameters of our GC sample and used these to predict the  $M/L_V$  ratios of the individual GCs. To verify our findings, we also predicted the slopes of their low-mass stellar mass functions. The computed dissolution timescales agree well with earlier empirical studies. The predicted  $M/L_V$  are in  $1\sigma$  agreement with the observations for 12 out of 24 GCs. The discrepancy for the other GCs probably arises because our predictions give global  $M/L$  ratios, while the observations represent extrapolated central values that are different from global ones in the case of mass segregation and a long dissolution timescale. The GCs in our sample that likely have dissimilar global and central  $M/L$  ratios can be excluded by imposing limits on the dissolution timescale and King parameter. For the remaining GCs, the observed and predicted average  $M/L_V$  are  $78^{+9}_{-11}\%$  and  $78 \pm 2\%$  of the canonically expected values, while the values are  $74^{+6}_{-7}\%$  and  $85 \pm 1\%$  for the entire sample. The predicted correlation between the slope of the low-mass stellar mass function and  $M/L_V$  drop is found to be qualitatively consistent with observed mass function slopes. The dissolution timescales of Galactic GCs are such that the  $\sim 20\%$  gap between canonically expected and observed  $M/L_V$  ratios is bridged by accounting for the preferential

---

<sup>†</sup>Reproduced with permission © ESO.

loss of low-mass stars, also when considering individual clusters. It is concluded that the variation in  $M/L$  ratio due to dissolution and low-mass star depletion is a plausible explanation for the discrepancy between the observed and canonically expected  $M/L$  ratios of GCs.

## 5.1 Introduction

The topic of dynamical mass-to-light ( $M/L$ ) ratios of old compact stellar systems has attracted increasing attention during recent years (McLaughlin & van der Marel 2005, Haşegan et al. 2005, Rejkuba et al. 2007, Hilker et al. 2007, Evstigneeva et al. 2007, Dabringhausen et al. 2008, Mieske et al. 2008, Kruijssen 2008, Baumgardt & Mieske 2008, Chilingarian et al. 2008, Forbes et al. 2008). The outcome of these studies can be summarised as follows.

- For the mass regime of ultra-compact dwarf galaxies (UCDs,  $M \geq 2 \times 10^6 M_{\odot}$ ), dynamical  $M/L$  ratios tend to be some 50% above predictions from stellar population models (Dabringhausen et al. 2008, Mieske et al. 2008, Forbes et al. 2008).
- For the mass regime of globular clusters (GCs,  $M \leq 2 \times 10^6 M_{\odot}$ ), dynamical  $M/L$  ratios tend to be some 25% below predictions from simple stellar population (SSP) models that assume a canonical IMF (Rejkuba et al. 2007, Kruijssen 2008, Kruijssen & Lamers 2008, Mieske et al. 2008).
- As a consequence, the dynamical  $M/L$  ratios of UCDs are on average about twice as high as those of GCs, at comparable metallicities.

Regarding GCs, a viable solution for obtaining *lower*  $M/L$  ratios is a deficit in low-mass stars with respect to a canonical initial mass function (IMF) (Kroupa 2001). This is known to arise naturally from two-body relaxation in star clusters, which causes a depletion of low-mass stars (Vesperini & Heggie 1997, Baumgardt & Makino 2003). In Kruijssen (2008) we studied how the preferential loss of low-mass stars due to dynamical evolution of a star cluster in a tidal field reduces the  $M/L$  ratios of star clusters. There, we constrained the ranges of dissolution timescales necessary for this loss of low-mass stars to quantitatively account for the drop in  $M/L$  observed for GCs. For the Galactic GC system, it was found that dissolution timescales in the range  $t_0 = 0.6\text{--}\geq 20$  Myr (corresponding to total disruption times of  $t_{\text{dis}}^{\text{total}} \approx 3\text{--}100$  Gyr for a  $10^6 M_{\odot}$  cluster) are required to explain the observed  $M/L$  ratio decline. It was also shown that the  $M/L$  ratio decrease is strongest for low-mass GCs, which explains the observed correlation of increasing  $M/L$  ratio with mass discovered by Mandushev et al. (1991). We concluded that the scatter around this relation is caused by spreads in metallicity and dissolution timescale.

As noted already in Kruijssen & Lamers (2008, hereafter KL08), the next step is to apply these analytical cluster models including preferential loss of low-mass stars to *individual* clusters. This would then account for variations in metallicity and dissolution timescale. Such a study will naturally be restricted to GCs with measured  $M/L$  ratios for which realistic estimates of their individual dissolution timescale are available from information on their actual orbit within the Milky Way potential. With the database of individual dissolution time scales at hand, the loss of low-mass stars can be quantified according to the prescriptions

of Kruijssen (2008) and KL08, leading to predictions for the drop of  $M/L$  for *individual* GCs. Those predictions are to be contrasted with the actual observed  $M/L$  ratios of these GCs. This will allow us to quantitatively test the hypothesis that the loss of low-mass stars is responsible for the too low  $M/L$  ratios of GCs, and hence also partially for the discrepancy of  $M/L$  between GCs and UCDS.

Previous studies assessing the preferential loss of low-mass stars in Galactic GCs focus both on observations (e.g. De Marchi et al. 2007) and theory (e.g. Baumgardt et al. 2008). In De Marchi et al. (2007), the slopes of the stellar mass functions in GCs are measured for stars between 0.3 and 0.8  $M_{\odot}$ , thereby directly reflecting possible low-mass star depletion. The study by Baumgardt et al. (2008) predicts the same slopes using  $N$ -body models and different degrees of mass segregation, assuming dissolution by two-body relaxation. The aforementioned papers both do not consider the  $M/L$  ratios of the GCs in question.

In this study, the reference sample for dynamical  $M/L$  ratios of Galactic GCs is that of McLaughlin & van der Marel (2005), obtained by the fitting of single-mass King profiles. It contains data for 38 GCs. Only a subsample can be used for our analysis, namely those clusters for which accurate proper motions and radial velocities are measured and can be translated to orbital parameters. Next to the destruction rates due to two-body relaxation, also the influence of disc shocking on the cluster dissolution needs to be taken into account. Both have to be derived from the orbital parameters. Several studies in which orbital information is derived and used to compute destruction rates are available in the literature (Gnedin & Ostriker 1997, Dinescu et al. 1999, Allen et al. 2006, 2008), all with certain benefits and trade-offs. Specifically, Gnedin & Ostriker (1997) assign statistically sampled orbits conforming to the bulk motion of the GC system in an axisymmetric potential to derive destruction rates of 119 globular clusters. Dinescu et al. (1999) use proper motions and radial velocities to compute the orbits and destruction rates of 38 clusters in two axisymmetric potentials (Paczynski 1990, Johnston et al. 1995). Allen et al. (2006, 2008) follow the same procedure, but consider both axisymmetric and barred potentials (Allen & Santillan 1991, Pichardo et al. 2004, respectively) for 54 globular clusters. They do not find a significant deviation between the results for both potentials. However, they do note that their calculated destruction rates are multiple orders of magnitude lower than others in literature and recommend combining their orbital information with the more rigorous Fokker-Planck approach used by Gnedin & Ostriker (1997) to derive the destruction rates.

We choose to adopt the orbital data and destruction rate due to disc shocking from Dinescu et al. (1999). Our study cannot be based on statistically assigned orbits but requires the actual orbits of individual clusters, thus excluding the estimated orbits from Gnedin & Ostriker (1997). In addition, the Dinescu et al. (1999) destruction rates seem to be in better agreement with the observations than those from Allen et al. (2006, 2008).

In Table 5.1 the observed properties are listed of the 24 Galactic globular clusters for which the  $V$ -band mass-to-light ratios ( $M/L_V$ ) and orbital parameters are available, i.e. the sample that is covered both by Dinescu et al. (1999) and McLaughlin & van der Marel (2005). The masses and observed  $M/L_V$  ratios represent dynamical values. For all clusters, the standard error in  $[\text{Fe}/\text{H}]$  is assumed to be 0.15 when computing the error propagation (see Sect. 5.3), which represents a conservative accuracy estimate (see, e.g. Carretta & Gratton 1997). These errors determine the uncertainty on  $(M/L_V)_{\text{can}}$  in the last column, since the

**Table 5.1:** Observed properties for the cluster sample, together with their  $1\sigma$  standard errors. Consecutive columns list the cluster NGC number, logarithm of the present-day cluster mass  $M$  ( $M_\odot$ ), observed  $V$ -band mass-to-light ratio  $(M/L_V)_{\text{obs}}$  (in  $M_\odot L_\odot^{-1}$ ), metallicity  $[\text{Fe}/\text{H}]$ , galactocentric radius  $R_{\text{gc}}$  (in kpc), King parameter  $W_0$  and canonically expected  $V$ -band mass-to-light ratio  $(M/L_V)_{\text{can}}$  (in  $M_\odot L_\odot^{-1}$ ).

Cluster properties						
NGC	$\log M^*$	$(M/L_V)_{\text{obs}}^*$	$[\text{Fe}/\text{H}]^{\dagger, \diamond}$	$R_{\text{gc}}^\dagger$	$W_0^*$	$(M/L_V)_{\text{can}}$
104	$5.804^{+0.157}_{-0.193}$	$1.33^{+0.48}_{-0.59}$	-0.76	7.4	$8.6^{+0.1}_{-0.1}$	$2.68 \pm 0.25$
288	$4.892^{+0.162}_{-0.198}$	$2.15^{+0.80}_{-0.98}$	-1.24	12.0	$4.8^{+0.2}_{-0.2}$	$2.20 \pm 0.08$
1851	$5.407^{+0.156}_{-0.192}$	$1.61^{+0.58}_{-0.71}$	-1.22	16.7	$8.1^{+0.1}_{-0.2}$	$2.21 \pm 0.09$
1904	$4.984^{+0.157}_{-0.195}$	$1.16^{+0.42}_{-0.52}$	-1.57	18.8	$7.5^{+0.1}_{-0.1}$	$2.08 \pm 0.04$
4147	$4.394^{+0.159}_{-0.202}$	$1.01^{+0.37}_{-0.47}$	-1.83	21.3	$8.0^{+0.2}_{-0.1}$	$2.03 \pm 0.02$
4590	$4.644^{+0.156}_{-0.194}$	$0.92^{+0.33}_{-0.41}$	-2.06	10.1	$6.6^{+0.1}_{-0.1}$	$2.00 \pm 0.01$
5139	$6.503^{+0.200}_{-0.159}$	$2.54^{+1.17}_{-0.93}$	-1.29	6.4	$6.2^{+0.1}_{-0.2}$	$2.18 \pm 0.07$
5272	$5.443^{+0.156}_{-0.197}$	$1.39^{+0.50}_{-0.63}$	-1.57	12.2	$8.2^{+0.1}_{-0.1}$	$2.08 \pm 0.04$
5466	$4.687^{+0.162}_{-0.200}$	$1.61^{+0.60}_{-0.74}$	-2.22	16.2	$4.2^{+0.2}_{-0.2}$	$1.99 \pm 0.01$
5904	$5.252^{+0.156}_{-0.195}$	$0.78^{+0.28}_{-0.35}$	-1.27	6.2	$7.6^{+0.1}_{-0.1}$	$2.19 \pm 0.08$
6093	$5.597^{+0.161}_{-0.205}$	$2.67^{+0.99}_{-1.26}$	-1.75	3.8	$7.5^{+0.1}_{-0.1}$	$2.04 \pm 0.03$
6121	$4.864^{+0.178}_{-0.243}$	$1.27^{+0.52}_{-0.71}$	-1.20	5.9	$7.4^{+0.1}_{-0.1}$	$2.22 \pm 0.09$
6171	$4.922^{+0.172}_{-0.241}$	$2.20^{+0.87}_{-1.22}$	-1.04	3.3	$7.0^{+0.1}_{-0.2}$	$2.34 \pm 0.13$
6205	$5.469^{+0.158}_{-0.201}$	$1.51^{+0.55}_{-0.70}$	-1.54	8.7	$7.0^{+0.1}_{-0.1}$	$2.08 \pm 0.04$
6218	$4.918^{+0.157}_{-0.206}$	$1.77^{+0.64}_{-0.84}$	-1.48	4.5	$6.1^{+0.1}_{-0.2}$	$2.10 \pm 0.05$
6254	$5.234^{+0.169}_{-0.223}$	$2.16^{+0.84}_{-1.11}$	-1.52	4.6	$6.5^{+0.1}_{-0.1}$	$2.09 \pm 0.04$
6341	$5.084^{+0.163}_{-0.202}$	$0.88^{+0.33}_{-0.41}$	-2.28	9.6	$7.5^{+0.1}_{-0.1}$	$1.99 \pm 0.01$
6362	$4.764^{+0.161}_{-0.191}$	$1.16^{+0.43}_{-0.51}$	-0.95	5.1	$5.3^{+0.3}_{-0.2}$	$2.42 \pm 0.16$
6656	$5.606^{+0.172}_{-0.241}$	$2.07^{+0.82}_{-1.15}$	-1.64	4.9	$6.5^{+0.1}_{-0.2}$	$2.06 \pm 0.03$
6712	$4.906^{+0.175}_{-0.241}$	$0.99^{+0.40}_{-0.55}$	-1.01	3.5	$5.1^{+0.4}_{-0.4}$	$2.37 \pm 0.14$
6779	$4.911^{+0.207}_{-0.165}$	$1.05^{+0.50}_{-0.40}$	-1.94	9.7	$6.5^{+0.3}_{-0.2}$	$2.01 \pm 0.02$
6809	$5.219^{+0.054}_{-0.067}$	$3.23^{+0.40}_{-0.50}$	-1.81	3.9	$4.5^{+0.2}_{-0.1}$	$2.03 \pm 0.02$
6934	$5.099^{+0.155}_{-0.193}$	$1.51^{+0.54}_{-0.67}$	-1.54	12.8	$7.0^{+0.1}_{-0.2}$	$2.08 \pm 0.04$
7089	$5.561^{+0.160}_{-0.195}$	$0.98^{+0.36}_{-0.44}$	-1.62	10.4	$7.2^{+0.1}_{-0.1}$	$2.06 \pm 0.03$

\* From McLaughlin & van der Marel (2005).

† From Harris (1996).

◇ The value for NGC 5139 ( $\omega$ Cen) is derived from Bedin et al. (2004).

canonical  $M/L$  ratio only depends on metallicity. The galactocentric radii used to compute the orbits in Dinescu et al. (1999) are from Zinn, private communication. In extreme cases this may cause a small disagreement between the galactocentric radius quoted here and the apogalactic distance predicted by Dinescu et al. (1999) (see Table 5.2).

A first inspection of the observed  $M/L_V$  ratios in Table 5.1 can be made by comparing them to the ('canonical')  $M/L_V$  ratios from SSP models, which only depend on metallicity due to the invariance of the shape of the stellar mass function in these models. In Fig. 5.1

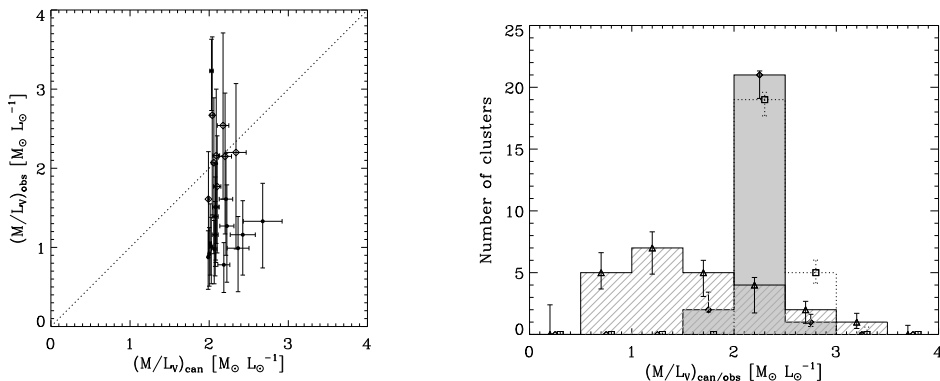


**Figure 5.1:** *Left:* Observed mass-to-light ratio  $(M/L_V)_{\text{obs}}$  versus the canonically expected mass-to-light ratio  $(M/L_V)_{\text{can}}$ , together with their  $1\sigma$  standard errors (see Table 5.1). The dotted line follows the 1:1 relation. Clusters for which the disagreement is larger than  $1\sigma$  are plotted as dots. *Right:* Number histogram of  $(M/L_V)_{\text{can}}$  (diamonds, shaded area) and  $(M/L_V)_{\text{obs}}$  (triangles, hashed area). For comparison, canonically expected  $M/L_V$  ratios from Bruzual & Charlot (2003) for a Chabrier (2003) IMF are overplotted (squares, dotted line). Again, the error bars denote  $1\sigma$  deviations, which were determined from 30k random realisations of the underlying data.

(left), the observed  $M/L_V$  ratios of our sample are plotted versus the canonically expected values that were computed by interpolating SSP models. These were emulated with the models from KL08 neglecting the preferential loss of low-mass stars. The discrepancy between observed and expected  $M/L_V$  ratio is evident, as the canonical  $M/L_V$  are constrained to a much narrower and generally higher range than the observed ones. The number histogram of the two  $M/L_V$  (Fig. 5.1, right) further substantiates this dissimilarity. The observed  $M/L_V$  ratios are on average  $74^{+6}_{-7}\%$  of the canonically expected values.

With the present chapter we aim to quantify the contribution of dynamical effects such as the preferential loss of low-mass stars and the selective loss of stellar remnants (see KL08) to the discrepancy between the observed and canonically expected  $M/L$  ratios. In Sect. 5.2, we summarise the cluster models from KL08 and highlight the aspects that are particularly relevant to this study. The dissolution timescales for the cluster sample are computed in Sect. 5.3, whereas the predicted mass and  $M/L_V$  evolution are considered and compared to the observations in Sect. 5.4. We predict slopes of the low-mass stellar mass function and discuss observational tests to verify the preferential loss hypothesis for appropriate clusters in Sect. 5.5. In the final Sect. 5.6, we discuss the results and present our conclusions.

## 5.2 Cluster evolution models and $M/L_V$ evolution

In order to study the evolution of clusters on specific orbits, we use analytical cluster models (SPACE, see KL08) that incorporate the effects of stellar evolution, stellar remnant production, cluster dissolution and energy equipartition. They are summarised here and are treated in more detail in KL08. In the second part of this section, the dependence of mass-to-light ratio evolution on initial mass, metallicity and dissolution timescale is assessed (for a more detailed description, see Kruijssen 2008).

### 5.2.1 Summary of the models

In the SPACE cluster models, clusters gradually lose mass due to stellar evolution and dissolution. The total cluster mass evolution is determined by

$$\frac{dM_{\text{cl}}}{dt} = \left( \frac{dM_{\text{cl}}}{dt} \right)_{\text{ev}} + \left( \frac{dM_{\text{cl}}}{dt} \right)_{\text{dis}}, \quad (5.1)$$

where the first term denotes mass loss due to stellar evolution and the second represents mass loss by dissolution. Additionally, the formation of stellar remnants and the mass-dependent loss of stars by dissolution are taken into account, thus providing a description of the changing mass function and cluster mass in remnants.

Stellar evolution is included by using the Padova 1999 isochrones<sup>1</sup>. These are available for metallicities  $Z = \{0.0004, 0.004, 0.008, 0.02, 0.05\}$  (with corresponding iron-to-hydrogen ratios of  $[\text{Fe}/\text{H}] = \{-1.7, -0.7, -0.4, 0.0, 0.4\}$ ), which thus restricts our model computations to these values. Stellar evolution removes the most massive stars from the cluster and increases the non-luminous cluster mass by turning stars into remnants, which is included by adopting an initial-remnant mass relation<sup>2</sup>. A Kroupa (2001) IMF is assumed.

Cluster dissolution represents the dynamical cluster mass loss due to stars passing the tidal radius, which acts on the timescale  $\tau_{\text{dis}}$ :

$$\left( \frac{dM_{\text{cl}}(t)}{dt} \right)_{\text{dis}} = -\frac{M_{\text{cl}}(t)}{\tau_{\text{dis}}} = -\frac{M_{\text{cl}}(t)^{1-\gamma}}{t_0}, \quad (5.2)$$

where  $M_{\text{cl}}(t)$  represents the present day cluster mass and the second equality follows from the relation derived by Lamers et al. (2005a):

$$\tau_{\text{dis}} = t_0 [M_{\text{cl}}(t)/M_{\odot}]^{\gamma}. \quad (5.3)$$

The characteristic timescale  $t_0$  depends on the environment and determines the strength of dissolution. For example, in the case of dissolution by two-body relaxation  $t_0$  depends on tidal field strength and therefore on the angular velocity of the cluster orbit. Typical values are  $t_0 =$

<sup>1</sup>These isochrones are based on Bertelli et al. (1994), but use the AGB treatment as in Girardi et al. (2000).

<sup>2</sup>For white dwarfs, this relation is taken from Kalirai et al. (2008), while for neutron stars the relation from Nomoto et al. (1988) is used. Black hole masses are assumed to be constant at  $8 M_{\odot}$ , in agreement with observations (Casares 2007). For more details, see KL08.



$10^5$ — $10^8$  yr (e.g. Lamers et al. 2005b), translating into a total disruption time  $t_{\text{dis}}^{\text{total}} \approx 10^8$ — $10^{11}$  yr for a  $10^5 M_{\odot}$  cluster. The exponent  $\gamma$  is found to be  $\gamma \approx 0.62$ , both from observations (Boutloukos & Lamers 2003, Gieles et al. 2005) and from the Baumgardt & Makino (2003)  $N$ -body simulations of tidal dissolution for clusters with King parameter  $W_0 = 5$  (Lamers et al. 2005b). However, it is recently derived by Lamers et al. (2010) that  $\gamma = 0.70$  for King parameter  $W_0 = 7$ . Since this concentration more closely resembles the mean King parameter for Galactic GCs (see Table 5.1), we adopt  $\gamma = 0.70$  throughout this study.

The effect of dissolution on the mass function depends on the dynamical state of the cluster. As it evolves towards energy equipartition, low-mass stars are preferentially lost from the cluster. This mass loss (in the ‘preferential mode’, KL08) is approximated by increasing the minimum stellar mass (Lamers et al. 2006), while evaporation that is independent of stellar mass (mass loss in the ‘canonical mode’, KL08) is accounted for by decreasing the normalisation of the mass function. In our models, both modes coexist to allow for intermediate modes of mass loss. Their relative contributions are fitted such that the  $M/L_V$  ratio evolution matches the  $N$ -body simulations by Baumgardt & Makino (2003).

Cluster photometry is computed by integrating the stellar mass function over the stellar isochrones, yielding cluster magnitude evolution  $M_{\lambda}(t, M_{\text{cl},i})$  for a passband  $\lambda$  and a cluster with initial mass  $M_{\text{cl},i}$ .

## 5.2.2 Dependence of mass-to-light ratio on model parameters

The models described in Sect. 5.2.1 yield a mass-to-light ratio evolution that depends on the dissolution timescale, metallicity and initial cluster mass. In canonical models, i.e. without the preferential loss of low-mass stars,  $M/L$  monotonously increases with time. For a given age and metallicity, these models provide  $M/L$  ratios that are independent of cluster mass. On the other hand, our models including dynamical effects predict a mass-dependent drop in mass-to-light ratio due to the ejection of low-mass, high- $M/L$  stars (Kruijssen 2008, KL08). In Fig. 5.2, the  $V$ -band mass-to-light ratio evolution  $M/L_V$  is shown for two metallicities and several initial cluster masses. In both panels, the upper curve marks the canonical mass-to-light ratio evolution, while the others correspond to cluster evolution including the preferential loss of low-mass stars for different initial masses. Since low-mass clusters evolve on shorter timescales than massive ones, the deviation of their mass-to-light ratio evolution with respect to canonical models arises at earlier times than for massive clusters.

The mass-to-light ratio decrease can be quantified by considering the ratio of the observed or predicted  $M/L$  to its canonical value to divide out their metallicity dependence:

$$Q_{\text{obs/pred}} \equiv \frac{(M/L_V)_{\text{obs/pred}}}{(M/L_V)_{\text{can}}}. \quad (5.4)$$

Figure 5.3 shows the predicted fraction of the canonical  $M/L$  ratio  $Q_{\text{pred}}$  as a function of  $t/t_{\text{dis}}^{\text{total}}$  for clusters with initial masses in the range  $M_{\text{cl},i} = 2 \times 10^4$ — $10^8 M_{\odot}$ , dissolution timescales  $t_0 = \{1, 10\}$  Myr and metallicities  $Z = \{0.0004, 0.004\}$ . It shows that  $Q_{\text{pred}}$  is independent of metallicity, initial cluster mass and dissolution timescale when considered as a function of the elapsed fraction of the total disruption time  $t/t_{\text{dis}}^{\text{total}}$ . The three-component

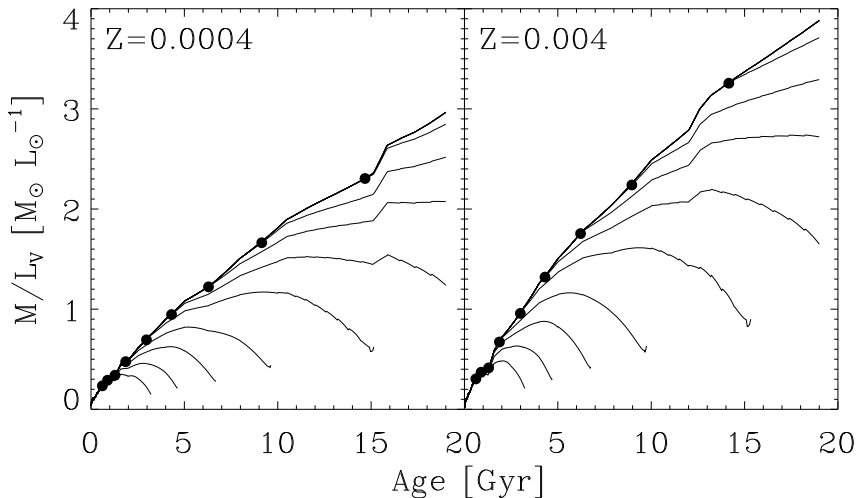


**Figure 5.2:** *Left:* V-band mass-to-light ratio evolution  $M/L_V$  for  $t_0 = 1$  Myr,  $Z = 0.0004$  and initial masses in the range  $\log M_{\text{cl},i} = 5\text{--}8$  with 0.25-dex intervals. *Right:* same graph, but for  $Z = 0.004$ . From top to bottom, different curves represent the  $M/L_V$  evolution for decreasing initial cluster masses.

linear approximation illustrates the well-defined uniform correlation and is given by

$$Q_{\text{pred}} = \begin{cases} 1 & \text{for } t/t_{\text{dis}}^{\text{total}} < 0.2, \\ 1.142 - 0.71t/t_{\text{dis}}^{\text{total}} & \text{for } 0.2 \leq t/t_{\text{dis}}^{\text{total}} < 0.7, \\ 1.471 - 1.18t/t_{\text{dis}}^{\text{total}} & \text{for } t/t_{\text{dis}}^{\text{total}} \geq 0.7, \end{cases} \quad (5.5)$$

which applies for all initial conditions, i.e. is independent of the cluster properties or environment<sup>3</sup>. Equation 5.5 does not include possible effects of primordial mass segregation on the change of the mass function. From model runs where we did assume the preferential depletion of low-mass stars from  $t = 0$  on we know that its effects become about 10% stronger with respect to purely dynamically induced low-mass star depletion (KL08). This number should be treated with some care, because our models are based on  $N$ -body simulations of clusters that did not start out in a mass-segregated state (Baumgardt & Makino 2003).

The relation between the predicted fraction of the canonical mass-to-light ratio  $Q_{\text{pred}}$  and the elapsed fraction of the total disruption time is expected, since in our models the decrease of  $M/L$  is the result of dynamical evolution. It is in agreement with studies by Richer et al. (1991) and Baumgardt & Makino (2003), who find that the depletion of the low-mass stellar mass function in globular clusters is closely related to the elapsed fraction of the total disruption time. Considering the physical processes driving dissolution, the result is not surprising either. Two-body relaxation is known to preferentially eject low-mass stars

<sup>3</sup>Please note that a Kroupa IMF was assumed here. For substantially different IMFs the relation will vary.

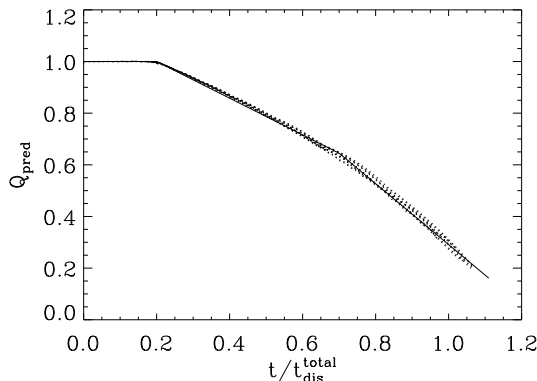


**Figure 5.3:** The ratio of predicted to canonical mass-to-light ratio  $Q_{\text{pred}}$  as a function of the elapsed fraction of the total disruption time  $t/t_{\text{dis}}^{\text{total}}$ . Dotted curves denote model predictions for a broad range of initial conditions (varying initial masses, dissolution timescales and metallicities), while the solid line describes a three-component linear approximation to the models.

(Hénon 1969) and tidal shocks remove the outer parts of the cluster, which in the case of mass segregation are constituted by low-mass stars.

The evolution of cluster mass and  $M/L_V$  can both be considered in the  $\{M, M/L_V\}$ -plane. The resulting ‘evolutionary tracks’ are shown in Fig. 5.4 for two different dissolution timescales and again for two metallicities and a range of initial cluster masses as in Fig. 5.2. Clusters start with their initial masses and with  $M/L_V$  ratios close to zero, corresponding to an initial position on the  $x$ -axis of Fig. 5.4. As time progresses, clusters initially evolve to lower masses and increasing  $M/L_V$  due to the death of massive stars, translating into up- and leftward motion in the  $\{M, M/L_V\}$ -plane. When the preferential loss of low-mass stars becomes an important mechanism (the onset of which is marked by dots for each evolutionary track), the  $M/L_V$  increase is turned into a decrease instead, as also illustrated in Fig. 5.2. In Fig. 5.4, the thus attained maximum in the  $M/L_V$  evolution is best visible for low cluster masses and  $t_0 = 1$  Myr.

Since Galactic globular clusters generally share the same ages (e.g. Vandenberg et al. 1990), the observed distribution of GCs in the  $\{M, M/L_V\}$ -plane would follow curves of equal age in Fig. 5.4 if there were no spreads in metallicity and dissolution timescale. These curves, or cluster isochrones, are shown for ages  $t = \{10, 12, 14\}$  Gyr. Along the isochrones,  $M/L_V$  increases with cluster mass since massive clusters have spent a smaller fraction of their total disruption time than low-mass clusters and will therefore have experienced a smaller  $M/L_V$  decrease due to low-mass star depletion. The curves flatten at the highest masses, since these clusters have not yet exhibited significant preferential low-mass star ejection.

From Fig. 5.4 we infer the influences of dissolution timescale and metallicity on the mass-to-light ratio evolution. The dissolution timescale sets the cluster mass for which the down-bend of the cluster evolutionary tracks can occur and therefore also determines the location

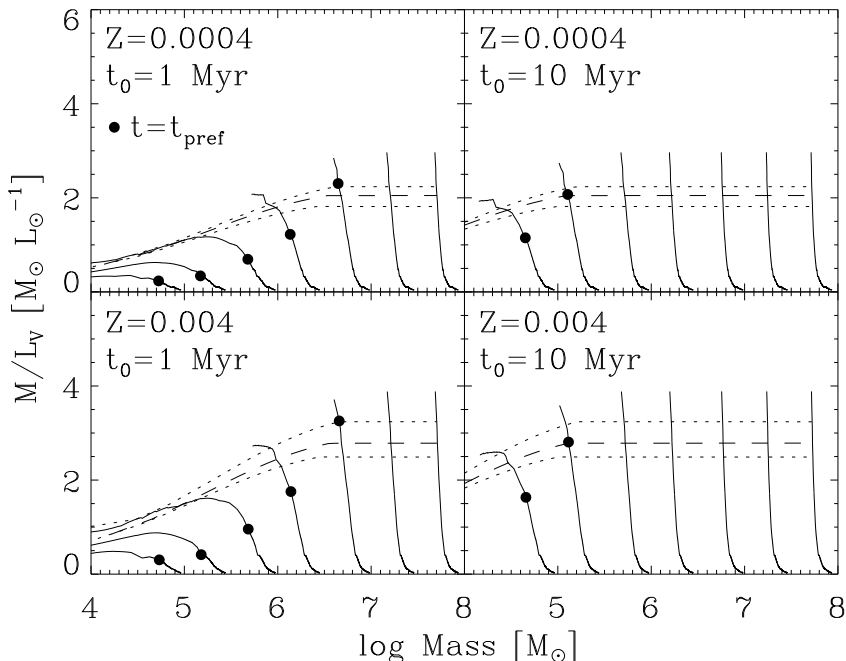


**Figure 5.4:** Cluster evolution in the  $\{M, M/L_V\}$ -plane for  $t_0 = \{1, 10\}$  Myr and  $Z = \{0.0004, 0.004\}$ . Solid curves represent cluster evolutionary tracks for initial cluster masses in the range  $M_{cl,i} = 10^5$ — $10^8 M_\odot$  with 0.5-dex intervals. Cluster isochrones at  $t = 12$  Gyr are described by dashed lines, while these at  $t = 10$  and  $t = 14$  Gyr are denoted by dotted lines (bottom and top, respectively). Dots denote the onset of the preferential loss of low-mass stars for each evolutionary track.

of the ‘knee’ in the cluster isochrones. The metallicity determines the vertical extent of the cluster evolutionary tracks and thus the  $M/L_V$ -normalisation of the cluster isochrones. As set forth in Kruijssen (2008), the natural spread in dissolution timescale and metallicity thus explains the scatter around the relation between  $M/L$  and cluster mass observed by Mandushev et al. (1991).

### 5.3 Determining the dissolution timescale

To assess the influence of the preferential loss of low-mass stars on the low observed mass-to-light ratios, the orbital parameters of individual clusters are to be translated into the appropriate dissolution timescales  $t_0$  for use in our cluster models. The computation is treated in this section.

**Table 5.2:** Orbital parameters for the cluster sample, together with their  $1\sigma$  standard errors. Consecutive columns list the cluster NGC number, apogalactic radius  $R_a$  (in kpc), perigalactic radius  $R_p$  (in kpc), eccentricity  $e$ , orbital period  $P$  (in Myr), and circular velocity of the gravitational potential at the distance of apogalacticon  $V_{c,a}$  (in  $\text{km s}^{-1}$ ).

Orbital parameters					
NGC	$R_a^*$	$R_p^*$	$e^*$	$P^*$	$V_{c,a}^\dagger$
104	$7.3 \pm 0.1$	$5.3 \pm 0.3$	$0.16 \pm 0.04$	$193 \pm 4$	$221.4 \pm 0.2$
288	$11.1 \pm 0.4$	$1.8 \pm 0.5$	$0.72 \pm 0.06$	$237 \pm 12$	$213.5 \pm 0.8$
1851	$34.7 \pm 5.9$	$5.7 \pm 1.2$	$0.72 \pm 0.02$	$685 \pm 114$	$195.9 \pm 1.4$
1904	$20.4 \pm 1.3$	$4.4 \pm 1.7$	$0.64 \pm 0.10$	$422 \pm 32$	$201.9 \pm 1.0$
4147	$26.8 \pm 3.4$	$4.0 \pm 1.9$	$0.74 \pm 0.08$	$551 \pm 74$	$198.4 \pm 1.4$
4590	$30.0 \pm 3.7$	$8.7 \pm 0.4$	$0.55 \pm 0.03$	$650 \pm 78$	$197.2 \pm 1.2$
5139	$6.4 \pm 0.1$	$1.2 \pm 0.1$	$0.69 \pm 0.02$	$123 \pm 1$	$222.8 \pm 0.1$
5272	$14.0 \pm 0.8$	$5.4 \pm 0.8$	$0.44 \pm 0.06$	$321 \pm 18$	$208.6 \pm 1.2$
5466	$69.8 \pm 29.6$	$6.7 \pm 1.4$	$0.83 \pm 0.03$	$1340 \pm 595$	$192.1 \pm 1.4$
5904	$46.1 \pm 12.8$	$2.5 \pm 0.2$	$0.90 \pm 0.02$	$995 \pm 286$	$193.9 \pm 1.6$
6093	$3.2 \pm 0.2$	$1.0 \pm 0.6$	$0.54 \pm 0.21$	$65 \pm 6$	$213.3 \pm 1.8$
6121	$5.8 \pm 0.3$	$0.7 \pm 0.1$	$0.79 \pm 0.03$	$114 \pm 3$	$223.2 \pm 0.1$
6171	$3.3 \pm 0.2$	$2.8 \pm 0.3$	$0.08 \pm 0.07$	$99 \pm 7$	$214.2 \pm 1.7$
6205	$25.3 \pm 6.9$	$5.7 \pm 0.5$	$0.63 \pm 0.07$	$526 \pm 132$	$199.0 \pm 3.3$
6218	$5.3 \pm 0.1$	$2.8 \pm 0.3$	$0.30 \pm 0.04$	$130 \pm 4$	$223.0 \pm 0.1$
6254	$5.0 \pm 0.2$	$3.4 \pm 0.4$	$0.18 \pm 0.05$	$132 \pm 7$	$222.7 \pm 0.3$
6341	$9.9 \pm 0.4$	$1.3 \pm 0.1$	$0.78 \pm 0.03$	$208 \pm 12$	$216.0 \pm 0.8$
6362	$5.3 \pm 0.1$	$2.6 \pm 0.2$	$0.35 \pm 0.04$	$124 \pm 2$	$223.0 \pm 0.1$
6656	$9.6 \pm 0.7$	$2.8 \pm 0.2$	$0.55 \pm 0.01$	$197 \pm 14$	$216.6 \pm 1.5$
6712	$5.9 \pm 0.3$	$0.9 \pm 0.1$	$0.74 \pm 0.04$	$126 \pm 11$	$223.2 \pm 0.1$
6779	$13.0 \pm 1.9$	$0.8 \pm 0.3$	$0.88 \pm 0.03$	$249 \pm 30$	$210.2 \pm 3.1$
6809	$6.0 \pm 0.3$	$1.7 \pm 0.2$	$0.56 \pm 0.04$	$136 \pm 5$	$223.1 \pm 0.2$
6934	$46.8 \pm 19.8$	$6.7 \pm 1.6$	$0.75 \pm 0.06$	$990 \pm 434$	$193.8 \pm 2.4$
7089	$42.2 \pm 17.9$	$6.3 \pm 1.2$	$0.74 \pm 0.06$	$860 \pm 379$	$194.5 \pm 2.7$

\* From Dinescu et al. (1999).

† Computed using the galactic potential from Paczynski (1990).

### 5.3.1 Cluster dissolution timescales from orbital parameters

For globular clusters, dissolution due to two-body relaxation in the Galactic tidal field<sup>4</sup> and disc shocking are the main dissolution mechanisms (e.g. Chernoff et al. 1986). The total dissolution timescale  $t_{0,\text{tot}}$  can be written as

$$\frac{1}{t_{0,\text{tot}}} = \frac{1}{t_{0,\text{evap}}} + \frac{1}{t_{0,\text{sh}}}, \quad (5.6)$$

<sup>4</sup>This includes the effect of bulge shocks, which occur in clusters on eccentric orbits.

where  $t_{0,\text{evap}}$  denotes the dissolution timescale due to two-body relaxation or evaporation (carrying the subscript ‘evap’) and  $t_{0,\text{sh}}$  the dissolution timescale due to disc shocking.

For the dissolution timescale due to two-body relaxation, we use the expression for the total disruption time from Baumgardt & Makino (2003, Eq. 10) as approximated by Lamers et al. (2005b) to write

$$t_{0,\text{evap}} = t_{0,\text{evap}}^{\odot} \left( \frac{R_{\text{gc,a}}}{8.5 \text{ kpc}} \right) \left( \frac{V_{\text{c,a}}}{220 \text{ km s}^{-1}} \right)^{-1} (1 - e), \quad (5.7)$$

with  $t_{0,\text{evap}}^{\odot}$  the dissolution timescale due to two-body relaxation for a circular orbit at the solar galactocentric radius,  $R_{\text{gc,a}}$  the apogalactic radius of the cluster orbit,  $V_{\text{c,a}}$  the circular velocity of the gravitational potential at the distance of apogalacticon and  $e$  the orbital eccentricity. Values for  $R_{\text{gc,a}}$  are taken from Dinescu et al. (1999), while the circular velocities are computed for the galactic potential from Paczynski (1990). This potential, as well as the one from Johnston et al. (1995), is used by Dinescu et al. (1999) in the determination of the cluster orbits. By comparing our models to the  $N$ -body simulations by Baumgardt & Makino (2003) we find  $t_{0,\text{evap}}^{\odot} = 21.3$  Myr for clusters with  $W_0 = 5$  King profiles, in very close agreement with earlier reported values of 20.9 Myr (Lamers et al. 2005a) and 22.8 Myr (Lamers & Gieles 2006). Using the same method for  $\gamma = 0.7$ , corresponding to  $W_0 = 7$  King profiles (see Sect. 5.2.1), we obtain  $t_{0,\text{evap}}^{\odot} = 10.7$  Myr. This is the adopted value in this chapter.

The dissolution timescale due to disc shocking can be obtained from the globular cluster destruction rates due to disc shocking  $\nu_{\text{sh}}$  from Dinescu et al. (1999). Following from Eq. 5.3, a present destruction rate  $\nu(t)$  is related to a dissolution timescale  $t_0$  by

$$\nu(t) = \frac{10^{10}}{t_0 (M_{\text{cl}}(t)/M_{\odot})^{\gamma}}, \quad (5.8)$$

with  $\nu$  in units of  $(10 \text{ Gyr})^{-1}$ ,  $t_0$  in years, and  $M_{\text{cl}}(t)$  denoting the cluster mass at age  $t$ . The denominator represents an estimate for the total cluster lifetime. This expression can be inverted to obtain  $t_{0,\text{sh}}$  from  $\nu_{\text{sh}}$ . However, in Dinescu et al. (1999) constant  $M/L_V = 3 M_{\odot} L_{\odot}^{-1}$  is assumed to compute the cluster masses. Since their destruction rates are derived from a relation  $\nu_{\text{sh}} \propto M^{-1}$ , these should be corrected for the actual mass-to-light ratios. We define the correction factor

$$x_{\text{corr}} = \frac{(M/L_V)_{\text{cst}}}{(M/L_V)_{\text{obs}}}, \quad (5.9)$$

with the numerator the constant mass-to-light ratio  $(M/L_V)_{\text{cst}} = 3 M_{\odot} L_{\odot}^{-1}$  and the denominator the observed dynamical mass-to-light ratio from McLaughlin & van der Marel (2005) (see Table 5.1). This allows us to express the dissolution timescale due to disc shocking as

$$t_{0,\text{sh}} = \frac{10^{10}}{x_{\text{corr}} \nu_{\text{sh}} (M_{\text{cl}}(t)/M_{\odot})^{\gamma}}. \quad (5.10)$$

Substitution of Eqs. 5.7 and 5.10 into Eq. 5.6 then yields the total dissolution timescale  $t_{0,\text{tot}}$ .

**Table 5.3:** Computed dissolution timescales (for  $\gamma = 0.70$ ) due to two-body relaxation ( $t_{0,\text{evap}}$ ), disc shocking ( $t_{0,\text{sh}}$ ) and both mechanisms ( $t_{0,\text{tot}}$ ), together with their  $1\sigma$  standard errors. The table also includes the destruction rate due to disc shocking  $\nu_{\text{sh}}$  (in  $(10 \text{ Gyr})^{-1}$ ) from Dinescu et al. (1999). All dissolution timescales are in Myr and are rounded to one decimal.

Dissolution timescales ( $\gamma = 0.70$ )				
NGC	$t_{0,\text{evap}}$	$\nu_{\text{sh}}$	$t_{0,\text{sh}}$	$t_{0,\text{tot}}$
104	$7.7 \pm 0.4$	$(0.501 \pm 0.134) \times 10^{-2}$	$76.6^{+33.9}_{-35.1}$	$7.0^{+0.4}_{-0.4}$
288	$4.0 \pm 0.9$	$(0.739 \pm 0.186) \times 10^0$	$3.6^{+5.0}_{-2.6}$	$1.9^{+1.4}_{-0.7}$
1851	$13.7 \pm 2.6$	$(0.804 \pm 0.286) \times 10^{-3}$	$1095.3^{+553.9}_{-545.0}$	$13.6^{+2.6}_{-2.6}$
1904	$10.1 \pm 2.9$	$(0.592 \pm 0.540) \times 10^{-2}$	$211.9^{+204.8}_{-136.4}$	$9.6^{+2.7}_{-2.6}$
4147	$9.7 \pm 3.3$	$(0.208 \pm 0.098) \times 10^{-1}$	$135.9^{+79.7}_{-73.8}$	$9.1^{+2.9}_{-2.9}$
4590	$19.0 \pm 2.8$	$(0.208 \pm 0.050) \times 10^{-2}$	$827.6^{+356.2}_{-375.1}$	$18.5^{+2.6}_{-2.6}$
5139	$2.5 \pm 0.2$	$(0.373 \pm 0.082) \times 10^0$	$0.6^{+0.3}_{-0.2}$	$0.5^{+0.2}_{-0.2}$
5272	$10.4 \pm 1.3$	$(0.209 \pm 0.108) \times 10^{-2}$	$343.3^{+208.5}_{-187.7}$	$10.1^{+1.2}_{-1.2}$
5466	$17.1 \pm 8.0$	$(0.110 \pm 0.074) \times 10^0$	$25.6^{+19.6}_{-15.3}$	$10.2^{+4.3}_{-3.8}$
5904	$6.6 \pm 2.3$	$(0.117 \pm 0.048) \times 10^{-1}$	$46.8^{+24.8}_{-24.0}$	$5.8^{+1.8}_{-1.8}$
6093	$1.9 \pm 0.9$	$(0.121 \pm 0.085) \times 10^{-1}$	$88.9^{+124}_{-88.4}$	$1.9^{+0.9}_{-0.8}$
6121	$1.5 \pm 0.2$	$(0.280 \pm 0.072) \times 10^0$	$6.0^{+5.1}_{-3.8}$	$1.2^{+0.3}_{-0.2}$
6171	$3.9 \pm 0.4$	$(0.125 \pm 0.037) \times 10^0$	$21.0^{+10.6}_{-10.9}$	$3.3^{+0.4}_{-0.4}$
6205	$13.0 \pm 4.5$	$(0.154 \pm 0.068) \times 10^{-2}$	$485.3^{+272.4}_{-257.4}$	$12.7^{+4.3}_{-4.3}$
6218	$4.6 \pm 0.3$	$(0.235 \pm 0.075) \times 10^{-1}$	$90.6^{+42.5}_{-44.3}$	$4.4^{+0.3}_{-0.3}$
6254	$5.1 \pm 0.4$	$(0.261 \pm 0.074) \times 10^{-1}$	$59.8^{+28.0}_{-29.1}$	$4.7^{+0.4}_{-0.4}$
6341	$2.8 \pm 0.4$	$(0.167 \pm 0.060) \times 10^{-1}$	$48.5^{+25.9}_{-25.1}$	$2.6^{+0.4}_{-0.4}$
6362	$4.3 \pm 0.3$	$(0.491 \pm 0.125) \times 10^0$	$3.6^{+1.6}_{-1.6}$	$2.0^{+0.5}_{-0.5}$
6656	$5.5 \pm 0.5$	$(0.441 \pm 0.114) \times 10^{-1}$	$18.6^{+8.7}_{-9.2}$	$4.3^{+0.5}_{-0.6}$
6712	$1.9 \pm 0.3$	$(0.114 \pm 0.041) \times 10^0$	$10.7^{+52.9}_{-9.5}$	$1.6^{+0.6}_{-0.3}$
6779	$2.1 \pm 0.6$	$(0.407 \pm 0.142) \times 10^0$	$3.1^{+6.4}_{-2.4}$	$1.2^{+1.0}_{-0.4}$
6809	$3.3 \pm 0.3$	$(0.177 \pm 0.048) \times 10^0$	$13.5^{+3.2}_{-3.9}$	$2.6^{+0.3}_{-0.3}$
6934	$16.7 \pm 8.3$	$(0.149 \pm 0.112) \times 10^{-2}$	$910.7^{+750.3}_{-556.0}$	$16.4^{+8.0}_{-8.0}$
7089	$15.6 \pm 7.7$	$(0.818 \pm 1.220) \times 10^{-3}$	$511.3^{+773.0}_{-371.0}$	$15.2^{+7.3}_{-7.3}$

In Table 5.2, our cluster sample is listed with the orbital parameters from Dinescu et al. (1999) for the Paczynski (1990) potential and our computed circular velocities of the gravitational potential at the distance of apogalacticon. The circular velocities are computed in the galactic plane ( $z = 0$ ). Because the gravitational potentials of the disc and bulge decrease with  $|z|$ , this implies that for clusters with  $R_a < 10 \text{ kpc}$  the actual  $V_{c,a}$  can be 5—15% lower.

The corresponding dissolution timescales can be found in Table 5.3. The values for the dissolution timescale range from  $t_{0,\text{tot}} = 0.5$ —20 Myr, corresponding to total disruption times for a  $10^6 M_\odot$  cluster in the range  $t_{\text{dis}}^{\text{total}} = 8$ —300 Gyr. This is in good agreement with the range that is required for low-mass star depletion to explain the observed mass-to-light ratio drop (Kruijssen 2008). By comparing the dissolution timescales for two-body relaxation  $t_{0,\text{evap}}$  and disc shocking  $t_{0,\text{sh}}$ , we can see that the latter destruction mechanism is important

(i.e. lowers the total dissolution timescale  $t_{0,\text{tot}}$  by more than 40% with respect to  $t_{0,\text{evap}}$ ) for the clusters NGC 288, 5139 ( $\omega$ Cen), 6362, and 6779. These clusters all have perigalactic radii smaller than 3 kpc (see Table 5.2). For the error analysis of Tables 5.2 and 5.3 and of the rest of this chapter we refer to the Appendix Sect. 5.A.

## 5.4 Predicted and observed mass-to-light ratios

In this section we combine our cluster models and the derived dissolution timescales to study the mass-to-light ratio evolution for our sample of 24 Galactic globular clusters. Present-day  $M/L_V$  ratios are predicted for the cluster sample and are compared to the observations. We also discuss the possible causes for the individual clusters that still lack convincing agreement.

### 5.4.1 Predicted mass-to-light ratios for the cluster sample

We employ the cluster models treated in Sects. 5.2 and 5.3 to predict  $M/L_V$  ratios for the cluster sample. The input parameters for the models are the dissolution timescale  $t_0$  and metallicity  $Z$ . The latter is derived from the iron abundance  $[\text{Fe}/\text{H}]$  (see Table 5.1) according to

$$Z = Z_{\odot} \times 10^{[\text{Fe}/\text{H}]}, \quad (5.11)$$

with  $Z_{\odot} = 0.02$ , while the dissolution timescale is taken from Table 5.3 ( $t_{0,\text{tot}}$ ). Since all clusters in the sample have metallicities  $Z < 0.004$ , for each cluster the models are computed with metallicities  $Z = \{0.0004, 0.004\}$  and the appropriate dissolution timescales. The evolution is computed for a grid of initial cluster masses, yielding cluster evolution tracks for the mass and V-band mass-to-light ratio  $M/L_V$ . For both metallicities, at  $t = 12$  Gyr the tracks are interpolated over the mass grid to match the observed cluster mass. This provides predictions for  $M/L_V$ , the initial cluster mass  $M_{\text{cl},i}$  and the total disruption time  $t_{\text{dis}}^{\text{total}}$  for two metallicities. These are then interpolated over metallicity to obtain the model predictions for the appropriate metallicity.

Examples of the  $M/L_V$  evolution with time and mass are shown in Fig. 5.5 for NGC 5466 and 6779. The predicted  $M/L_V$  are slightly offset with respect to the model curves because the models here are computed at  $Z = 0.0004$  while the predictions are interpolated over metallicity. However, the variation with metallicity is small for the displayed clusters, since their metallicities are close to  $Z = 0.0004$ . It is evident that low-mass star depletion has a much stronger effect in the case of NGC 6779 than for NGC 5466. Considering their dissolution timescales ( $t_0 = 1.2$  Myr versus  $t_0 = 10.2$  Myr, respectively) and the resulting mass evolution, this is not surprising since NGC 6779 has suffered much stronger mass loss than NGC 5466.

The predicted mass-to-light ratios  $M/L_V$ , initial masses  $M_{\text{cl},i}$  and remaining lifetimes  $t_{\text{dis}}^{\text{total}} - t$  are listed for our entire GC sample in Table 5.4. In addition, the observed and predicted fractions of the canonical  $M/L_V$  ratios  $Q_{\text{obs}}$  and  $Q_{\text{pred}}$  are shown, as well as the agreement between our predicted  $M/L_V$  and the observed values. Combining Tables 5.3



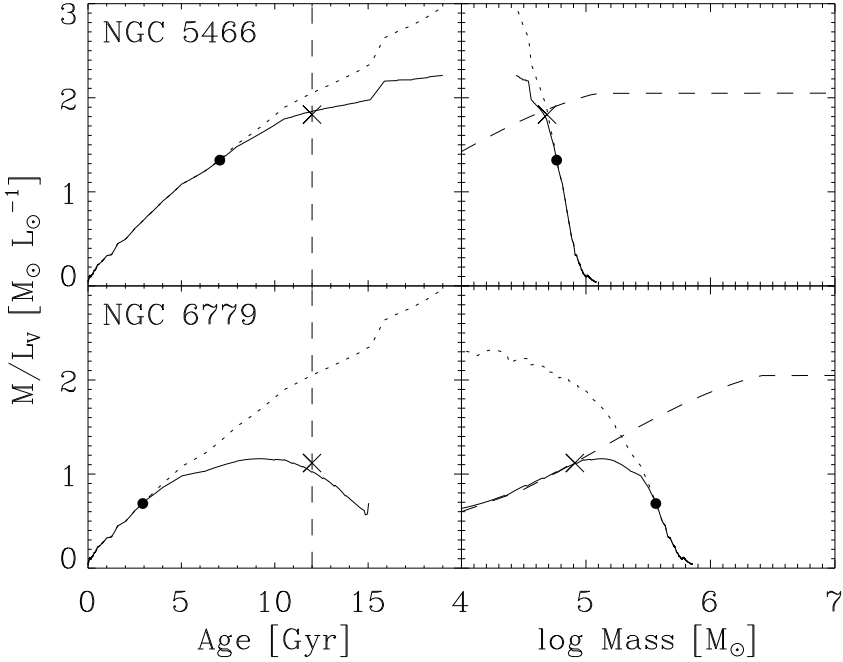


**Figure 5.5:** *Top left:* Time-evolution of  $M/L_V$  for NGC 5466. The solid line represents the  $Z = 0.0004$  model with the dissolution timescale of the cluster ( $t_0 = 10.2$  Myr), while the dotted curve indicates the canonical  $M/L_V$  evolution, i.e. if the preferential loss of low-mass stars were omitted. The dashed line denotes constant age of  $t = 12$  Gyr. The predicted  $M/L_V$  of NGC 5466 is marked by a cross and the onset of the preferential loss of low-mass stars is specified with a dot. *Top right:* Evolution in the  $\{M, M/L_V\}$ -plane for NGC 5466. Curves and symbols have the same meaning as in the top-left panel. *Bottom left:* same as top left, but for NGC 6779 ( $t_0 = 1.2$  Myr). *Bottom right:* same as top right, but for NGC 6779.

and 5.4, we see that GCs with short dissolution timescales indeed have low predicted  $M/L$  ratios.

#### 5.4.2 Comparison of predictions to observations

The fifth column in Table 5.4 indicates the ratio between observed and predicted mass-to-light ratio  $\mathcal{Q}_{\text{obs}} \equiv (M/L_V)_{\text{obs}}/(M/L_V)_{\text{can}}$ . Analogously, the sixth column gives the ratio between predicted and canonical mass-to-light ratio  $\mathcal{Q}_{\text{pred}} \equiv (M/L_V)_{\text{pred}}/(M/L_V)_{\text{can}}$ . On average, the former ratio is  $0.74^{+0.06}_{-0.07}$ , while the latter ratio is  $0.85 \pm 0.01$  for the 24 GCs investigated. There are factors that introduce biases when comparing the predictions to the observations. Specifically, the observations are likely biased to central  $M/L$  ratios for some GCs, while we

**Table 5.4:** Our model predictions with their  $1\sigma$  standard errors. The first four columns list the cluster NGC number, the predicted  $V$ -band mass-to-light ratio  $(M/L_V)_{\text{pred}}$  (in  $M_\odot L_\odot^{-1}$ ), the logarithm of the initial cluster mass  $M_{\text{cl},i}$  (in  $M_\odot$ ) and the remaining lifetime  $t_{\text{dis}}^{\text{total}} - t$  (in Gyr). In the fifth and sixth column, respectively the ratios of observed to canonical mass-to-light ratio  $Q_{\text{obs}}$  and predicted to canonical mass-to-light ratio  $Q_{\text{pred}}$  are listed. The seventh column gives the level of agreement between the observed mass-to-light ratio  $(M/L_V)_{\text{obs}}$  and predicted mass-to-light ratio  $(M/L_V)_{\text{pred}}$  (see text).

Model predictions						
NGC	$(M/L_V)_{\text{pred}}$	$\log M_{\text{cl},i}$	$t_{\text{dis}}^{\text{total}} - t$	$Q_{\text{obs}}$	$Q_{\text{pred}}$	Agreement
104	$2.68^{+0.25}_{-0.25}$	$6.10^{+0.14}_{-0.18}$	$102.1^{+26.6}_{-32.4}$	$0.50^{+0.19}_{-0.23}$	$1.00^{+0.00}_{-0.00}$	3
288	$1.42^{+0.37}_{-0.29}$	$5.73^{+0.15}_{-0.26}$	$6.3^{+3.6}_{-2.7}$	$0.98^{+0.37}_{-0.45}$	$0.64^{+0.16}_{-0.13}$	1
1851	$2.21^{+0.09}_{-0.09}$	$5.71^{+0.14}_{-0.17}$	$105.4^{+33.5}_{-38.5}$	$0.73^{+0.26}_{-0.32}$	$1.00^{+0.00}_{-0.00}$	2
1904	$2.02^{+0.07}_{-0.13}$	$5.38^{+0.13}_{-0.16}$	$37.7^{+14.9}_{-16.8}$	$0.56^{+0.20}_{-0.25}$	$0.97^{+0.03}_{-0.06}$	2
4147	$1.64^{+0.16}_{-0.20}$	$4.99^{+0.12}_{-0.14}$	$13.2^{+6.1}_{-6.9}$	$0.50^{+0.18}_{-0.23}$	$0.81^{+0.08}_{-0.10}$	2
4590	$1.97^{+0.03}_{-0.09}$	$5.03^{+0.13}_{-0.16}$	$41.9^{+13.3}_{-15.9}$	$0.46^{+0.16}_{-0.20}$	$0.99^{+0.02}_{-0.05}$	4
5139	$1.96^{+0.19}_{-0.19}$	$6.98^{+0.15}_{-0.13}$	$22.9^{+11.9}_{-9.4}$	$1.17^{+0.54}_{-0.43}$	$0.90^{+0.08}_{-0.08}$	1
5272	$2.08^{+0.04}_{-0.04}$	$5.76^{+0.14}_{-0.18}$	$83.5^{+23.9}_{-29.1}$	$0.67^{+0.24}_{-0.30}$	$1.00^{+0.00}_{-0.00}$	2
5466	$1.82^{+0.13}_{-0.18}$	$5.15^{+0.13}_{-0.16}$	$24.7^{+12.3}_{-12.4}$	$0.81^{+0.30}_{-0.37}$	$0.91^{+0.07}_{-0.09}$	1
5904	$2.10^{+0.11}_{-0.16}$	$5.66^{+0.13}_{-0.16}$	$34.9^{+14.2}_{-15.7}$	$0.36^{+0.13}_{-0.16}$	$0.96^{+0.04}_{-0.07}$	5
6093	$1.79^{+0.19}_{-0.27}$	$6.10^{+0.14}_{-0.16}$	$19.5^{+11.3}_{-11.3}$	$1.31^{+0.49}_{-0.62}$	$0.88^{+0.09}_{-0.13}$	1
6121	$1.18^{+0.18}_{-0.22}$	$5.91^{+0.09}_{-0.11}$	$3.7^{+1.5}_{-1.8}$	$0.57^{+0.23}_{-0.32}$	$0.53^{+0.07}_{-0.09}$	1
6171	$1.81^{+0.17}_{-0.21}$	$5.56^{+0.10}_{-0.13}$	$11.3^{+3.2}_{-4.2}$	$0.94^{+0.38}_{-0.52}$	$0.78^{+0.05}_{-0.07}$	1
6205	$2.08^{+0.04}_{-0.04}$	$5.77^{+0.15}_{-0.18}$	$109.1^{+45.2}_{-49.9}$	$0.72^{+0.26}_{-0.34}$	$1.00^{+0.00}_{-0.00}$	2
6218	$1.74^{+0.12}_{-0.15}$	$5.48^{+0.10}_{-0.12}$	$15.0^{+4.7}_{-6.1}$	$0.84^{+0.31}_{-0.40}$	$0.83^{+0.05}_{-0.07}$	1
6254	$1.94^{+0.09}_{-0.12}$	$5.68^{+0.12}_{-0.16}$	$27.5^{+9.2}_{-12.0}$	$1.03^{+0.40}_{-0.53}$	$0.93^{+0.04}_{-0.05}$	1
6341	$1.56^{+0.12}_{-0.14}$	$5.71^{+0.10}_{-0.12}$	$11.8^{+4.2}_{-5.1}$	$0.44^{+0.17}_{-0.21}$	$0.78^{+0.06}_{-0.07}$	2
6362	$1.47^{+0.21}_{-0.24}$	$5.67^{+0.10}_{-0.11}$	$5.3^{+2.0}_{-2.2}$	$0.48^{+0.18}_{-0.21}$	$0.60^{+0.05}_{-0.07}$	1
6656	$2.05^{+0.03}_{-0.09}$	$5.98^{+0.14}_{-0.20}$	$45.9^{+14.0}_{-18.8}$	$1.01^{+0.40}_{-0.56}$	$0.99^{+0.01}_{-0.04}$	1
6712	$1.45^{+0.25}_{-0.25}$	$5.80^{+0.09}_{-0.16}$	$5.5^{+2.6}_{-2.4}$	$0.42^{+0.17}_{-0.23}$	$0.61^{+0.09}_{-0.09}$	1
6779	$1.12^{+0.38}_{-0.22}$	$5.91^{+0.15}_{-0.33}$	$4.1^{+4.2}_{-2.3}$	$0.52^{+0.25}_{-0.20}$	$0.56^{+0.19}_{-0.11}$	1
6809	$1.68^{+0.06}_{-0.07}$	$5.79^{+0.04}_{-0.05}$	$14.8^{+2.0}_{-2.3}$	$1.59^{+0.20}_{-0.25}$	$0.83^{+0.03}_{-0.03}$	4
6934	$2.08^{+0.04}_{-0.06}$	$5.42^{+0.14}_{-0.17}$	$77.7^{+42.5}_{-44.8}$	$0.72^{+0.26}_{-0.32}$	$1.00^{+0.00}_{-0.02}$	2
7089	$2.06^{+0.03}_{-0.03}$	$5.85^{+0.15}_{-0.18}$	$151.0^{+81.4}_{-85.3}$	$0.47^{+0.17}_{-0.21}$	$1.00^{+0.00}_{-0.00}$	3

predict global values. In Sect. 5.4.3 a more detailed consideration is provided in which the comparison of the predictions to the observations is refined.

The seventh column in Table 5.4 gives the level of agreement between the observed and predicted mass-to-light ratios, which is defined as  $n$  if  $(n-1)\sigma < |\Delta M/L_V| \leq n\sigma$  for  $\Delta M/L_V \equiv (M/L_V)_{\text{pred}} - (M/L_V)_{\text{obs}}$  and  $\sigma^2 \equiv \sigma_{(M/L)_{\text{obs}}}^2 + \sigma_{(M/L)_{\text{pred}}}^2$ . Within the  $1\sigma$  uncertainty, the predicted  $M/L_V$  agree with the observed values for 12 clusters out of the 24-cluster sample. A Gaussian distribution of errors would yield an expected 16 out of 24 clusters to be found within  $1\sigma$ .

As a first comparison and analogously to the presentation in Mandushev et al. (1991) and

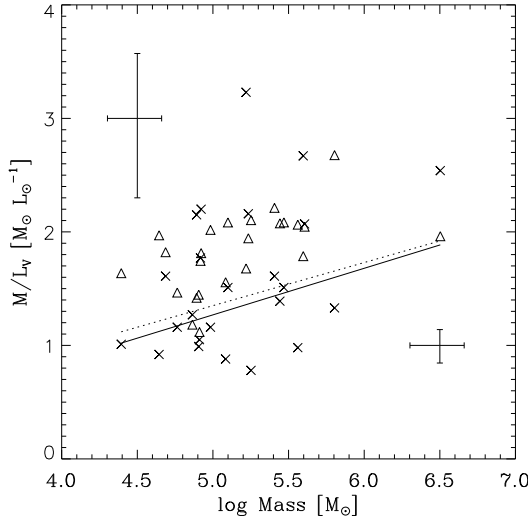


**Figure 5.6:** Observed (crosses) and predicted (triangles) distribution of GCs in the  $\{M, M/L_V\}$ -plane. The solid line represents our linear fit to the observations, while the dotted line denotes the relation found by Mandushev et al. (1991). The error bars in the top left corner denote the average  $1\sigma$  uncertainty on the observations, while the error bars in the bottom right corner represent the average  $1\sigma$  uncertainty on the predictions.

Rejkuba et al. (2007), in Fig. 5.6 the distribution of GCs in the  $\{M, M/L_V\}$ -plane is shown for the observed and predicted mass-to-light ratios. Both populations fall within the same range and follow comparable trends of increasing  $M/L_V$  with cluster mass. Mandushev et al. (1991) already provided an expression for the observed logarithm of the mass as a function of magnitude, which allows for a derivation of the expected trend in Fig. 5.6. They fit

$$\log(M/M_\odot) = (-0.456 \pm 0.024)M_V + (1.64 \pm 0.21), \quad (5.12)$$

where  $M_V$  represents the V-band absolute magnitude of the cluster. Adopting a solar value of  $M_{V,\odot} = 4.83$ , the relation between  $M/L_V$  and mass from Mandushev et al. (1991) can then be expressed as

$$\log(M/L_V) = (-0.12 \pm 0.05) \log(M/M_\odot) - (0.49 \pm 0.21). \quad (5.13)$$

A first-order Taylor expansion of  $M/L_V$  around  $\log(M/M_\odot) = 5.2$  then gives

$$M/L_V \approx 0.38 \log(M/M_\odot) - 0.55, \quad (5.14)$$

which has a linear slope of 0.38. The best fitting slope for our sample is  $0.41 \pm 0.28$ , thus agreeing with the value from Mandushev et al. (1991). The large uncertainty arises from the scatter in Fig. 5.6.

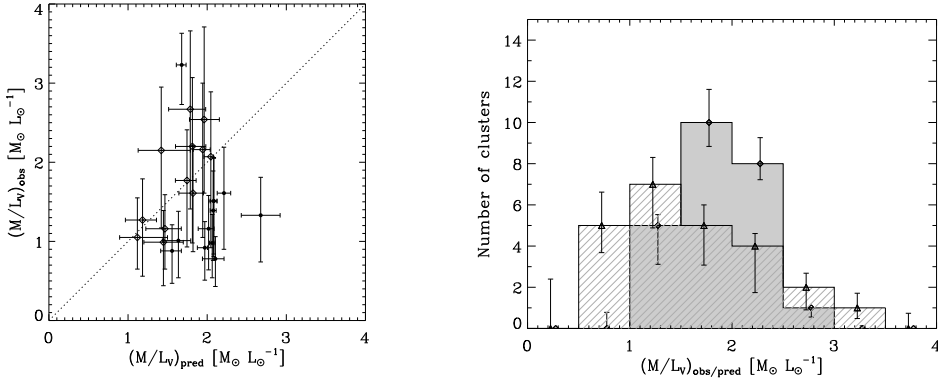


**Figure 5.7:** *Left:* Observed mass-to-light ratio  $(M/L_V)_{\text{obs}}$  versus the predicted mass-to-light ratio  $(M/L_V)_{\text{pred}}$ , together with their  $1\sigma$  standard errors. The dotted line follows the 1:1 relation. Clusters for which the disagreement is larger than  $1\sigma$  are plotted as dots. *Right:* Number histogram of  $(M/L_V)_{\text{pred}}$  (diamonds, shaded area) and  $(M/L_V)_{\text{obs}}$  (triangles, hashed area). Again, the error bars denote  $1\sigma$  deviations, which were determined from 30k random realisations of the underlying data.

The trend of increasing mass-to-light ratio with mass is expected from the models shown in Fig. 5.4 and the discussion in Sec. 5.2.2. However, there the slope is  $\sim 0.6$ – $1.0$  for metallicities  $Z = 0.0004$ – $0.004$  and increases with  $Z$ . For some metallicities, the model slope is thus more than  $1\sigma$  steeper than the fitted slope. This is not surprising, because the models each have a single dissolution timescale and metallicity, while in reality both quantities have a spread that causes horizontal and vertical scatter, respectively. It turns out that the spread in dissolution timescale has a stronger effect on  $M/L$  than the spread in metallicity (Kruijssen 2008), implying that the scatter in the horizontal direction is largest and that the slope fitted to the entire sample is shallower than that of a single model.

In Fig. 5.7, a more specific comparison is made between the observations and model predictions using the same framework as for the canonical expectations in Fig. 5.1. Again, the left-hand panel plots the observed versus the predicted mass-to-light ratios, while the right-hand panel shows the number histograms of the two. In the left-hand panel it is shown that the predictions for half of the clusters are such that they reach down to the appropriate mass-to-light ratios. When comparing this panel to its analog in Fig. 5.1, the improved agreement with the observations is evident. Nonetheless, there is an aggregate of deviating GCs *below* the 1:1 relation at  $(M/L_V)_{\text{pred}} \approx 2 M_{\odot} L_{\odot}^{-1}$ , representing the clusters for which no strong low-mass star depletion is expected from the models due to their long disruption times. Consequently, the predicted  $M/L_V$  for these clusters are similar or equal to the canonical values. Except for NGC 6809, there are no clusters above the 1:1 relation that are inconsistent with the observations. The number histogram of the observed and predicted mass-to-light ratios in the right-hand panel of Fig. 5.7 confirms both the improved agreement between observed and

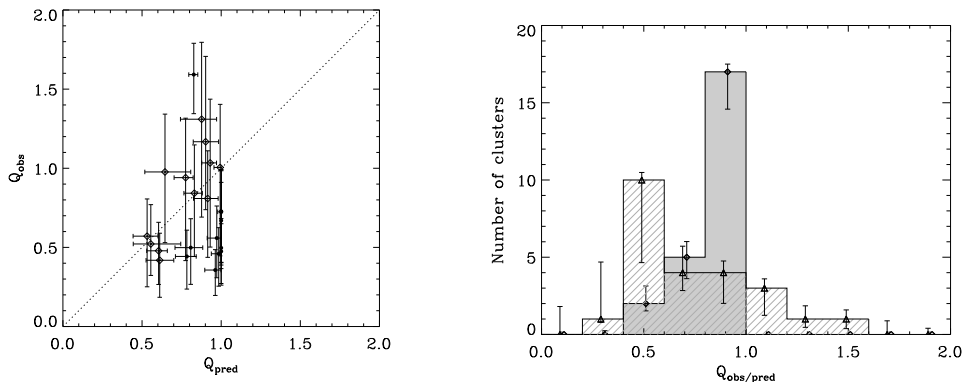


**Figure 5.8:** *Left:* The ratio of the observed mass-to-light ratio  $(M/L_V)_{\text{obs}}$  to the canonically expected  $(M/L_V)_{\text{can}}$  versus the ratio of the predicted mass-to-light ratio  $(M/L_V)_{\text{pred}}$  to  $(M/L_V)_{\text{can}}$ , together with their  $1\sigma$  standard errors. The dotted line follows the 1:1 relation. Clusters for which the disagreement is larger than  $1\sigma$  are plotted as dots. *Right:* Number histogram of the ratio  $Q_{\text{pred}}$  (diamonds, shaded area) and  $Q_{\text{obs}}$  (triangles, hashed area). Again, the error bars denote  $1\sigma$  deviations, which were determined from 30k random realisations of the underlying data.

predicted  $M/L_V$  with respect to Fig. 5.1 and the accumulation of a number of clusters near the canonical  $M/L_V$  in the model predictions.

### 5.4.3 Discussion of discrepant clusters

In total, there are twelve clusters with a worse than  $1\sigma$  agreement between the model predictions and observations. Five of these have worse than  $2\sigma$  agreement, while we would expect only one. Here, we discuss possible reasons behind the discrepancy.

The deviant clusters below the 1:1 relation in the left-hand panel of Fig. 5.7, being NGC 104, 1851, 1904, 4147, 4590, 5272, 5904, 6205, 6341, 6934 and 7089, generally share properties such as relatively wide orbits and long dissolution timescales. Due to their long dissolution timescales, they are all predicted to have near-canonical  $M/L_V$ . This is illustrated in Fig. 5.8, where the fraction of  $(M/L_V)_{\text{obs}}$  and  $(M/L_V)_{\text{pred}}$  with respect to the canonical  $(M/L_V)_{\text{can}}$  is shown in panels similar to Fig. 5.7. In both the left- and right-hand panels of Fig. 5.8, the accumulation of too high predicted mass-to-light ratios occurs near or at  $Q_{\text{pred}} = 1$ . Since per definition  $(M/L_V)_{\text{pred}} \leq (M/L_V)_{\text{can}}$ , no values  $Q_{\text{pred}} > 1$  are found. In that range, the apparent disagreement between the observed and predicted histograms is disputable since all but one cluster (NGC 6809) are in  $1\sigma$  agreement with their canonical mass-to-light ratios.

While our predicted mass-to-light ratios are global (i.e. cluster-wide) values, the observations from McLaughlin & van der Marel (2005) are derived from central velocity dispersion

measurements from Pryor & Meylan (1993) and are extrapolated to global values using surface brightness profiles (McLaughlin & van der Marel 2005, and references therein). They fit isotropic single-mass King models and thus neglect any radial gradients of  $M/L$  ratio or mass function slope. Consequently, the values of  $(M/L_V)_{\text{obs}}$  do not contain any information about such gradients and for some clusters only accurately reflect the  $M/L_V$  ratio in their central parts. The global  $M/L_V$  ratios of clusters with strong radial  $M/L$  gradients are at best *approximated* (McLaughlin, private communication). For instance, the centre of a mass-segregated cluster may be populated with massive, i.e. luminous stars, yielding a lower  $M/L_V$  ratio than its global value.

The disagreement between the global and central  $M/L$  is expected to be largest for clusters that have suffered relatively weak mass loss but are internally evolved. In that case, the low-mass stars are outside the core but still bound to the cluster and are included in the global  $M/L$ , while they do not play a role in the value derived by McLaughlin & van der Marel (2005). This indeed applies for the discrepant GCs in our sample, which not only have long dissolution timescales but also higher King parameters  $W_0$ , implying that mass segregation can be reached on relatively shorter timescales. For the GCs with worse than  $1\sigma$  agreement below the 1:1 line in Figs. 5.7 and 5.8 we have average King parameter  $\overline{W_0} = 7.6$ , while for the  $1\sigma$ -consistent GCs we find  $\overline{W_0} = 6.1$ , both with standard errors  $< 0.1$ . This further validates our explanation for the difference between the central and global  $M/L$  ratios of these GCs.

In a recent study, De Marchi et al. (2007) find that extended (low-concentration and low- $W_0$ ) GCs are depleted in low-mass stars, which they confirm to be in accordance with predictions by theoretical studies (Chernoff & Weinberg 1990, Takahashi & Portegies Zwart 2000), while GCs with high values of  $W_0$  have close to canonical mass functions. This is in agreement with our predicted  $M/L_V$  for these clusters and suggests that the observed  $M/L_V$  are indeed underestimated. A more precise check can be made by comparing the low-mass star depletion from De Marchi et al. (2007) with the observed and predicted fractions of the canonical  $M/L_V$  ratios  $Q_{\text{obs}/\text{pred}}$ . This can be done for four GCs with worse than  $1\sigma$  agreement, being NGC 104, 5272, 6341 and 6809. For NGC 104 and 5272 the observed depletion is not strong enough to draw any definitive conclusions, while for NGC 6341 and 6809 the results from De Marchi et al. (2007) are clearly more consistent with our predictions than with the observed  $M/L_V$  (see also Sect. 5.5 and Fig. 5.9). This substantiates the claim that some GCs have observed  $M/L$  ratios that are biased to lower numbers. To test this assertion, *global* observational measurements of the velocity dispersion would be needed to enhance the accuracy of the present observed  $M/L$  ratios.

We now revisit the mean  $M/L_V$  fractions of the canonical value presented in Sect. 5.4.2 by leaving out the GCs that may have strongly different central and global  $M/L$  ratios. It was shown by Baumgardt & Makino (2003) that for a  $10^5 M_\odot$  cluster core collapse is reached within a Hubble time if  $W_0 \geq 7$ . This timescale is increased by a factor three for a GC with typical initial mass of  $10^6 M_\odot$ , but mass segregation manifests itself on a shorter timescale than the core collapse time. The relative mass loss due to dissolution of a  $10^6 M_\odot$  GC is smaller than 10% after 12 Gyr for dissolution timescales  $t_{0,\text{tot}} \geq 5$  Myr. These limits could separate GCs with similar global and central  $M/L$  ratios from those with pronounced differences between the two. We exclude GCs with both  $t_{0,\text{tot}} \geq 5$  Myr and  $W_0 \geq 7$ , as well

as NGC 6809 (which has a  $M/L_V$  ratio that cannot be explained by any model as it is 1.6 times the canonical value). This yields an average observed fraction of the canonical  $M/L_V$  of  $Q_{\text{obs}} = 0.78^{+0.09}_{-0.11}$  and a predicted value of  $Q_{\text{pred}} = 0.78 \pm 0.02$ . For the excluded GCs, we have  $Q_{\text{obs}}^{\text{excl}} = 0.68^{+0.05}_{-0.06}$  and  $Q_{\text{pred}}^{\text{excl}} = 0.96 \pm 0.01$ , reflecting the fundamental difference between both values. Although the cuts we made represent only ‘educated guesses’, it is evident that the agreement between theory and observations is much better for those GCs for which we can be more certain that the central  $M/L_V$  reflects the global value. For these GCs, our models confirm an average  $M/L$  ratio drop of about 20% due to low-mass star depletion, corresponding to about 1/4 of the observed difference in  $M/L_V$  between GCs and UCDs.

Another option could be that the dissolution timescales of GCs on wide orbits are overestimated (as suggested for different reasons by Kruijssen & Portegies Zwart 2009), possibly due to a dissolution mechanism that is not included in our analysis. White dwarf kicks (Fregeau et al. 2009) could be a candidate for such a mechanism. This would imply that some of our predicted dissolution timescales and  $M/L$  ratios are overestimated. Also, we do not assume clusters to be initially mass-segregated. Some of the clusters under consideration here are likely not to have reached energy equipartition within a Hubble time, but still exhibit evidence of mass segregation (e.g. Anderson & King 1996). This points to primordial mass segregation in these cases, which is shown by Baumgardt et al. (2008) to effect additional low-mass star depletion that we did not account for (see also Sect. 5.2.2). The additional modeled  $M/L$  ratio decrease would be  $\sim 10\%$  (KL08). However, this is not sufficient to lift the discrepancy for any of the deviating GCs.

## 5.5 Observational verification

If the decrease of  $M/L$  ratio with respect to the canonical value is indeed due to low-mass star depletion, one would expect a correlation between the observed slope of the low-mass MF  $\alpha_{\text{obs}}$  and the ratio of the predicted and canonical  $M/L_V$  ratios  $Q_{\text{pred}}$ . Specifically, for a powerlaw MF with  $n \propto m^{-\alpha}$ , a low value of  $Q_{\text{pred}}$  would be signified by a reduced value of  $\alpha_{\text{obs}}$ .

In a study by De Marchi et al. (2007), MF slopes are determined in the stellar mass range  $m = 0.3\text{--}0.8 M_{\odot}$  for several Galactic globular clusters, based on a compilation of results from HST imaging of different sources. By reanalysing the Baumgardt & Makino (2003)  $N$ -body data, Baumgardt et al. (2008) conclude that for a Kroupa (2001) IMF the canonical slope in that mass range is  $\alpha_0 = 1.74$ , which is thus expected to be measured for clusters with canonical  $M/L$  ratios or  $Q_{\text{pred}} = 1$ . In addition, they provide a fourth-order powerlaw fit to the  $N$ -body simulations from Baumgardt & Makino (2003) for  $\alpha$  as a function of  $t/t_{\text{dis}}^{\text{total}}$ , the elapsed fraction of the total disruption time. By inverting our relation between  $Q_{\text{pred}}$  and  $t/t_{\text{dis}}^{\text{total}}$  (Eq. 5.5) and inserting the outcome into  $\alpha(t/t_{\text{dis}}^{\text{total}})$  from Baumgardt et al. (2008, Eq. 4), we obtain an expression for the predicted MF slope  $\alpha_{\text{pred}}$  between 0.3 and  $0.8 M_{\odot}$  as a function of the fraction of the canonical  $M/L_V$  ratio  $Q_{\text{pred}}$ . Inversion of Eq. 5.5 yields

$$t/t_{\text{dis}}^{\text{total}} = \begin{cases} 1.25 - 0.85 Q_{\text{pred}} & \text{for } Q_{\text{pred}} \leq 0.645, \\ 1.61 - 1.41 Q_{\text{pred}} & \text{for } 0.645 < Q_{\text{pred}} < 1, \\ 0..0.2 & \text{for } Q_{\text{pred}} = 1, \end{cases} \quad (5.15)$$

**Table 5.5:** Coefficients for the fourth-order powerlaw approximation of  $\alpha_{\text{pred}}$  as a function of  $\mathcal{Q}_{\text{pred}}$  (see Eq. 5.16).

$\alpha_{\text{pred}}$ coefficients					
$n$	0	1	2	3	4
$a_n$	-4.31	17.76	-22.10	13.17	-3.02
$b_n$	-17.04	74.41	-116.76	84.13	-23.06

where the uncertainty  $t/t_{\text{dis}}^{\text{total}} = 0..0.2$  for  $\mathcal{Q}_{\text{pred}} = 1$  arises due to the range of  $t/t_{\text{dis}}^{\text{total}}$  over which it is constant in our models. Combination of this expression and Eq. 4 from Baumgardt et al. (2008) then provides the relation between  $\alpha_{\text{pred}}$  and  $\mathcal{Q}_{\text{pred}}$ :

$$\alpha_{\text{pred}} = \begin{cases} \sum_{n=0}^4 a_n \mathcal{Q}_{\text{pred}}^n & \text{for } \mathcal{Q}_{\text{pred}} \leq 0.645, \\ \sum_{n=0}^4 b_n \mathcal{Q}_{\text{pred}}^n & \text{for } 0.645 < \mathcal{Q}_{\text{pred}} < 1, \\ 1.68...1.74 & \text{for } \mathcal{Q}_{\text{pred}} = 1, \end{cases} \quad (5.16)$$

with the coefficients  $\{a, b\}_n$  listed in Table 5.5 and again the uncertainty  $\alpha_{\text{pred}} = 1.68...1.74$  emerging from the degeneracy of  $\mathcal{Q}_{\text{pred}} = 1$  that was mentioned earlier<sup>5</sup>.

In Fig. 5.9, the correlation between  $\mathcal{Q}_{\text{obs/pred}}$  and the observed low-mass MF slope  $\alpha_{\text{obs}}$  is assessed for the subsample of clusters from the present study that is also considered in De Marchi et al. (2007). For comparison, the relation for the predicted low-mass MF slope  $\alpha_{\text{pred}}$  as a function of  $\mathcal{Q}_{\text{obs/pred}}$  is included as well. Most of the observed data match the predicted relation between  $\alpha$  and  $\mathcal{Q}$  within their error bars, albeit with substantial scatter. This is due to the large uncertainties of the observations and possibly also related to biases introduced by comparing central and global mass-to-light ratios (see Sect. 5.4.3). The poor quality of the observations is illustrated by this spread and by the large error bars. For the predicted mass-to-light ratios the trend is more well-defined, but for low values of  $\alpha_{\text{obs}}$  it does not extend down to the mass-to-light ratios that are predicted by theory. This could imply that either  $\alpha_{\text{obs}}$  or  $\mathcal{Q}_{\text{pred}}$  are biased. If the latter is true, it suggests that some GCs perhaps dissolve more rapidly than presently included in the models.

As shown in Sect. 5.4.3, comparison of  $\alpha_{\text{obs}}$  with the observed and predicted fractions of the canonical  $M/L_V$  ratios  $\mathcal{Q}_{\text{obs/pred}}$  for the GCs with agreement parameter  $\geq 2$  (see Table 5.4) provides an independent check of our predicted  $M/L_V$  ratios. While for NGC 104 and 5272 this does not allow for any definitive conclusions, for NGC 6341 and 6809 the observed mass functions are clearly more consistent with our predicted  $M/L_V$  ratios than with the observed values.

<sup>5</sup>Consequently, it represents the same uncertainty as  $t/t_{\text{dis}}^{\text{total}} = 0..0.2$ , with  $\alpha_{\text{pred}} = 1.68$  corresponding to  $t/t_{\text{dis}}^{\text{total}} = 0.2$  and  $\alpha_{\text{pred}} = 1.74$  to  $t/t_{\text{dis}}^{\text{total}} = 0$ . Since for most GCs under consideration the elapsed fractions of the total disruption time are closer to  $t/t_{\text{dis}}^{\text{total}} = 0.2$  than to  $t/t_{\text{dis}}^{\text{total}} = 0$  (see Table 5.4), we adopt  $\alpha_{\text{pred}} = 1.68$  if  $\mathcal{Q}_{\text{pred}} = 1$ .



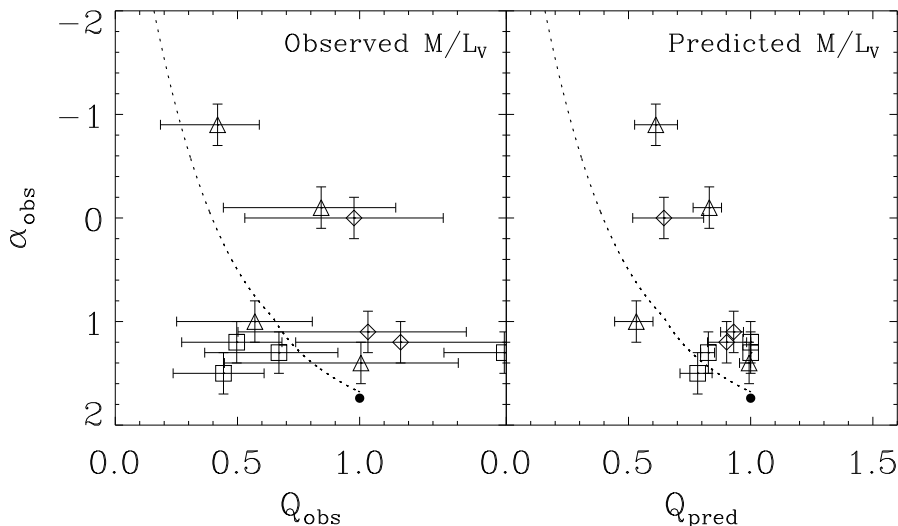


**Figure 5.9:** Correlation between the observed slope of the low-mass stellar mass function  $\alpha_{\text{obs}}$  and the relative mass-to-light ratio with respect to the canonical value  $Q$ . The dotted curves indicate the theoretically predicted relation between  $\alpha$  and  $Q$  (not a fit), with the dot at the right-hand tip representing the canonical values of  $\alpha_0 = 1.74$  and  $Q = 1$ . Values of  $\alpha$  representing the *global* MF are marked with triangles, while those for clusters with worse than  $1\sigma$  agreement between  $Q_{\text{obs}}$  and  $Q_{\text{pred}}$  are denoted by squares. *Left:* For the observed mass-to-light ratio fraction  $Q_{\text{obs}}$ . *Right:* For the predicted mass-to-light ratio fraction  $Q_{\text{pred}}$ .

With Eq. 5.16, we can also *predict* the slope of the low-mass MF for clusters that were not considered by De Marchi et al. (2007). The predicted slopes are listed in Table 5.6. For most clusters with observed values of  $\alpha$ , the agreement between observed and predicted  $\alpha$  is reasonable. Only for NGC 6218 and 6712 there is a strong discrepancy. For NGC 6218, we expect the deviation to arise from the observed value of  $\alpha_{\text{obs}}$ , since the predicted and observed  $M/L_V$  are in excellent agreement (see Table 5.4). On the other hand, for NGC 6712 the incompatibility may be due to a slight overestimation of  $(M/L_V)_{\text{pred}}$  and thus of  $Q_{\text{pred}}$  and  $\alpha_{\text{pred}}$ .

In this context it must be noted that the compilation of  $\alpha$  values from De Marchi et al. (2007) is drawn from a sample of literature estimates, most based on HST data, observed in somewhat different radial regions of each cluster. Four of the eleven GCs that coincide with our sample of 24 GCs do have a direct estimate for their global mass function (see Table 5.6). For the remaining seven other GCs from De Marchi et al. (2007), that estimate is taken from measurements restricted to the region around the half-mass radius  $r_h$ , of which it is known that the shape of the MF is comparable to the global (i.e. cluster-wide) MF (Richer et al. 1991, Baumgardt & Makino 2003, De Marchi & Pulone 2007). However, the uncertainty of these slopes is larger, and they do not provide a self-consistent way to derive the global MF.

**Table 5.6:** Observed and predicted stellar mass function (MF) slopes  $\alpha$  in the range  $m = 0.3\text{--}0.8 M_{\odot}$ . Listed are the cluster NGC numbers (first column), observed MF slopes from De Marchi et al. (2007) (second column), and predicted MF slopes (third column). The observed low-mass MF slope of clusters representing *global* MFs from multi-mass Michie-King models are denoted in boldface, while the other values designate local values close to the half-mass radius (see text). The standard errors on  $\alpha_{\text{obs}}$  is  $\sigma_{\alpha} = 0.2$  for the global MFs and  $\sigma_{\alpha} = 0.3$  for the other values (De Marchi, private communication).

MF slopes		
NGC	$\alpha_{\text{obs}}$	$\alpha_{\text{pred}}$
104	$1.2 \pm 0.3$	$1.68^{+0.00}_{-0.00}$
288	$0.0 \pm 0.3$	$0.96^{+0.40}_{-0.31}$
1851		$1.68^{+0.00}_{-0.00}$
1904		$1.65^{+0.03}_{-0.07}$
4147		$1.40^{+0.14}_{-0.18}$
4590		$1.66^{+0.02}_{-0.05}$
5139	$1.2 \pm 0.3$	$1.55^{+0.12}_{-0.11}$
5272	$1.3 \pm 0.3$	$1.68^{+0.00}_{-0.00}$
5466		$1.57^{+0.09}_{-0.12}$
5904		$1.64^{+0.04}_{-0.08}$
6093		$1.52^{+0.14}_{-0.20}$
6121	<b><math>1.0 \pm 0.2</math></b>	$0.62^{+0.25}_{-0.32}$
6171		$1.34^{+0.10}_{-0.15}$
6205		$1.68^{+0.00}_{-0.00}$
6218	<b><math>-0.1 \pm 0.2</math></b>	$1.44^{+0.09}_{-0.11}$
6254	$1.1 \pm 0.3$	$1.59^{+0.05}_{-0.07}$
6341	$1.5 \pm 0.3$	$1.35^{+0.12}_{-0.15}$
6362		$0.85^{+0.15}_{-0.21}$
6656	<b><math>1.4 \pm 0.2</math></b>	$1.67^{+0.01}_{-0.04}$
6712	<b><math>-0.9 \pm 0.2</math></b>	$0.87^{+0.24}_{-0.24}$
6779		$0.70^{+0.63}_{-0.37}$
6809	$1.3 \pm 0.3$	$1.44^{+0.04}_{-0.06}$
6934		$1.68^{+0.00}_{-0.02}$
7089		$1.68^{+0.00}_{-0.00}$

It is clear that a direct determination of the global stellar mass function for most of the 24 GCs investigated in this study would allow one to verify the predictions of the present study with much higher confidence.

In Fig. 5.10 we investigate how feasible it is to observationally verify the predicted drop of  $\alpha$  for our full sample of 24 GCs. We plot the apparent V-band magnitude of stars with 0.3 solar masses  $V_{0.3}$  for each cluster versus the predicted slope  $\alpha_{\text{pred}}$  of the stellar mass function for  $0.3 < m/M_{\odot} < 0.8$ .  $V_{0.3}$  is obtained from the distance modulus of each GC and from the assumption that  $M_{V_{0.3}} = 9.8$  mag (Baraffe et al. 1997). We also plot the angular size of each cluster versus  $\alpha_{\text{pred}}$ . As a consequence of their generally higher galactocentric distance, those

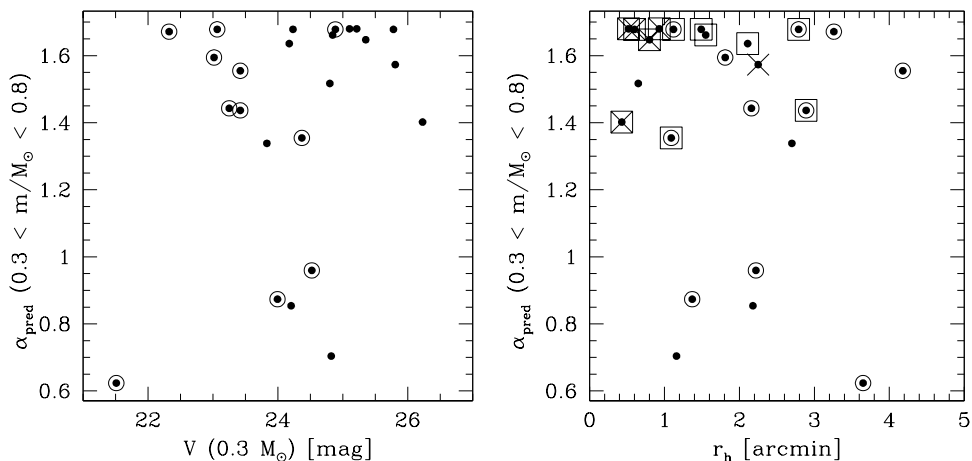


**Figure 5.10:** Feasibility of observational tests of low-mass star depletion. *Left:* For the 24 GCs investigated in this chapter, the apparent  $V$ -band magnitude of stars with 0.3 solar masses  $V_{0.3}$  is plotted versus the predicted slope  $\alpha_{\text{pred}}$  of the stellar mass function for  $0.3 < m/M_{\odot} < 0.8$ . Data points with large circles are those with available observational data from HST imaging (compiled by de Marchi et al. 2007). *Right:* The half-mass radius in arcminutes (Harris 1996) is plotted versus  $\alpha_{\text{pred}}$ . Data points with crosses indicate GCs with  $V_{0.3} > 25$  mag. Data points with large squares indicate GCs whose predicted  $M/L_V$  deviates by more than  $1\sigma$  from the observed value. These are all GCs with agreement parameter  $\geq 2$  in Table 5.4.

GCs with the faintest  $V_{0.3} > 25$  mag would not be expected to exhibit a strong low-mass star depletion. The angular half-mass diameters of the GCs with  $V_{0.3} < 25$  range between 2 and 8 arcminutes. To obtain a representative estimate of the global mass function, it is clear that wide-field ground-based imaging is required for most GCs. For this wide-field imaging, a completeness magnitude of  $V \sim 26$  mag is desirable, which will allow moderately precise photometry already for  $V \sim 25$  mag. For 8m class telescopes and with optical seeing in the range 0.8 to 1.0'', this requires 1-2 hours integration time per filter, or 2-4 hours for a two-band exposure. With wide-field imagers such as VIMOS@VLT, IMACS@Magellan, or SuprimeCam@SUBARU, single-shot images will be sufficient to cover at least 2-3 half-light radii for most clusters. From Fig. 5.10 we conclude that the best candidate that also complements the compilation by De Marchi et al. (2007) is NGC 6779, followed by NGC 6362 and possibly NGC 6171.

## 5.6 Discussion and conclusions

In this section, we provide a summary and a discussion of our results. We consider the effects of the assumptions that were made and reflect on the implications of the results.

### 5.6.1 Summary

In this study, we have investigated the dynamical mass-to-light ratios of 24 Galactic globular clusters. We have tested the hypothesis of the preferential loss of low-mass stars as the main explanation for the fact that the average observed mass-to-light ratios of the Galactic GCs in our entire sample are only  $74^{+6}_{-7}\%$  of the expectations from stellar population models. Accounting for the orbital parameters we derived dissolution timescales due to two-body relaxation and disc shocking for our globular cluster sample and calculated the evolution of their masses and photometry using the SPACE analytical cluster models from Kruijssen & Lamers (2008, throughout this chapter KL08). These models account for the preferential loss of low-mass stars which is fitted to the  $N$ -body simulations by Baumgardt & Makino (2003) and therefore provide non-canonical  $M/L_V$  predictions. We find the derived dissolution timescales to be in good agreement with the range required for low-mass star depletion to explain the observed  $M/L$  ratio decrease from Kruijssen (2008).

The present-day ( $t = 12$  Gyr)  $M/L_V$  ratios have been compared to the observed values from McLaughlin & van der Marel (2005), yielding  $1\sigma$  agreement for 12 out of 24 GCs. We considered possible causes for the remaining  $> 1\sigma$  discrepancies that occur for the other GCs. It is found that 11 of these clusters have predicted  $M/L_V$  very close to the canonically expected  $M/L_V$  ratios due to their long dissolution timescales and the correspondingly modest low-mass star depletion, while their observed  $M/L_V$  are lower. This is probably due to the method by which the observed  $M/L_V$  are derived, which is biased towards the central  $M/L_V$  while our models predict global  $M/L_V$ . For mass-segregated GCs with long dissolution timescales, both values can be substantially different. The discrepant GCs have higher than average King parameters  $W_0$ , which should indeed reach mass segregation on shorter timescales (see e.g. Baumgardt & Makino 2003). This explanation for the discrepancy between some of the observed and predicted  $M/L$  ratios is confirmed by a study of low-mass star depletion in GCs by De Marchi et al. (2007), whose observed mass functions are in good agreement with our predictions. The average observed  $M/L_V$  ratio of  $74^{+6}_{-7}\%$  of the canonical expectations would therefore be underestimated. Excluding GCs which likely have dissimilar global and central  $M/L$  ratios by making cuts in dissolution timescale and King parameter, we find that the observed and predicted  $M/L_V$  ratios are consistent at  $78^{+9}_{-11}\%$  and  $78 \pm 2\%$  of the canonical values, respectively. For the entire sample, the average predicted fraction of the canonical  $M/L_V$  ratio is  $85 \pm 1\%$ .

To assess the imprint of low-mass star depletion on the slope of the low-mass stellar mass function, we compared the observed mass function slopes  $\alpha_{\text{obs}}$  from De Marchi et al. (2007) for 11 GCs contained in our study to the values predicted by our models as well as to the observed and predicted mass-to-light ratio fractions of the canonical values  $Q_{\text{obs}}$  and  $Q_{\text{pred}}$ . Most of the measured slopes agree with the predictions, but exhibit considerable scatter. Since most of them are values derived at around the half-mass radius and are extrapolated to global values, we also discuss the feasibility of observations for *directly* measuring global mass functions of most of the GCs investigated. We show that deep (ground-based) wide-field imaging would be necessary, with point source detection limits  $V \sim 26$  mag. The most suitable candidate for such a campaign would be NGC 6779.

## 5.6.2 Propagation of assumptions

In the course of the study presented in this chapter, several assumptions were made that affect the results to different extents. Their implications are as follows.

- (1) We have adopted the SPACE cluster models (KL08), of which the stellar evolution and photometry are based on the Padova 1999 isochrones (see Sect. 5.2). Consequently, the predicted cluster photometry and corresponding mass-to-light ratios are affected by that choice. To indicate the level of the deviation with the cluster models from Bruzual & Charlot (2003), in Fig. 5.1 we compared the canonically expected  $M/L_V$  from SPACE to the Bruzual & Charlot (2003) values for our cluster sample. The difference between both is inadequate to explain any systematic tendency of low mass-to-light ratio with respect to the SPACE models. Therefore, we conclude that the adopted cluster models do not effect substantial implications for the predicted  $M/L$  ratios<sup>6</sup>.
- (2) Due to the treatment of the preferential loss of low-mass stars in the SPACE cluster models, there are indications that the predicted mass-to-light ratios could be underestimated during the final  $\sim 15\%$  of the total cluster lifetime (KL08). Table 5.4 shows that none of the GCs in our sample reside in this regime. On the other hand, we did not include primordial mass segregation, which could decrease the predicted  $M/L$  ratios by  $\sim 10\%$  (KL08).
- (3) By adopting the average cluster orbits from Dinescu et al. (1999), we assume constant orbital parameters over the total cluster lifetimes. Considering the ballistic nature of the orbits, such an assumption is legitimate as long as the external conditions do not strongly differ. The Galactic potential was only substantially different from its present state during the formation of the Milky Way. A more extended distribution of mass during these early epoch would obviously increase the dissolution timescale due to disc shocking, and would affect the dissolution timescale due to two-body relaxation in a similar way because of the reduced tidal field. Consequently, this would imply that the mass loss during the first  $\sim 1$  Gyr of our models is overestimated, causing our initial masses to be overestimated as well. However, the extended nature of the Milky Way would cause dissolution due to giant molecular cloud encounters to become an important mechanism (e.g. Gieles et al. 2006b), thereby counteracting the previous effect. Although we cannot rule out any consequences, a residual influence would only be relevant for a small fraction (the first  $\sim 10\%$ ) of the total cluster lifetime, where mass loss by dissolution is much less effective than later on during cluster evolution. Therefore, this likely only affects our analysis within the error margins.
- (4) We have compared our predictions to the observed mass-to-light ratios from McLaughlin & van der Marel (2005), which are biased towards central  $M/L$  values. As treated more extensively in Sect. 5.4.3, this yields underestimated observed  $M/L$  ratios for mass-segregated clusters with long dissolution timescales. Therefore, based on the

---

<sup>6</sup>Of course, if the preferential loss of low-mass stars is accounted for, i.e. non-canonical models are considered, the SPACE cluster models predict very different photometric evolution than canonical cluster models such as Bruzual & Charlot (2003).

earlier discussion and the parameter range in which discrepancies arise, we consider the dynamical  $(M/L_V)_{\text{obs}}$  from McLaughlin & van der Marel (2005) to be subject to improvement for GCs with both dissolution timescales  $t_{0,\text{tot}} \geq 5$  Myr and King parameters  $W_0 \geq 7$ .

### 5.6.3 Consequences and conclusions

The consequences of our findings are not only relevant to studies of the  $M/L$  ratios of compact stellar systems, but also to other properties of these structures. Here we list them together with the conclusions of this work.

- (1) When constraining our sample to the subset for which the observed  $M/L_V$  likely reflect the global values, we find that the preferential loss of low-mass stars can account for the  $\sim 20\%$  discrepancy between observed dynamical mass-to-light ratios of Galactic GCs and those expected from stellar population models that assume a canonical present day mass function (Kroupa 2001). This alleviates the factor of two offset in  $M/L$  between GCs and UCDs by about 25%. Still, some additional dark mass with respect to a canonical IMF is required to explain the  $M/L$  of most UCDs.
- (2) Accounting for the orbital parameters, present-day masses and chemical compositions of *individual* clusters, we find that there is good agreement between our model predictions and observations of the  $M/L_V$  ratios of these clusters. For the GCs with worse than  $1\sigma$  agreement there are strong indications that the discrepancy is due to an underestimation of the observed  $M/L$  ratio. In mass-segregated clusters with long dissolution timescales, the observed  $M/L_V$  ratios represent central values that do not reflect the global  $M/L_V$  ratio.
- (3) The ideal way to confirm the validity of our explanation for the reduced  $M/L$  ratios of GCs for *individual* clusters will be to obtain a homogeneous set of deep wide-field imaging for most GCs. This would expand and complement the currently available heterogeneous data sets of space based GC imaging, which is restricted to small fields in each GC, at different radial ranges. By this, the global mass and luminosity functions could be measured directly for individual GCs and be compared quantitatively to the predictions of this chapter regarding the low-mass star depletion due to dynamical evolution. In addition, velocity dispersion measurements would allow for the determination of global  $M/L$  ratios, thus providing an update to those from McLaughlin & van der Marel (2005).
- (4) The topic of globular cluster self-enrichment and multiple stellar populations can also be considered within the framework of this chapter. In a recent study by Marino et al. (2008) it is shown that NGC 6121 contains two stellar populations that are probably due to primordial variations in their respective chemical compositions. It is mentioned that the present-day mass of NGC 6121 is an order of magnitude smaller than that of known multiple-population GCs such as NGC 1851, 2808 and 5139. Consequently, Marino et al. (2008) pose the question how the enriched material could have remained in such a shallow potential and argue that multiple populations are unlikely to be strictly internal

to GCs, unless they are the remnant of much larger structures. In the case of NGC 6121, our calculations seem to explain the issue, as it is the *initially fifth most massive GC* of our sample ( $M_{\text{cl},i} \sim 10^6 M_{\odot}$ ). As a result, mass could have been retained much more easily, implying that the multiple populations of NGC 6121 are no reason to invoke external processes for enrichment and to abandon the self-enrichment scenario.

We conclude that the variation of  $M/L$  ratio due to cluster dissolution and low-mass star depletion is statistically significant and serves as a plausible explanation for the difference between observed and canonical  $M/L$  ratios. Moreover, it has several implications that should be accounted for in GC studies, since its effects can be accurately quantified. We also suggest that the  $M/L$  decrease is considered in independent observational verifications to further constrain the evolution of the stellar mass function in dissolving globular clusters.

**Acknowledgements** We thank the anonymous referee for valuable comments that improved the manuscript. We are grateful to Dana Casetti-Dinescu for interesting discussions and for providing the disc shocking destruction rates from Dinescu et al. (1999). Christine Allen is acknowledged for providing the data from Allen et al. (2006, 2008) in electronic form. We thank Guido De Marchi for sharing the uncertainties on the mass function slopes from De Marchi et al. (2007). We particularly enjoyed stimulating discussions with Holger Baumgardt, Mark Gieles, Dean McLaughlin, Simon Portegies Zwart, Frank Verbunt and Reinier Zeldenrust. JMDK is grateful to Henny Lamers for support, advice and constructive comments on the manuscript. This work is supported by the Netherlands Organisation for Scientific Research (NWO), grant number 021.001.038.

## 5.A Appendix: Error analysis

In this Appendix, the error propagation through our computations is discussed. The errors in Tables 5.2 and 5.3 are standard errors, most of them determined by computing the formal error propagation. For a function  $f(x_1, x_2, \dots, x_i)$  this implies

$$\sigma_f^2 = \left( \frac{\partial f}{\partial x_1} \right)^2 \sigma_{x_1}^2 + \left( \frac{\partial f}{\partial x_2} \right)^2 \sigma_{x_2}^2 + \dots + \left( \frac{\partial f}{\partial x_i} \right)^2 \sigma_{x_i}^2, \quad (5.17)$$

with  $\sigma_i$  the error in the parameter  $i$ . Asymmetric errors on each parameter are both separately propagated by employing the same recipe, while inverse relations are accounted for by swapping the positive and negative errors. However, Eq. 5.17 assumes an approximately constant derivative over the standard error interval. For very large errors on non-linear relations this assumption does not hold. The first of two parameters where we have to correct for this effect is  $t_{0,\text{sh}}$ . It is inversely related to the destruction rate  $\nu_{\text{sh}}$  from Dinescu et al. (1999), which is a parameter with very large relative errors, even to the extent that after computing the error propagation one can have  $t_{0,\text{sh}} - \sigma_{t_{0,\text{sh}}}^- < 0$ . Because dissolution timescales below zero are not physical, instead the negative error on  $t_{0,\text{sh}}$  is determined by computing

$$\sigma_{t_{0,\text{sh}}}^- = t_{0,\text{sh}}(\nu_{\text{sh}}, M_{\text{cl}}, x_{\text{corr}}) - t_{0,\text{sh}}(\nu_{\text{sh}} - \sigma_{\nu_{\text{sh}}}^-, M_{\text{cl}} - \sigma_{M_{\text{cl}}}^-, x_{\text{corr}} - \sigma_{x_{\text{corr}}}^-), \quad (5.18)$$

where  $\sigma_i^-$  indicates the negative error in a parameter  $i$ . In the context of Eq. 5.17, this approach is equivalent to assuming the derivative equals the mean slope of  $f(x)$  over the interval  $[x - \sigma_x, x]$ . On two occasions (NGC 6093 and 6712), a strongly asymmetric error in  $t_{0,\text{sh}}$  propagates into  $t_{0,\text{tot}}$  such that  $t_{0,\text{tot}} + \sigma_{t_{0,\text{tot}}}^+ \gg \min(t_{0,\text{evap}} + \sigma_{t_{0,\text{evap}}}^+, t_{0,\text{sh}} + \sigma_{t_{0,\text{sh}}}^+)$ . However, since a very large positive error in  $t_{0,\text{sh}}$  or  $t_{0,\text{evap}}$  would make the term vanish in the inverse addition of Eq. 5.6, it should not propagate into a similarly large error in  $t_{0,\text{tot}}$ . This brings up the second parameter we have to correct for the propagation of large errors through non-linear relations. We define the error in  $t_{0,\text{tot}}$  for NGC 6093 and 6712 such that  $t_{0,\text{tot}} + \sigma_{t_{0,\text{tot}}}^+ = t_{0,\text{evap}} + \sigma_{t_{0,\text{evap}}}^+$ .

The error margins on our predictions in Table 5.4 are determined by numerically evaluating Eq. 5.17 for the desired quantities. Our predictions depend on the observed mass, metallicity and dissolution timescale. The derivatives of  $M/L_V$  with respect to the former two are trivial since  $M/L_V$  is determined by interpolating over these parameters. For the dissolution timescale, we compute additional models at  $t_{0,\text{tot}} - \sigma_{t_{0,\text{tot}}}^-$  to obtain the numerical derivative of  $M/L_V$  with respect to  $t_{0,\text{tot}}$ . In fact, this is the differential rather than the derivative, because for long dissolution timescales  $M/L_V$  can be locally constant, while it varies over a larger range. The only case where a non-linearity forces us to derive alternative errors is for the positive standard error on  $M/L_V$ . Although the uncertainty in metallicity could increase the predicted mass-to-light above its canonical value, the uncertainty in mass and dissolution timescale cannot due to the flattening of the cluster isochrones in the  $\{M, M/L_V\}$ -plane (see Fig. 5.4). Therefore, the combined positive standard error of the mass-to-light ratio due to the uncertainty in mass and dissolution timescale  $\sigma_{M/L_V}^{+,M,t_0}$  is defined as

$$\sigma_{M/L_V}^{+,M,t_0} = \min \left[ \bar{\sigma}_{M/L_V}^{+,M,t_0}, (M/L_V)_{\text{can}} - (M/L_V)_{\text{pred}} \right], \quad (5.19)$$

with  $\bar{\sigma}_{M/L_V}^{+,M,t_0}$  the standard error according to Eq. 5.17,  $(M/L_V)_{\text{can}}$  the canonically expected mass-to-light ratio and  $(M/L_V)_{\text{pred}}$  the predicted value. This definition ensures that the positive standard error is never larger than the difference between the canonical and predicted mass-to-light ratios.

Except for the alternative error in Eq. 5.19 that is specific to  $M/L_V$ , the standard errors on the predicted initial masses are determined analogously to the above. For the remaining lifetimes, numerical derivatives with respect to mass, metallicity and dissolution timescale are simply obtained by reintegrating Eq. 5.1 for slightly different initial conditions.

Finally, for the predicted slopes in Table 5.6, the errors are computed using Eq. 5.17 and restricted such that  $\alpha + \sigma_\alpha \leq \alpha_0$  (analogous to Eq. 5.19).



# Chapter 6

---

## On the interpretation of the globular cluster luminosity function

J. M. Diederik Kruijssen and Simon F. Portegies Zwart  
*Astrophysical Journal*, v. 698, p. L158–L162 (2009)<sup>†</sup>

**Abstract** The conversion of the globular cluster luminosity function (GCLF;  $dN/d \log L$ ) to the globular cluster mass function (GCMF;  $dN/d \log M$ ) is addressed. Dissolving globular clusters (GCs) become preferentially depleted in low-mass stars, which have a high mass-to-light ratio ( $M/L$ ). This has been shown to result in an  $M/L$  that increases with GC luminosity or mass, because more massive GCs have lost a smaller fraction of their stars than low-mass GCs. Using GC models, we study the influence of the luminosity dependency of  $M/L$  on the inferred GCMF. The observed GCLF is consistent with a powerlaw or Schechter type GC initial mass function in combination with a cluster mass-dependent mass loss rate. Below the peak, the logarithmic slope of the GCMF is shallower than that of the GCLF (0.7 versus 1.0), whereas the peak mass is 0.1–0.3 dex lower when accounting for the variability of  $M/L$  than in the case where a constant  $M/L$  is adopted.

### 6.1 Introduction

The present-day globular cluster mass function (GCMF;  $dN/d \log M$ ) is derived from the globular cluster luminosity function (GCLF;  $dN/d \log L$ ) by assuming a constant mass-to-light ratio ( $M/L$ ) for all globular clusters (GCs; e.g. Fall & Zhang 2001, Vesperini et al. 2003, Jordán et al. 2007, McLaughlin & Fall 2008). The resulting GCMF is strongly depleted in low-mass GCs with respect to the mass distribution of young star clusters, which is well described by a power law with index  $-2$  in various environments down to a few  $100 M_{\odot}$ . This has led to a number of pioneering studies explaining its shape by cluster evaporation at a cluster mass-independent mass-loss rate (equivalent to a disruption time  $t_{\text{dis}}^{\text{total}} \propto M$ , e.g. Fall & Zhang 2001, Vesperini 2001) acting on a power law or Schechter (1976) cluster initial

---

<sup>†</sup>Reproduced with permission © AAS.

mass function (CIMF, e.g. Harris & Pudritz 1994, McLaughlin & Pudritz 1996, Elmegreen & Efremov 1997, Burkert & Smith 2000, Gieles et al. 2006a).

Although the observed peaked shape of the GCMF is reproduced in the above studies, the underlying assumptions are not entirely satisfactory because a cluster mass-dependent mass-loss rate (equivalent to  $t_{\text{dis}}^{\text{total}} \propto M^\gamma$  with  $\gamma \sim 0.7$ , see Equation 6.1) is found in theory (e.g. Baumgardt 2001, Baumgardt & Makino 2003, Gieles & Baumgardt 2008) and observations (e.g. Lamers et al. 2005a, Gieles & Bastian 2008, Larsen 2009, Gieles 2009). This arises from the nonlinear scaling of the disruption time with the half-mass relaxation time ( $t_{\text{dis}}^{\text{total}} \propto t_{\text{rh}}^{0.75}$ ), which is caused by the non-zero escape time of stars with velocities above the escape velocity from a tidally limited cluster (Fukushige & Heggie 2000). The physical effect of a lower  $\gamma$  is that the dissolution rate of low-mass clusters is slowed down relative to higher cluster masses and higher  $\gamma$ .

The low-mass slope of a dissolution-dominated mass function like the GCMF is always equal to the exponent  $\gamma$  (Fall & Zhang 2001, Lamers et al. 2005a). A mass-dependent mass-loss rate conflicts with the observations, as it yields a higher number of low-mass GCs compared to cluster mass-independent mass loss ( $\gamma = 1$ ). The disagreement between cluster mass-dependent mass loss and the observed sparse population of low-mass GCs is illustrated in Figure 6.1(a). The slope of the modeled low-mass GCMF is  $\sim 0.7$  for mass-dependent mass loss ( $\gamma = 0.7$ ), whereas for cluster mass-independent mass loss ( $\gamma = 1$ ) the slope is  $\sim 1.0$ , in agreement with the observations. The peak (or ‘turnover’) masses also differ by  $\sim 0.3$  dex. These differences show that a lower mass-loss rate for low-mass GCs ( $\gamma = 0.7$ ) yields a higher number of these relative to massive GCs than in the case of a constant mass-loss rate ( $\gamma = 1$ ).

Recent studies show that the  $M/L$  ratios of GCs are not constant with luminosity or mass (Rejkuba et al. 2007, Kruijssen 2008), contrary to the assumption of a constant  $M/L$  ratio in previous studies. This agrees with an earlier analysis by Mandushev et al. (1991), who determined dynamical masses of Galactic GCs. These studies show that  $M/L$  increases with mass and luminosity because low-mass GCs are more strongly depleted in low-mass stars. This variation of  $M/L$  will affect the conversion of the GCLF to a mass function. Specifically, the smaller  $M/L$  ratios of low-mass GCs imply that the masses of low-mass clusters are overestimated and consequently, that the low-mass end of the GCMF would be shallower than presently expected. The variability of  $M/L$  could therefore strongly affect the interpretation of the GCLF.

We show that the relation between the GCLF and the GCMF is affected by low-mass star depletion, which arises from two-body relaxation (e.g. Meylan & Heggie 1997). In Section 6.2, we discuss the influence of a luminosity-dependent  $M/L$  on the inferred GCMF, and we model the GCLF in Section 6.3, alleviating the observationally expensive need for accurate  $M/L$  ratios to derive the GCMF to allow for a comparison with theory. By including a mass-dependent mass-loss rate and a variable  $M/L$  ratio, our model provides an improvement to the Fall & Zhang (2001) model.

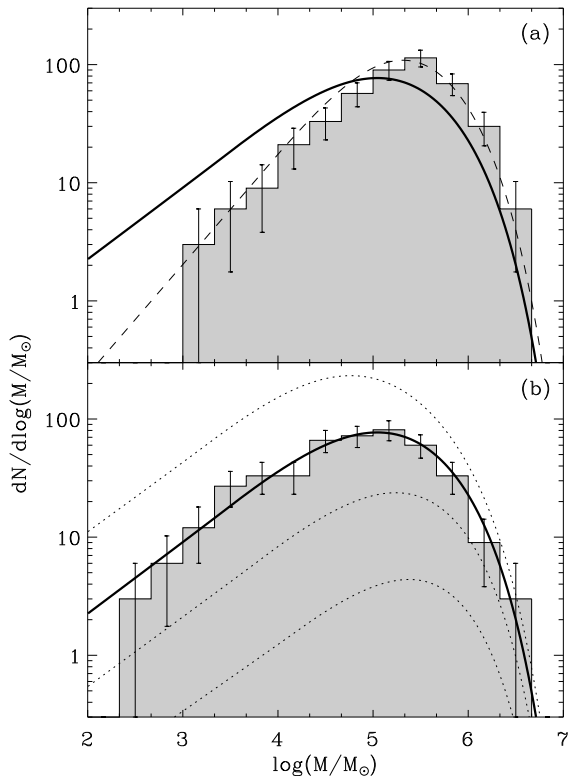


**Figure 6.1:** The inferred GCMF of Galactic GCs (Harris 1996, histogram). Panel (a): GCMF derived using  $M/L_V = 3$  (as in Fall & Zhang 2001). Overplotted is our model MF with a mass-dependent mass-loss rate (solid line, see Section 6.2) adopting a dissolution timescale  $t_0 = 1.3$  Myr. Using  $t_{\text{dis}}^{\text{total}} = t_0 M^\gamma$  (Lamers et al. 2005a), for a  $10^6 M_\odot$  GC and  $\gamma = 0.7$  this corresponds to a disruption time of  $t_{\text{dis}}^{\text{total}} = 21$  Gyr. The dashed line shows the model for a cluster mass-independent mass-loss rate (as in Fall & Zhang 2001). Panel (b): GCMF derived from the GCLF using the luminosity-dependent  $M/L_V$  (see Figure 6.4). The solid curve is the same as above while the dotted curves represent models for (from bottom to top)  $\log(t_0/\text{Myr}) = \log 1.3 + \{-0.5, -0.25, 0.25\}$ , corresponding to  $t_{\text{dis}}^{\text{total}} = 7\text{--}37$  Gyr. Error bars are  $1\sigma$  Poissonian.

## 6.2 Implications of a luminosity-dependent $M/L$

We model the evolution of star clusters in order to quantify the influence of the luminosity dependence of  $M/L$  on the relation between the GCLF and the GCMF. Our model, called SPACE (Kruijssen & Lamers 2008), includes mass loss by stellar evolution and by evaporation. The mass loss by evaporation is parameterized with the simple relation (Lamers et al.

2005a):

$$\left(\frac{dM}{dt}\right)_{\text{dis}} = -\frac{M}{t_{\text{dis}}} = -\frac{M^{1-\gamma}}{t_0}. \quad (6.1)$$

Here,  $\gamma = 0.7$  for clusters with a King parameter typical to GCs of  $W_0 = 7$  (Lamers et al. 2010) and  $t_0$  is the dissolution timescale which depends on the environment. We illustrate the effect of a variable  $M/L$  ratio by adopting a unique value for  $t_0$ , which we assume to be the same for all clusters (a realistic spread in  $t_0$  is considered in Section 6.3). We subsequently convert the observed LF of the sample of GCs to a MF by adopting the corresponding relation between  $L_V$  and  $M/L_V$  that is computed with SPACE (see Figure 6.4). In Figure 6.1(b), we show the resulting MF for the 146 GCs from the Harris (1996) catalog<sup>1</sup>. Overplotted are the model MFs with different values for  $t_0$ , adopting a metallicity  $Z = 0.0004$ , a Kroupa (2001) stellar IMF, and a Schechter CIMF with power-law index  $-2$  and exponential truncation mass  $M_* = 2.5 \times 10^6 M_\odot$ . As expected from Equation 6.1, the slope of the MF is independent of the dissolution timescale.

By comparing panels (a) and (b) in Figure 6.1, we see that the luminosity dependency of  $M/L$  gives rise to two effects: (1) the slope at the low-mass end of the inferred GCMF drops to  $\sim 0.7$ , which is the expected value for models with cluster a mass-dependent cluster mass-loss rate (Lamers et al. 2005a) and (2) the peak in the MF (the so-called turnover mass) shifts to a lower mass with  $\sim 0.3$  dex. About half this shift is due to the already high value of  $M/L = 3$  adopted by Fall & Zhang (2001). The slope of the GCMF at the low-mass end is different from the slope of the GCLF, and therefore also different from the GCMF slope ( $\sim 1$ ) that would be inferred from the GCLF when using a constant  $M/L$  ratio.

## 6.3 Models of the Galactic GC system

In our above analysis, we have assumed a single dissolution timescale for the entire GC system. In reality, there is a range of timescales on which the GCs dissolve. We now consider a more detailed Monte Carlo model of the Galactic GC system in which the dependency of the dynamical evolution of GCs on their orbits is included. Our aim is to directly model the GCLF, rather than to obtain it by converting the GCMF.

The initial positions of the GCs with respect to the Milky Way are taken from the power-law-like density profile (see, e.g. Fall & Zhang 2001, Equation 26) that arises from the isothermal sphere, with an outward increase of the velocity anisotropy (Eddington 1915). Our choice of parameters for the kinematic model are (1) an initial anisotropy radius  $R_A = 1$  kpc, (2) a circular velocity of the gravitational potential  $V_c = 220 \text{ km s}^{-1}$ , and (3)  $(V_c/v)^2 = 3.5$ , which determines the slope of the density profile (Fall & Zhang 2001), with  $v$  denoting the radial velocity dispersion. The initial velocities of the GCs are assigned according to the corresponding velocity ellipsoid (Aguilar et al. 1988, Equation 4), including a systemic rotation of  $V_{\text{rot}} = 60 \text{ km s}^{-1}$ . We do not claim that this is the correct kinematic model for the Milky Way, but we consider it an appropriate ansatz. The resulting dissolution timescales agree with the

<sup>1</sup>We adopt the 2003 edition of the data, which is available online at <http://www.physics.mcmaster.ca/~harris/mwgc.dat>

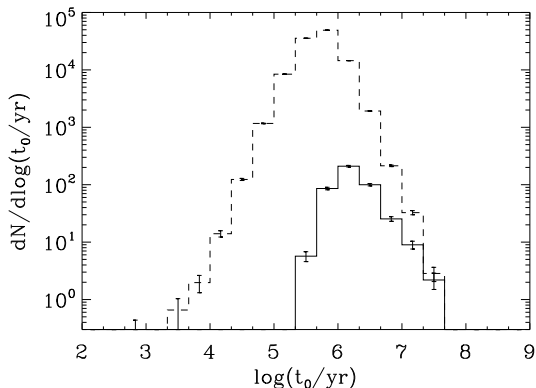


**Figure 6.2:** Histograms of the initial (dashed) and present-day (solid) distributions of dissolution timescales  $t_{0,tot}$ .

range that is expected from observations. For less anisotropy, the mean dissolution timescale of surviving clusters would be longer. The initial cluster masses are drawn from a Schechter (1976) function with index  $-2$  and exponential truncation mass  $M_* = 3 \times 10^6 M_\odot$  (also see Jordán et al. 2007, Harris et al. 2009)<sup>2</sup>. We sample the metallicities from their observed distribution in the Harris (1996) catalog.

The GC orbits are integrated in the Galactic potential from Johnston et al. (1995), consisting of a bulge, disc, and halo. We adopt a fourth-order Runge–Kutta integration scheme with a variable time step, in which the angular momentum and energy are conserved within  $10^{-5}$  during each time step. To compute the evolution of a GC with a given initial mass and metallicity, we derive its instantaneous dissolution timescale from the orbital parameters. Tidal evaporation due to two-body relaxation and disc shocks are the main dissolution mechanisms (Chernoff et al. 1986). Following Baumgardt & Makino (2003) for the dissolution timescale due to two-body relaxation we write

$$t_{0,\text{evap}} = 10.7 \text{ Myr} \left( \frac{R_a}{8.5 \text{ kpc}} \right) \left( \frac{V_{c,a}}{220 \text{ km s}^{-1}} \right)^{-1} (1 - e), \quad (6.2)$$

where  $R_a$  is the apogalactic radius of the cluster orbit,  $V_{c,a}$  is the circular velocity of the gravitational potential at  $R_a$ , and  $e$  is the orbital eccentricity. The dissolution timescale due to disc shocks is expressed as (Gnedin & Ostriker 1997, Kruijssen et al., in preparation)

$$t_{0,\text{disc}} = 7.35 \text{ Myr} \left( \frac{V_{z,5}}{g_{m,-10}} \right)^2 P_2 A_w^{-1}(x), \quad (6.3)$$

<sup>2</sup>This number is slightly larger than in Section 6.2, because the spread in dissolution timescales implies that surviving massive GCs on average have a smaller dissolution timescale than surviving low-mass GCs. We correct for the resulting deficiency of massive GCs by increasing  $M_*$ .

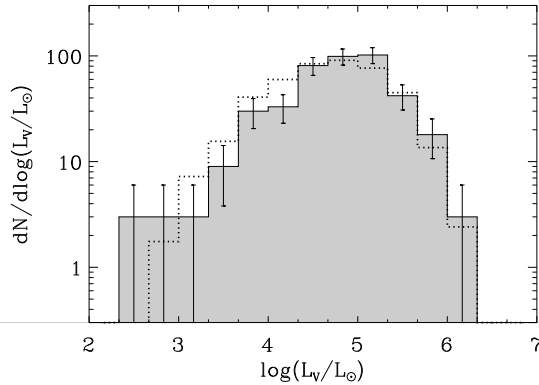


**Figure 6.3:** Histograms of the observed (filled) and modeled (dotted) GCLFs.

where  $V_{z,5}$  is the velocity in the  $z$ -direction during disc crossing at  $z = 0$  in units of  $10^5 \text{ m s}^{-1}$ ,  $P_2$  is the (radial) orbital period in units of  $10^2 \text{ Myr}$ ,  $g_{m,-10}$  is the orbital maximum of the acceleration due to the disc  $-\partial\Phi_{\text{disc}}/\partial z$  in units of  $10^{-10} \text{ m s}^{-2}$ , and  $A_w(x)$  is the Weinberg (1994a,b,c) adiabatic correction<sup>3</sup> (see also Gnedin & Ostriker 1997). For mathematical simplicity, we assume a very weak mass–radius relation<sup>4</sup> of  $r_h \propto M^{0.1}$  (Larsen 2004) in the derivation of Equation 6.3.

Over a timespan of 12 Gyr, the dissolution timescales due to tidal evaporation and disc shocks are computed for every orbital revolution, measured between subsequent passages of the apogalacticon. The dissolution timescale that describes the mass-loss rate (see Equation 6.1) due to both effects is determined by adding the averaged inverses of both timescales

$$\frac{1}{t_{0,\text{tot}}} = \frac{1}{t_{0,\text{evap}}} + \frac{1}{t_{0,\text{disc}}}. \quad (6.4)$$

The resulting initial and present-day distributions of  $t_{0,\text{tot}}$  are shown in Figure 6.2. GCs with short dissolution timescales are easily destroyed, leading to the depletion of the quickly dissolving end of the distribution (at low values of  $t_0$ ). The surviving GCs have dissolution timescales that are in excellent agreement with other studies (Kruijssen 2008, Kruijssen & Mieske 2009). Although their mean galactocentric radius is a factor 2 smaller than that of the observed Galactic GC system, the slopes of both density profiles are comparable.

The evolution of GC mass and photometry is computed with SPACE, using the setup discussed in Section 6.2. In total 507,079 GCs are generated with initial masses  $M \geq 5 \times 10^3 M_\odot$ , of which 2,000 survive until  $t = 12 \text{ Gyr}$ . The present-day mass and luminosity functions are scaled to match the observed numbers, of which the scale factor can be used to

<sup>3</sup>The parameter  $x$  implicitly depends on the GC mass (e.g. Gnedin & Ostriker 1997). We adopt 0.6 times the initial GC mass, in agreement with the average mass loss per Hubble time from Kruijssen & Mieske (2009).

<sup>4</sup>Compared to adopting a constant GC radius, this assumption effects a  $\sim 0.45$  dex scatter of  $t_{0,\text{disc}}$ . Because  $\log(t_{0,\text{disc}}/t_{0,\text{tot}}) > 0.75$  for all surviving GCs, this does not affect our results.

derive properties of the initial Galactic GC system (see below). The computed  $V$ -band GCLF is compared to the observed distribution in Figure 6.3. The distributions are in satisfactory agreement, with a KS-test  $p$ -value of 0.02. At low luminosities, there is a slight discrepancy, which could be caused by incompleteness due to obscuration by the Galactic bulge (Gieles et al., in preparation).

The  $M/L_V$  ratios of our modeled GCs are compared to observations from McLaughlin & van der Marel (2005) in Figure 6.4. If low-mass star depletion is neglected (panel (a)), the  $M/L_V$  ratios of the models are completely set by their metallicities and they agree poorly with the observations. When including low-mass star depletion (panel (b)), the modeled  $M/L_V$  ratios are affected by dynamical evolution and are in good agreement with the observations. The same approach can be used to explain the observations of Cen A, M31 and the LMC compiled by Rejkuba et al. (2007), which gives results that are consistent with our analysis in Figure 6.4.

The McLaughlin & van der Marel (2005) sample is not representative of the entire Galactic GC population, as it lacks GCs that are much fainter than the turnover and represents central rather than global  $M/L_V$  ratios for certain GCs, only allowing for a first-order comparison (for a discussion, see Kruijssen & Mieske 2009). The observed slopes of the low-mass stellar mass functions of 20 GCs from De Marchi et al. (2007) provide an independent check. Their compilation exhibits a clear trend of mass function slope with GC luminosity. Splitting their sample at about the turnover luminosity ( $\log(L_V/L_\odot) = 5.1$ ), for a mass function  $n \propto m^{-\alpha}$  the mean slopes in the stellar mass range  $m = 0.3\text{--}0.8 M_\odot$  are  $\alpha_{\text{bright}} = 1.42 \pm 0.10$  and  $\alpha_{\text{faint}} = 0.56 \pm 0.07$  for the bright and faint GCs, respectively. Faint GCs are indeed more depleted in low-mass stars than bright GCs, substantiating our model results.

The initial properties of the Galactic GC system are obtained by scaling the present-day number of modeled GCs to the observed number and applying the same scale factor to the CIMF. In Figure 6.5, we show the CIMF, the modeled GCMF, the GCMF that would be obtained from Figure 6.3 if a constant  $M/L$  ratio were adopted, and the initial mass distribution of the surviving GCs. The modeled GCMF for a single dissolution timescale from Figure 6.1(b) is overplotted for comparison, illustrating its acceptable agreement with our detailed model. The disagreement for GC masses  $< 10^3 M_\odot$  is due to the use of logarithmic time steps in our models, causing some GCs to lose their last few  $100 M_\odot$  within a single time step at large ages. For a lower mass limit of the CIMF of  $5 \times 10^3 (10^2) M_\odot$ , we find a surviving GC number fraction of  $3.9 (0.1) \times 10^{-3}$ , with an initial total mass of about  $1.1 (1.8) \times 10^9 M_\odot$  and a present-day mass of  $2.8 \times 10^7 M_\odot$ . If the stellar halo ( $\sim 10^9 M_\odot$ ; Bell et al. 2008) is constituted by disrupted GCs and coeval stars (in spite of chemical analyses; e.g. Gratton et al. 2000), our comparable initial total GC mass implies that either nearly all star formation occurred in clusters at the epoch of GC formation, or that most of these stars now constitute the Galactic bulge.

## 6.4 Discussion

We have shown that the interpretation of the GCLF as a one-to-one representation of the GCMF is incorrect. This follows from the  $M/L$  ratio decrease due to the low-mass star

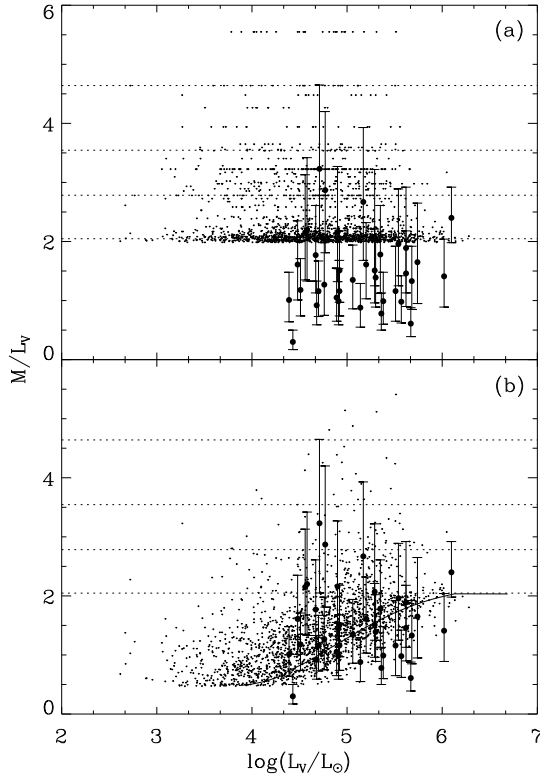


**Figure 6.4:** Comparison of observed  $M/L_V$  ratios of Galactic GCs (thick dots; McLaughlin & van der Marel 2005) with our modeled  $M/L_V$  ratios (thin dots). Error bars are  $1\sigma$ . Dotted horizontal lines denote the constant  $M/L_V$  ratios that are expected if low-mass star depletion is neglected (from bottom to top  $Z = \{0.0004, 0.004, 0.008, 0.02\}$ ). Panel (a): thin dots represent modeled  $M/L_V$  ratios without low-mass star depletion. Panel (b): thin dots denote modeled  $M/L_V$  ratios including low-mass star depletion. The solid line represents the relation between  $M/L_V$  and  $L_V$  that was adopted in the simple model of Figure 6.1(b).

depletion that arises from two-body relaxation. There is no equivalence of the luminosity function and the mass function as both have intrinsically different low-mass slopes ( $\sim 1$  and  $\sim 0.7$ , respectively). In addition, the turnover mass is overestimated by 0.1—0.3 dex if a one-to-one conversion from GCLF to GCMF is applied, depending on the adopted  $M/L$  ratio. We have shown that the present-day GCLF and GCMF arise from a cluster mass-dependent mass-loss rate ( $t_{\text{dis}}^{\text{total}} \propto M^{0.7}$  and  $t_{\text{dis}}^{\text{total}} \propto t_{\text{th}}^{0.75}$ ), starting from a Schechter-type CIMF. Therefore, neither is consistent with a cluster mass-independent mass-loss rate (e.g. Fall & Zhang 2001). The GCMF that is computed using a spread in dissolution timescale  $t_0$  only marginally differs from that for a single, mean value of  $t_0$ .



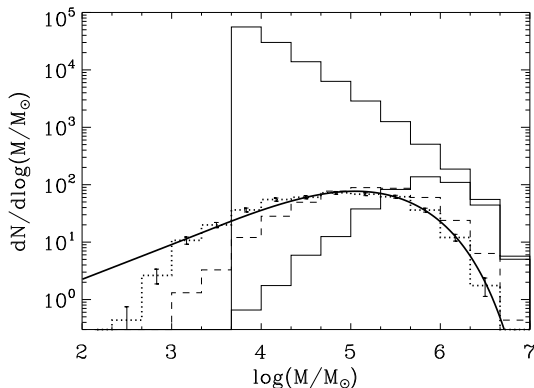


**Figure 6.5:** Histograms of the mass distributions of the modeled GCs. Represented are the CIMF (upper solid) and the present-day GCMF (dotted, with  $1\sigma$  Poissonian error bars). The GCMF for a single dissolution timescale (Figure 6.1(b)) is represented by the continuous solid curve. The dashed line gives the GCMF that would be obtained from Figure 6.3 if a constant  $M/L$  ratio were adopted. The initial mass distribution of the surviving GCs is given by the lower solid line.

The low-mass slope of a dissolution-dominated mass function like the GCMF is equal to  $\gamma$  (see Equation 6.1), independent of the CIMF (Fall & Zhang 2001, Lamers et al. 2005a). For cluster mass-dependent mass loss ( $\gamma = 0.7$ ), the GCMF that is inferred from the GCLF is accurately matched by the models (see Figure 6.1(b)). To verify whether this perhaps holds for all values of  $\gamma$ , we have also considered cluster mass-independent mass loss ( $\gamma = 1$ ; Fall & Zhang 2001) and found that the luminosity dependency of  $M/L$  (see Figure 6.4) is steepened compared to cluster mass-dependent mass loss. The conversion of the observed GCLF to a GCMF then gives an inferred GCMF slope that is even lower ( $\sim 0.6$ ), in bad agreement with the expected ( $\sim 1$ ) value. We conclude that the match between the models and the observations only exists for values of  $\gamma \approx 0.7$ . Of course, the precise description of mass loss does not affect the fundamental principle of low-mass star depletion due to two-body relaxation. The luminosity dependence of  $M/L$  flattens the inferred low-mass GCMF in any scenario.

We have not yet considered the radial variation of the turnover luminosity  $L_{TO}$ , which has been shown to be independent of galactocentric radius in M87 (Vesperini et al. 2003). Our prescription for dynamical evolution in Section 6.3 yields a higher turnover luminosity near the galactic center than at large distances. However, our method is aimed at investigating the influence of a representative spread in dissolution timescales on our results, rather than making an exact model of the Galactic GC system. It should be emphasized that the difference between the GCLF and the GCMF persists, even though it remains to be explained why  $L_{TO}$  appears to be constant. It could be that the outer GCs dissolve more rapidly than expected. Potential explanations could be that GCs on wide orbits originate from accreted dwarf galaxies (Prieto & Gnedin 2008), or a dissolution mechanism that has not yet been

included (see also Kruijssen & Mieske 2009), like the dynamical implications of white dwarf kicks (Fregeau et al. 2009), stellar evolution (Vesperini & Zepf 2003, Vesperini et al. 2009), or gas expulsion (Baumgardt & Kroupa 2007).

The results of this chapter do not only apply to the Milky Way, but also to other galaxies. We see that the properties of the inferred GCMF are affected by the mass and luminosity dependence of  $M/L$  that ensues from low-mass star depletion. It is advised for observational and theoretical studies to be cautious when comparing GCLFs and GCMFs. At present an observed GCMF cannot be accurately obtained, because for most observed GCs only photometric masses are determined (for which by definition a constant  $M/L$  ratio is assumed) instead of dynamical masses. Considering the intrinsically different shapes of the GCLF and GCMF, the presently most feasible way of comparing theory and observations would be if models of GC systems are aimed at explaining the GCLF rather than the mass distribution.

**Acknowledgements** We thank the anonymous referee for constructive comments that improved the manuscript. We acknowledge Dana Casetti-Dinescu, Mike Fall and Dean McLaughlin for stimulating discussions, and Mark Gieles for comments on the manuscript. JMDK is grateful to Sophie Goldhagen and Henny Lamers for support, advice and comments on the manuscript. The Kavli Institute for Theoretical Physics in Santa Barbara is acknowledged for their hospitality and hosting an excellent globular cluster workshop and conference. This research is supported by the Netherlands Advanced School for Astronomy (NOVA), the Leids Kerkhoven-Bosscha Fonds and the Netherlands Organisation for Scientific Research (NWO), grant numbers 021.001.038 and 643.200.503.

# Chapter 7

---

## The evolution of the stellar mass function in star clusters\*

J. M. Diederik Kruijssen

*Astronomy & Astrophysics*, v. 507, p. 1409–1423 (2009)<sup>†</sup>

**Abstract** The dynamical escape of stars from star clusters affects the shape of the stellar mass function (MF) in these clusters, because the escape probability of a star depends on its mass. This is found in  $N$ -body simulations and has been approximated in analytical cluster models by fitting the evolution of the MF. Both approaches are naturally restricted to the set of boundary conditions for which the simulations were performed. The objective of this chapter is to provide and to apply a simple physical model for the evolution of the MF in star clusters for a large range of the parameter space. It should also offer a new perspective on the results from  $N$ -body simulations. A simple, physically self-contained model for the evolution of the stellar MF in star clusters is derived from the basic principles of two-body encounters and energy considerations. It is independent of the adopted mass loss rate or initial mass function (IMF), and contains stellar evolution, stellar remnant retention, dynamical dissolution in a tidal field, and mass segregation. The MF evolution in star clusters depends on the disruption time, remnant retention fraction, initial-final stellar mass relation, and IMF. Low-mass stars are preferentially ejected after  $t \sim 400$  Myr. Before that time, masses around 15–20% of the maximum stellar mass are lost due to their rapid two-body relaxation with the massive stars that still exist at young ages. The degree of low-mass star depletion grows for increasing disruption times, but can be quenched when the retained fraction of massive remnants is large. The highly depleted MFs of certain Galactic globular clusters are explained by the enhanced low-mass star depletion that occurs for low remnant retention fractions. Unless the retention fraction is exceptionally large, dynamical evolution always decreases the mass-to-light ratio. The retention of black holes reduces the fraction of the cluster mass in remnants because white dwarfs and neutron stars have masses that are efficiently ejected by black holes. The modeled evolution of the MF is consistent with  $N$ -body simulations when adopting identical boundary conditions. However, it is found that the results from  $N$ -body simulations only hold for their specific

---

\*The models presented in this chapter are publicly available in electronic form at the CDS via anonymous ftp to <http://cdsweb.u-strasbg.fr/> (130.79.128.5) or via <http://cdsweb.u-strasbg.fr/cgi-bin/qcat?J/A+A/>.

<sup>†</sup>Reproduced with permission © ESO.

boundary conditions and should not be generalised to all clusters. It is concluded that the model provides an efficient method to understand the evolution of the stellar MF in star clusters under widely varying conditions.

## 7.1 Introduction

The evaporation of star clusters is known to change the shape of the underlying stellar mass function<sup>1</sup> (Hénon 1969, Chernoff & Weinberg 1990, Vesperini & Heggie 1997, Takahashi & Portegies Zwart 2000, Portegies Zwart et al. 2001, Baumgardt & Makino 2003). This phenomenon has been used to explain the observed MFs in globular clusters (Richer et al. 1991, De Marchi et al. 2007, De Marchi & Pulone 2007), which are flatter than typical initial mass functions (IMFs, e.g. Salpeter 1955, Kroupa 2001). In addition, the effect of a changing MF on cluster photometry has been investigated (Lamers et al. 2006, Kruijssen & Lamers 2008, Anders et al. 2009). This has been shown to explain the low mass-to-light ratios of globular clusters (Kruijssen 2008, Kruijssen & Mieske 2009) and to have a pronounced effect on the inferred globular cluster mass function (Kruijssen & Portegies Zwart 2009).

The existing parameterised cluster models that incorporate a description of low-mass star depletion are restricted by the physically self-contained models on which they are based. Some studies (Lamers et al. 2006, Kruijssen & Lamers 2008) assume an increasing lower stellar mass limit to account for the evolving MF, others (Anders et al. 2009) fit a changing MF slope to  $N$ -body simulations. In both cases, the models are accurate for a certain range of boundary conditions, but they do not include a physical model and are therefore lacking flexibility. While  $N$ -body simulations do include the appropriate physics, they are very time-consuming. As a result, only a limited number of clusters can be simulated and the applicability of the simulations is thus restricted to the specific set of boundary conditions for which they have been run.

It would be desirable to obtain a simple physical model for the evolution of the MF, which would have a short runtime and could be used independently of  $N$ -body simulations. Forty years ago, a pioneering first approach to such a model was made by Hénon (1969), who considered the stellar mass-dependent escape rate of stars from star clusters. However, the applicability of his model was limited due to a number of assumptions that influenced the results. First of all, Hénon (1969) assumed that the clusters exist in isolation and neglected the tidal field. As a consequence, the escape of a star could only occur by a single, close encounter and the repeated effect of two-body relaxation was not included. Secondly, the distribution of stars was independent of stellar mass, i.e. mass segregation was not included. Both mass segregation and the influence of a tidal field are observed in real clusters, and can be expected to affect the evolution of the MF.

The aim of this chapter is to derive a physical description of the evolution of the stellar MF in star clusters, alleviating the assumptions that were made by Hénon (1969). This should explain the results found in  $N$ -body simulations and observations, while providing the required flexibility to explore the properties of star clusters with simple, physically self-contained models. The outline of this chapter is as follows. In Sect. 7.2, total mass evolution

---

<sup>1</sup>Hereafter, ‘mass function’ is referred to as ‘MF’.

of star clusters is discussed. A recipe for the evolution of the MF is derived in Sect. 7.3, covering stellar evolution, the retain of stellar remnants, dynamical dissolution and mass segregation. The model is compared to  $N$ -body simulations in Sect. 7.4. In Sect. 7.5, the model is applied to assess the evolution of the MF for different disruption times and remnant retention fractions. The consequences for other cluster properties are also considered. This chapter is concluded with a discussion of the results and their implications.

## 7.2 The mass evolution of star clusters

The mass of star clusters decreases due to stellar evolution and dynamical dissolution. This is expressed mathematically as

$$\frac{dM}{dt} = \left( \frac{dM}{dt} \right)_{\text{ev}} + \left( \frac{dM}{dt} \right)_{\text{dis}}, \quad (7.1)$$

with  $M$  the cluster mass, and the subscripts ‘ev’ and ‘dis’ denoting stellar evolution and dynamical dissolution. The contribution of stellar evolution to the mass loss is derived from the decrease of the maximum stellar mass with time and depends on the adopted stellar evolution model.

The dynamical evaporation of star clusters is increasingly well understood. Over the past years it has become clear that clusters lose mass on a disruption timescale  $t_{\text{dis}}$  that is proportional to a combination of the half-mass relaxation time  $t_{\text{th}}$  and the crossing time  $t_{\text{cr}}$  as  $t_{\text{dis}} \propto t_{\text{th}}^x t_{\text{cr}}^{1-x}$  (e.g. Baumgardt 2001, Baumgardt & Makino 2003, Gieles & Baumgardt 2008). It is found that  $x = 0.75$ – $0.80$ , depending on the concentration ( $c = \log(r_t/r_c)$ ) or King parameter ( $W_0$ ) of the cluster (Baumgardt & Makino 2003). This proportionality leads to a disruption timescale that scales with the present day mass as (Lamers et al. 2005a):

$$t_{\text{dis}} = t_0 M^\gamma, \quad (7.2)$$

with  $M$  the cluster mass,  $t_0$  the dissolution timescale parameter which sets the rapidity of dissolution and depends on the cluster environment, and  $\gamma$  a constant related to  $x$ . Lamers et al. (2009, in prep.) find  $\gamma = 0.62$  for  $W_0 = 5$  and  $\gamma = 0.70$  for  $W_0 = 7$ . This timescale implies a mass loss rate due to dissolution that can be described with the simple relation

$$\left( \frac{dM}{dt} \right)_{\text{dis}} = -\frac{M}{t_{\text{dis}}} = -\frac{M^{1-\gamma}}{t_0}, \quad (7.3)$$

which can be integrated for the mass evolution of the cluster due to dynamical dissolution.

The above formulation of the cluster mass evolution was extended to include stellar remnants, photometric cluster evolution, and a simple description of the MF in the SPACE cluster models (Kruijssen & Lamers 2008). Stellar remnants were accounted for by assuming initial-final mass relations (similar to Sect. 7.3.1 of the present work), while the photometric evolution was computed by integrating stellar isochrones from the Padova group (Bertelli et al. 1994, Girardi et al. 2000). The description of low-mass star depletion followed the simple

model from Lamers et al. (2006) in which the minimum stellar mass of the MF increases with time.

The present study provides a new description of the evolution of the MF which is based on fundamental principles, and does not depend on the above prescription for the total mass evolution. In addition, the latest Padova models (Marigo et al. 2008) are incorporated to calculate the photometric cluster evolution. These improvements update the SPACE cluster models.

## 7.3 The evolution of the stellar mass function

To describe the evolution of the MF, the effects of stellar evolution, stellar remnant production, and dynamical dissolution need to be included. While the focus of this chapter lies with the effects of dissolution, a proper treatment of stellar evolution is essential. This is described first, before presenting a model for cluster dissolution.<sup>2</sup>

### 7.3.1 Stellar evolution

The influence of stellar evolution on the MF is twofold. First of all, the maximum stellar mass decreases, because at any time during cluster evolution the most massive stars reach the end of their lives. Secondly, the stellar remnants that are created upon the death of these massive stars constitute a part of the MF that can only be lost from the cluster by dynamical mechanisms.

The maximum stellar mass in the cluster as a function of its age is taken from the Padova 2008 isochrones (Marigo et al. 2008) for metallicities in the range  $Z = 0.0001$ – $0.03$ . The stellar remnant masses  $m_{\text{sr}}$  are computed from their progenitor stellar mass  $m$  using initial-final mass relations. Following Kruijssen & Lamers (2008), for white dwarfs ( $m < 8 M_{\odot}$ ) the relation from Kalirai et al. (2008) is adopted:

$$m_{\text{wd}} = 0.109m + 0.394 M_{\odot}, \quad (7.4)$$

which holds for all ages that are covered by the Padova isochrones. For neutron stars ( $8 M_{\odot} \leq m < 30 M_{\odot}$ ) the relation from Nomoto et al. (1988) is used:

$$m_{\text{ns}} = 0.03636(m - 8 M_{\odot}) + 1.02 M_{\odot}, \quad (7.5)$$

while for black holes ( $m \geq 30 M_{\odot}$ ) a simple relation is assumed that is in acceptable agreement with theoretically predicted masses of stellar mass black holes (Fryer & Kalogera 2001):

$$m_{\text{bh}} = 0.06(m - 30 M_{\odot}) + 8.3 M_{\odot}. \quad (7.6)$$

With these relations, the remnant MF is computed from conservation of numbers as

$$N_{\text{sr}}(m_{\text{sr}}) = f_{\text{ret,sr}}(M)N(m(m_{\text{sr}}))\frac{dm}{dm_{\text{sr}}}, \quad (7.7)$$

---

<sup>2</sup>The model presented in this chapter is independent of the mass loss rate and of the form of the IMF  $N_i(m)$ , but for explanatory purposes a Kroupa (2001) IMF is adopted later on.

with  $\text{sr} = \{\text{wd}, \text{ns}, \text{bh}\}$  denoting the appropriate remnant type,  $N_{\text{sr}}(m_{\text{sr}})$  representing its MF,  $f_{\text{ret},\text{sr}}(M)$  denoting the cluster mass-dependent fraction of these remnants that is retained after applying kick velocities, and  $N(m(m_{\text{sr}}))$  representing the progenitor MF.

For a given velocity dispersion of remnants, the retention fraction of each remnant type depends on the local escape velocity  $v_{\text{esc}}$ , which is related to the potential  $\psi$  as  $v_{\text{esc}} = \sqrt{2\psi}$ . Stellar remnants are predominantly produced in the cluster centre in the case of mass segregation, which is reached most rapidly for massive stars (see Sect. 7.3.2). For a Plummer (1911, also see Eq. 7.9) potential this implies that upon remnant production  $v_{\text{esc}} = \sqrt{2GM/r_0}$ , with  $G$  the gravitational constant and  $r_0$  the Plummer radius. Adopting a Maxwellian distribution of velocities that is truncated at  $v_{\text{esc}}$ , it is straightforward to show that

$$f_{\text{ret},\text{sr}}(x) = A \left[ \text{erf} \left( \frac{x}{\sqrt{2}} \right) - \sqrt{\frac{2}{\pi}} x e^{-x^2/2} \right], \quad (7.8)$$

where  $A$  is a normalisation constant to account for the truncation of the velocity distribution and  $x^2 \equiv 2GM/r_0\sigma_{\text{sr}}^2$ , with  $\sigma_{\text{sr}}^2 = \sigma_0^2 + \sigma_{\text{kick},\text{sr}}^2$  denoting the total velocity dispersion of the produced remnant type, which arises from the central velocity dispersion in the cluster  $\sigma_0^2 = GM/3r_0$  (e.g. Heggie & Hut 2003) and the velocity dispersion of the exerted kick  $\sigma_{\text{kick}}$ . The normalisation constant then follows as  $A^{-1} = \text{erf}\sqrt{3} - 2\sqrt{3/\pi} \exp(-3)$ .

Typical values of the kick velocity dispersion  $\sigma_{\text{kick},\text{sr}}$  are given in literature. White dwarf kicks have recently been proposed to be of order  $\sigma_{\text{kick},\text{wd}} = 4 \text{ km s}^{-1}$  (Davis et al. 2008, Fregeau et al. 2009). For neutron stars  $\sigma_{\text{kick},\text{ns}} = 100 \text{ km s}^{-1}$  is adopted, which is a somewhat conservative estimate with respect to theory, but it agrees reasonably well with observed neutron star numbers in globular clusters and represents a compromise between single star and binary channels (for estimates of the retention fraction and discussions of the ‘neutron star retention problem’ see Lyne & Lorimer 1994, Drukier 1996, Arzoumanian et al. 2002, Pfahl et al. 2002). Gravitational wave recoils are thought to exert black hole kicks of order  $\sigma_{\text{kick},\text{bh}} = 80 \text{ km s}^{-1}$  (Moody & Sigurdsson 2009). This value depends on metallicity, but for simplicity I assume a single, typical value here.

The retention fractions following from Eq. 7.8 are shown as a function of cluster mass per unit Plummer radius in Fig. 7.1. This quantity best reflects the retention fraction because  $x^2 \propto M/r_0$  in Eq. 7.8. Open clusters (with initial masses  $M_i$  such that typically  $M_i/r_0 < 3 \times 10^4 M_{\odot} \text{ pc}^{-1}$ , Larsen 2004) do not retain any neutron stars or black holes, while globular clusters ( $M_i/r_0 \sim 3 \times 10^4 - 3 \times 10^5 M_{\odot} \text{ pc}^{-1}$ , Harris 1996) retain 0.1–4% of the neutron stars and 0.3–7% of the black holes. These values are in excellent agreement with other studies (e.g. Pfahl et al. 2002, Moody & Sigurdsson 2009), but are still lower than the large observed number of neutron stars in a number of globular clusters (the aforementioned ‘retention problem’).

### 7.3.2 Dissolution and the evolution of the mass function

Dissolution alters the shape of the stellar MF in star clusters due to the effects of two-body relaxation and energy equipartition. In a pioneering paper, Hénon (1969) derived the escape rate of stars of different masses from an isolated cluster. The cluster was represented by a

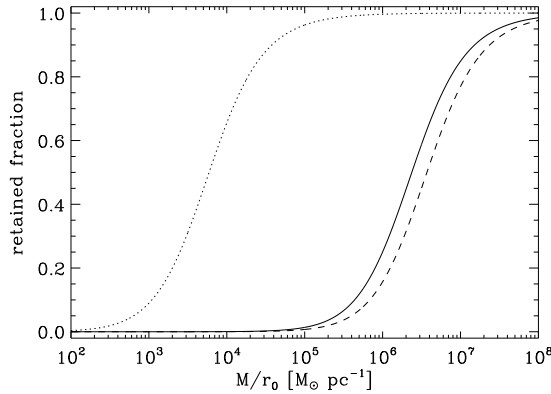


**Figure 7.1:** Retention fraction of stellar remnants as a function of cluster mass per unit Plummer radius  $M/r_0$ , for black holes (solid), neutron stars (dashed) and white dwarfs (dotted).

Plummer (1911) gravitational potential:

$$\psi(r) = \psi_0 \left( 1 + \frac{r^2}{r_0^2} \right)^{-1/2}, \quad (7.9)$$

where  $r_0$  denotes the Plummer radius setting the concentration of the cluster and  $\psi_0 \equiv GM/r_0$  represents the central potential, with  $G$  the gravitational constant and  $M$  the cluster mass. It was argued by Hénon (1960) that the only way for stars to escape such an isolated cluster is by a single, close encounter. The corresponding stellar mass-dependent escape rate was found to be (Hénon 1969):

$$\frac{dN(m)}{dt} = -\frac{|E|^{3/2}N(m)}{GM^{9/2}} \int_0^\infty N(m')F\left(\frac{m}{m'}\right) m'^2 dm', \quad (7.10)$$

with  $N(m)$  the MF,  $m$  the stellar mass,  $E$  the total energy of the cluster, and  $F(\mu)$  a function related to the escape probability for a star of mass  $m$  in a close encounter with a star of mass  $m'$  and a corresponding mass ratio  $\mu \equiv m/m'$ . The expression in Eq. 7.10 is independent of the adopted IMF. The function  $F$  will be referred to as the ‘Hénon function’ and is shown in Fig. 7.2. The original expression consists of several integrals that have to be solved numerically. In Hénon (1969), a table is given for the Hénon function, but it can also be fitted by:

$$F(\mu) = (0.32 + 0.55\mu^{0.35} + 13.26\mu^{2.5})^{-1}. \quad (7.11)$$

This approaches the power law  $F(\mu) = 0.075398\mu^{-5/2}$  for  $\mu > 1$ , as was derived explicitly by Hénon (1969).

The total mass loss rate corresponding to Eq. 7.10 conflicts with  $N$ -body simulations (as was already noted by Wielen 1971) because only ejections by single, close encounters are



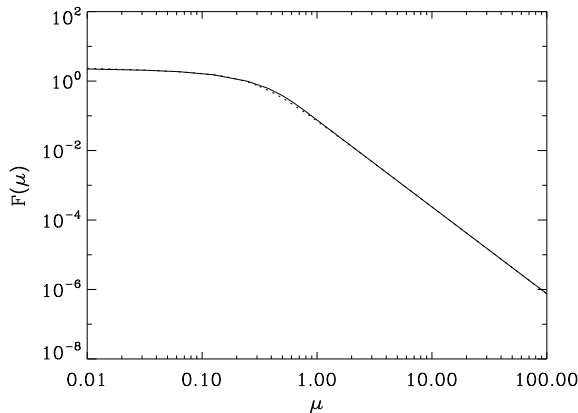


**Figure 7.2:** Hénon function  $F(\mu)$ , which is a measure for the escape probability of a star of mass  $m$  in a two-body interaction with mass ratio  $\mu \equiv m/m'$ . The dotted line shows the fit from Eq. 7.11.

included. This restriction implies that the disruption timescale  $t_{\text{dis}}$  is proportional to the half-mass relaxation time  $t_{\text{rh}}$  times the Coulomb logarithm  $\ln \Lambda$  ( $t_{\text{dis,Hénon}} \propto t_{\text{rh}} \ln \Lambda$ ), while  $N$ -body simulations show that it scales with a combination of the half-mass relaxation time and the crossing time ( $t_{\text{dis}} \propto t_{\text{rh}}^{0.75} t_{\text{cr}}^{0.25}$ ) due to two-body relaxation, i.e. the repeated effect of soft encounters (e.g. Fukushige & Heggie 2000, Baumgardt & Makino 2003). Nonetheless, the escape rate from Hénon (1969) does accurately describe what happens if two stars interact and can therefore be used as a starting point for a more complete description of the evolution of the MF. For that purpose, it is convenient to scale Eq. 7.10 to the mass loss rate found in  $N$ -body simulations and only use the relative or ‘differential’ stellar mass dependence from Hénon (1969). This is allowed if the ratio  $t_{\text{dis,Hénon}}/t_{\text{dis}} = \ln \Lambda (t_{\text{rh}}/t_{\text{cr}})^{0.25}$  only depends on global cluster properties. It is straightforward to show (e.g. Spitzer 1987, Heggie & Hut 2003) that indeed this is the case as  $t_{\text{rh}}/t_{\text{cr}} \propto N/\ln \Lambda$ . As such, one can write

$$\frac{dN(m)}{dt} = \left( \frac{dM}{dt} \right)_{\text{dis}} \chi(m), \quad (7.12)$$

with  $(dM/dt)_{\text{dis}}$  the mass loss rate from Eq. 7.3 (Lamers et al. 2005a) and  $\chi(m)$  the stellar mass-dependent escape rate per unit mass loss rate. The quantity  $\chi(m)$  is completely independent of the prescription for the total mass evolution. In order to derive  $\chi(m)$ , I start from Eq. 7.10 and express  $\chi(m)$  as

$$\chi(m) = \frac{N(m) \int_0^\infty N(m') F(m/m') \lambda(m, m') m'^2 dm'}{\int_0^\infty m'' N(m'') \int_0^\infty N(m') F(m''/m') \lambda(m'', m') m'^2 dm' dm''}, \quad (7.13)$$

where  $\lambda(m, m')$  represents a correction factor to account for additional physics (see below). The numerator reflects the escape rate, while the denominator is proportional to the mass loss rate.

For mathematical simplicity<sup>3</sup> Hénon (1969) made the following assumptions in the derivation of Eq. 7.10.

- (1) The cluster exists in isolation and the tidal field is neglected. Therefore, escape can only occur by a single, close encounter and the repeated effect of soft encounters (two-body relaxation) is not accounted for. This underestimates the escape rate of massive stars.
- (2) The distribution of stars is independent of stellar mass, i.e. mass segregation is not included. Depending on the balance between their encounter rate and their proximity to the escape energy, this over- or underestimates the escape rate of low-mass stars from Hénon (1969). Considering the results from Baumgardt & Makino (2003), the latter seems to be the case.

The remainder of this section concerns the derivation of the factor  $\lambda(m, m')$  in Eq. 7.13 that corrects for the above assumptions.

Let us assume that the distribution of stars over radius and velocity space is initially independent of their mass. This implies that mass segregation is dynamically created and not primordial, which is discussed in Sect. 7.6. For such an initial distribution, the separation from the escape energy  $\Delta E$  is independent of mass. As the cluster evolves, energy equipartition is reached between the stars and the radius, velocity and proximity to the escape energy become a function of stellar mass. I first consider this effect on the escape rate before including the timescale on which two-body relaxation occurs for different stellar masses. Please note that the formulation of Eq. 7.13 with  $\lambda(m, m')$  appearing in the numerator and the denominator implies that only the proportionality of  $\lambda(m, m')$  is important. Its exact value is determined by constants that drop out when substituting in Eq. 7.13.

It is intuitive to express the dependence of the escape rate on the energy needed for escape as  $dN(m)/dt \propto [\Delta E(m)]^{-1}$ . The energy that is required for escape  $\Delta E$  is related to the position and velocity of the star.<sup>4</sup> For the potential in Eq. 7.9 it is given by

$$\Delta E(r, v) = \psi(r) - \frac{v^2}{2} = \psi_0 \left( 1 + \frac{r^2}{r_0^2} \right)^{-1/2} - \frac{v^2}{2}, \quad (7.14)$$

with  $r$  and  $v$  the radial position and velocity of the star, and  $v_{\text{esc}} \equiv \sqrt{2\psi(r)}$  its escape velocity. If the cluster is in ‘perfect’ energy equipartition and correspondingly perfect mass segregation, the radius and velocity become a monotonous function of stellar mass (Heggie & Hut 2003, Ch. 16). Mass segregation is strongest in the cluster centre, which for a Plummer (1911) potential can be approximated with a harmonic potential  $\psi \propto r^2$ . For a cluster in a tidal field the potential is truncated, and the harmonic approximation serves as a crude but reasonable approximation for the entire cluster (Heggie & Hut 2003, Ch. 16). Energy

<sup>3</sup>And because this is the only way to obtain an analytical solution as in Eq. 7.10.

<sup>4</sup>The energy difference  $\Delta E$  that is discussed here concerns the energy that needs to be added to reach the escape energy. As such, it differs from the separation from the escape energy in Fukushima & Heggie (2000) and Baumgardt (2001), who are considering the *excess* energy of stars and its relation to the escape time, resulting in the aforementioned relation  $t_{\text{dis}} \propto t_{\text{th}}^{0.75} t_{\text{cr}}^{0.25}$ .

equipartition yields

$$v^2(m) = \langle v \rangle^2 \frac{\langle m \rangle}{m}, \quad (7.15)$$

with  $\langle v \rangle^2 \propto \psi_0$  the mean speed of all stars squared and  $\langle m \rangle$  the mean stellar mass. For the harmonic potential, this translates to a similar relation for the radial position:

$$r(m) = r_0 \sqrt{\frac{\langle m \rangle}{m}}, \quad (7.16)$$

where  $r_0$  represents the typical radius of the system, in this case the Plummer radius. This relation assumes that there is no particular stellar mass which dominates the mass spectrum. The decrease of radial position with stellar mass implied by Eq. 7.16 is a direct consequence of the energy loss endured by massive stars<sup>5</sup> as the system evolves towards energy equipartition. Substituting Eqs. 7.15 and 7.16 into Eq. 7.14 and dividing out the proportionality  $\langle v \rangle^2 \propto \psi_0$  gives an expression for  $\Delta E(m)$ :

$$\Delta E(m) = \left(1 + \frac{\langle m \rangle}{m}\right)^{-1/2} - c_1 \frac{\langle m \rangle}{m}, \quad (7.17)$$

with  $c_1 = \langle v \rangle^2 / 2\psi_0$  denoting the ratio of the mean speed squared to the central escape velocity squared. This constant mainly depends on the degree of mass segregation. Consequently, it will depend on the IMF. By comparing the models to the  $N$ -body simulations with a mass spectrum by Baumgardt & Makino (2003) the value is constrained to  $c_1 = 0.020$  for a Kroupa IMF, using King (1966) potentials with King parameter  $W_0 = 5-7$  (see Sect. 7.4). For reference, an unevolved Plummer (1911) potential has  $\langle v \rangle^2 / 2\psi_0 = 3\pi/64 = 0.147$ .

By comparing the models to  $N$ -body simulations (provided by M. Gieles, private communication) with different IMF power law slopes  $\alpha$  and a ratio between the maximum and minimum mass of 10, the approximate relation  $\log c_1 \approx \alpha - 3.76$  is found<sup>6</sup> for a MF  $n_s \propto m^{-\alpha}$ . Fitting the Kroupa IMF with a single power law in the mass range 0.08—15  $M_\odot$  (as used by Baumgardt & Makino 2003) yields  $\alpha = 2.06$ , resulting in  $c_1 = 0.020$  as mentioned earlier.<sup>7</sup> The comparison with  $N$ -body simulations also showed that a single value of  $c_1$  suffices to determine the MF evolution, even though it does not remain constant over the full cluster lifetime.

Because  $dN(m)/dt \propto [\Delta E(m)]^{-1}$ , Eq. 7.17 indicates that the escape rate of low-mass stars is increased if a cluster is in complete energy equipartition. However, the timescale on which two-body relaxation occurs between different stellar masses has not yet been considered. For a cluster starting with a stellar mass-independent distribution of radial positions and velocities, the equipartition timescale  $t_e$  scales as

$$t_e(m, m') \propto m^{-1} m'^{-1}, \quad (7.18)$$

<sup>5</sup>And the energy *gain* experienced by low-mass stars.

<sup>6</sup>This prescription for  $c_1$  implies that the condition for the stars in the cluster to be physically bound  $\Delta E(m) > 0$  is satisfied for all  $\alpha < 3.63$ .

<sup>7</sup>Nonetheless, the relation for  $c_1$  should be expected to exhibit some variation for different mass ranges.

for equipartition between stars of masses  $m$  and  $m'$  (Heggie & Hut 2003). This is a modified version of the relaxation timescale, which shows a very similar proportionality ( $t_r \propto m^{-2}$ ). It illustrates that two-body relaxation occurs on a shorter timescale for massive stars than for low-mass stars, increasing their escape rate  $dN(m)/dt \propto t_e^{-1}$ .

The correction factor for the escape rate  $\lambda(m, m')$  that appears in the integrals of Eq. 7.13 now follows from Eqs. 7.17 and 7.18 as

$$\lambda(m, m') = t_e^{-1}(m, m')[\Delta E(m)]^{-1} = mm' \left[ \left( 1 + \frac{\langle m \rangle}{m} \right)^{-1/2} - c_1 \frac{\langle m \rangle}{m} \right]^{-1}. \quad (7.19)$$

It was mentioned before that the proportionalities of  $\Delta E(m)$  and  $t_e(m, m')$  rather than their exact values suffice for the computation of  $\lambda(m, m')$  due to the renormalisation of the total mass loss rate that appears in Eq. 7.13: *only the stellar mass-dependence is important*.

The influence of the tidal field is now included in two ways. First of all, the escape of stars no longer occurs by a single, close encounter but arises due to two-body relaxation on the equipartition timescale, representing the repeated effect of soft encounters. Secondly, the above derivation of the separation from the escape energy assumes a potential which approximates tidally limited clusters. As a result, the escape rate of massive stars is increased with respect to clusters in the model of Hénon (1969), which was derived for an isolated cluster. On the other hand, the effect of mass segregation is included by introducing a stellar mass-dependence for the energy needed by stars to reach the escape velocity. Low-mass stars are closer to the tidal radius than massive stars, leading to a lower energy that is needed for escape and an increased escape rate. It depends on the shape of the MF which mechanism dominates.

The evolution of the MF of various cluster components is obtained from Eqs. 7.12, 7.13 and 7.19 by writing

$$\frac{d \log N_{\text{comp}}(m)}{dt} = \frac{d \log N(m)}{dt}, \quad (7.20)$$

where the MFs of stars, white dwarfs, neutron stars and black holes are represented by  $N_{\text{comp}}(m)$ , with  $\text{comp} = \{s, \text{wd}, \text{ns}, \text{bh}\}$ . The overall cluster evolution is computed by combining the results of this section with the prescription for stellar evolution from Sect. 7.3.1.

If stellar evolution is included, the resulting mass loss causes an expansion of the cluster, during which stars are lost independently of their masses. This delays the onset of mass segregation and the stellar mass-dependent mass loss that is described above. The moment of transition to stellar mass-dependent mass loss can be characterised by a certain fraction of the initial cluster mass that has been lost by dissolution  $f_{\text{diss}} \equiv M_{\text{diss}}/M_i$ . It is assumed that the fraction  $f_{\text{smd}}$  of the mass loss for which the escape rate depends on the stellar mass grows exponentially<sup>8</sup> between 0 and 1 as

$$f_{\text{smd}} = C \left( e^{f_{\text{diss}}/f_{\text{diss,seg}}} - 1 \right), \quad (7.21)$$

---

<sup>8</sup>This form assumes that the increase of the fraction of the mass loss that is stellar mass-dependent scales with the total dynamical mass loss, which is a compromise between a step function and a linear increase.

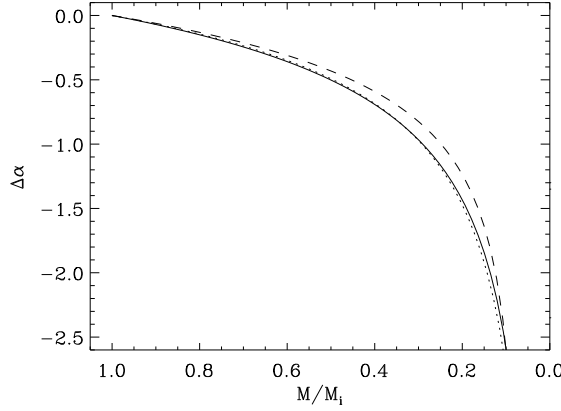


**Figure 7.3:** MF slope change  $\Delta\alpha$  in the range  $m = 0.1\text{--}0.5 M_{\odot}$  versus the remaining mass fraction for a Kroupa IMF (solid), Salpeter IMF (dotted), and a power law IMF with  $\alpha = 1.35$  (dashed). In all cases, the IMF mass range is  $m = 0.1\text{--}1 M_{\odot}$ . The displayed relation is valid if stellar evolution is excluded.

where the subscript ‘smd’ denotes ‘stellar mass-dependent’,  $f_{\text{diss,seg}} \equiv M_{\text{diss,seg}}/M_1$  is the fraction of the initial mass that has been lost by dissolution at which mass segregation is reached, and  $C = (e - 1)^{-1}$  is a constant to normalise  $f_{\text{smd}} = 1$  at the reference value  $f_{\text{diss}} = f_{\text{diss,seg}}$ . For  $f_{\text{diss}} > f_{\text{diss,seg}}$ , per definition  $f_{\text{smd}} = 1$ , indicating that all mass loss is stellar mass-dependent. The timescale  $t_{\text{seg}}$  on which mass segregation is reached and the transition to stellar mass-dependent mass loss is completed is proportional to the initial half-mass relaxation time ( $t_{\text{seg}} \propto t_{\text{rh,i}}$ ). It has been shown in several studies that for Roche lobe-filling clusters the disruption timescale  $t_{\text{dis}} \propto t_{\text{rh,i}}^{0.75} t_{\text{cr}}^{0.25}$  (Vesperini & Heggie 1997, Baumgardt & Makino 2003, Gieles & Baumgardt 2008), implying that  $t_{\text{seg}}/t_{\text{dis}} \propto t_{\text{dis}}^{0.33}$ . The expression for  $t_{\text{dis}}$  in Eq. 7.2 then leads to  $t_{\text{seg}}/t_{\text{dis}} \propto t_0^{0.33} M_1^{0.33\gamma}$ . Assuming that the cluster mass evolution is close to linear, the first-order relation  $f_{\text{diss,seg}} \propto t_{\text{seg}}/t_{\text{dis}}$  is obtained, implying

$$f_{\text{diss,seg}} = c_2 \left( \frac{t_0}{t_0^{\odot}} \right)^{0.33} \left( \frac{M_1}{10^4 M_{\odot}} \right)^{0.21}, \quad (7.22)$$

for a King parameter of  $W_0 = 5$ , with the dissolution timescale parameter at the solar galactocentric radius  $t_0^{\odot} = 21.3$  Myr. For a King parameter of  $W_0 = 7$ , the exponent of the initial cluster mass  $M_1$  becomes 0.23 and  $t_0^{\odot} = 10.7$  Myr (Kruijssen & Mieske 2009). In this relation,  $c_2$  represents a constant that is fixed by comparing the model to the results of  $N$ -body simulations from Baumgardt & Makino (2003), giving  $c_2 = 0.25$  for  $W_0 = 5$  and  $c_2 = 0.15$  for  $W_0 = 7$  (see Sect. 7.4). The variation with King parameter arises because two-body relaxation is faster for more concentrated clusters. If stellar evolution were neglected, at all ages  $c_2 = 0$  and  $f_{\text{smd}} = 1$ .

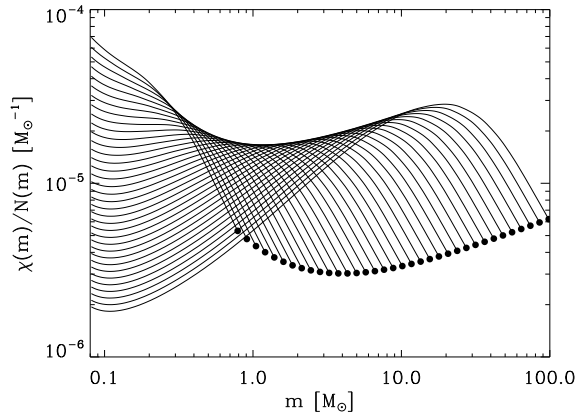


**Figure 7.4:** Relative escape rate  $\chi(m)/N(m)$  as a function of stellar mass, shown for a Kroupa MF with different maximum masses. The end point of each curve (dot) marks its maximum mass. The quantity  $\chi(m)/N(m) \equiv (d \log N(m)/dt)/(dM/dt)$  represents the escape rate per unit mass loss rate normalised to the number of stars at each mass (also see Eq. 7.13).

The modeled MF slope change  $\Delta\alpha$  in the mass range  $m = 0.1\text{--}0.5 M_{\odot}$  is shown in Fig. 7.3 for different IMFs covering  $m = 0.1\text{--}1 M_{\odot}$ . Evidently,  $\Delta\alpha$  is a function of the remaining mass fraction and is insensitive to the slope of the IMF, as long as that the ratio between the maximum and minimum mass is kept fixed and stellar evolution is excluded. This is an interesting observation in view of the MF evolution of globular clusters, in which  $m \approx 0.1\text{--}1 M_{\odot}$  and stellar evolution only plays a minor role. Figure 7.3 shows that the slope of the MF in globular clusters could be a possible indicator for the mass fraction that has been lost due to dissolution, provided that the IMF does not vary and the remnant retention fractions were not substantially dissimilar during the early evolution of different globular clusters (see Sect. 7.5.2 and Fig. 7.19).

For the particular example of a Kroupa MF that is truncated at different maximum masses  $m_{\text{max}}$ , the relative escape rate per unit mass loss rate  $\chi(m)/N(m)$  (see Eqs. 7.12 and 7.13) is shown in Fig. 7.4. This quantity is proportional to  $d \log N(m)/dt$  and reflects the probability that a star of a certain mass is ejected. Figure 7.4 illustrates that the mass of the highest relative escape rate is related to the maximum mass of the MF. The peak occurs at intermediate masses if the MF is truncated at a high mass. This implies that there is a typical mass where the stars are not too far from the escape energy *and* have an equipartition timescale with the massive stars that is short enough to eject them efficiently. This ‘sweet spot’ depends on the maximum mass of the MF. If the MF is truncated at an intermediate mass, the combination of quick two-body relaxation and proximity to the escape energy favours the escape rate of stars at the lowest masses.

The maximum stellar mass at which the transition from ‘sweet spot’-depletion to low-mass star depletion happens, is determined by the proximity of the low-mass stars to the

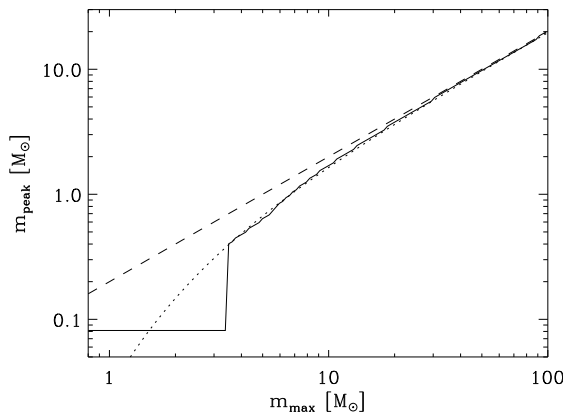


**Figure 7.5:** Mass of the highest relative escape rate  $m_{\text{peak}}$  as a function of the maximum stellar mass of the MF  $m_{\text{max}}$  (solid line). The dashed line represents the relation  $m_{\text{peak}} = 0.2m_{\text{max}}$ , while the dotted line describes an eyeball fit for masses  $m_{\text{max}} > 3 M_{\odot}$  and includes an exponential truncation at the low-mass end (see Eq. 7.23).

escape energy. In Fig. 7.5, the mass of the peak relative escape rate is shown as a function of the maximum stellar mass. At low truncation masses, the peak occurs at the minimum mass, indicating strong low-mass star depletion. Around  $m_{\text{max}} \sim 3 M_{\odot}$ , the relative escape rate at  $m_{\text{peak}} \sim 0.4 M_{\odot}$  becomes larger than its value at the lowest masses, which causes a jump in Fig. 7.5. For even higher values of  $m_{\text{max}}$ , the peak relative escape rate typically occurs at 15–20% of the maximum mass, approximately following the relation

$$m_{\text{peak}} = 0.2m_{\text{max}}e^{-2M_{\odot}/m_{\text{max}}}. \quad (7.23)$$

Even though its quantitative properties only hold for a Kroupa MF, the variation of the relative escape rate with the maximum mass of the MF has several implications for star cluster evolution. The change of  $m_{\text{max}}$  in Figs. 7.4 and 7.5 can be interpreted as an example of what happens when stellar evolution removes the most massive stars in the cluster, provided that the remnants are all ejected by their kick velocities. If dynamical evolution does not affect the shape of the MF too much before  $m_{\text{max}}(t) \sim 3 M_{\odot}$ , or  $t \sim 400$  Myr, the subsequent evolution of the MF will be dominated by low-mass star depletion. If substantial dissolution occurs earlier on, it is dominated by the ‘sweet spot’ depletion of intermediate masses. Only the retention of massive stellar remnants will make the evolution of the MF deviate from these basic estimates, because remnant retention can provide a fixed maximum (remnant) mass of the MF. This is treated in more detail in Sect. 7.5.

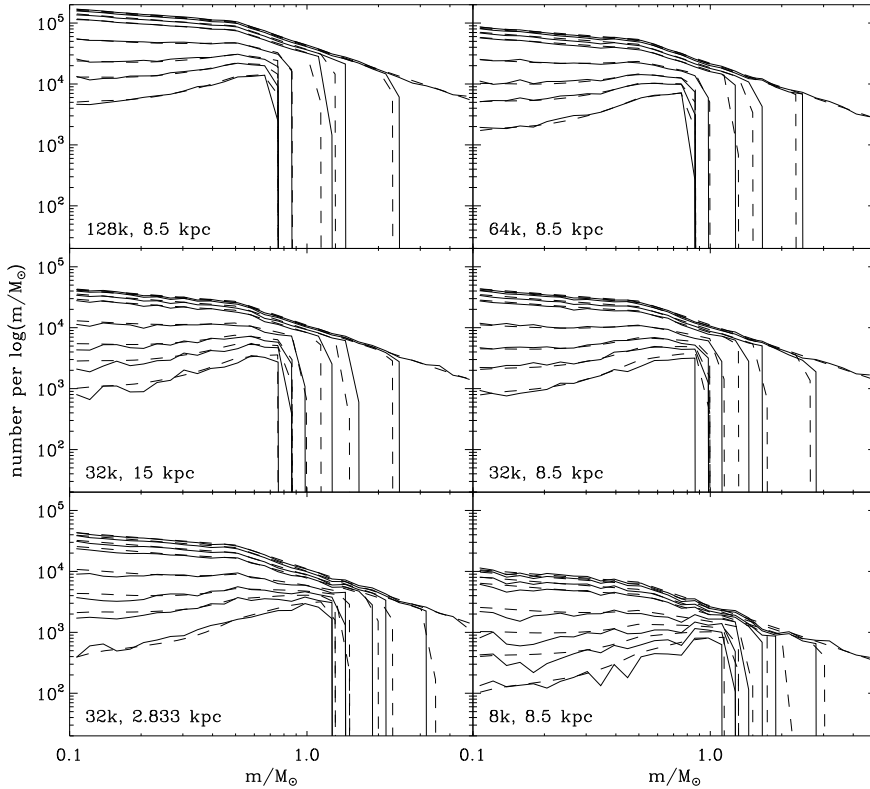


**Figure 7.6:** Comparison of the evolution of the stellar MF from the models (dashed) to the  $N$ -body runs from Baumgardt & Makino (2003, solid) for the exact same boundary conditions. The initial number of particles and the galactocentric radius are indicated in the bottom-left corner of each panel. From top to bottom, the subsequent MFs in each panel are shown for the times at which the remaining cluster mass fraction equals  $M/M_i = \{1, 0.75, 0.6, 0.5, 0.3, 0.2, 0.15, 0.1\}$ .

## 7.4 Comparison to $N$ -body simulations

The model described in Sect. 7.3 can be easily verified by running it for the exact same boundary conditions as the  $N$ -body simulations<sup>9</sup> by Baumgardt & Makino (2003) and comparing the results. They conducted simulations of Roche lobe-filling clusters between 8k and 128k particles, which were evolved in the Galactic tidal field at galactocentric radii in the range 2.833—15 kpc. The boundary conditions for the  $N$ -body runs of Baumgardt & Makino (2003) differ from those described in Sect. 7.3 by neglecting kick velocities and defining the

<sup>9</sup>These were performed using NBODY4 (Aarseth 1999).



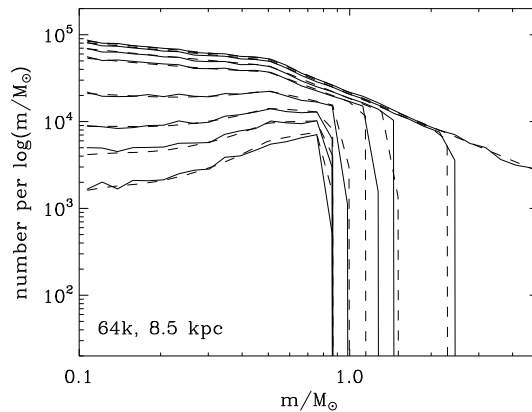


**Figure 7.7:** Comparison of the evolution of the stellar MF from the models (dashed) to the  $N$ -body run from Baumgardt & Makino (2003, solid) with  $W_0 = 7$  for the exact same boundary conditions. From top to bottom, the subsequent MFs are shown for the times at which the remaining cluster mass fraction equals  $M/M_i = \{1, 0.75, 0.6, 0.5, 0.3, 0.2, 0.15, 0.1\}$ .

Kroupa stellar IMF between  $0.1$  and  $15 M_\odot$ , thereby excluding black holes. For this particular comparison, the same IMF, stellar evolution prescription, and initial-final mass relation for stellar remnants are used in the model that is presented in this chapter.

In Fig. 7.6, the modeled evolution of the (luminous) stellar MF is compared to the  $N$ -body runs with King parameter  $W_0 = 5$  for a range of cluster masses and total disruption times. As time progresses, the maximum stellar mass decreases due to stellar evolution and the MF is lowered due to the dynamical dissolution of the star cluster. The slope of the MF changes due to the preferential escape of low-mass stars, which have energies closer to their escape energies, even to the extent that it dominates over their relatively slow two-body relaxation. For both the models and the  $N$ -body simulations, the MF develops a slight bend at  $m \sim 0.3 M_\odot$  when approaching total disruption. The bend arises as an optimum between on the one hand high energies but slow relaxation for the lowest stellar masses, and on the other hand quick relaxation but low energies for the highest stellar masses (see the discussion at the end of Sect. 7.3).

In all cases, the resemblance of the models and the  $N$ -body simulations is striking. The models reproduce all key aspects of the  $N$ -body runs, such as the amount of low-mass star depletion, the changing slope at  $m \sim 0.3 M_\odot$  for clusters close to dissolution, the survival of the Kroupa bend at  $m = 0.5 M_\odot$ , and the dependence of the low-mass depletion on the total lifetime of the cluster (compare the three 32k runs). The only difference occurs at the high-mass end of the MF, where the maximum stellar masses do not match at young ages. This is due to a minor dissimilarity of the total mass evolution (also see Lamers et al. 2005a, Kruijssen & Lamers 2008). Because the maximum stellar mass only depends on the age of the cluster, this causes a difference in maximum stellar mass when showing the MFs at

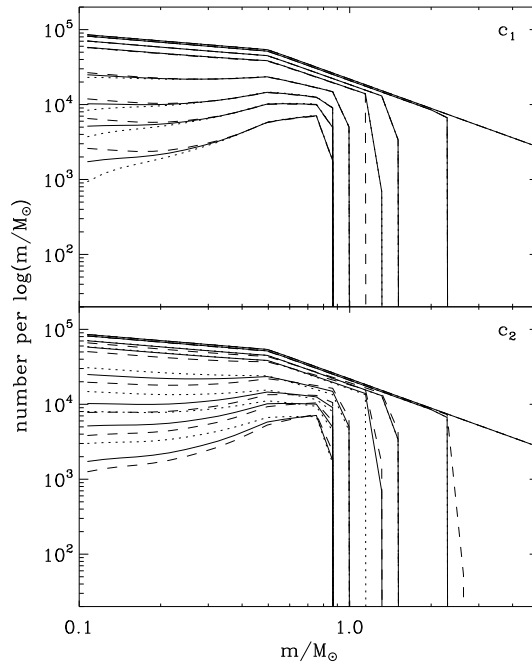


**Figure 7.8:** Influence of the constants  $c_1$  and  $c_2$  on the evolution of the stellar MF. From top to bottom, the subsequent MFs in each panel are shown for the times at which the remaining cluster mass fraction equals  $M/M_i = \{1, 0.75, 0.6, 0.5, 0.3, 0.2, 0.15, 0.1\}$ . *Top panel:* the values  $c_1 = \{0.010, \mathbf{0.020}, 0.030\}$  are represented by dashed, solid and dotted lines, respectively. *Bottom panel:* the values  $c_2 = \{0, \mathbf{0.25}, 0.40\}$  are represented by dashed, solid and dotted lines, respectively. For both  $c_1$  and  $c_2$ , the second (boldfaced) value is the one obtained from the comparison to the  $N$ -body simulations with  $W_0 = 5$  in Fig. 7.6.

fixed remaining cluster mass fractions. The contrast is clearest at young ages, since there the maximum stellar mass most rapidly decreases.

In the description of the model in Sect. 7.3, two constants have been determined from the  $N$ -body simulations by Baumgardt & Makino (2003). These constants are the ratio of the mean speed squared to the central escape velocity squared ( $c_1$ , see Eq. 7.17) and the proportionality constant for the relation marking the transition to stellar mass-dependent mass loss ( $c_2$ , see Eq. 7.22). As mentioned in Sect. 7.3, for a Kroupa IMF and King parameter  $W_0 = 5$  one obtains  $c_1 = 0.020$  and  $c_2 = 0.25$ . To illustrate the robustness of the models, in Fig. 7.7 they are compared to a 64k  $N$ -body run with  $W_0 = 7$ . For such a cluster with a higher concentration, the early mass segregation implies  $c_2 = 0.15$ . Again, the model and the simulation are in excellent agreement.

The dependence of the MF evolution on both constants is considered in Fig. 7.8. For  $c_1$ ,

the dependence of the evolution of the MF on its value is shown in the upper panel of Fig. 7.8, while for  $c_2$  it is shown in the bottom panel of Fig. 7.8. Both panels show the evolution of the MF for the 64k cluster in Fig. 7.6 for different values of  $c_1$  and  $c_2$ .

The ratio of the mean speed squared to the central escape velocity squared  $c_1$  affects the escape probability of the stars with the lowest masses. Because these stars are closest to their escape energies in a mass-segregated cluster, they are most strongly influenced by the value of  $c_1$ . For higher  $c_1$ , the MF gets more depleted in low-mass stars due to their closer proximity to the escape energy, while for lower  $c_1$  more low-mass stars are retained as the balance between close proximity to the escape energy and slow relaxation shifts to the latter.

The proportionality constant for the transition to stellar mass-dependent dissolution  $c_2$  in Eq. 7.22 affects the MF as a whole. For lower  $c_2$ , the transition occurs earlier and more low-mass stars are lost, while for higher  $c_2$  the onset of the depletion is delayed and the slope of the MF remains closer to its initial value. If one were to assume a constant  $f_{\text{diss,seg}}$ , which is contrary to the adopted relation with cluster mass in Eq. 7.22, this would therefore yield a stellar MF in massive clusters that is underpopulated in low-mass stars, and a MF in low-mass clusters that is overabundant in low-mass stars.

## 7.5 Star cluster evolution

In this section, the described model is applied to compute the evolution of clusters for a variety of boundary conditions. The stellar content as well as integrated photometry are addressed, using the boundary conditions from Sect. 7.3 instead of those that were adopted to compare the model to  $N$ -body simulations in Sect. 7.4. The most important differences are the mass range of the IMF, the inclusion of remnant kick velocities, and the initial-final mass relation.

The model that will be referred to as the ‘standard model’ uses a metallicity  $Z = 0.004$  (which is typical of globular clusters), a King parameter<sup>10</sup> of  $W_0 = 7$  (corresponding to  $\gamma = 0.7$  in Eq. 7.2), a dissolution timescale parameter  $t_0 = 1$  Myr, and a Kroupa IMF between  $m = 0.08 M_\odot$  and the maximum stellar mass given by the Padova isochrones at  $\log t = 6.6$ , which is typically  $m \sim 70 M_\odot$ . For the computation of the retained remnant fraction (see Eq. 7.8), the Plummer radius  $r_0$  is related to the half-mass radius  $r_h$  as  $r_h = 1.3r_0$ . The half-mass radius is assumed to remain constant during the cluster lifetime (e.g. Aarseth & Heggie 1998). For the relation between  $r_h$  and initial cluster mass  $M_i$  the expression from Larsen (2004) is adopted:

$$r_h = 3.75 \text{ pc} \left( \frac{M_i}{10^4 M_\odot} \right)^{0.1}. \quad (7.24)$$

The models that are used in this section are computed from  $10^7$  yr to  $1.65 \times 10^{10}$  yr (the maximum age of the Padova isochrones) for initial masses between  $10^2 M_\odot$  and  $10^7 M_\odot$ , spaced by 0.25 dex intervals.

<sup>10</sup>For  $W_0 = 5$ , or  $\gamma = 0.62$ , the results vary only marginally.

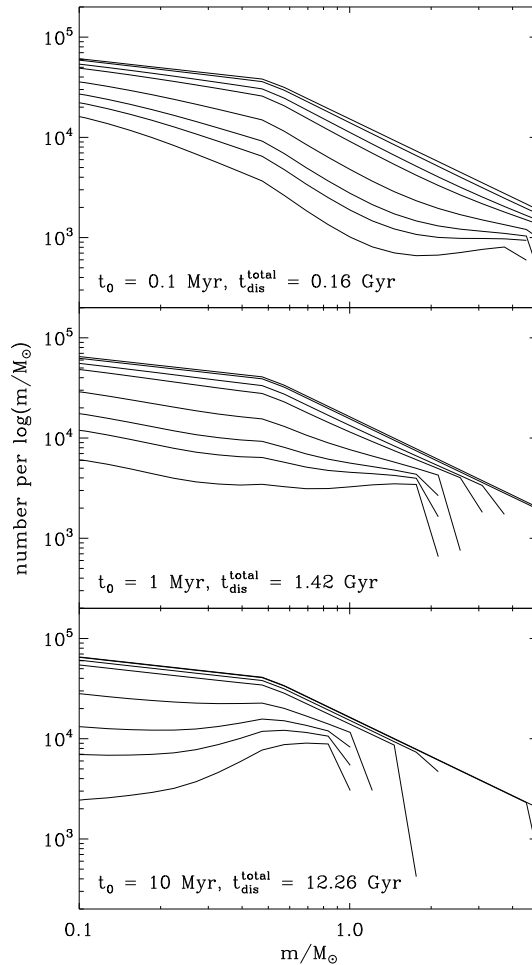


**Figure 7.9:** Influence of the disruption time on the evolution of the stellar MF for a cluster with a low remnant retention fraction ( $\log(M_i/M_\odot) = 4.5$ ). From top to bottom, the subsequent MFs in each panel are shown for the times at which the remaining cluster mass fraction equals  $M/M_i = \{1, 0.75, 0.6, 0.5, 0.3, 0.2, 0.15, 0.1\}$ .

### 7.5.1 The influence of the disruption time

The disruption time of a cluster affects the evolution of the MF and of the integrated photometric properties. To assess the influence of the disruption time on cluster evolution, clusters with low and high remnant retention fractions should be treated separately, because the presence of massive remnants also has a pronounced effect on the results (see Sect. 7.5.2). As

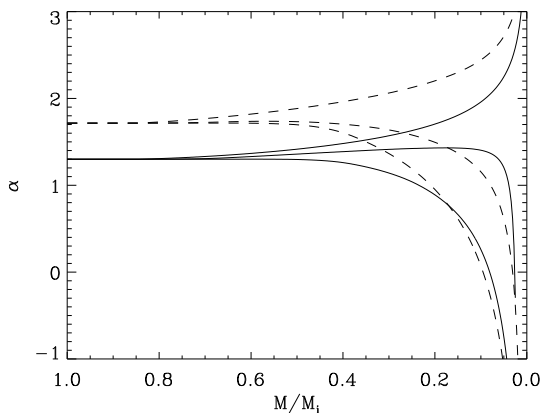


**Figure 7.10:** Influence of the disruption time on the stellar MF slope  $\alpha$  in the range  $0.1 < m/M_{\odot} < 0.5$  (solid) and  $0.3 < m/M_{\odot} < 0.8$  (dashed) for a cluster with a low remnant retention fraction ( $\log(M_i/M_{\odot}) = 4.5$ ). Shown is  $\alpha$  versus the remaining cluster mass fraction. From top to bottom, for each mass range the lines represent  $t_0 = \{0.1, 1, 10\}$  Myr, corresponding to  $t_{\text{dis}}^{\text{total}} = \{0.16, 1.42, 12.26\}$  Gyr.

shown in Fig. 7.1, for a given kick velocity dispersion the remnant retention fraction is set by the cluster mass. This means that the division between low and high remnant retention fractions can be made by making a cut in initial cluster mass.

In Fig. 7.9, the impact of the disruption time on the evolution of the MF is shown for a cluster with initial mass  $\log(M_i/M_{\odot}) = 4.5$ , representing the evolution for low remnant retention fractions.<sup>11</sup> The range of the dissolution timescale parameter  $t_0$  and resulting total disruption times that are considered in Fig. 7.9 cover two orders of magnitude. As the total lifetime increases, the depletion of the low-mass stellar MF close to total disruption becomes more prominent. Conversely, the MF of short-lived clusters is depleted around  $m \sim 1 M_{\odot}$ . As introduced in the last paragraphs of Sect. 7.3, this difference is caused by the fixed timescale on which stellar evolution decreases the maximum stellar mass, implying that the masses of the most massive stars are larger in quickly dissolving clusters than in slowly dissolving ones. Because in short-lived clusters the massive stars are still present when the bulk of the dissolution occurs, their rapid two-body relaxation with intermediate-mass stars dominates over the relatively close proximity to the escape energy of low-mass stars, yielding a depletion at intermediate masses. In long-lived clusters, this cannot occur because the very massive stars have disappeared before the mass loss by dissolution becomes important, thus resulting in the depletion of the very low-mass end of the MF. As a rule of thumb, for  $t < 400$  Myr (which is the lifetime of a  $3 M_{\odot}$  star) the depletion typically occurs around 15–20% of the mass of the most massive star (see Sect. 7.3). In terms of the total disruption

<sup>11</sup>High remnant retention fractions will be treated in the discussion of the influence of the retention fraction in Sect. 7.5.2.

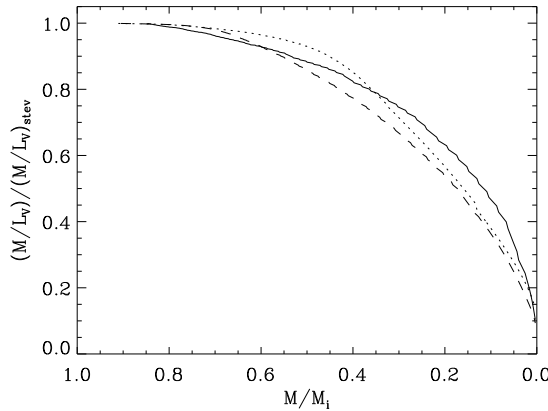


**Figure 7.11:** Influence of the disruption time on the  $M/L_V$  ratio evolution for a cluster with a low remnant retention fraction ( $\log(M_i/M_\odot) = 4.5$ ). Shown is the relative  $M/L_V$  ratio decrease with respect to the value expected for stellar evolution  $(M/L_V)_{\text{stev}}$  versus the remaining cluster mass fraction. The solid, dashed and dotted lines represent  $t_0 = \{0.1, 1, 10\}$  Myr, respectively, corresponding to  $t_{\text{dis}}^{\text{total}} = \{0.16, 1.42, 12.26\}$  Gyr.

time, the transition from intermediate-mass star depletion to low-mass star depletion occurs around  $t_{\text{dis}}^{\text{total}} \sim 1$  Gyr.

A quantifiable way to look at the evolution of the stellar MF in star clusters is to consider the slope of the MF  $n_s \propto m^{-\alpha}$  in certain mass intervals (Richer et al. 1991, De Marchi et al. 2007, De Marchi & Pulone 2007, Vesperini et al. 2009). For the commonly used mass intervals  $0.1 < m/M_\odot < 0.5$  ( $\alpha_1$ ) and  $0.3 < m/M_\odot < 0.8$  ( $\alpha_2$ ), Fig. 7.10 shows the evolution of the slope  $\alpha$  for the same clusters as before. Like Fig. 7.9, this illustrates that for short disruption times the slope steepens as the cluster dissolves, while for long disruption times the slope flattens with time. The presented models and other model runs indicate that  $\alpha_1$  increases with time for  $t_{\text{dis}}^{\text{total}} < 1$  Gyr and decreases for  $t_{\text{dis}}^{\text{total}} > 2$  Gyr. For total disruption times in between these values, the slope first increases and then decreases. The slope in the second mass interval  $\alpha_2$  shows the same behaviour. It increases for  $t_{\text{dis}}^{\text{total}} < 0.5$  Gyr and decreases for  $t_{\text{dis}}^{\text{total}} > 1$  Gyr.

The mass-to-light ( $M/L$ ) ratio evolution of star clusters is affected by the evolution of the MF due to the large variations in  $M/L$  ratio between stars of different masses. Massive stars have lower  $M/L$  ratios than low-mass stars, implying that a cluster with a MF that is depleted in low-mass stars will have a reduced  $M/L$  ratio (Baumgardt & Makino 2003, Kruijssen 2008, Kruijssen & Lamers 2008). As such, one would also expect a correlation between the slope of the MF and  $M/L$  ratio.

In Fig. 7.11, the evolution of the ratio of the V-band  $M/L_V$  to the mass-to-light ratio due to stellar evolution  $(M/L_V)_{\text{stev}}$  is shown for the same clusters as in Figs. 7.9 and 7.10. This quantity reflects the relative  $M/L_V$  ratio change induced by dynamical evolution with

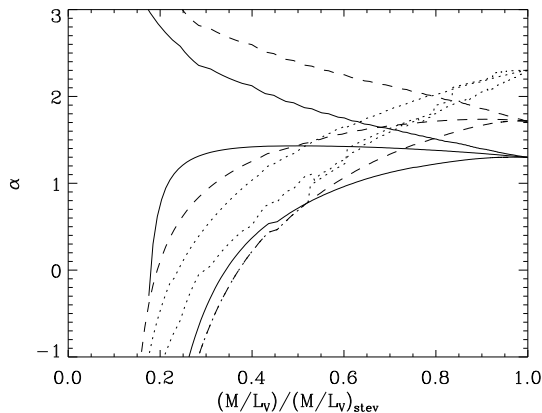


**Figure 7.12:** Influence of the disruption time on the combined evolution of the MF slope  $\alpha$  and the  $M/L_V$  ratio for a cluster with a low remnant retention fraction ( $\log(M_i/M_\odot) = 4.5$ ). Shown is  $\alpha$  versus the relative  $M/L_V$  ratio decrease due to dynamical evolution. All clusters start at the vertical line  $(M/L_V)/(M/L_V)_{\text{stev}} = 1$ . Solid lines denote the slope in the mass range  $0.1 < m/M_\odot < 0.5$ , dashed lines designate the mass range  $0.3 < m/M_\odot < 0.8$ , and dotted lines represent the mass range  $0.3m_{\text{max}}(t) < m/M_\odot < 0.8m_{\text{max}}(t)$ , with from top to bottom  $t_0 = \{0.1, 1, 10\}$  Myr, corresponding to  $t_{\text{dis}}^{\text{total}} = \{0.16, 1.42, 12.26\}$  Gyr.

respect to evolutionary fading only. If the escape rate would be independent of stellar mass, the evolution would follow a horizontal line at  $(M/L_V)/(M/L_V)_{\text{stev}} = 1$ . However, when accounting for dynamical evolution, the  $M/L$  ratio is always smaller than that for stellar evolution only. Somewhat surprisingly, this is also the case for clusters for which the slope of the MF increases (see Fig. 7.10). This is explained by looking at the evolution of the entire MF in Fig. 7.9. Even though the slope at low masses increases for short disruption times due to the escape of intermediate-mass stars, the most massive stars that dominate the cluster light are still retained. Because stars of intermediate masses are lost instead, the  $M/L$  ratio decreases.

Because the slope of the stellar MF either increases or decreases at masses  $m < 1 M_\odot$ , the decrease of the  $M/L$  ratio implies a large range of MF slopes that can occur at low  $M/L$  ratios. This is shown in Fig. 7.12, where the relation between  $\alpha$  and the  $M/L$  ratio drop is presented. The slope of the stellar MF in a certain mass range does not necessarily reflect the  $M/L$  ratio of the entire cluster. Considering the aforementioned rule of thumb stating that for total disruption times  $t_{\text{dis}}^{\text{total}} < 1$  Gyr the depletion of the MF occurs around 15–20% of the mass of the most massive star  $m_{\text{max}}(t)$ , it is useful to define the slope in a mass range that is related to  $m_{\text{max}}(t)$ . In Fig. 7.12, the relation between slope and  $M/L$  ratio is also shown for the slope in the stellar mass range  $0.3m_{\text{max}}(t) < m/M_\odot < 0.8m_{\text{max}}(t)$ . In such a relative mass range, the slope follows a much narrower relation with  $M/L$  ratio. The range between 30% and 80% of  $m_{\text{max}}(t)$  was chosen to maximise this effect.

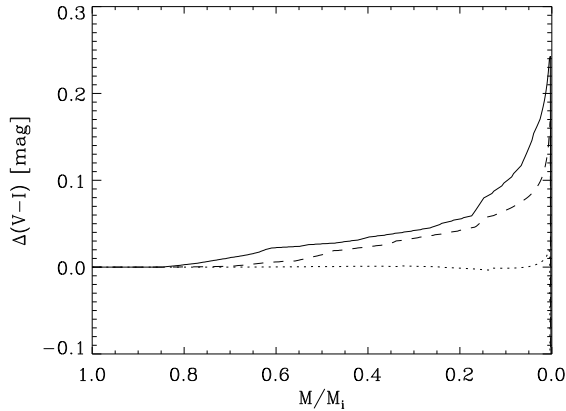


**Figure 7.13:** Influence of the disruption time on the  $V - I$  colour for a cluster with a low remnant retention fraction ( $\log(M_i/M_\odot) = 4.5$ ). Shown is the colour offset due to dynamical evolution  $\Delta(V - I)$  versus the remaining mass fraction. The solid, dashed and dotted lines represent  $t_0 = \{0.1, 1, 10\}$  Myr, respectively, corresponding to  $t_{\text{dis}}^{\text{total}} = \{0.16, 1.42, 12.26\}$  Gyr.

For the slopes in the fixed stellar mass ranges ( $\alpha_1$  and  $\alpha_2$ , see above), the relation with the  $M/L$  ratio becomes better defined for long-lived clusters. It is shown in Figs. 7.10—7.12 that both the slope and the  $M/L$  ratio decrease for clusters with long disruption times, indicating that both quantities are more clearly related for globular cluster-like lifetimes.

The colour of star clusters is also influenced by the evolution of the MF, due to the colour differences between stars of different masses. The  $V - I$  magnitude difference  $\Delta(V - I)$  with respect to the  $V - I$  value that a cluster would have if dynamical evolution were neglected is shown in Fig. 7.13. As the clusters dissolve, their colours become redder due to the escape of main sequence stars. The magnitude difference in  $V - I$  exceeds  $\Delta(V - I) = 0.1$  mag for total disruption times  $\leq 1.5$  Gyr. In redder passbands (e.g. the  $V - K$  colour), the difference grows to several tenths of magnitudes. For longer total disruption times only stars of the lowest masses are ejected (see Fig. 7.9), which hardly contribute to the cluster light and colour, implying that the colours are only marginally affected.

## 7.5.2 The influence of the remnant retention fraction

The formation of stellar remnants introduces massive bodies in the MF that do not end their lives due to stellar evolution like massive stars do. Depending on their kick velocities, stellar remnants can be retained in (massive) clusters. If they are retained, they keep affecting the evolution of the stellar MF until the cluster is disrupted. Especially black holes can have a pronounced effect on cluster evolution.

The remnant retention fraction arises from the cluster mass, radius and the kick velocity dispersion (see Eq. 7.8). In this section, the mass-radius relation from Eq. 7.24 is used.



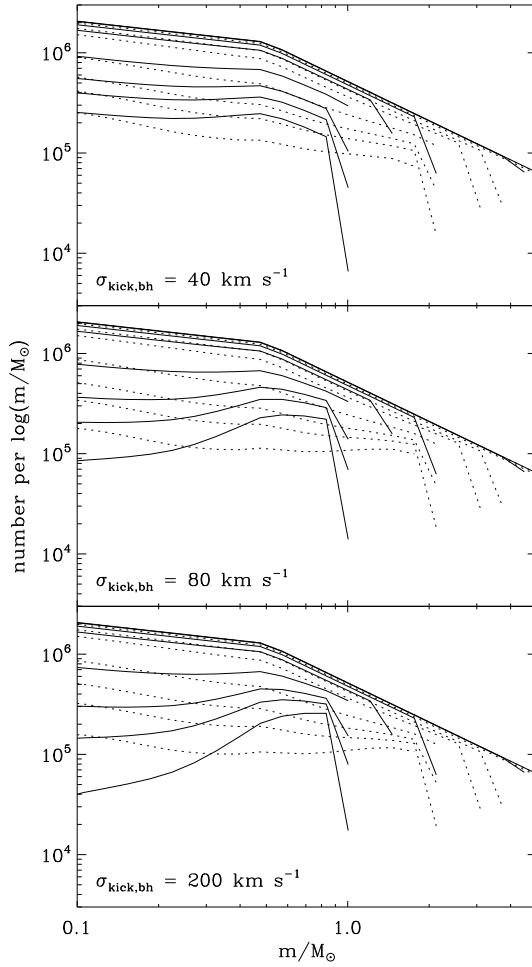


**Figure 7.14:** Influence of the black hole kick velocity dispersion and disruption time on the evolution of the stellar MF for an initial cluster mass  $M_i = 10^6 M_\odot$ . From top to bottom, the subsequent MFs in each panel are shown for the times at which the remaining cluster mass fraction equals  $M/M_i = \{1, 0.75, 0.6, 0.5, 0.3, 0.2, 0.15, 0.1\}$ . Solid lines denote  $t_0 = 1$  Myr ( $t_{\text{dis}}^{\text{total}} = 15.13$  Gyr), while dotted lines represent  $t_0 = 0.1$  Myr ( $t_{\text{dis}}^{\text{total}} = 1.66$  Gyr).

Although the results will differ for other relations, it has been verified that for commonly used alternatives,<sup>12</sup> the change is only marginal and does not affect the nature of the conclusions. To separate the effect of remnant retention from that of the disruption time, a fixed initial

<sup>12</sup>Such as a constant radius or density.

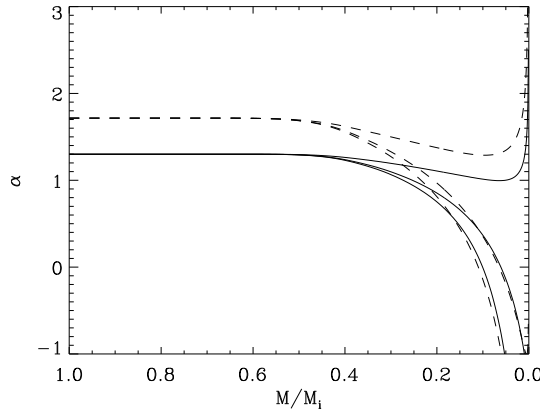


**Figure 7.15:** Influence of the black hole retention fraction on the stellar MF slope  $\alpha$  in the range  $0.1 < m/M_{\odot} < 0.5$  (solid) and  $0.3 < m/M_{\odot} < 0.8$  (dashed) for an initial cluster mass  $M_i = 10^6 M_{\odot}$ . Shown is  $\alpha$  versus the remaining cluster mass fraction. From top to bottom, for each mass range the lines represent  $\sigma_{\text{kick,bh}} = \{40, 80, 200\} \text{ km s}^{-1}$ , corresponding to  $f_{\text{ret,bh}} = \{0.219, 0.041, 0.003\}$  for a  $10^6 M_{\odot}$  cluster.

cluster mass of  $10^6 M_{\odot}$  is assumed while independently varying the velocity dispersion of the remnant kick velocities and the disruption time. The corresponding evolution of the stellar MF is shown in Fig. 7.14, for the standard model (see the beginning of this section) with black hole kick velocity dispersions  $\sigma_{\text{kick,bh}} = \{40, 80, 200\} \text{ km s}^{-1}$ , equivalent to  $f_{\text{ret,bh}} = \{0.219, 0.041, 0.003\}$  for a  $10^6 M_{\odot}$  cluster, and for dissolution timescale parameters  $t_0 = \{0.1, 1\} \text{ Myr}$ , which for a  $10^6 M_{\odot}$  cluster implies  $t_{\text{dis}}^{\text{total}} = \{1.66, 15.13\} \text{ Gyr}$ . Assuming an age of 12 Gyr, the present-day mass in the case of  $t_0 = 1 \text{ Myr}$  is about  $M \sim 6 \times 10^4 M_{\odot}$ , comparable to globular clusters. The remaining fraction of the initial mass is  $M/M_i \sim 0.06$ .

If the velocity dispersion of black hole kicks is low and a relatively large fraction of black holes is retained, then the escape rate of massive stars is increased with respect to high kick velocity dispersions. This arises due to the quick two-body relaxation between the massive stars and the black holes, which will have masses larger than the most massive stars after a few Myr of stellar evolution. As a result, the escape rate of low-mass stars is largest in clusters containing only few black holes. This happens for clusters with either long or short disruption times, but the effect is largest for long-lived clusters (the solid lines in Fig. 7.14). In these clusters the maximum stellar mass is more strongly decreased by stellar evolution than in short-lived clusters, implying that the black hole masses are larger compared to the most massive stars in these clusters. For long disruption times, the presence of massive remnants therefore has a more pronounced effect on the escape rate of massive stars than for short disruption times. If these long-lived clusters retain a sufficiently large fraction of the stellar remnants, their stellar MF may even become depleted in massive stars.

The top panel of Fig. 7.14 also shows that for a cluster with a high remnant retention

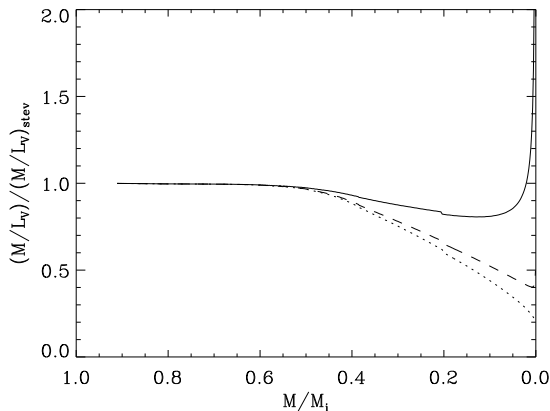


**Figure 7.16:** Influence of the black hole retention fraction on the  $M/L_V$  ratio evolution for an initial cluster mass  $M_i = 10^6 M_\odot$ . Shown is the relative  $M/L_V$  ratio decrease with respect to the value expected for stellar evolution  $(M/L_V)_{\text{stev}}$  versus the remaining cluster mass fraction. The solid, dashed and dotted lines represent  $\sigma_{\text{kick,bh}} = \{40, 80, 200\} \text{ km s}^{-1}$ , corresponding to  $f_{\text{ret,bh}} = \{0.219, 0.041, 0.003\}$  for a  $10^6 M_\odot$  cluster.

fraction, the impact of the disruption time on the MF evolution is similar to that of clusters with low retention fractions (see Fig. 7.9). However, the influence of the disruption time becomes smaller when more remnants are retained. This explains why Baumgardt & Makino (2003) only found a very weak dependence of the evolution of the MF on the disruption time (also see Fig. 7.6), since they neglected remnant kick velocities and retained all remnants in their simulations.

Analogous to Fig. 7.10 in Sect. 7.5.1, the evolution of the MF slope in different mass ranges is shown in Fig. 7.15 for the clusters with  $t_0 = 1 \text{ Myr}$  from Fig. 7.14.<sup>13</sup> The kick velocity dispersion has an effect on the MF that is more uniform than the consequences of variations in the disruption time, leading to very similar slope evolutions in the two different stellar mass ranges. Independent of the mass range, an increase in remnant retention fraction is reflected by an increase of  $\alpha$ . The model that is displayed for  $\sigma_{\text{kick,bh}} = 40 \text{ km s}^{-1}$ ,  $t_0 = 1 \text{ Myr}$ , and  $M_i = 10^6 M_\odot$  (the upper dashed and solid lines in Fig. 7.15) marks the transition between an increase or decrease of the MF slope by dynamical evolution. For an initial  $f_{\text{ret,bh}} < 0.25$ , low-mass stars are preferentially ejected during most of the cluster lifetime, while for  $f_{\text{ret,bh}} > 0.25$  mainly the massive stars escape. For shorter disruption times, the transition is located at a smaller black hole retention fraction.

Because the black hole retention fraction affects the overall slope of the stellar MF, the

<sup>13</sup>For the clusters with relatively long disruption times that are considered in this section, the variable stellar mass range that was introduced in Sect. 7.5.1 to trace the relation between MF slope and  $M/L$  ratio gives an evolution of the slope that is comparable that for the fixed mass ranges. It is omitted from the figures in this section to improve their clarity.

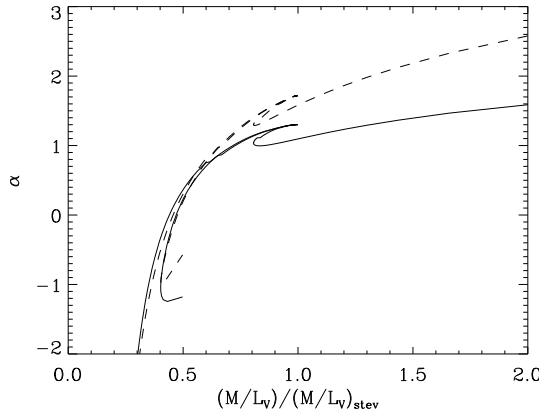


**Figure 7.17:** Influence of the black hole retention fraction on the combined evolution of the MF slope  $\alpha$  and the  $M/L_V$  ratio for an initial cluster mass  $M_i = 10^6 M_\odot$ . Shown is  $\alpha$  versus the relative  $M/L_V$  ratio decrease due to dynamical evolution. All clusters start at the vertical line  $(M/L_V)/(M/L_V)_{\text{stev}} = 1$ . Solid lines denote the slope in the mass range  $0.1 < m/M_\odot < 0.5$  and the dashed lines designate the mass range  $0.3 < m/M_\odot < 0.8$ , with from right to left  $\sigma_{\text{kick,bh}} = \{40, 80, 200\} \text{ km s}^{-1}$ , corresponding to  $f_{\text{ret,bh}} = \{0.219, 0.041, 0.003\}$  for a  $10^6 M_\odot$  cluster.

changes in  $\alpha$  are matched by corresponding changes in the  $M/L$  ratio. In Fig. 7.16, the relative  $M/L_V$  ratio change due to dynamical evolution is shown for same clusters as in Fig. 7.15. Contrary to the clusters with low remnant retention fractions in Sect. 7.5.1, the  $M/L$  ratio of the clusters in Fig. 7.16 does not monotonously decrease. Close to total disruption, the massive remnants are the last bodies to be ejected. During that short phase of cluster evolution, the  $M/L$  ratio is increased by dynamical evolution and exceeds the value it would have due to stellar evolution alone.

The behaviour of  $M/L$  ratio for different black hole kick velocity dispersions has interesting implications for the relation between MF slope and  $M/L$  ratio, which is shown in Fig. 7.17. In combination with Fig. 7.12 (note the different axes), it shows possible evolutionary tracks of star clusters in this plane, indicating that nearly every location may be reached. However, when limiting ourselves to long-lived clusters, Fig. 7.17 illustrates that these clusters will follow a trend of decreasing slope with decreasing  $M/L$  ratio, albeit with excursions to high  $M/L$  ratios and slightly higher  $\alpha$  close to their total disruption. This explains the trend that was found by Kruijssen & Mieske (2009), who considered the relation between the observed MF slopes and  $M/L$  ratios of Galactic globular clusters.

The colour change due to dynamical evolution is only very small for clusters with  $t_{\text{dis}}^{\text{total}} > 1.5 \text{ Gyr}$  (see Sect. 7.5.1). Because clusters in which remnants are retained are massive, their lifetimes are correspondingly long. As a result, the colour evolution is largely unaffected for the clusters in which the remnant retention fraction could play a role ( $\Delta(V-I) < 0.03 \text{ mag}$ ). The colour change is even smaller if more massive remnants are retained, because then the

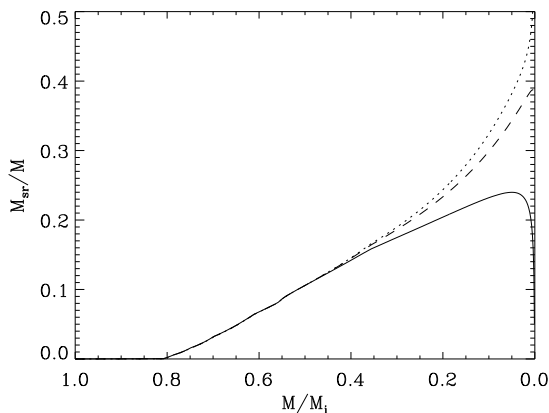


**Figure 7.18:** Influence of the black hole retention fraction on the total remnant mass fraction. Shown is the ratio of the total mass in stellar remnants  $M_{\text{sr}}$  to the cluster mass  $M$  versus the remaining cluster mass fraction. The solid, dashed and dotted lines represent  $\sigma_{\text{kick,bh}} = \{40, 80, 200\} \text{ km s}^{-1}$ , corresponding to  $f_{\text{ret,bh}} = \{0.219, 0.041, 0.003\}$  for a  $10^6 M_{\odot}$  cluster.

stellar MF more closely resembles its initial form (see the upper panel of Fig. 7.14). Long-lived clusters generally appear  $\sim 0.005$  mag bluer in  $V-I$  due to dynamical evolution during the last  $\sim 3-20\%$  of their lifetimes and reach a similar reddening upon their total disruption, which is well within observational errors. The colours of old clusters are thus only marginally affected by dynamical evolution.

The evolution of the total remnant mass fraction is shown in Fig. 7.18 for different black hole kick velocity dispersions. The seemingly counterintuitive result is that the fraction of the cluster mass that is constituted by remnants is smaller when more black holes are retained. As shown in Fig. 7.14, the retention of black holes suppresses the depletion of the low-mass end of the MF due to the ‘sweet spot’ escape (see Sect. 7.3) of massive ( $\sim 1 M_{\odot}$ ) stars by the black holes. After  $\sim 1$  Gyr, white dwarfs and neutron stars have masses that are similar to those of the massive stars, implying that their escape rate is also increased when more black holes are retained. Because the total mass constituted by white dwarfs and neutron stars is larger than the combined mass of all black holes, the fraction of the total cluster mass that is constituted by remnants decreases if these low-mass remnants are ejected by the more massive black holes.

## 7.6 Discussion and applications

The results of this chapter show that the stellar MFs in star clusters differ strongly from their initial forms due to dynamical cluster evolution. The specific kinds of these differences depend on the properties of the star clusters and their tidal environment, most importantly on

the disruption time, remnant retention fraction, and IMF.<sup>14</sup>

A physical model for the evolution of the stellar MF is presented in which two-body relaxation leads to a stellar mass dependence of the escape rate. For any particular stellar mass, the escape rate is determined by the typical proximity of that mass to the escape energy and by the timescale on which the two-body relaxation with the other stars takes place. Combined with a prescription for stellar evolution, stellar remnant production, and remnant retention using kick velocity dispersions, this provides a description for the total evolution of the MF. *This description is independent of the adopted total mass evolution.* The model shows that the slope of the mass function is a possible indicator for the mass fraction that has been lost due to dissolution, provided that the IMF does not vary and the remnant retention fraction has been fairly similar for young globular clusters.<sup>15</sup>

For the exact same initial conditions, the model shows excellent agreement with  $N$ -body simulations of the evolving MF by Baumgardt & Makino (2003). However, an important advantage of the presented model compared to the (more accurate)  $N$ -body simulations is its short runtime and corresponding flexibility. It can be easily applied to compute the evolution of clusters for a large range of initial conditions. The results can then be used to identify interesting cases for more detailed and less simplified calculations with  $N$ -body or Monte Carlo models.

The most important simplification of the model is neglecting the effect of binary encounters on the stellar mass dependence of the escape rate. To incorporate binaries, a conclusive census of the binary population in star clusters would be required, which is not yet available. Nonetheless, it is possible to make a qualitative estimate for the effect of binaries. The encounter rate of binaries would typically be higher than that of individual stars, because the cross section of binaries is larger. This would increase the relative escape rate at the stellar mass for which the binary fraction<sup>16</sup> peaks. This binary fraction is found to increase with primary mass (see e.g. Kouwenhoven et al. 2009). Because massive stars are removed by stellar evolution, this implies that the binary fraction decreases with age, which is in agreement with the low binary fraction observed in globular clusters ( $\sim 2\%$ , e.g. Richer et al. 2004). The effect of binaries on the evolution of the mass function would thus be most notable if the majority of the dynamical mass loss occurs at ages  $< 50$  Myr (the typical lifetime of an  $8 M_{\odot}$  star), in which case it would somewhat enhance the relative escape rate of the most massive stars. The influence is expected to be small, since the presence of binaries mainly affects ejections by hard encounters and leaves the overall evaporation rate largely unchanged (Küpper et al. 2008). On the other hand, neglecting binary encounters of massive remnants such as black holes could underestimate their escape rate for times beyond 50 Myr. This would imply that the model overestimates the impact of the black hole retention fraction on the evolution of the MF.

The model is applied to investigate the influence of the disruption time and remnant retention on the evolution of the MF and integrated photometric properties of star clusters. For total disruption times  $t_{\text{dis}}^{\text{total}} < 1$  Gyr, the modeled relative escape rate is highest at a certain

---

<sup>14</sup>Although not specifically shown in this chapter (but not surprisingly), the differences also depend on the initial-final stellar mass relation.

<sup>15</sup>Any variability of the retention fraction would induce substantial scatter, see Sect. 7.5.2 and Fig. 7.19.

<sup>16</sup>The fraction of stars residing in binary or multiple systems.

‘sweet spot’ mass that is typically 15—20% of the mass of the most massive objects in the cluster. For longer lifetimes, the evolution of the MF is dominated by low-mass star depletion, unless the retention fraction of massive stellar remnants is larger than 0.25. Only in the particular case of such a high retention fraction, the  $M/L$  ratio is increased by dynamical evolution when the cluster approaches total disruption. In all other scenarios, the  $M/L$  ratio decreases because the most massive (luminous) stars are kept.<sup>17</sup> When defining the slope of the MF in the range 30—80% of the maximum stellar mass, this gives a clear relation between the MF slope and the  $M/L$  ratio. For slopes that are defined in fixed mass ranges, there is not necessarily a correlation between slope and  $M/L$  ratio if  $t_{\text{dis}}^{\text{total}} < 1$  Gyr. In clusters with a longer total disruption time, both quantities are related. Dynamical cluster evolution is found to induce some reddening of the integrated cluster colours, amounting up to 0.1—0.2 mag in  $V - I$  for total disruption times  $t_{\text{dis}}^{\text{total}} < 1.5$  Gyr. The fraction of the cluster mass that is constituted by remnants surprisingly decreases if more black holes are retained, because the black holes preferentially eject bodies around the masses of white dwarfs and neutron stars, which contain most of the total remnant mass.

Contrary to what is suggested by other studies (e.g. Baumgardt & Makino 2003, Anders et al. 2009), the evolution of the MF is not homologous. The reason that these studies concluded that its evolution is very similar for all clusters (also see Figs. 7.6 and 7.7), is that they assumed that all remnants were retained. It is illustrated in Fig. 7.14 that the differences between clusters with dissimilar disruption times disappear when the retention fraction increases. For realistic retention fractions, differences do arise. If two clusters with different initial masses have the same total disruption time, their MF evolution will be dissimilar due to their different remnant retention fractions and the impact of the retained remnants on the dynamical cluster evolution. Alternatively, if two clusters have equal initial masses but different total disruption times, for instance due to differences in their galactic location or environment, their MF evolution will be dissimilar due to the dynamical impact of the evolution of the maximum stellar mass.

The larger variation of MF evolution that is found with presented model may also be able to explain observations of globular clusters in which the MF cannot be characterised by a single power law (De Marchi et al. 2000). If the evolution of the MF were homologous, these features would likely be primordial (Baumgardt & Makino 2003), but this is not necessarily the case when using realistic retention fractions. Most other differences between the results presented in Sect. 7.5 and those from Baumgardt & Makino (2003) are also due to their assumption of full remnant retention. For example, their  $M/L$  ratio evolution shows a smaller decrease than in Fig. 7.11. This is explained in Fig. 7.16, where it is shown that dynamical evolution reduces the  $M/L$  ratio by a smaller amount if the retention fraction is larger.

Studies on the fractal nature of cluster formation show that star clusters are initially substructured (Elmegreen 2000, Bonnell et al. 2003). Even though this substructure is typically erased on a crossing time, it can induce primordial mass segregation in star clusters (McMillan et al. 2007, Allison et al. 2009a). The influence of primordial mass segregation on the evolution of the MF has recently been investigated by Baumgardt et al. (2008) and Vesperini et al. (2009). While Baumgardt et al. (2008) do not include stellar evolution and concentrate

<sup>17</sup>This process differs from a possible variability of the proportionality between the velocity dispersion and the cluster mass, which concerns a much shorter timescale (e.g. Boily et al. 2009).

on two-body relaxation, Vesperini et al. (2009) do include stellar evolution. They show that for some degrees of primordial mass segregation, the mass loss by stellar evolution can induce additional dynamical mass loss that strongly decreases the total disruption time. For clusters that survive for a Hubble time, the MF evolution in the case of primordial mass segregation is very similar to an initially unsegregated cluster. Vesperini et al. (2009) conclude that the evolution of the MF is only affected by primordial mass segregation for clusters in which the total disruption time is sufficiently decreased by the induced mass loss. In that case, the slope of the MF remains much closer to its initial value than it would in clusters without primordial mass segregation. Their conclusion is consistent with the model presented in this chapter, because the evolution of the MF is determined by the most massive stars at the time when the largest mass loss occurs (see Figs. 7.4 and 7.9). This induced mass loss enters the model in terms of the absolute mass loss rate in Eq. 7.3, not in the stellar mass-dependent escape rate per unit mass loss rate of Eq. 7.13.

A change in total mass loss rate is not the only consequence of primordial mass segregation. Baumgardt et al. (2008) have shown that low-mass star depletion is enhanced for clusters without stellar evolution that are primordially mass-segregated. This occurs because energy equipartition is reached on a shorter timescale and because of their use of a fixed ( $m_{\max} = 1.2 M_{\odot}$ ) maximum stellar mass. As a result, there are no massive bodies to increase the escape rate of intermediate mass stars (see Fig. 7.5), implying that only the low-mass stars are preferentially lost. In the present chapter, mass segregation is assumed to arise dynamically, but the model could in principle be adapted to cover primordial mass segregation by setting  $c_2 = 0$  and adjusting  $c_1$  to the initial velocity distribution until it is erased by dynamical evolution (see Eq. 7.22), after which the values from Sect. 7.3 can be used.<sup>18</sup> This does not necessarily yield enhanced low-mass star depletion for clusters with a complete IMF (including masses  $m > 1.2 M_{\odot}$ ) because of the presence of massive stars or remnants.

The presented model can be applied to the MFs of Galactic globular clusters that are observed by De Marchi et al. (2007). These MFs are more strongly depleted than is found in the  $N$ -body simulations by Baumgardt & Makino (2003), which has been attributed to primordial mass segregation (Baumgardt et al. 2008). However, the observations can also very accurately be explained with the realistic remnant retention fractions that are used in the present chapter. This is shown in Fig. 7.19, where the observed MF slopes and remaining lifetimes of the globular clusters from De Marchi et al. (2007) are compared with the globular cluster-like models from Sect. 7.5.2 ( $t_0 = 1$  Myr). The models are in much better agreement with the data than the  $N$ -body runs with complete remnant retention from Baumgardt & Makino (2003). Deviations to other values of  $\alpha$  can occur due to variations in disruption time and remnant retention fractions, as is also shown in Fig. 7.19. For example, a variation of the remnant kick velocity with metallicity in combination with the known variation of the disruption time (see e.g. Kruijssen & Mieske 2009, Kruijssen & Portegies Zwart 2009) should be sufficient to cover the observed scatter.

The above line of reasoning provides an explanation for the depleted MFs in Fig. 7.19 that

---

<sup>18</sup>As explained in Sect 7.3,  $c_1$  represents the ratio of the mean speed squared to the central escape velocity squared that depends on the degree of mass segregation (and thus on the IMF). On the other hand,  $c_2$  is a proportionality constant in the expression for the onset of the stellar mass-dependent escape of stars, which depends on the concentration or King parameter.



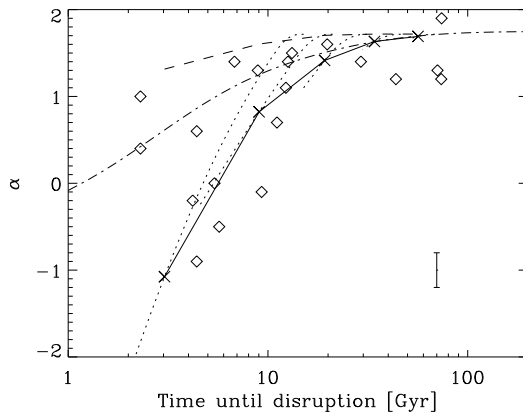


**Figure 7.19:** MF slope versus remaining lifetime (assuming a globular cluster age of 12 Gyr). Diamonds represent the observed values from De Marchi et al. (2007), with typical errors as shown by the error bar in the lower right corner. The remaining lifetimes are taken from Baumgardt et al. (2008). Dotted curves represent the model evolutionary tracks of clusters with  $\log(M_i/M_\odot) = \{6, 6.25, 6.5, 6.75, 7\}$  from Sect. 7.5.2 with  $\{\sigma_{\text{kick,wd}}, \sigma_{\text{kick,ns}}, \sigma_{\text{kick,bh}}\} = \{4, 100, 200\}$  km s $^{-1}$ , corresponding to  $\{f_{\text{ret,wd}}, f_{\text{ret,ns}}, f_{\text{ret,bh}}\} = \{0.983, 0.022, 0.003\}$  for a  $10^6 M_\odot$  cluster. The solid line connects the present-day locations of the modeled clusters in the diagram (crosses), while the dashed line represents the same relation for  $\sigma_{\text{kick,bh}} = 40$  km s $^{-1}$  ( $f_{\text{ret,bh}} = 0.219$  for a  $10^6 M_\odot$  cluster). The dash-dotted line shows the homologous cluster evolution from Baumgardt & Makino (2003).

is consistent with the simulations by Vesperini et al. (2009), who showed that the effects of primordial mass segregation are in fact suppressed in long-lived clusters due to the expansion caused by stellar evolution. This increases the relaxation time and yields an evolution of the MF that is very similar to the initially unsegregated scenario, indicating that primordial mass segregation is not a likely explanation for strongly depleted MFs. Observations of the remnant composition of these globular clusters could reveal a definitive answer as to whether the depleted MFs are explained by primordial mass segregation or by dynamical evolution with a realistic remnant retention fraction.

Dynamical cluster evolution does not appear to have a large effect on the colours of old (globular) clusters. The only way in which the colours could be affected beyond typical observational errors, is if globular clusters have lost substantial fractions of their masses during the first  $\sim$  Gyr after their formation. In that case, the dynamical evolution of the stellar MF in globular clusters may have implications for studies of colour bimodality (e.g. Larsen et al. 2001) or the blue tilt (e.g. Harris et al. 2006). It could then also possibly explain the trend of increasing  $V - K$  colour with decreasing  $M/L_V$  ratio found by Strader et al. (2009) for globular clusters in M31, because quickly dissolving clusters generally become redder and have reduced  $M/L$  ratios. More research is needed to determine the role of the changing MF in the above properties of globular cluster systems.

It can be concluded that the evolution of the stellar MF in star clusters is not as similar for all clusters as previously thought. Its precise evolution is determined by cluster characteristics like the disruption time, the remnant retention fraction, initial-final stellar mass relation, and the IMF. In order to decipher the evolution of observed star clusters, it is essential to record these characteristics and to relate them to possible scenarios for the internal evolution of clusters. That way, observables like the slope of the MF, the  $M/L$  ratio, the broadband colours, and the mass fraction in remnants can be better understood.

**Acknowledgements** I thank Henny Lamers and Simon Portegies Zwart for support, advice and constructive comments on the manuscript. I also thank Douglas Heggie for inspiring suggestions during the KITP conference on globular clusters in Santa Barbara and for commenting on the manuscript. Holger Baumgardt is acknowledged for interesting discussions and for kindly providing the data from Baumgardt & Makino (2003) and Baumgardt et al. (2008). I would like to thank Nate Bastian, Mark Gieles and Peter Kruijssen for constructive comments on the manuscript. I am indebted to Mark Gieles for kindly providing  $N$ -body runs for different IMFs. The referee, Thijs Kouwenhoven, is thanked for thoughtful comments. The Institute of Astronomy in Cambridge is gratefully acknowledged for their kind hospitality during my visit, when a large part of this work was carried out. This research is supported by the Netherlands Organisation for Scientific Research (NWO), grant number 021.001.038.

# **Part C – The co-evolution of star clusters and galaxies**



# Chapter 8

---

## Modelling the formation and evolution of star cluster populations in galaxy simulations

J. M. Diederik Kruijssen, F. Inti Pelupessy, Henny J. G. L. M. Lamers,  
Simon F. Portegies Zwart and Vincent Icke  
*Monthly Notices of the Royal Astronomical Society*, in press (2011)<sup>†</sup>

**Abstract** The formation and evolution of star cluster populations are related to the galactic environment. Cluster formation is governed by processes acting on galactic scales, and star cluster disruption is driven by the tidal field. In this chapter, we present a self-consistent model for the formation and evolution of star cluster populations, for which we combine an  $N$ -body/SPH galaxy evolution code with semi-analytic models for star cluster evolution. The model includes star formation, feedback, stellar evolution, and star cluster disruption by two-body relaxation and tidal shocks. The model is validated by a comparison to  $N$ -body simulations of dissolving star clusters. We apply the model by simulating a suite of 9 isolated disc galaxies and 24 galaxy mergers. The evolutionary histories of individual clusters in these simulations are discussed to illustrate how the environment of clusters changes in time and space. It is found that the variability of the disruption rate with time and space affects the properties of star cluster populations. In isolated disc galaxies, the mean age of the clusters increases with galactocentric radius. The combined effect of clusters escaping their dense formation sites ('cluster migration') and the preferential disruption of clusters residing in dense environments ('natural selection') implies that the mean disruption rate of the population decreases with cluster age. This affects the slope of the cluster age distribution, which becomes a function of the star formation rate density (star formation rate per unit volume). The evolutionary histories of clusters in a galaxy merger vary widely and determine which clusters survive the merger. Clusters that escape into the stellar halo experience low disruption rates, while clusters orbiting near the starburst region of a merger are disrupted on short timescales due to the high gas density. This impacts the age distributions and the locations of the surviving clusters at all times during a merger. The chapter includes a discussion of potential improvements for the model and a brief exploration of possible applications. We conclude that accounting for the interplay between the formation, disruption, and orbital histories of clusters enables a more sophisticated interpretation of

---

<sup>†</sup>Reproduced with permission © RAS.

observed properties of cluster populations, thereby extending the role of cluster populations as tracers of galaxy evolution.

## 8.1 Introduction

It is one of the central aims in current astrophysics to constrain the formation and evolution of galaxies, and their assembly through hierarchical merging (e.g. Sanders & Mirabel 1996, Kennicutt 1998a, Cole et al. 2000, Conselice et al. 2003, Kauffmann et al. 2003, van Dokkum 2005, McConnachie et al. 2009, Hopkins et al. 2010). Galaxy mergers play a fundamental role in hierarchical cosmology (White & Rees 1978), introducing the evolution of the galaxy population as a prime tool to verify cosmological models (e.g. Kauffmann et al. 1993, Somerville & Primack 1999, Bell et al. 2005). Since the late 1980s, observational studies have uncovered a wealth of stellar clusters in galaxy interactions. Because star clusters are easily observed up to distances of several tens of megaparsecs, it is often said that star clusters can be used to probe the formation and evolution of galaxies. This would enable the reconstruction of the merger histories of their parent galaxies (Schweizer 1987, Ashman & Zepf 1992, Schweizer & Seitzer 1998, Larsen et al. 2001, Bastian et al. 2005).

The differences between populations of young (massive) star clusters and globular cluster systems show the impact of nearly a Hubble time of evolution (e.g. Elmegreen & Efremov 1997, Vesperini 1998, 2001, Fall & Zhang 2001, Kruijssen & Portegies Zwart 2009), under the assumption that globular clusters initially shared most of the properties of current young star clusters (e.g. Elmegreen & Efremov 1997). These differences suggest that cluster populations can indeed be used to trace galaxy evolution, especially because their formation and evolution are known to be governed by their galactic environment (Spitzer 1987, Ashman & Zepf 1992, Baumgardt & Makino 2003, Lamers et al. 2005b, Gieles et al. 2006b). It is therefore crucial to assess *how* a cluster population is affected by environmental effects.

There have been substantial efforts in theoretical studies to describe the formation and evolution of star cluster systems. Possible formation sites of star clusters in general and globular clusters in particular have been addressed in theoretical studies (e.g. Harris & Pudritz 1994, Elmegreen & Efremov 1997, Shapiro et al. 2010) and numerical simulations (Bekki et al. 2002, Li et al. 2004, Bournaud et al. 2008, Renaud et al. 2008). These studies all point to gas-rich environments with high pressures and densities as the possible formation sites of rich star cluster systems. However, they do not reproduce populations of star clusters and globular clusters that are presently observed, because they focus on cluster formation and either contain only a very simplified description for star cluster evolution or none at all. As they age, star clusters leave their primordial regions and dynamically decouple from the gas of their formation sites. More importantly, star clusters experience extensive dynamical evolution after their formation, which shapes the characteristics of the star cluster populations that are observed today.

Theoretical and numerical studies on the evolution of star clusters have shown that clusters dissolve due to two-body relaxation in a steady tidal field (e.g. Spitzer 1987, Fukushige & Heggie 2000, Portegies Zwart et al. 2001, Baumgardt & Makino 2003) and due to heating by tidal shocks (e.g. Spitzer 1958, Ostriker et al. 1972, Chernoff et al. 1986, Spitzer 1987,

Aguilar et al. 1988, Chernoff & Weinberg 1990, Kundic & Ostriker 1995, Gnedin & Ostriker 1997, Gieles et al. 2006b). This dynamical evolution leaves a pronounced imprint on the population that survives disruption. In particular, the age and mass distributions of star cluster populations have emerged as excellent tools to trace the disruption histories of clusters (e.g. Vesperini 2001, Fall & Zhang 2001, Lamers et al. 2005a, Prieto & Gnedin 2008). This implies that the strength of the disruption processes will determine how and to what extent the characteristics of evolved cluster populations still trace the conditions of their formation.

The census of the formation and evolution of star clusters has been applied to populations of star clusters in several studies that focus on the modeling of the observed cluster age and mass (or luminosity) distributions (e.g. Elmegreen & Efremov 1997, Boutloukos & Lamers 2003, Hunter et al. 2003, Gieles et al. 2005, Lamers et al. 2005a, Smith et al. 2007, Larsen 2009). These studies show that the disruption rate of star clusters varies among different galaxies, and also that peaks in the age distributions of star clusters can be used to trace interaction-induced starbursts. Interestingly, the galaxy sample for which the typical disruption rates have been derived shows higher disruption rate for galaxies with high star formation rates.

The above analyses of the formation and disruption of cluster populations are based on two key assumptions:

- (1) The formation rate of stars and clusters is assumed to be constant throughout a galaxy and often also in time. If not assumed constant in time, it is parameterised with a simple function, often a sequence of step functions.
- (2) The disruption rate of star clusters is assumed to be constant throughout a galaxy and in time.

While these assumptions can be made for a first-order approach to the formation and evolution of star cluster populations, it is known from theoretical principles of star formation and cluster disruption that they do not hold in actual galaxies. Particularly the observation that the disruption rate of star clusters varies among different galaxies shows that it should also vary within a galaxy: for individual clusters as they pass through different galactic regions, but also for the entire cluster population as a galaxy evolves. The variation with time and space of the cluster formation and disruption rates may or may not affect the observable properties of star cluster populations.

Galaxy interactions provide a clear example of the formation and destruction of cluster populations and the dependence thereof on the local galactic environment. Large numbers of star clusters are formed in the nuclear starbursts occurring during galaxy interactions (Holtzman et al. 1992, Whitmore & Schweizer 1995, Schweizer et al. 1996, Whitmore et al. 1999). These starbursts are triggered by the angular momentum loss of the gas in the progenitor galaxy discs and the subsequent inflow of the gas (Hernquist 1989, Mihos & Hernquist 1996, Hopkins et al. 2006). As a result, the gas density in certain locations within galaxy mergers is very high. It was shown by Gieles et al. (2006b) that star clusters are efficiently disrupted by the tidal shocks that arise when they gravitationally interact with passing giant molecular clouds (GMCs). Because the GMC density in central regions of galaxy mergers is high, we should expect tidal disruption to be important. This leaves us with the possible, intriguing combination of the enhanced formation and destruction of star clusters during certain

episodes in the hierarchical buildup of galaxies (see Kruijssen et al. 2011b). The violent circumstances in the nuclear region contrast with the outer regions of a galaxy merger, where cluster formation and destruction proceed more temperately.

In general, the galactic conditions under which star cluster populations have been formed and have evolved over the history of the universe may have varied widely (e.g. Reddy & Steidel 2009). The use of star cluster populations to trace galactic histories would therefore benefit from a thorough understanding of the co-formation and co-evolution of galaxies and star clusters. Such a census can only be achieved by simultaneously assessing all relevant physical mechanisms, i.e. combining the formation and evolution of star clusters in a single model and allowing for variations with environment.

A thorough way of modeling cluster evolution would be to perform collisional  $N$ -body simulations of the evolving cluster population in a changing galactic tidal field. This has been done in several studies, for a limited range of cluster masses, orbits and tidal histories (e.g. Vesperini & Heggie 1997, Baumgardt & Makino 2003, Praagman et al. 2010). However, these papers only consider the effects of smooth potentials and ignore the disruptive effect of GMCs and other substructure in the gas distribution, thereby limiting the application of such models to globular cluster systems and extremely gas-poor galaxies. Moreover,  $N$ -body modeling is computationally so expensive that it is not possible to calculate the evolution of the millions of clusters that are formed during the lifetime of a galaxy. In order to self-consistently compute the formation and evolution of an entire cluster population, the best approach would be to implement semi-analytic cluster models in numerical simulations of galaxies.  $N$ -body simulations of dissolving clusters in time-dependent tidal fields can then be used to provide benchmarks for the semi-analytic cluster evolution models.

In this chapter, we aim to self-consistently model the formation and evolution of cluster populations in numerical simulations of (interacting) galaxies. For that purpose, we have combined semi-analytic star cluster models (SPACE, Kruijssen & Lamers 2008, Kruijssen 2009) with an  $N$ -body/Smoothed Particle Hydrodynamics (SPH) code for modeling galaxies (Stars, Pelupessy et al. 2004, Pelupessy 2005). As discussed above, the physical mechanisms that play a role in the formation and evolution of star clusters have all been studied separately in detail. Combining them should allow us to obtain a better picture of how different galactic environments affect their star cluster populations.

Prieto & Gnedin (2008) combined cosmological simulations with a semi-analytic description for the dynamical evolution of globular clusters. Their aim was to model the population of globular clusters from high redshift to the present day, and not the self-consistent modeling of the entire star cluster population including a range of destruction and formation mechanisms in different galactic environments. Particular examples of differences with our approach are the following:

- (1) We include clusters with masses down to a fiducial lower mass limit of  $100 M_{\odot}$ . In Prieto & Gnedin (2008), only clusters with initial masses  $M_i > 10^5 M_{\odot}$  are considered. While this does not influence the present day globular cluster system due to the destruction of lower mass clusters over nearly a Hubble time of evolution, it does obstruct the modeling of young (globular) cluster populations, in which the cluster masses do go down to a physical lower mass limit of around  $100 M_{\odot}$  (see e.g. Portegies Zwart et al.



2010).

- (2) In our simulations, the clusters are continuously formed at the sites of star formation that are calculated in the  $N$ -body/SPH simulation. This is one of the main aspects of our model that enables a self-consistent modeling of the formation and evolution of the cluster population. Conversely, Prieto & Gnedin (2008) assume that the initial distribution of clusters follows the distribution of the baryonic surface density, which does not necessarily match sites of star and cluster formation.
- (3) In our cluster evolution model, the dynamical mass loss rate of clusters due to two-body relaxation depends on environmental effects, because it is known that the tidal field strength determines the mass loss rate (see e.g. Baumgardt & Makino 2003). This aspect of cluster disruption was not included by Prieto & Gnedin (2008).

Smaller differences include the exact prescription for mass loss from clusters due to tidal shocks and the evolution of the cluster half-mass radius.

The chapter is structured as follows. In Sect. 8.2, we first discuss the simulation code, divided in a section on the galaxy ( $N$ -body/SPH) model, and a section on the derivation, construction and testing of the star cluster evolution model. The model runs are summarised in Sect. 8.3, while some key results are presented in Sects. 8.4 (isolated disc galaxies) and 8.5 (galaxy mergers). The chapter is concluded with a summary and a discussion of possible improvements and potential applications of the model.

Throughout the chapter, we adopt a standard  $\Lambda$ CDM cosmology and follow the consensus values after the WMAP results (e.g. Spergel et al. 2007), with vacuum energy and matter densities  $\Omega_\Lambda = 0.7$  and  $\Omega_M = 0.3$ , and present-day Hubble constant  $H_0 = 70 \text{ km s}^{-1} \text{ Mpc}^{-1}$ .

## 8.2 Simulation code

Our simulations are performed using a collisionless  $N$ -body/SPH code in which the formation and evolution of star clusters are included as a sub-grid model. The simulated galaxies contain particles for the stellar, gaseous and dark matter components.

### 8.2.1 Galaxy model

The evolution of the stellar and dark matter components are governed by pure collisionless Newtonian dynamics, calculated using the Barnes-Hut tree method (Barnes & Hut 1986). The particles sample the underlying phase space distribution of positions and velocities and are smoothed on length scales of approximately 0.2 kpc to maintain the collisionless dynamics and to reduce the noise in the tidal field (which is used for the cluster evolution, see 8.2.2). The Euler equations for the gas dynamics are solved using smoothed particle hydrodynamics, a Galilean invariant Lagrangian method for hydrodynamics based on a particle representation of the fluid (Monaghan 1992), in the conservative formulation of Springel & Hernquist (2002). This is supplemented with a model for the thermodynamic evolution of the gas in order to represent the physics of the interstellar medium (ISM). Photo-electric heating of UV

radiation from young stars is included (assuming optically thin transport of non-ionizing photons). The UV field is calculated from stellar UV luminosities derived from stellar population synthesis models (Bruzual & Charlot 2003). Line cooling from eight elements (the main constituents of the ISM H and He as well as the elements C, N, O, Ne, Si and Fe) is included. We calculate ionization equilibrium including cosmic ray ionization. Further details of the ISM model can be found in Pelupessy et al. (2004) and Pelupessy (2005).

Star formation is implemented by using a gravitational instability criterion based on the local Jeans mass  $M_J$ :

$$M_J \equiv \frac{\pi \rho}{6} \left( \frac{\pi s^2}{G \rho} \right)^{3/2} < M_{\text{ref}}, \quad (8.1)$$

where  $\rho$  is the local density,  $s$  the local sound speed,  $G$  the gravitational constant and  $M_{\text{ref}}$  a reference mass scale (chosen to correspond to observed giant molecular clouds). This selects cold, dense regions for star formation, which then form stars on a timescale  $\tau_{\text{sf}}$  that is set to scale with the local free fall time  $t_{\text{ff}}$ :

$$\tau_{\text{sf}} = f_{\text{sf}} t_{\text{ff}} = \frac{f_{\text{sf}}}{\sqrt{4\pi G \rho}}, \quad (8.2)$$

where the delay factor  $f_{\text{sf}} \approx 10$ . Numerically, the code stochastically spawns stellar particles from gas particles that are unstable according to Eq. 8.1 with a probability  $1 - \exp(-dt/\tau_{\text{sf}})$ . The code also assigns a formation time for use by the stellar evolution library, and sets the initial stellar and cluster population mass distributions (see below). Mechanical heating of the interstellar medium by stellar winds from young stars and supernovae is implemented by means of pressure particles (Pelupessy et al. 2004, Pelupessy 2005), which ensures the strength of feedback is insensitive to numerical resolution effects. In this way, the global efficiency of star formation is determined by the number of young stars needed to quench star formation by UV and supernova heating, which is set by the cooling properties of the gas and the energy input from the stars.

## 8.2.2 Star cluster model

### Cluster formation

Star clusters are formed in the simulations when a Jeans-unstable gas particle produces a star particle as described above. It is presently not possible to simulate clusters as individual particles for the full cluster mass range, because even with modern computational facilities it would require following too many particles to allow reasonable computation times. Therefore, we choose to spawn the star clusters as the “sub-grid” content of a new-born star particle. Their masses are generated from a power law distribution with an exponential truncation at high masses (Schechter 1976):

$$NdM \propto M^{-2} \exp(-M/M_*) dM, \quad (8.3)$$

where  $N$  is the number of clusters,  $M$  is the cluster mass, and  $M_* = 2.5 \times 10^6 M_\odot$  is the adopted exponential truncation mass, which is needed to explain the present day mass function of Galactic globular clusters (see e.g. Kruijssen & Portegies Zwart 2009). We allocate

90% of the new-born particle mass for the star clusters (the “cluster formation efficiency” or CFE). Because we adopt a single value of the CFE for all particles, its precise value is not important and merely acts as a normalisation of the number of clusters. The remaining 10% of the mass is considered to be born in unbound associations of stars that immediately disperse into the field after they are formed<sup>1</sup>. This dispersion does not occur physically in the simulation, because the star particle contains both the field stars and the star clusters. All stars have masses distributed according to a Kroupa (2001) IMF in the mass range  $0.08 M_{\odot} - m_{\max}$ , where  $m_{\max}$  is the maximum stellar mass at  $\log(t/\text{yr}) = 6.6$  (which is the minimum age of the adopted stellar evolution models, see Sect. 8.2.2).

Owing to the sub-grid nature of the cluster implementation, the maximum mass of the formed star clusters is determined by the gas particle mass, star formation efficiency<sup>2</sup> and CFE, as the mass of a single cluster can not exceed the mass of the star particle it is part of. As a result, the typical maximum cluster mass is  $\log(M/M_{\odot}) \approx 5.8$ . We have chosen the number of particles in the simulation such as to optimally cover the cluster mass range of interest and to have sufficient numerical resolution. An algorithm that allows for simultaneous star formation in groups of gas particles is being included in a future study.

### Cluster evolution

After their formation, star clusters evolve by losing mass by stellar evolution and dynamical evolution. The star cluster evolution is computed with the SPACE models (Kruijssen & Lamers 2008, Kruijssen 2009), which include a semi-analytic description of the evolution of cluster mass and its stellar content. They include stellar evolution from the Padova models (Marigo et al. 2008), stellar remnant production, remnant kick velocities (e.g. Lyne & Lorimer 1994), dynamical disruption (Lamers et al. 2005a) and the evolution of the stellar mass function owing to the stellar mass dependence of the ejection rate of stars from the cluster (Kruijssen 2009). The total mass loss rate is constituted by the contribution from stellar evolution,  $(dM/dt)_{\text{ev}}$ , and the contribution from tidal disruption,  $(dM/dt)_{\text{dis}}$ :

$$\left(\frac{dM}{dt}\right) = \left(\frac{dM}{dt}\right)_{\text{ev}} + \left(\frac{dM}{dt}\right)_{\text{dis}}. \quad (8.4)$$

The mass loss due to stellar evolution is computed using the Padova isochrones by following the decrease of the maximum stellar mass over one timestep, and integrating the mass function within the cluster over the corresponding mass interval. This method assumes the instantaneous removal of stars and ignores the gradual nature of stellar winds. Stars typically only lose mass during the last  $\sim 10\%$  of their lifetime, during which the maximum stellar mass decreases by merely a few percent, and the total cluster mass by even less. The mass loss rates of the most massive stars are also comparable during the enclosed time interval, which implies that the instantaneous removal of the most massive stars is balanced by the delay of mass loss from slightly less massive stars. This ensures that the obtained mass loss rate is very similar to the actual rate due to stellar winds and supernovae at any time (see e.g.

<sup>1</sup>We do not distinguish between the formation of unbound field stars and the early disruption of star clusters during gas expulsion, which is known as “infant mortality” (Lada & Lada 2003, Goodwin & Bastian 2006).

<sup>2</sup>This is the fraction of the gas mass that is used to form the star particle.

Kruijssen & Lamers 2008). We include the production and retention of stellar remnants as discussed in Kruijssen (2009).

The mass loss rate due to disruption is driven by two-body relaxation and tidal shocks:

$$\left(\frac{dM}{dt}\right)_{\text{dis}} = \left(\frac{dM}{dt}\right)_{\text{rlx}} + \left(\frac{dM}{dt}\right)_{\text{sh}}, \quad (8.5)$$

where the subscripts ‘dis’, ‘rlx’, and ‘sh’ denote disruption, two-body relaxation and tidal shocks, respectively. We now describe the contributions from both mass loss mechanisms<sup>3</sup>.

The mass loss rate due to two-body relaxation is determined by the strength of the tidal field and the cluster mass (Baumgardt & Makino 2003, Gieles & Baumgardt 2008). To describe the mass loss, we adopt the semi-analytic approach of Lamers et al. (2005a) that has been extensively tested against  $N$ -body simulations of dissolving star clusters and observations (e.g. Lamers et al. 2005b, Gieles et al. 2005, Bastian et al. 2005, Lamers & Gieles 2006). The mass decreases exponentially on a disruption timescale that decreases as the cluster mass decreases  $t_{\text{dis}} \equiv (d \ln M / dt)^{-1}$ :

$$\left(\frac{dM}{dt}\right)_{\text{rlx}} = -\frac{M}{t_{\text{dis}}} = -\frac{M^{1-\gamma}}{t_0}, \quad (8.6)$$

where the disruption timescale is given by  $t_{\text{dis}} = t_0 M^\gamma$ . Here, the exponent  $\gamma = 0.6\text{--}0.8$  is the mass dependence of the disruption timescale, and increases with the King parameter  $W_0$  of the cluster density profile (Baumgardt & Makino 2003, Lamers et al. 2010). The normalisation constant  $t_0$  is the dissolution timescale parameter, which sets the rapidity of the disruption and is determined by the tidal field<sup>4</sup>. For clusters on circular orbits in a logarithmic potential,  $t_0$  has been related to the angular frequency of the orbit, and subsequently to the ambient density  $\rho_{\text{amb}}$  as  $t_0 \propto \rho_{\text{amb}}^{-1/2}$  (Baumgardt & Makino 2003, Lamers et al. 2005b). The physical driving force behind cluster disruption is the tidal field. According to Poisson’s law, the tidal field strength  $T$  is proportional to the ambient density, implying a more fundamental relation:

$$t_0 = t_{0,\odot} (T/T_\odot)^{-1/2}, \quad (8.7)$$

where  $t_{0,\odot}$  is the dissolution timescale in a logarithmic potential at the galactocentric radius of the sun  $R_{\text{ge},\odot}$  and  $T_\odot \approx 7.01 \times 10^2 \text{ Gyr}^{-2}$  is the tidal field strength at that location for a circular velocity of  $220 \text{ km s}^{-1}$ . For  $\gamma = 0.62$  one obtains  $t_{0,\odot} = 21.3 \text{ Myr}$ , while for  $\gamma = 0.70$  we have  $t_{0,\odot} = 10.7 \text{ Myr}$  (Kruijssen & Mieske 2009). We adopt a density profile with King parameter  $W_0 = 5$  for the clusters and consequently  $\gamma = 0.62$ . This ‘typical’ King

<sup>3</sup>We neglect a third mass loss mechanism, namely the dynamical mass loss that is induced by the shrinking of the Jacobi radius resulting from the mass loss due to stellar evolution (Lamers et al. 2010). This is allowed if clusters initially do not fill their Roche lobes. In the irregular tidal fields that we are considering, the Jacobi radius constantly changes. This implies that the equilibrium situation of a cluster filling its Roche lobe is unlikely to occur.

<sup>4</sup>Throughout the chapter, we do not only use the term ‘disruption time(scale)’, but also the more intuitive ‘disruption rate’, which is related to the inverse of the timescale. While the disruption timescale is specific to the properties of a cluster and depends on its mass and (for tidal shocks) half-mass radius, the term ‘disruption rate’ is used to refer to the general ‘disruptiveness’ of the environment.

parameter is consistent with observations of open clusters (Portegies Zwart et al. 2010) and rapidly dissolving globular clusters (McLaughlin & van der Marel 2005, Kruijssen & Mieske 2009). Clusters with lower King parameters ( $W_0 \sim 3$ ) are susceptible to rapid disruption due to stellar evolution-induced mass loss (Fukushige & Heggie 1995, Baumgardt & Makino 2003, Lamers et al. 2010), while high King parameters of  $W_0 \gtrsim 7$  are typically achieved after core collapse of the most massive systems such as old globular clusters. To illustrate the influence of the concentration on cluster disruption, we also consider the case of  $W_0 = 7$  in the rest of the derivation of the model.

To determine the tidal field strength, we first evaluate the tidal field tensor

$$T_{ij} = -\frac{\partial^2 \Phi}{\partial x_i \partial x_j}, \quad (8.8)$$

where  $\Phi$  is the gravitational potential and  $x_i$  is the  $i$ -th component of the position vector. In the simulations, the tidal tensor is computed by numerical differentiation of the force field, which is smoothed on scales of 200 pc, thereby minimising the sensitivity of the evolution of the star clusters to discreteness noise. We use 1% of the smoothing length for the differentiation interval. The tidal tensor has three eigenvectors, which denote the principal axes of the action of the tidal field. The corresponding eigenvalues represent the magnitude of the force gradient along these axes, with negative eigenvalues denoting compressive components of the tidal field, and positive eigenvalues indicating extensive components (e.g. Renaud et al. 2008). The tidal field strength  $T$ , i.e. the quantity that sets the tidal boundary of the cluster, is thus equal to the largest eigenvalue of the tidal tensor. If the tidal field is fully compressive, i.e. all eigenvalues of the tidal tensor are negative, we assume  $(dM/dt)_{\text{tlx}} = 0$ . The eigenvalues are computed with the routines by Kopp (2008).

Tidal shocks disrupt star clusters by increasing the energy of the stars that are bound to the cluster. It was shown by Kundic & Ostriker (1995) that the first- and second-order energy inputs induced by tidal shocks contribute more or less equally to the disruption of star clusters, while higher-order terms can be neglected. For the mass loss rate due to tidal shocks we write

$$\left(\frac{dM}{dt}\right)_{\text{sh}} = -\frac{M}{t_{\text{sh}}}, \quad (8.9)$$

where  $t_{\text{sh}}$  denotes the disruption time for tidal shocks. It can be separated in the disruption times due to the first- and second-order energy input,  $t_{\text{sh},1}$  and  $t_{\text{sh},2}$ :

$$t_{\text{sh}} = \left(t_{\text{sh},1}^{-1} + t_{\text{sh},2}^{-1}\right)^{-1}. \quad (8.10)$$

Both components of the disruption time depend on several properties of the cluster and its environment, and will change over time.

The derivation of  $t_{\text{sh}}$  has been treated extensively in literature (e.g. Spitzer 1958, 1987, Ostriker et al. 1972, Kundic & Ostriker 1995, Gnedin & Ostriker 1997, Gieles et al. 2007a, Prieto & Gnedin 2008), though the details of these approaches differ. For example, some studies correctly observe that not all of the energy input by the tidal shock is converted into

mass loss (Gieles et al. 2007a), while others add the second-order disruption component  $t_{\text{sh},2}$  (Kundic & Ostriker 1995). Also, most studies consider the tidal perturbation of clusters on closed orbits, for which the frequency of disc and bulge shocks is predictable. However, for more erratic tidal shocks,  $t_{\text{sh}}$  should be linked to the tidal field (Prieto & Gnedin 2008). Especially when modeling the evolution of star clusters in galaxy mergers this is an important improvement. We follow the lines of most of the above studies, and combine their refinements.

We first compute the first-order disruption timescale due to tidal shocks, which can be expressed as (e.g. Gieles et al. 2007a):

$$t_{\text{sh},1} = \frac{\Delta t}{f} \left| \frac{E}{\Delta E} \right|, \quad (8.11)$$

where  $E$  denotes the cluster energy<sup>5</sup> per unit mass and  $\Delta t$  is the time since the previous shock. The parameter  $f$  is the fraction of the relative energy change that is converted to a change in cluster mass. This number is smaller than unity, because stars escape the cluster with velocities above the escape velocity. It is defined as  $f \equiv d \ln M / d \ln E$ , and has been found to be  $f \simeq 0.25$  for two-dimensional (2D) shocks<sup>6</sup> (Gieles et al. 2006b). The internal energy per unit cluster mass  $E$  is given by

$$E = -\frac{\eta GM}{2r_{\text{h}}}, \quad (8.12)$$

with  $\eta \simeq 0.4$  a proportionality constant (e.g. Spitzer 1987),  $G$  the gravitational constant, and  $r_{\text{h}}$  the half-mass radius of the cluster.

We combine the approaches of Gieles et al. (2007a) and Prieto & Gnedin (2008) to express the average energy change  $\Delta E$  of the ensemble of stars in the cluster as a function of their average radial position  $r$  and the tidal heating parameter  $I_{\text{tid}}$ :

$$\Delta E = \frac{1}{2}(\Delta v)^2 = \frac{1}{6}I_{\text{tid}}\overline{r^2}. \quad (8.13)$$

The tidal heating parameter is written as a function of the tidal tensor (Gnedin et al. 1999, Prieto & Gnedin 2008):

$$I_{\text{tid}} = \sum_{i,j} \left( \int T_{ij} dt \right)^2 A_{\text{w},ij}(x), \quad (8.14)$$

in which the integration is performed over the duration of the tidal shock for the particular component of the tidal tensor. The factor  $A_{\text{w},ij}(x)$  represents a parameterised version of the Weinberg adiabatic correction (Weinberg 1994a,b,c). It is defined for each component of the tidal tensor and describes the absorption of the energy injection by the adiabatic expansion of

<sup>5</sup>This is the sum of the internal kinetic energy and the internal potential.

<sup>6</sup>Most tidal shocks occur in the orbital plane of the interaction between the cluster and the perturbing object, e.g. a GMC. This corresponds to a 2D shock. A 1D shock resembles a head-on encounter with the perturbing object, which is relatively rare compared to a more distant passage.

the cluster. The adiabatic correction depends on the product of the average angular frequency of the stars within the cluster  $\bar{\omega}$  and the timescale  $\tau_{ij}$  of the shock for the corresponding component of the tidal tensor (Gnedin & Ostriker 1997, 1999):

$$A_{w,ij} = (1 + \bar{\omega}^2 \tau_{ij}^2)^{-3/2}. \quad (8.15)$$

The value of  $\bar{\omega}$  is constant when expressed in  $N$ -body units (Heggie & Mathieu 1986, Gieles et al. 2007a), but when converted back to physical units it becomes:

$$\bar{\omega} = C_\omega \sqrt{\frac{8\eta^3 GM}{r_h^3}}, \quad (8.16)$$

where  $C_\omega$  denotes a proportionality constant, which for King parameters  $W_0 = \{5, 7\}$  is  $C_\omega = \{0.68, 0.82\}$  (Gieles et al. 2007a). The timescale of the shock  $\tau_{ij}$  is the time interval in which the corresponding component of the tidal tensor drops by 39%, coinciding with the definition of one standard deviation in a Gaussian distribution.

Substitution of Eqs. 8.12—8.14 in Eq. 8.11 now gives the disruption timescale due to the first-order effects of tidal shocks:

$$t_{\text{sh},1} = \frac{3\eta}{f} \frac{GM}{r_h^3} \frac{r_h^2}{r^2} I_{\text{tid}}^{-1} \Delta t, \quad (8.17)$$

with the ratio  $r^2/r_h^2 = \{2, 3.5\}$  for King profile parameters  $W_0 = \{5, 7\}$  (Gieles et al. 2006b). This equation should be complemented with the disruption timescale due the second-order energy input, or “shock-induced relaxation” (Kundic & Ostriker 1995), which is expressed as

$$t_{\text{sh},2} = \frac{\Delta t}{f} \left| \frac{E^2}{(\Delta E)^2} \right|, \quad (8.18)$$

where  $(\Delta E)^2$  denotes the stellar ensemble-averaged mean square energy change. Following Kundic & Ostriker (1995), we write

$$(\Delta E)^2 = \overline{(v\Delta v)^2} = \frac{1}{5} I_{\text{tid}} \overline{\omega^2 r^4}. \quad (8.19)$$

The stellar ensemble-average  $\overline{\omega^2 r^4}$  then follows:

$$\overline{\omega^2 r^4} = \overline{GM(r)r} \equiv \zeta GM r_h, \quad (8.20)$$

where  $M(r)$  represents the mass within radius  $r$ , and the constant  $\zeta$  is defined as

$$\zeta \equiv \frac{\overline{M(r)r}}{M r_h}. \quad (8.21)$$

For King profile parameters  $W_0 = \{5, 7\}$  the values are  $\zeta = \{0.81, 1.03\}$  (M. Gieles, private communication).

Substitution of Eqs. 8.12 and 8.19 in Eq. 8.18 now gives the disruption timescale due to the second-order effects of tidal shocks:

$$t_{\text{sh},2} = \frac{5\eta^2 GM}{4f\zeta r_{\text{h}}^3} I_{\text{tid}}^{-1} \Delta t = \frac{5\eta}{12\zeta} \frac{\bar{r}^2}{r_{\text{h}}^2} t_{\text{sh},1}. \quad (8.22)$$

Using Eq. 8.10, the disruption time due to the combined first- and second order effects of tidal shocks then becomes:

$$t_{\text{sh}} = (t_{\text{sh},1}^{-1} + t_{\text{sh},2}^{-1})^{-1} = \left(1 + \frac{12\zeta r_{\text{h}}^2}{5\eta \bar{r}^2}\right)^{-1} t_{\text{sh},1} \equiv C_{\text{sh}} t_{\text{sh},1}, \quad (8.23)$$

where for  $W_0 = \{5, 7\}$  we have  $C_{\text{sh}} = \{0.29, 0.36\}$ , indicating that the contribution of the second-order energy input is most important for low-concentration clusters. The mass loss due to shocks is applied upon the completion of a shock in any of the components of the tidal tensor. Numerically, this means that  $I_{\text{tid}} = 0$  unless a shock is completed, i.e. one of the components of  $|T_{ij}|$  reaches a minimum that is at most 88% of the preceding maximum<sup>7</sup>.

We have thus far not defined any prescription for the half-mass radius  $r_{\text{h}}$ . In semi-analytic models that do not contain any information regarding the structural evolution of star clusters, this is often related to the (initial) mass according to a power law relation:

$$r_{\text{h}} = r_{\text{h},4} \left( \frac{M_{(i)}}{10^4 M_{\odot}} \right)^{\delta}, \quad (8.24)$$

where  $r_{\text{h},4}$  is the half-mass radius of a  $10^4 M_{\odot}$  cluster,  $M_{(i)}$  represents the (initial) cluster mass, and  $\delta$  is the power law index. The disruption timescale due to tidal shocks  $t_{\text{sh}}$  and the adiabatic correction  $A_{\text{w}}$  both depend on the half-mass radius of the cluster (see Eqs. 8.15 and 8.17), implying that the value of  $\delta$  influences the mass dependence of  $t_{\text{sh}}$ . It is therefore important to include a reliable prescription for the half-mass radius. We have tested several dependences of  $r_{\text{h}}$  on the initial and present cluster mass when comparing the models to the  $N$ -body simulations by Baumgardt & Makino (2003). The best agreement is found for  $\delta = 0.225$  and  $r_{\text{h},4} = 4.35$  pc, and when using the present-day mass (see Sect. 8.2.2). These parameters are within an acceptable range of the ‘mass loss-dominated mode’ of the radius evolution reported in Gieles et al. (2011).

It should be emphasised that the mass-radius relation quoted in Eq. 8.24 does not have the same meaning as the mass-radius relation that can be observed for real star cluster populations (e.g. Larsen 2004). Instead, it approximates the evolution of the half-mass radius for a single cluster, given a certain initial radius. In a population of star clusters, which is constituted by clusters of a range of ages, initial masses, initial radii, and mass loss histories, the resulting mass-radius relation of the entire population may be very different, as it is set by the collection of states in which these different clusters happen to exist at the time of the observation. When using a power law formulation, both types of mass-radius relation will only be similar if the initial half-mass radius of the clusters is also set by the cluster mass as in Eq. 8.24. For mathematical simplicity, we do choose to set the initial half-mass radius according to Eq. 8.24

<sup>7</sup>In a Gaussian distribution, this contrast coincides with the location of  $1\sigma$ .



(see Sect. 8.2.2), but it is not a requirement. This approximation is supported by clusters in  $N$ -body simulations, which tend towards a well-defined evolutionary sequence (Küpper et al. 2008), suggesting that the initial radius may be erased after a couple of relaxation times. It is currently not known how the half-mass radius evolves in the erratic tidal fields of real galaxies, which contain GMCs and spiral arms. We therefore choose to adopt the ‘conservative’ formulation of Eq. 8.24. In a future work, we will include a more sophisticated evolution of the half-mass radius.

The mass loss rates due to two-body relaxation and tidal shocks are combined with a model to compute the evolution of the stellar mass function of the dissolving clusters (Kruijssen 2009). In most cases, two-body relaxation gives a depletion of the mass function at low masses, because low-mass stars have a higher probability to escape than massive stars (Hénon 1969, Vesperini 1997, Takahashi & Portegies Zwart 2000, Baumgardt & Makino 2003, Kruijssen 2009). As a result, the integrated photometric properties of star clusters evolve due to dynamical disruption (e.g. Baumgardt & Makino 2003, Kruijssen 2008). By including this, we can use the presented models to trace dynamical information of the simulated galaxies down to the stellar level. The stars that are lost from clusters are added to the field star population of the star particle in which the cluster resides.

The star cluster model is implemented in the galaxy evolution code to operate ‘on the fly’, simultaneously with the galactic evolution, rather than having the cluster evolution calculated *a posteriori* as in Prieto & Gnedin (2008). While this approach is already beneficial because it potentially allows for a two-way interaction between a galaxy and its cluster population, it also implies that the tidal history of each cluster is only saved for the most recent time steps, which improves the memory efficiency of the simulation and allows us to model the full star cluster population all the way down to our adopted minimum mass of  $100 M_{\odot}$ .

### Star cluster model testing: method

We have compared the prescription for star cluster evolution from Sect. 8.2.2 to the  $N$ -body models of dissolving star clusters by Baumgardt & Makino (2003). These simulations follow the dynamical evolution of initially Roche-lobe filling star clusters in a logarithmic potential with a circular velocity of  $220 \text{ km s}^{-1}$ . The runs contain clusters on circular and eccentric orbits between galactocentric radii in the range 2.833–15 kpc. The stars in the clusters follow King (1966) density profiles with  $W_0 = 5$  or  $W_0 = 7$ , and the stellar masses are distributed according to a Kroupa (2001) initial mass function between 0.1 and  $15 M_{\odot}$ .

In this section, we exclusively consider clusters on eccentric orbits, because these clusters experience shocks during each pericentre passage. This allows us to test both disruption mechanisms rather than only two-body relaxation in a steady tidal field, for which the semi-analytic model has been tested extensively in previous studies (e.g. Lamers et al. 2005a). While the mass loss rate due to two-body relaxation contains no free parameters (see Eqs. 8.6 and 8.7), the description for tidal shocks depends on the adopted relation between the half-mass radius and the cluster mass (see Eq. 8.24), which is governed by the parameters  $\delta$  and  $\bar{r}_{h,4}$ . Their values are obtained from the comparison.

To compare our models to the simulations from Baumgardt & Makino (2003), in Fig. 8.1 we show the time after which 95% of the initial cluster mass is lost ( $t_{95\%}$ ) for our models and

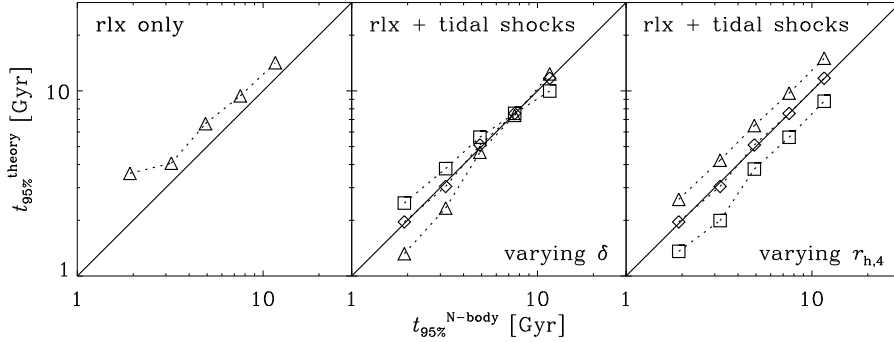


**Figure 8.1:** Comparison of our analytically estimated cluster lifetimes with the lifetimes found in  $N$ -body simulations of clusters on eccentric orbits (eccentricity  $e = 0.5$ ) from Baumgardt & Makino (2003). Connected symbols represent different initial cluster masses, characterised by different numbers of stars (8k, 16k, 32k, 64k, and 128k), while the solid line shows the 1:1 correspondence between our  $t_{95\%}$  and that from the  $N$ -body models. *Left:* without tidal shocks. *Middle:* Including tidal shocks, for  $\delta = \{0.15, \mathbf{0.225}, 0.35\}$  (triangles, diamonds, squares) and  $r_{h,4} = 4.35$  pc. *Right:* Including tidal shocks, for  $\delta = 0.225$  and  $r_{h,4} = \{3, \mathbf{4.35}, 5\}$  pc (triangles, diamonds, squares). The values at which the agreement between both approaches is best are written in boldface and are denoted by diamonds in the figure.

for their  $N$ -body runs. The figure shows poor agreement if only two-body relaxation is included, but good agreement when tidal shocks are accounted for. Additionally, the influence of  $\delta$  and  $r_{h,4}$  on  $t_{95\%}$  is shown. As can be expected from Eq. 8.24,  $\delta$  affects the mass dependence of the disruption time due to shocks (increasing  $\delta$  reduces the contrast between the disruption times of different masses), while  $r_{h,4}$  impacts the normalisation of the disruption time (compact clusters live longer).

As was mentioned in Sect. 8.2.2 and is visible in Fig. 8.1, the best match between our models and the  $N$ -body runs is found for  $\delta = 0.225$  and  $r_{h,4} = 4.35$  pc. These values should therefore approximate the actual evolution of the half-mass radii in the  $N$ -body models of the clusters. This is verified in Fig. 8.2, where our adopted mass-radius relation is compared to the actual evolution of the half-mass radii of the clusters in Fig. 8.1, showing good agreement. The clusters follow evolutionary tracks in the mass-radius plane that are very similar to each other, indicating that the clusters tend to evolve to a common cooling track, analogous to a ‘main sequence of star clusters’ as discussed by Küpper et al. (2008). The obtained mass-radius relation implies that upon losing stars due to disruption, clusters will always slowly evolve towards filling their Roche lobes, because the Jacobi radius depends on mass as  $r_J \propto M^{1/3}$ , implying  $r_h/r_J \propto M^{-0.1}$ . The slope of the mass-radius relation is also consistent with the ‘mass loss-dominated mode’ from the work by Gieles et al. (2011).

In principle, the mass-radius evolution of the clusters could be a relic of the initial conditions of the  $N$ -body simulations, in which the clusters initially fill their Roche lobes. How-

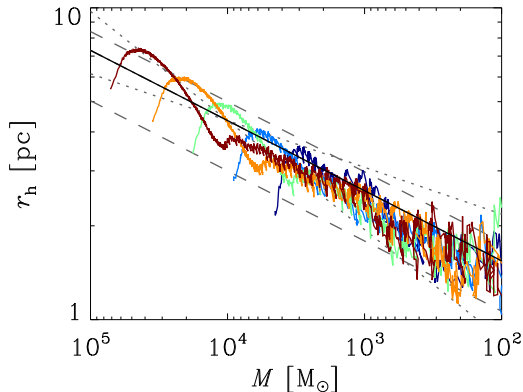


**Figure 8.2:** Evolution of the half-mass radius as a function of the remaining mass for the  $N$ -body simulations shown in Fig. 8.1, with from left to right the initial numbers of stars being 128k, 64k, 32k, 16k, and 8k (coloured irregular lines). The solid line shows our adopted relation between half-mass radius and mass, with  $r_{h,4} = 4.35$  pc and  $\delta = 0.225$ . The dashed and dotted lines show the variations of  $r_{h,4}$  and  $\delta$  from Fig. 8.1, with dashed denoting  $r_{h,4} = \{3, 5\}$  pc (bottom, top) and dotted denoting  $\delta = \{0.15, 0.35\}$  (shallow, steep).

ever, we are considering clusters on eccentric orbits, for which the tidal radius continuously changes, suggesting that whether or not a cluster initially fills its Roche lobe may be irrelevant after a couple of orbits. This would be even more important in more realistic, erratic tidal fields. Most importantly though, the evolution of the half-mass radius shown in Fig. 8.2 also includes the time after core collapse, when any possible imprint of the initial conditions will have been erased. Therefore, we do not expect that the details of the initial conditions of the  $N$ -body simulations would affect the slope or normalisation of the mass-radius relation, especially given its simplicity. Nonetheless, the mass-radius relation of clusters in erratic tidal fields could deviate from our adopted one. We discuss possible improvements of our approach in Sect. 8.6.2.

### Star cluster model testing: numerical resolution

For any numerical model, it is necessary to check at which numerical resolutions the results are reliable. Within a realistic galactic environment, the tidal field experienced by star clusters is very erratic, contrary to the well-defined tidal shocks occurring during each pericentre passage in the Baumgardt & Makino (2003) simulations. Testing the resolution requirements of the models (both in time and space) should therefore be done for tidal histories that are taken from our simulations.

To explore how the time resolution of the tidal field affects our modeled star cluster disruption, we computed the mass evolution of a  $2 \times 10^4 M_{\odot}$  cluster for 200 tidal histories

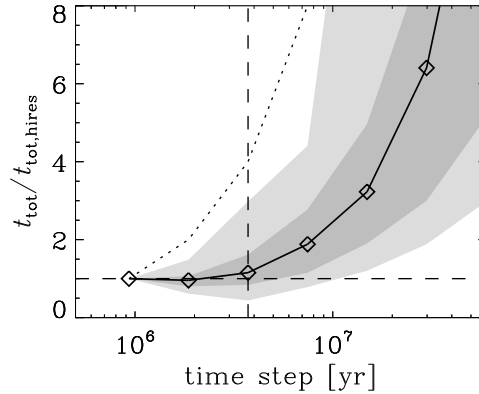


**Figure 8.3:** The mean total disruption time of a  $2 \times 10^4 M_{\odot}$  cluster for different time steps, scaled to that for the smallest time step (diamonds/solid line). The horizontal dashed line indicates unity, which coincides with the leftmost diamond per definition. The dark grey tinted area spans the space covered by one standard deviation of the distribution at each time step, while the light grey represents two standard deviations. The dotted line represents the relation for when  $t_{\text{tot}}/t_{\text{tot,hires}}$  were proportional to the time step. The maximum time step used in our simulations is indicated by the vertical dashed line.

that were randomly drawn from the particles in one of our galaxy disc simulations. For each of these histories, the evolution was computed seven times, using fixed time steps of  $\{1, 2, 4, 8, 16, 32, 64\} \times 0.932$  Myr. For each time step, we then scaled the total disruption time of the cluster  $t_{\text{tot}}$  to the total disruption time found for that cluster when using the smallest time step ( $t_{\text{tot,hires}}$ ). This ratio can be used to trace the relative change of the total lifetime due to resolution effects. Because tidal shocks are events with a certain duration, some of them could be skipped when increasing the time step, suggesting that in that regime  $t_{\text{tot}}/t_{\text{tot,hires}}$  becomes proportional to the time step.

The mean  $t_{\text{tot}}/t_{\text{tot,hires}}$  of the 200 tidal histories is shown as a function of the time step in Fig. 8.3. The relation that would be expected if  $t_{\text{tot}}/t_{\text{tot,hires}}$  were proportional to the time step is also included. The figure shows that for large time steps ( $\gtrsim 10$  Myr), the total disruption time indeed becomes proportional to the time step, as the durations of some shocks are then short enough to be skipped, while for smaller time steps the total disruption time converges. The maximum time step of the particles in our simulations (3.73 Myr) is such that time resolution effects should not play an important role, particularly because the maximum time step is only used for very weakly accelerated particles in dynamically quiet regions. In the simulations, we do not use fixed time steps, but adaptive ones instead, increasing the resolution as the force on a particle increases (Pelupessy et al. 2004, Pelupessy 2005), up to a maximum resolution increase of a factor 4096 (potentially yielding a time step of  $\sim 1000$  yr). This ensures that tidal shocks, which typically occur when the force on a particle is non-negligible, are always well-resolved. In this way, we minimise the effect of the time step on

our computed cluster lifetimes.

Whether or not the evolution of star clusters is affected by the spatial resolution of the simulations depends on the smoothing length and the number of particles used. The distribution of mass needs to be resolved in sufficient detail to ensure that encounters with individual particles do not disrupt the clusters. Such disruption would be artificial, because individual particles are discrete representations of a continuous mass distribution. Whether the resolution requirements are satisfied can be easily checked with an order-of-magnitude estimate.

Most of the disruption due to an encounter with an individual particle would be caused by the corresponding tidal shock. The presented simulations use a smoothing length of  $h = 200$  pc and typical particle masses of  $M_{\text{part}} = 8 \times 10^5 M_{\odot}$  (see Sect. 8.3). The typical duration of an encounter with a single particle is then approximately  $h/\sigma$ , with  $\sigma$  the velocity dispersion in a galaxy disc, which is of the order  $20 \text{ km s}^{-1}$ . This gives a typical shock duration of about 10 Myr. Since we are interested in an upper limit to the disruptive effect of individual particles, we ignore the adiabatic correction (Eq. 8.15) and assume that throughout the shock the heating is equal to the tidal heating encountered when the cluster is located at the centre of the particle. For a spline kernel smoothing, the central density of a particle is  $\rho_{\text{centre}} = M_{\text{part}}/(\pi h^3)$ . Due to the symmetry of a head-on encounter, the tidal tensor is diagonal with values  $T_{ij} = -4GM_{\text{part}}\delta_{ij}/(3h^3)$ , which for the quoted shock characteristics gives a tidal heating parameter of  $I_{\text{tid}} \approx 10^2 \text{ Gyr}^{-2}$ . If this type of shock would be continuously repeated over the entire lifetime of a cluster, it would take well over 120 Gyr to destroy a  $10^4 M_{\odot}$  cluster. As is evident from Fig. 8.1 and later sections of this chapter, such a disruption time is 1–3 orders of magnitude larger than typical disruption times. We conclude that for our choice of particle numbers and smoothing length, encounters with individual particles do not play an important role. Instead, the shocks that lead to the disruption of clusters are produced by groups of particles, such as spiral arms or complexes of molecular clouds, which do have a physical meaning. Consequently, the spatial resolution requirements are satisfied. Note that this strongly depends on the smoothing length  $h$ , because for the maximum tidal heating we have  $I_{\text{tid}} \propto T_{ij}^2 \propto M_{\text{part}}^2 h^{-6}$ . This implies that it is not possible to adopt a much smaller smoothing length, which would require vastly larger numbers of particles to reduce the particle mass and minimise the effect of encounters with individual particles.

The stability against resolution effects is illustrated in Fig. 8.4, which shows the dependence of the star formation rate and the number of clusters per unit star formation rate on the spatial resolution. The figure shows that the formation rates of stars and clusters converge with increasing resolution. The bottom panel gives a measure for star cluster disruption, and shows that the variation of the disruption rate with spatial resolution is of the order of the inherent scatter on the number of clusters. The number of clusters very slightly decreases for lower resolutions, because encounters with individual particles then become more important due to their higher masses. Simulations at higher resolutions also exhibit a slight decrease of the number of clusters, because in these the structure in the spatial distribution of the gas is resolved in more detail. While this may induce a small increase of the disruption rate, we do not expect that this continues at even higher resolutions, because the amount of tidal heating scales with the square of the mass of the structure causing the tidal shock, implying that resolving increasingly smaller structures results in a correspondingly smaller addition to the

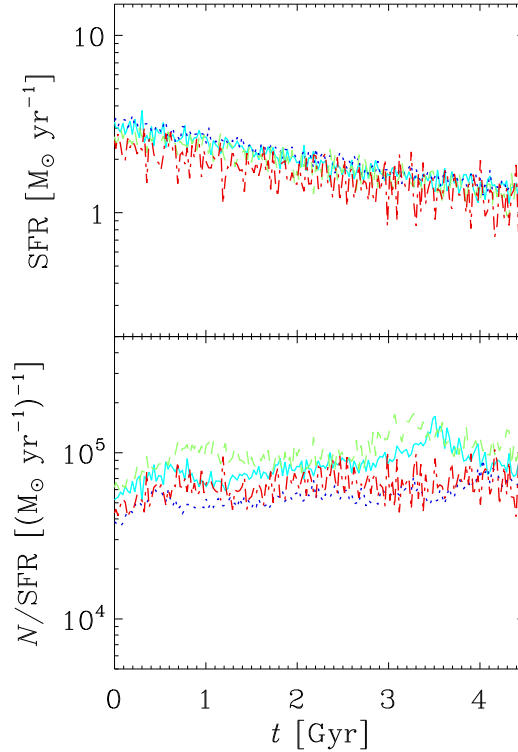


**Figure 8.4:** Dependence of the simulations on the spatial resolution. *Top:* star formation history as a function of time. *Bottom:* number of clusters per unit star formation rate as a function of time. Different lines denote simulation 1dB (see Sect. 8.3) run at different spatial resolutions. Particle numbers of  $\{1/4, 1/2, 1, 2\}$  times those used in simulation 1dB are represented by {dash-dotted red, dashed green, solid cyan, dotted blue} lines. The bumps in the bottom panel for simulations 1dB<sub>1/2</sub> (at  $t = 3.2$  Gyr), 1dB (at  $t = 3.5$  Gyr) and 1dB<sub>2</sub> (at  $t = 4.1$  Gyr) occur shortly after the (random) formation of holes in the gas due to feedback effects (see text).

tidal heating<sup>8</sup>. Figure 8.4 also illustrates that the mean disruption rate of star clusters is more sensitive to random fluctuations than the overall star formation rate. At certain times, the number of clusters briefly increases due to a decrease of the disruption rate. This is caused by the random, transient excavation of the gas due to feedback in certain star-forming regions, which causes large numbers of clusters to experience less disruption. The mean disruption rate, which depends on the distribution of the gas, then shows larger scatter than the star formation rate, which to good approximation is set by the mean surface density of the gas.

<sup>8</sup>Even for a population of GMCs that follows a power law mass distribution with index  $-2$ , the total tidal heating would (linearly) increase with GMC mass, despite the many more low-mass GMCs than massive ones.

### 8.3 Summary of the model runs

We construct model disc galaxies with parameters that can be related to the outcomes of cosmological  $\Lambda$ CDM galaxy formation models (Mo et al. 1998, Springel et al. 2005). They consist of a dark halo with a Hernquist (1990) profile<sup>9</sup>, an exponential stellar disc, a stellar bulge (except for one model) and a thin gaseous disc, constructed to be in self gravitating equilibrium if evolved autonomously (Springel et al. 2005). The disc galaxies are initially set up with  $10^5$ – $10^6$  particles for the dark matter halo, 22,938–51,250 particles for the stellar component, and 7,688–25,625 particles for the gas. The dark matter haloes have concentration parameters related to their total masses and condensation redshifts according to Bullock et al. (2001), implying that for a fixed mass the halo concentration increases with redshift. The total mass is related to the virial velocity  $V_{\text{vir}}$  and the Hubble constant  $H(z)$  at redshift  $z$  as  $M_{\text{vir}} = V_{\text{vir}}^3/[10GH(z)]$ . For all galaxies, the baryonic disc is constituted by a gaseous and stellar component, having a mass fraction  $m_{\text{d}} = 0.041$  of the total mass, while the bulge (when included) consists of a stellar component only, having a mass fraction  $m_{\text{b}} = 0.008$  of the total mass. These mass fractions are chosen to be consistent with the fiducial values from recent literature (e.g. Springel et al. 2005) and are based on the original constraint of  $0.03 < m_{\text{d}} < 0.05$  by Mo et al. (1998). The fraction of total angular momentum that is constituted by the disc ( $j_{\text{d}}$ ) is taken identical to  $m_{\text{d}}$ . The scale-length of the bulge and the vertical scale-length of the disc are 0.2 times the radial scale-length of the disc, which is determined by the degree of rotation (Mo et al. 1998) through the spin parameter  $\lambda \equiv J|E|/GM_{\text{vir}}^{5/2}$ , in which  $J$  is the angular momentum of the halo and  $E$  its total energy. Table 8.1 lists the remaining properties for the various model runs, i.e. the gas fraction of the baryonic disc  $f_{\text{gas}}$ , the total mass  $M_{\text{vir}}$ , the spin parameter  $\lambda$ , the number of particles in the different components of the model galaxies, and the particle masses of the halo particles  $M_{\text{part}}^{\text{halo}}$  and baryonic particles  $M_{\text{part}}^{\text{bary}}$ .

The gas fractions of the galaxy models are chosen to cover the range from typical star forming galaxies. Most of the total masses represent Milky Way type galaxies, with the two exceptions being one half and one tenth of that mass, enabling simulations of unequal-mass major and minor mergers. The parameter  $\lambda$  represents the degree of rotational support, and is set in accordance with typical spiral galaxies in cosmological simulations ( $\langle \lambda \rangle = 0.045$ , Vitvitska et al. 2002), except in one case, where we evaluate the influence of the radial scale-length of the disc on the cluster population. The number of halo particles is chosen to ensure sufficient smoothing of the dark matter halo, and the number of stellar disc, stellar bulge and gas particles are chosen to minimise the mass difference between the particles and alleviate two-body effects.

The model runs for galaxy mergers are initialised by positioning two disc galaxy models on Keplerian parabolic orbital trajectories<sup>10</sup> with initial separations of approximately 200 kpc.

<sup>9</sup>This density profile is very similar to profiles found in cosmological simulations (Navarro et al. 1996, 1997). The difference only occurs at radii much larger than the scale radius, where the density profile of the Hernquist (1990) profile falls off as  $\propto r^{-4}$  rather than  $r^{-3}$ . This does not affect the results in this chapter, because our galaxy merger simulations do not include galaxies on very wide orbits.

<sup>10</sup>About 50% of the mergers in cosmological simulations are on (near-)parabolic orbits (Khochfar & Burkert 2006).

**Table 8.1:** Details of the initial conditions for the disc galaxy models.

ID	$f_{\text{gas}}$	$M_{\text{vir}}^a$	$z$	$\lambda$	$N_{\text{halo}}$	$N_{\text{gas}}$	$N_{\text{disc}}^{\text{star}}$	$N_{\text{bulge}}^{\text{star}}$	$M_{\text{part}}^{\text{halo}^a}$	$M_{\text{part}}^{\text{bary}^a}$	Comments
1dA <sup>b</sup>	0.20	$10^{12}$	2	0.05	$10^6$	10250	41000	10000	$10^6$	$8 \times 10^5$	low gas fraction
1dB <sup>b,c,d</sup>	0.30	$10^{12}$	2	0.05	$10^6$	15375	35875	10000	$10^6$	$8 \times 10^5$	standard model
1dC	0.50	$10^{12}$	2	0.05	$10^6$	25625	25625	10000	$10^6$	$8 \times 10^5$	high gas fraction
1dD	0.30	$5 \times 10^{11}$	2	0.05	$5 \times 10^5$	7688	17938	5000	$10^6$	$8 \times 10^5$	half mass
1dE	0.30	$10^{12}$	2	0.05	$10^6$	15375	35875	0	$10^6$	$8 \times 10^5$	no bulge
1dF	0.30	$10^{11}$	2	0.05	$10^6$	15375	35875	10000	$10^5$	$8 \times 10^4$	low mass
1dG	0.30	$10^{12}$	2	0.10	$10^6$	15375	35875	10000	$10^6$	$8 \times 10^5$	high spin
1dH	0.30	$10^{12}$	0	0.05	$10^6$	15375	35875	10000	$10^6$	$8 \times 10^5$	low concentration
1dI	0.30	$10^{12}$	5	0.05	$10^6$	15375	35875	10000	$10^6$	$8 \times 10^5$	high concentration

<sup>a</sup>In solar masses ( $M_{\odot}$ ).

<sup>b</sup>To investigate the relative importance of the two disruption mechanisms, these models are also computed for disruption excluding tidal shocks (i.e. only two-body relaxation, ‘1dA/B<sub>rlx</sub>’) and for disruption excluding two-body relaxation (i.e. only tidal shocks, ‘1dA/B<sub>sh</sub>’).

<sup>c</sup>This model is also computed for  $i = \{1/4, 1/2, 2\}$  times the number of baryonic particles (i.e. ‘1dB<sub>*i*</sub>’).

<sup>d</sup>This model is also computed for a constant disruption parameter  $t_0 = 2$  Myr (see Eq. 8.6) and no tidal shocks (‘1dB<sub>fix</sub>’).



**Table 8.2:** Details of the initial conditions for the galaxy merger models.

ID	Progenitors	Mass ratio	$\theta_1$	$\phi_1$	$\theta_2$	$\phi_2$	$R_{\text{peri}}^a$	Comments
1m1	1dA/1dA	1:1	0	0	0	0	6	PP
1m2	1dB/1dB	1:1	0	0	0	0	6	PP
1m3	1dC/1dC	1:1	0	0	0	0	6	PP
1m4	1dB/1dD	1:2	0	0	0	0	6	PP
1m5	1dE/1dE	1:1	0	0	0	0	6	PP
1m6	1dF/1dF	1:1	0	0	0	0	6	PP
1m7	1dG/1dG	1:1	0	0	0	0	6	PP
1m8	1dH/1dH	1:1	0	0	0	0	6	PP
1m9	1dI/1dI	1:1	0	0	0	0	6	PP
1m10	1dB/1dB	1:1	60	45	-45	-30	6	PPi
1m11	1dB/1dB	1:1	180	0	0	0	6	PR
1m12	1dB/1dB	1:1	-120	45	-45	-30	6	PRi
1m13	1dB/1dB	1:1	180	0	180	0	6	RR
1m14	1dB/1dB	1:1	-120	45	135	-30	6	RRi
1m15	1dB/1dB	1:1	0	0	0	0	12	wide PP
1m16	1dC/1dG	1:1	-120	45	-45	-30	10	PRi
1m17	1dB/1dB	1:1	0	0	71	30	6	'Barnes'
1m18	1dB/1dB	1:1	-109	90	71	90	6	'Barnes'
1m19	1dB/1dB	1:1	-109	-30	71	-30	6	'Barnes'
1m20	1dB/1dB	1:1	-109	30	180	0	6	'Barnes'
1m21	1dB/1dB	1:1	0	0	71	90	6	'Barnes'
1m22	1dB/1dB	1:1	-109	-30	71	30	6	'Barnes'
1m23	1dB/1dB	1:1	-109	30	71	-30	6	'Barnes'
1m24	1dB/1dB	1:1	-109	90	180	0	6	'Barnes'

<sup>a</sup>In kpc. All angles are in degrees. In the comments, 'PP', 'PR' and 'RR' indicate prograde-prograde, prograde-retrograde and retrograde-retrograde orbits, respectively. The added 'i' indicates an inclined/near-polar orbit.

The actual orbit will decay due to dynamical friction, which leads to the merging of the galaxies. The orbital geometry of an interaction is characterised by the directions of the angular momentum vectors of the two galaxy discs and the pericentre distance of the parabolic orbit  $R_{\text{peri}}$ . The angular momentum vectors of the galaxies are determined in spherical coordinates by angles  $\theta$  (rotation perpendicular to the orbital plane) and  $\phi$  (rotation in the orbital plane). These and other relevant parameters are listed in Table 8.2, where the different model runs are summarised.

The initial conditions in Table 8.2 are divided in three categories. The first set of eight runs follow a common configuration, in which the discs rotate in the orbital plane. They are used to test the influence of the gas fraction and mass ratio of the progenitor discs, and of additional progenitor disc properties such as the presence of a bulge, total galaxy mass, and spin parameter (or the radial scale-length of the disc). The initial conditions for the six

subsequent runs are constructed to assess the impact of orbital parameters on the star cluster population. We rotate the progenitor discs to include retrograde rotation and near-polar orbits, which represent the opposite extreme with respect to the co-planar configurations of the first eight runs. The effect of a wider orbit (a larger pericentre distance) is also considered, and a ‘random’ major merger is also included, in which two progenitors with different spin parameters are placed on a near-polar, prograde-retrograde orbit. The third group contains the eight ‘random’ configurations from Hopkins et al. (2009) (see Barnes 1988), which all have equal probabilities of occurring in nature.

All galaxies are generated without any star clusters, and we set  $t = 0$  after 300 Myr of evolution to initialise the cluster population. As described in Sects. 8.2.2 and 8.2.2, the clusters have masses between  $10^2$  and  $\sim 10^{5.8} M_{\odot}$ , following a Schechter (1976) type initial mass function. The chemical composition of the clusters is set to solar metallicity, and we assume a King parameter of  $W_0 = 5$ .

The properties of the simulated disc galaxies and galaxy mergers are not intended to cover all of parameter space, but instead should provide a first indication of how the modeled star cluster populations are affected by their galactic environment. This set of simulations represent a basic library that can be used to predict certain characteristics of star cluster populations and to see how well the simulated cluster populations compare to observations.

## 8.4 Isolated disc galaxies

As a first application of the model, we consider the simulations of the isolated disc galaxies from Table 8.1. As discussed in Sect. 8.2.2, the cluster populations are simulated down to a lower mass limit of  $100 M_{\odot}$ , which for our assumed cluster formation efficiency and for the typical cluster formation and disruption rates of disc galaxies yields about  $1\text{--}3 \times 10^5$  clusters per galaxy (also see Kruijssen et al. 2011b). Below, we discuss the mechanisms driving the evolution of individual clusters, and show a number of key properties of the entire cluster population.

### 8.4.1 The evolution of individual star clusters in disc galaxies

To illustrate the effects of disruption due to two-body relaxation and tidal shocks, in Fig. 8.5 we show the orbits and the mass evolution of three star clusters with similar initial masses ( $M_i \sim 1.8 \times 10^4 M_{\odot}$ ) and times of formation ( $t \sim 2.20$  Gyr) from simulation 1dB. They are on different orbits and therefore experience differing tidal evolution. Clusters orbiting at small galactocentric radii evolve in a stronger tidal field (and generally have smaller Jacobi radii) than clusters orbiting at large galactocentric radii. Also, the number and intensity of tidal shocks is typically larger for clusters orbiting close to the galactic centre, due to the higher gas density in their environment. These differences result in contrasting mass loss histories and total disruption times, as the innermost cluster survives for about 100 Myr, the middle cluster persists for about 300 Myr, and the outer cluster is disrupted after 400 Myr, even though it has the lowest initial mass of the three clusters. The jumps in the mass loss history indicate the effect of tidal shocks, which are generally stronger (and potentially more

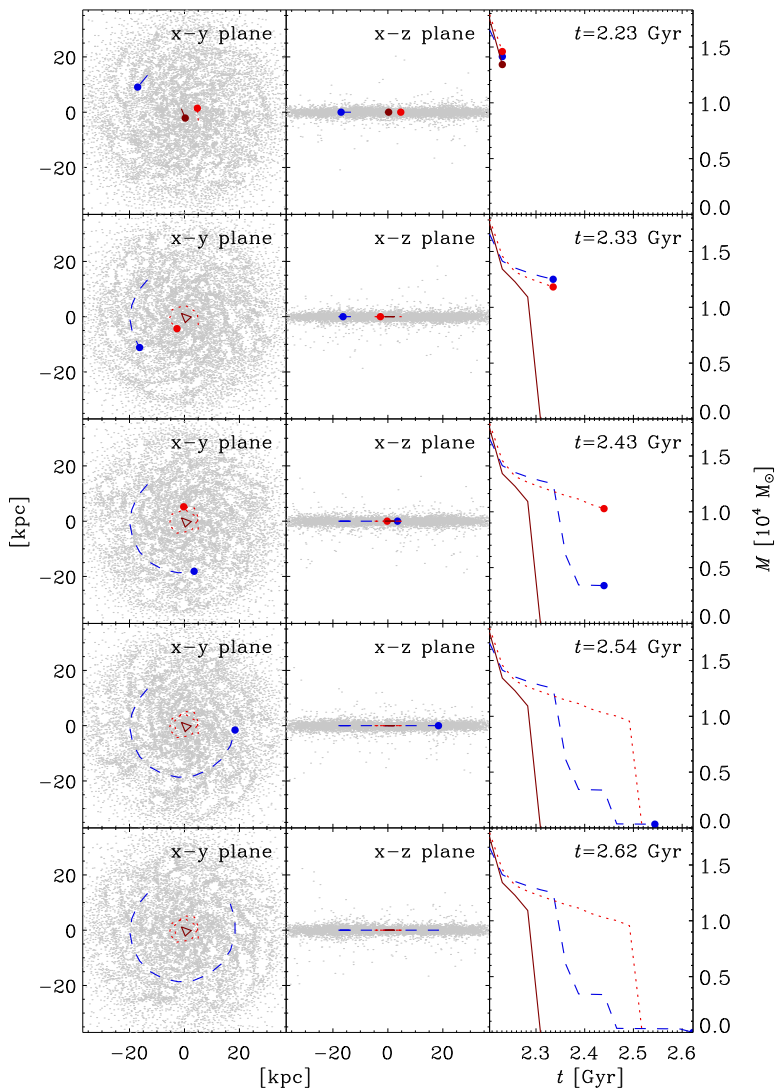


**Figure 8.5:** Evolution of the orbits and masses of three clusters orbiting at different galactocentric radii in isolated disc galaxy simulation 1dB. From top to bottom, the consecutive panels show the situation at different times  $t$ , while from left to right the orbital evolution in the x-y plane (face-on), the orbital evolution in the x-z plane (edge-on), and the mass evolution are shown. The innermost cluster is represented by the dark red solid lines, the middle cluster by red dotted lines, and the outermost cluster by blue dashed lines. If at any particular snapshot a cluster is still undisrupted, its position and mass are marked with thick dots. The orbital trajectories remain visible after the clusters are disrupted. The small grey dots in the x-y and x-z plane views map the distribution of the gas particles in the simulation.

frequent) for clusters on narrow orbits. Despite these trends, Fig. 8.5 also shows that a cluster can be disrupted by a single tidal shock almost anywhere in the galaxy, even at radii well beyond the solar galactocentric radius. This was also discussed by Gieles et al. (2006b), who showed that clusters with masses  $\lesssim 2 \times 10^4 M_\odot$  can be disrupted during a single encounter with a spatially extended GMC of  $10^6 M_\odot$ . Relative to disruption due to subsequent, small encounters, disruption by a single, violent GMC encounter is most prominent for cluster masses of about  $10^4 M_\odot$  (Gieles et al. 2006b). The clusters in Fig. 8.5 are characteristic examples of this. In general, the strongest tidal shocks occur at times when the clusters cross regions of high gas density, for instance during spiral arm passages. This is best seen in the snapshots at  $t = 2.33$  Gyr and  $t = 2.43$  Gyr, because between those snapshots the outer cluster is overtaken by a dense region<sup>11</sup>, causing it to lose almost 75% of its mass due to the rapid change of the tidal field.

Figure 8.6 illustrates the relation between the mass loss and the tidal field for the two long-lived clusters from Fig. 8.5. It shows the evolution of the cluster mass, together with the tidal field strength as defined in Sect. 8.2.2, and the running integral that is used to compute the tidal heating parameter  $I_{\text{tid}}$  in Eq. 8.14, which is defined as:

$$H_{\text{tid}}(t) = \sum_{i,j} \left( \int_{t_{\text{last}}}^t T_{ij} dt \right)^2, \quad (8.25)$$

where  $t_{\text{last}}$  is the time of the last shock and  $t$  is the current time. This quantity represents the accumulated tidal heating since the last shock, and resets after each shock is completed. Contrary to  $I_{\text{tid}}$ , it does not include the adiabatic correction. Therefore, it is only a measure for the tidal shock heating imposed by the tidal field and does not contain any information on the response of the cluster experiencing the shock.

The evolution of the tidal field strength for both clusters in Fig. 8.6 shows that it is indeed larger for the cluster orbiting at the smaller galactocentric radius. A comparison of the tidal field strengths experienced by the clusters just after their formation explains why the outer cluster loses its mass more slowly initially. The moments at which both clusters suffer their first violent mass decrease can be associated with jumps in the amount of shock heating, indicating the effect of tidal shocks. In the case of the inner cluster, this gives rise to its total disruption. The second moment of violent mass loss of the outer cluster cannot be coupled with an increase of the shock heating, because the shock took place in between two snapshots and is therefore skipped by the output of the simulation.

The evolution of the clusters in Figs. 8.5 and 8.6 illustrates that the disruption rate varies with time for individual clusters and varies with space when considering the cluster population as a whole. This is very important when interpreting observed star cluster populations. The time-variation of the disruption rate for individual clusters can mask the effect of a different mass dependence of star cluster disruption. For instance, if the disruption parameter  $t_0$  in Eq. 8.6 were to increase with time because a cluster is leaving a region with a high gas density (also see Elmegreen & Hunter 2010), for that time interval one would derive a lower value of  $\gamma$ , which is the mass-dependence of the disruption timescale.

---

<sup>11</sup>The outer cluster is situated beyond the co-rotation radius of the galaxy.

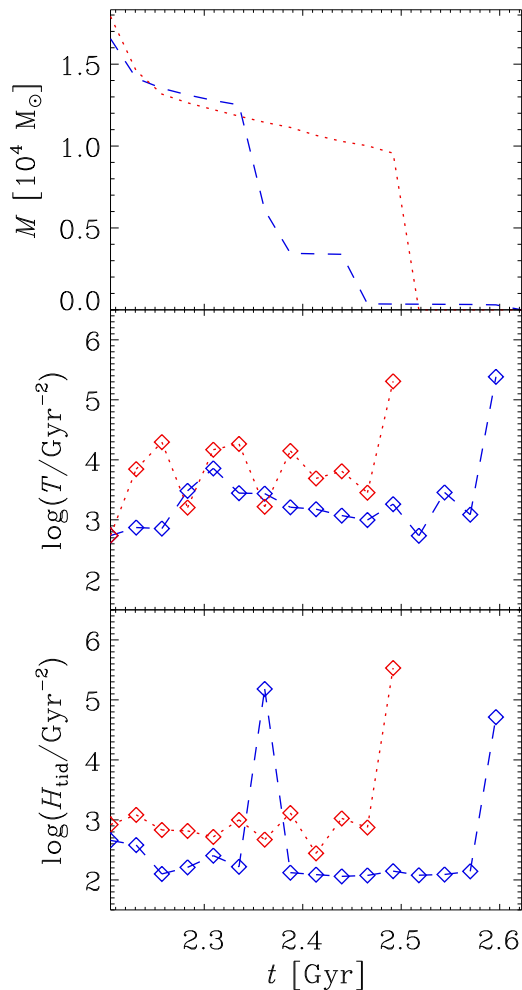


**Figure 8.6:** Evolution of the cluster mass and the tidal field for the two outer clusters from Fig. 8.5, indicated by the same colours and line styles. The diamonds in the middle and bottom panel indicate the times of each snapshot. *Top:* The mass evolution. *Middle:* Evolution of the tidal field strength experienced by each cluster, defined as the largest eigenvalue of Eq. 8.8 (see Sect. 8.2.2). *Bottom:* Running integral of the total amount of shock heating experienced by the cluster (see text and Eq. 8.25).

When considering the space-variation of the disruption rate throughout a population of clusters, it is inevitable that the mean disruption rate decreases with age<sup>12</sup>, because clusters in

<sup>12</sup>Provided that the galaxy and formation sites of the clusters do not change much on timescales of  $\sim 1$  Gyr.

disruptive environments have the shortest lifetimes and never reach old ages, while clusters in less violent settings become older. This process can be regarded as a form of ‘natural selection’ acting on the star cluster population, and tends to flatten the age distributions of star clusters (see Sect. 8.4.4).

The time-variation of the disruption rate is particularly interesting in view of recent discussions in literature, in which it is debated whether or not star cluster disruption depends on the cluster mass (e.g. Fall et al. 2005, Whitmore et al. 2007, Gieles & Bastian 2008, Larsen 2009, Bastian et al. 2009). It is crucial that environmental dependences are taken into account before inferring any conclusions about the mechanisms driving cluster disruption from observations, because the age and mass distributions of clusters are susceptible to variations in the environment. This holds particular relevance in non-equilibrium settings such as interacting galaxies (see Sect. 8.5).

### 8.4.2 The variation of the disruption rate with galactocentric radius

A second consequence of the variability of the disruption rate is related to its variation with space. It implies that the properties of the star cluster population, such as the slope of the age and mass distribution will depend on the local environment within a galaxy. Galaxy-wide distributions may indicate the average properties of the cluster population, but interpreting them can yield systematic errors when assuming the disruption rate is the same everywhere in the galaxy. For instance, the effects of cluster disruption are stronger towards the galactic centre than in the outskirts of a galaxy, implying that the properties of the cluster populations in both regions will differ.

The environmental dependences on the star cluster population can be qualitatively illustrated by considering two variations of simulation 1dB. Figure 8.7 shows the mean cluster age as a function of galactocentric radius for two galaxy disc simulations: one in which the disruption rate is calculated as described in Sect. 8.2.2 (model 1dB), and one with a disruption rate that is constant in time and space (using  $t_0 = 2$  Myr, see Eq. 8.6) and does not include tidal shocks (model 1dB<sub>fix</sub>). For the galaxy with the physically motivated disruption rate, the spatial distribution of the mean cluster age is as expected. The youngest clusters are found in the galactic centre, where the star formation rate density is highest. Due to the high gas density, clusters in the galactic centre disrupt on shorter timescales than in the outskirts of the galaxy, resulting in a mean cluster age that increases with galactocentric radius. This contrasts with the age profile of the cluster population in the galaxy with a fixed disruption rate, where the mean cluster age is approximately constant throughout the galaxy and the scatter is strictly due to local variations in the star formation history and stochastic effects<sup>13</sup>. Observations of cluster populations in real galaxies (e.g. van den Bergh & McClure 1980, Gieles

---

Galaxy mergers are a clear exception to this.

<sup>13</sup>The spatial variation of the star formation rate (SFR) cannot produce the behaviour of the mean cluster age that is shown in Fig. 8.7. Without a time-variation, the cluster age distributions at different galactocentric radii would still yield the same mean age, irrespective of the relative formation rates. Within a stable disc galaxy, the relative time variations at different galactocentric radii are not sufficiently large nor persistent enough to cause a spatial trend of the mean cluster age, as is also shown by the line denoting the galaxy with a fixed disruption rate. Indeed, Fig. 8.7 could have been made at any time in our simulation other than the time shown, and the mean age would have shown the same spatial variation.

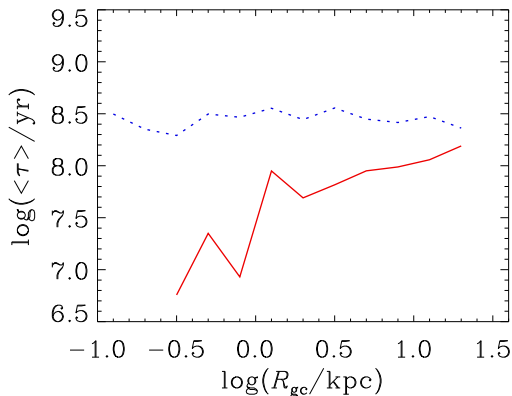


**Figure 8.7:** Mean age of star clusters  $\langle \tau \rangle$  as a function of galactocentric radius  $R_{\text{gc}}$  for two galaxy simulations at  $t = 2.5$  Gyr. The red solid line shows the relation for the physically computed disruption rate from Sect. 8.2.2, while the blue dotted line represents the result for a simulation with a fixed disruption rate.

et al. 2005, Froebrich et al. 2010) show that the mean age increases with galactocentric radius, contrary to the result for a fixed disruption rate. For the inner disc of M51, Gieles et al. (2005) find that the disruption rate varies by a factor 1.8 between radial intervals of 1–3 kpc and 3–5 kpc. Assuming that the mean age is directly proportional to the disruption timescale, this is of the same order of magnitude as for the model shown in Fig. 8.7, for which we find that the ratio between the mean ages of the clusters in these intervals is 1.4.

These results substantiate that star cluster disruption is indeed driven by environmental effects. Additionally, they show that the suggestion of a disruption rate that increases with the star formation rate, which is found when considering variations between different galaxies (e.g. Boutloukos & Lamers 2003, Lamers et al. 2005b), also holds within a single galaxy. This is easily understood by noting that both the formation and disruption of clusters peak in dense environments.

### 8.4.3 The relative importance of tidal shocks and two-body relaxation

The relative contributions to star cluster disruption of two-body relaxation and tidal shocks can be quantified by considering the number of clusters in simulations for which either mechanism is neglected. The fraction of the total disruption contributed by tidal shocks  $f_{\text{sh}}$  is then given by

$$f_{\text{sh}} \equiv 1 - \frac{N_{\text{both}}}{N_{\text{rlx}}}, \quad (8.26)$$

where  $N_{\text{both}}$  is the number of clusters in a simulation including both disruption mechanisms (e.g. 1dA and 1dB), and  $N_{\text{rlx}}$  is the number of clusters in a simulation for which only dis-

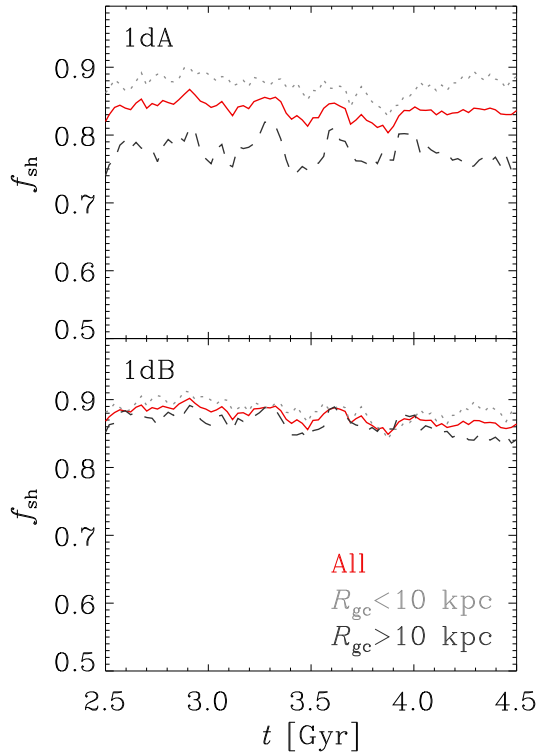


**Figure 8.8:** Fraction of disruption due to tidal shocks as a function of time. The red solid line shows the evolution for all clusters, while the light grey dotted line only includes clusters within a galactocentric radius of 10 kpc, and the dark grey dashed line represents the evolution for the clusters beyond 10 kpc. *Top:* disc galaxy with a gas fraction  $f_{\text{gas}} = 0.20$  (simulation 1dA). *Bottom:* disc galaxy with a gas fraction  $f_{\text{gas}} = 0.30$  (simulation 1dB).

ruption by two-body relaxation is included and tidal shocks are not considered (e.g. 1dA<sub>rlx</sub> and 1dB<sub>rlx</sub>). Per definition  $N_{\text{both}} < N_{\text{rlx}}$ . For different radial bins,  $f_{\text{sh}}$  is shown as a function of time in the top panel of Fig. 8.8 for two galaxies with different gas fractions (1dA and 1dB). The contribution by tidal shocks is typically 80–85% of all disruption, which is very similar to the analytic estimate by Lamers & Gieles (2006) for the solar neighbourhood. The value increases with the gas fraction of the disc, because GMCs and spiral arms are the most important sources of tidal shocks. For relatively gas-rich discs such as in simulation 1dB ( $f_{\text{gas}} = 0.30$ ), the contribution from shocks does not vary much with galactocentric radius, but for gas-poorer discs, shocks are more important in the inner regions of the disc. This occurs because beyond a certain galactocentric radius the gas density becomes too low to sustain star formation (e.g Kennicutt 1989, Schaye 2004, Pelupessy et al. 2004), yielding less or no



energy injection by feedback and a less filamentary gas distribution, which in turn implies that tidal shocks are less important. The characteristic radius for this transition is smaller in gas-poor galaxies, which is illustrated by the contrast between the inner and outer parts of the disc in the upper panel Fig. 8.8. Because discs also become more gas-poor as they age, the relative contribution by shocks slightly decreases with time.

For the adopted mass-radius relation, the ratio between the disruption timescales due to two-body relaxation and tidal shocks is  $t_{\text{rlx}}/t_{\text{sh}} \propto M^{0.3}I_{\text{tid}}$ . If this ratio is larger than unity, tidal shocks dominate cluster disruption, while a ratio below unity implies that disruption is mainly driven by two-body relaxation. The relative importance of tidal shocks increases with cluster mass until a few times  $10^4 M_{\odot}$ , when the adiabatic correction in the tidal heating parameter  $I_{\text{tid}}$  (see Eq. 8.14) becomes non-negligible and inhibits disruption due to tidal shocks. This means that the relative importance of tidal shocks peaks at a certain cluster mass. For the parameters in this chapter, this is  $f_{\text{sh}} \approx 0.9$  at  $M \sim 10^4 M_{\odot}$ , but the precise value depends on the mass-radius relation.

#### 8.4.4 The age distributions of star clusters in disc galaxies

The balance between cluster formation and destruction gives rise to a cluster population with a certain age distribution. The age distribution of star clusters is often used as a probe to study star cluster disruption (e.g. Gieles et al. 2005, Chandar et al. 2006), or to assess the formation history of a galaxy (Hunter et al. 2003, Gieles et al. 2005, Smith et al. 2007). In order to obtain a reliable interpretation of the cluster age distribution, it is important to understand its evolution in different galaxies.

To investigate possible correlations between the cluster age distribution and galaxy properties, we have fitted the logarithmic slope  $\alpha$  of the age distribution ( $dN/d\tau \propto \tau^{\alpha}$ ) in the age range  $\log(\tau/\text{yr}) = 7.7-9$  for all snapshots of our galaxy disc simulations. When constructing the age distribution, we consider all available clusters, implying that the samples are mass-limited with  $M \geq 100 M_{\odot}$ . We have also fitted the logarithmic slope  $\beta$  of the SFR-corrected age distributions in that range ( $[dN/d\tau]/\text{SFR} \propto \tau^{\beta}$ ). The age range has been chosen such that the effects of gas expulsion due to supernovae are no longer relevant and a sufficiently large part of the age distribution is covered to obtain a reliable slope. The fits have been made with 13 bins in the specified age range, using a variable bin width to accommodate equal numbers of clusters in each bin. The clusters outside the fitted age range are binned using the same number of clusters per bin. We have adopted Poissonian errors for  $dN/d\tau$ , scaling the square root of the number of parent star particles instead of using the number of clusters in each bin, because the ages of the clusters within a single star particle are identical (see Sect. 8.2.2). In practice, this means that the relative error decreases with age, because the mean number of clusters per particle decreases. To ensure a reliable fit, the slopes have only been measured at times when a galaxy contains clusters older than 1 Gyr.

Given the time interval between subsequent output snapshots, the above procedure results in 1175 fitted age distribution slopes, covering eight different disc galaxy models. These slopes should be considered ‘mean’ slopes for the specified age range, because the age distribution does not always follow a single logarithmic slope over the fitted age range. This is illustrated in Fig. 8.9, which shows (SFR-(un)corrected) age distributions for two differ-

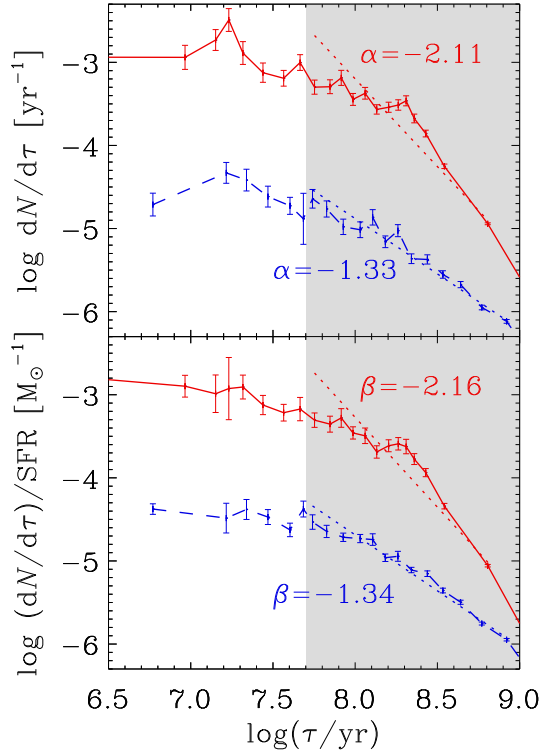


**Figure 8.9:** *Top:* Age distributions of clusters in simulations 1dB (red solid line) and 1dG (blue dashed line, vertically offset by 1.5 dex) at  $t = 3$  Gyr for ages in the range  $\log(\tau/\text{yr}) = 7.7\text{--}9$ . The dotted lines represent power law fits to the data in the age range indicated by the shaded area. *Bottom:* Same as above, but with the age distributions divided by the star formation rate (SFR-corrected). The error bars are computed as described in the text. In both panels the fitted slopes are indicated.

ent galaxies, of which the upper one (1dB) is indeed ill-fitted by a single power law. For the SFR-corrected age distributions, the negative slope is solely the result of disruption, with small variations due to stochastic effects. The SFR does not vary much in isolated galaxies, and therefore only affects the fitted slopes by a few hundredths.

In models with the same disruption rate for all clusters and a constant SFR, the ‘classical’ age distribution is characterised by two components (e.g. Boutloukos & Lamers 2003, Lamers et al. 2005a). At young ages, the age distribution is flat, because no clusters are disrupted within such a short time interval. Beyond the lifetime of the lowest mass cluster, the age distribution steepens. This is the disruptive (old) end of the age distribution, which has a slope of  $\beta = -1/\gamma$ , where  $\gamma$  is the mass dependence of the disruption timescale (see Eq. 8.6)<sup>14</sup>.

<sup>14</sup>It is assumed that the logarithmic slope of the cluster initial mass function ( $dN/dM$ ) is  $-2$ .

The models presented in this chapter assume a more realistic formulation, in which the disruption rate is affected by the variation of the tidal field strength and by tidal shocks. Nonetheless, for the sake of illustration it is important to indicate what the disruption-dominated slope of the age distribution would be if the tidal field strength would be the same throughout a galaxy, and all clusters would experience the same tidal shocks. In such a scenario, the adopted value of  $\gamma = 0.62$  for disruption due to two-body relaxation gives  $\beta = -1.61$ . For rapid shocks (i.e. a negligible adiabatic expansion during the shock), our adopted mass-radius relation yields  $\beta = -3.08$ , while for slow shocks (i.e. a dominant adiabatic expansion during the shock) we have  $\beta = -1.23$ . Fast disruption (i.e. rapid shocks) thus yields a steeper age distribution than slow disruption.

Evidently, the bulk properties of the cluster population are determined by a combination of the above mechanisms, covering a range of tidal field and shock strengths. As such, the fitted slope of the age distribution is not only determined by the mass dependence of the disruption timescale, but also by possible trends of the disruption rate with cluster age and by the rapidity of disruption in general.

The difference between the age distributions shown in Fig. 8.9 should be the result of the differences between the initial conditions of both simulations. Galaxy 1dG only differs from 1dB by its (larger) spin parameter (see Table 8.1), implying a correspondingly larger scale radius and lower (gas) density, which yields a lower disruption rate (see Sects. 8.4.1 and 8.4.2). Because of the more rapid disruption in simulation 1dB only very few clusters survive for  $\sim 1$  Gyr, causing the depletion in the oldest bin, which in turn steepens the fitted slope. Again, faster disruption implies less survivors and a potentially steeper fitted slope than for slow disruption.

Another effect is that the disruption rate due to tidal shocks will typically decrease as clusters age. This happens for two reasons (also see Fig. 8.10):

- (1) ‘Cluster migration’: because clusters move out of their primordial environment, the ambient gas density typically decreases as they age, giving rise to fewer tidal shocks and a lower disruption rate at older ages (see Elmegreen & Hunter 2010). This evolution of the mean disruption rate is more pronounced if the density contrast between the star forming region and its surroundings is large.
- (2) ‘Natural selection’: at any given time, clusters in regions with a high disruption rate are less likely to survive than clusters in low disruption rate regions. Such selection implies that at older ages only the clusters in low disruption rate regions are left, causing the disruption rate to decrease with age (also see Sect. 8.4.1 and Fig. 8.5). This evolution of the mean disruption rate is more pronounced if there is a large spread in disruption rates, like in galaxies with large density contrasts between different regions.

These two effects make the disruptive end of the age distribution shallower and steepen the young end of the age distribution. In the extreme case, this can lead to an age distribution following a single power law with a slope of  $-1$  over the majority of the age range. The effects of cluster migration and natural selection are strongest for galaxies with low gas densities, because in those galaxies the density contrast between star forming regions and their sur-

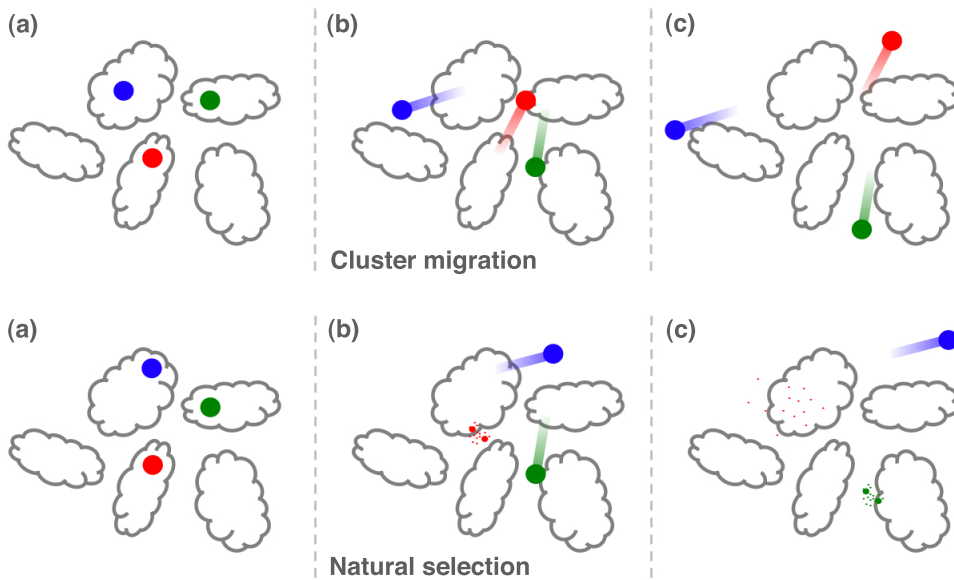


**Figure 8.10:** Schematic representation of the two processes leading to a cluster disruption rate that decreases with age. *Top:* Cluster migration. *Bottom:* Natural selection. The large dots mark star clusters, the small dots represent debris from disrupted clusters, and the clouds denote gas clouds. Time increases from left to right in both sequences.

roundings is larger than in high gas density galaxies per definition<sup>15</sup>. While already present in simulation 1dG, it could thus be even more important in dwarf galaxies, which have very low gas densities. For out-of-equilibrium systems such as galaxy mergers, the dependence of the age distribution on the mean gas density is different (see Sect. 8.5).

Above, we discussed: (1) the different disruption processes shaping the age distribution, (2) the effect of the largest possible cluster lifetime on the fitted slope, (3) the effect of cluster migration, and (4) the effect of natural selection. For all four of those, galactic environments with high gas densities steepen the slope. As discussed at length before, cluster disruption is governed by the gas density ( $\rho_{\text{gas}}$ ), implying that in isolated disc galaxies, the fitted slope of the age distribution can be used as a measure for the rapidity of cluster disruption. The gas density also sets the star formation rate density ( $\rho_{\text{SFR}}$ ) of a galaxy through the Schmidt-Kennicutt law (Schmidt 1959, Kennicutt 1998b). One would therefore expect a correlation between the fitted slopes of the age distributions in different galaxies and their star formation rate density. To obtain a measure for the star formation rate density that can be determined and compared for disc galaxies as well as for galaxy mergers at any time during their interaction,

<sup>15</sup>This holds for isolated galaxies.

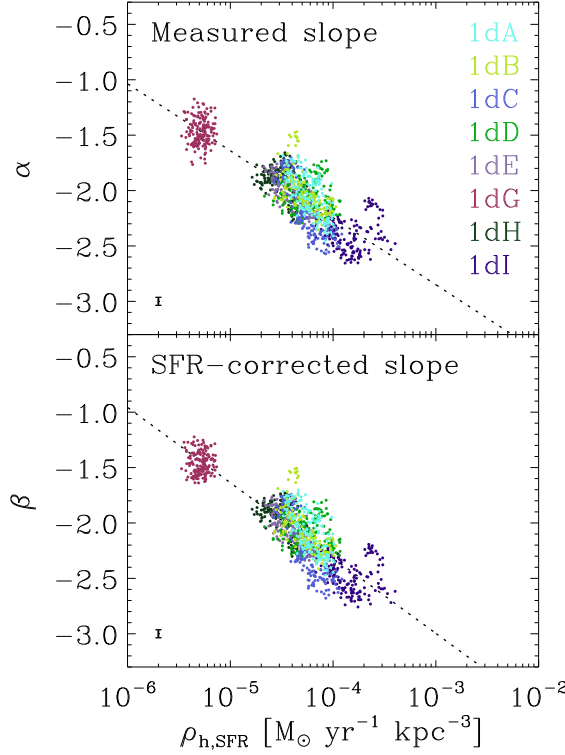


**Figure 8.11:** Relation between the fitted logarithmic slope of the cluster age distribution in the age range  $\log(\tau/\text{yr}) = 7.7\text{--}9$  and the mean star formation rate density  $\rho_{\text{h,SFR}}$ , which is defined for a sphere with a radius equal to the half-mass radius of the gas. Each point represents one galaxy snapshot. The snapshots from the different galaxy simulations are colour-coded as indicated in the legend. The best fit to the data is shown as a dotted line, while the typical error on each data point is indicated in the bottom left corner. *Top*: showing the measured (unaltered) slopes of the cluster age distributions. *Bottom*: showing slopes that are corrected for the variation of the star formation rate (SFR).

we define the mean star formation rate density within a sphere with a radius equal to the half-mass radius of the gas  $R_{\text{h,gas}}$ :

$$\rho_{\text{h,SFR}} \equiv \frac{\text{SFR}_{\text{h}}}{V_{\text{h,gas}}} = \frac{3}{4\pi} \frac{\text{SFR}_{\text{h}}}{R_{\text{h,gas}}^3}, \quad (8.27)$$

with  $V_{\text{h,gas}}$  the volume of the sphere, and  $\text{SFR}_{\text{h}}$  the star formation rate within  $V_{\text{h,gas}}$ . For isolated disc galaxies, most if not all of the star formation occurs within  $R_{\text{h,gas}}$ .

We show the relations between  $\rho_{\text{h,SFR}}$  and the fitted slope of the cluster age distribution  $\alpha$  and fitted slope of the SFR-corrected age distribution  $\beta$  in Fig. 8.11 for all 1175 fits. As

expected, it shows an inverse correlation between the slope of the cluster age distribution and the star formation rate density. For the uncorrected slope  $\alpha$ , the fitted relation is given by

$$\alpha = C - 0.60 \log \rho_{\text{h,SFR}}, \quad (8.28)$$

where  $C = -4.66$  is a fitting constant that has no particular physical meaning because we determine  $\rho_{\text{h,SFR}}$  for a sphere of which a non-negligible fraction is constituted by empty space. If the slopes of the age distributions are corrected for the variation of the SFR instead of using the raw age distributions, we obtain the relation

$$\beta = C - 0.68 \log \rho_{\text{h,SFR}}, \quad (8.29)$$

with  $C = -5.04$ . The errors on the fitted slopes in Eqs. 8.28 and 8.29 are smaller than the listed accuracy. The fitted slopes vary by less than 0.03 if the galaxy in the top-left corner of both panels in Fig. 8.11 (1dG) is excluded, which underlines the reliability of the fits.

The physical correlation between the slope of the age distribution and the star formation rate density is best described by Eq. 8.29, because in isolated discs  $\beta$  is independent of the variation of the SFR. Conversely, the relation between  $\alpha$  and  $\rho_{\text{h,SFR}}$  (Eq. 8.28) would be relevant for comparison with observations. Either way, the implication of both relations is that the rate of cluster disruption increases with the star formation rate density. In Kruijssen et al. (2011b), we present a similar result for galaxy mergers, in which the number of clusters decreases during a merger despite the large starbursts and corresponding cluster production. The net destruction of clusters is attributed to enhanced cluster disruption that is driven by the high gas density. The analysis of Kruijssen et al. (2011b) does not rely on the cluster age distributions, but instead considers the number of clusters as a function of time. The number of surviving clusters is found to decrease with increasing starburst intensity, which is similar to the relation presented here.

The scatter around the relation between the slope of the age distribution and the star formation rate density is substantial. Within a single galaxy,  $\alpha$  and  $\beta$  vary by 0.5 at a given star formation rate density, depending on the moment at which the galaxy is observed. Because it is relatively isolated in the displayed plane, galaxy 1dG in Fig. 8.11 provides a clear illustration of the spread. Recent debates in literature about the mass-dependence of cluster disruption involve differences of a similar magnitude, quoting slopes of  $-1$  (Whitmore et al. 2007, Chandar et al. 2010) to  $-1.5$  (Boutloukos & Lamers 2003). As is shown by Fig. 8.11, such variations may occur even within a single galaxy. Figure 8.11 also illustrates that a slope of  $-1$  is more likely to occur in galaxies with low star formation rate densities. As such, both sides of the debate show cases that can arise in the framework for star cluster disruption that is presented in this chapter<sup>16</sup>.

## 8.5 Galaxy mergers

We now consider the galaxy merger simulations from Table 8.2. We discuss the evolution of individual clusters, as well as the evolution of the cluster population as a whole. The section

<sup>16</sup>The starbursts in galaxy mergers are characterised by high star formation rate densities, yet the slope of the cluster age distribution is reported to be  $-1$  (Whitmore et al. 2007), seemingly contradicting Fig. 8.11 and Eq. 8.28. We discuss the inclusion of galaxy mergers in Sect. 8.5.

is concluded with a discussion of the cluster population in a merger remnant.

### 8.5.1 The evolution of individual clusters in galaxy mergers

Similar to Fig. 8.5 for disc galaxies, the evolution of the orbits and masses of three ‘representative’ clusters from simulation 1m2 are shown in Fig. 8.12. As in Sect. 8.4.1, the clusters have comparable initial masses ( $M_i \sim 1.5 \times 10^4 M_\odot$ ) and times of formation ( $t \sim 0.12$  Gyr), and the differences in their evolution are the result of their contrasting orbits in different environments.

The snapshots in Fig. 8.12 follow the merger during the first pericentre passage, when the orbital differences between the clusters are partially conserved. This is not the case during the final coalescence of the two galaxies, when violent relaxation randomises the cluster orbits. Just like in isolated disc galaxies (Fig. 8.5), the cluster closest to the centre of the galaxy has a low survival chance and is disrupted within  $\sim 200$  Myr. The two other clusters survive the first passage of the galaxies and experience different evolutionary scenarios. One is ejected from the disc of its parent galaxy (the red dotted cluster in Fig. 8.12), together with all the surrounding gas and stars, and ends up in the trailing tidal tail of the galaxy. It has a low velocity with respect to the tidal tail, but it does experience an intermediate tidal shock when entering the tidal arm at  $t = 0.32$  Gyr, and a strong tidal shock when it hits the densest part at  $t = 0.45$  Gyr, leading to the disruption of the cluster. The other cluster (blue dashed in Fig. 8.12) is ejected from the disc as well, but it decouples from the surrounding gas. This occurs because the gas collides with the other galaxy and is shocked, which slows it down to form the bridge between both galaxies. By contrast, the cluster retains a ballistic orbit and becomes part of the stellar halo surrounding the galaxies. As a result, the tidal field strength decreases and the frequency of tidal shocks becomes low, since the cluster is only shocked twice per orbit. The tidal shocks occur when the cluster crosses the bridge or the tidal arm and cause it to lose only a few percent of its mass. Under these conditions, the expected disruption time of the cluster is several gigayears. Even though the cluster mass is only  $10^4 M_\odot$ , this could increase to 10 Gyr or more when the tidal arms disperse and the merger consumes the remaining gas, provided that the cluster does not fall back into the central region of the merger. This shows that long-lived constituents of the stellar halo surrounding giant elliptical galaxies are already produced during the first pericentre passage of the progenitor galaxies (see Sect. 8.5.3).

The cluster evolution depicted in Fig. 8.12 illustrates the mechanisms of cluster migration and natural selection that were explained in Sect. 8.4.4 and Fig. 8.10. The cluster that decouples from the gas and is ejected into the stellar halo experiences a disruption rate that decreases as the cluster ages, showing how migration influences the evolution of the cluster population. On the other hand, the cluster that initially resides close to the galactic centre is quickly disrupted by the tidal shock of the first pericentre passage, while the two surviving clusters were situated in less dense environments and therefore survive. This shows how natural selection governs which clusters survive, and that the mean disruption rate of the population decreases with age as clusters in disruptive environments are destroyed.

The mass loss histories of the clusters in Fig. 8.12 can be understood by considering the evolution of the tidal field strength and the heating by tidal shocks. Similar to Fig. 8.6

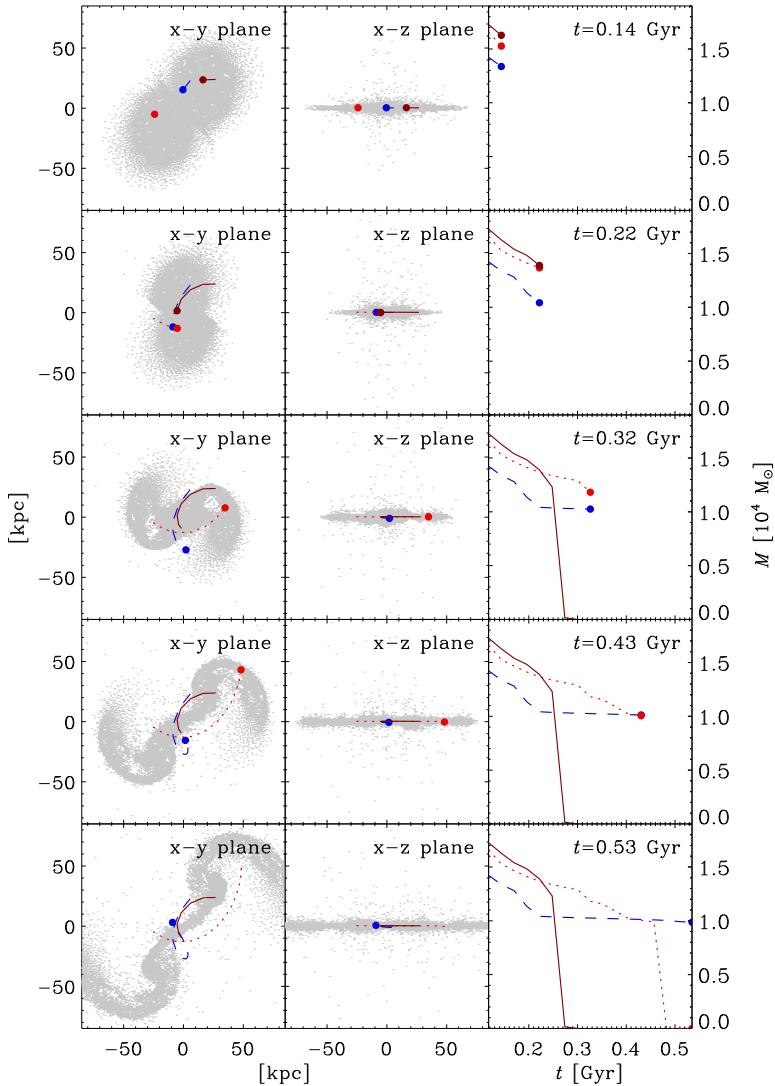


**Figure 8.12:** Evolution of the orbits and masses of three clusters in galaxy merger simulation 1m2 during the first pericentre passage of the galaxies. From top to bottom, the consecutive panels show the situation at different times  $t$ , while from left to right the orbital evolution in the x-y plane (face-on), the orbital evolution in the x-z plane (edge-on), and the mass evolution are shown. The respective clusters are represented by dark red solid lines, red dotted lines, and blue dashed lines. If at any particular snapshot a cluster is still undisrupted, its position and mass are marked with thick dots. The orbital trajectories remain visible after the clusters are disrupted. The small grey dots in the x-y and x-z plane views map the distribution of the gas particles in the simulation.



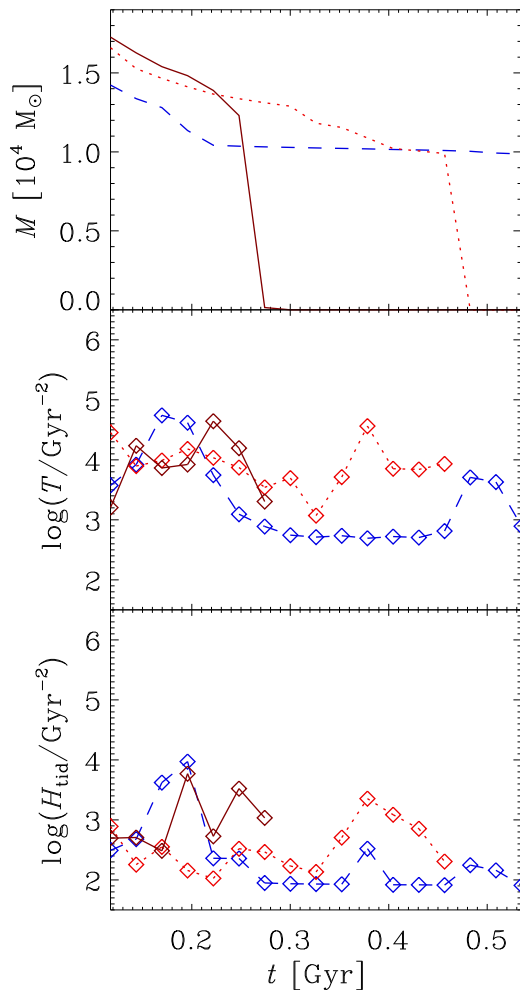


**Figure 8.13:** Evolution of the cluster mass and the tidal field for the three clusters from Fig. 8.12, indicated by the same colours and line styles. The diamonds in the middle and bottom panel indicate the times of each snapshot. *Top:* The mass evolution. *Middle:* Evolution of the tidal field strength experienced by each cluster, defined as the largest eigenvalue of Eq. 8.8 (see Sect. 8.2.2). *Bottom:* Running integral of the total amount of shock heating experienced by the cluster (see Sect. 8.4.1 and Eq. 8.25).

in Sect. 8.4.1, this is shown in Fig. 8.13 for the clusters in the merger. It confirms that the short-lived cluster indeed experiences a tidal field strength and tidal shock heating that is only rivaled by the cluster that ends up in the halo. The reason that the halo cluster is not disrupted

on the same timescale as the short-lived cluster is that its migration to the halo occurs before disruption would have led to its complete dispersion, thereby decreasing the tidal field strength it experiences. The halo cluster therefore only sustains enhanced disruption when it passes through the bridge between the two galaxies (at  $t = 0.5$  Gyr), while the short-lived cluster stays in a dense environment and is completely disrupted by two subsequent tidal shocks. By contrast, the cluster in the tidal tail continuously experiences tidal shocks and a stronger tidal field than the halo cluster, because it is moving with the tidal tail and its environment does not change. This leads to an almost constant mass loss rate, which is enhanced by the tidal shocks occurring when the cluster first enters the tidal tail and also when it hits the dense centre of the tail. This second tidal shock occurs in between two snapshots and the corresponding shock heating is therefore not visible in Fig. 8.13. The decrease of the mean tidal field strength and tidal shock heating with age illustrate the mechanism of natural selection, i.e. the higher survival chances of clusters in quiescent tidal environments. The effects of cluster migration and natural selection are stronger in galaxy mergers than in isolated disc galaxies, because both mechanisms are driven by the variation of the environment with time and space. Such variations are evidently more common in galaxy mergers than in disc galaxies.

## 8.5.2 The age distributions of star clusters in galaxy mergers

The variation of the environment in galaxy mergers leads to a corresponding evolution of the cluster age distribution. Similar to Sect. 8.4.4, we have fitted the slope of the cluster age distributions in the range  $\log(\tau/\text{yr}) = 7.7\text{--}9$  for all galaxy merger simulations, up to the moment of their largest starburst, which typically occurs early on during the final coalescence of both galaxies. The slope is not fitted for later times, because the gas is rapidly consumed during the starburst. At first, this makes the variation of the cluster formation rate dominate the shape of the cluster age distribution, implying that a power law fit is very inaccurate, while later on the age distribution becomes discontinuous due to episodes without any surviving clusters (see Sect. 8.5.3 and Fig. 8.17). Similar to Sect. 8.4.4, we consider all clusters when constructing the age distribution, i.e. the samples are mass-limited with  $M \geq 100 M_{\odot}$ .

In Fig. 8.14, the star formation history and evolution of the fitted slope of the age distribution are shown for merger simulation 1m14 (see Table 8.2). The slope widely changes over the course of the merger, and is shallowest at the times when the star formation rate and star formation rate density are highest, with typical slopes between  $-0.5$  and  $-1$ . This behaviour is opposite to what is found in Sect. 8.4.4 for isolated disc galaxies, in which the age distribution becomes steeper for higher star formation rate densities. As was discussed in Sect. 8.4.4, a shallow slope indicates that cluster migration and natural selection are important, i.e. that there are large density contrasts in a galaxy, particularly between star forming regions and their surroundings. In isolated disc galaxies, such a large contrast exists for galaxies with an overall low gas density, which then contrasts with the dense star forming regions. This low gas density translates to a low star formation rate density, and gives the relation of Eqs. 8.28 and 8.29. In galaxy mergers, the effects of cluster migration and natural selection are largest at the height of the interaction. At that point, the star formation rate (density) peaks, because all gas is funneled to the central regions, leading to a pronounced density contrast between

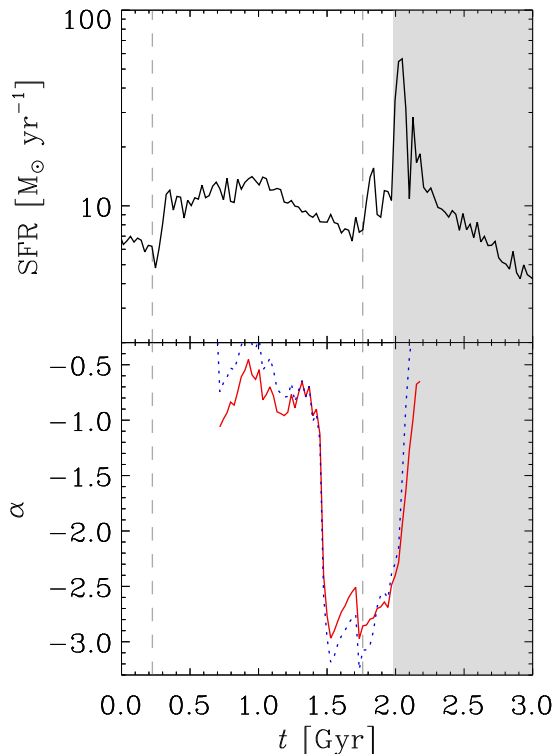


**Figure 8.14:** Time evolution of (top) the star formation rate and (bottom) the fitted slope of the age distribution in the range  $\log(\tau/\text{yr}) = 7.7\text{--}9$  for merger simulation 1m14, with the red solid line denoting the fit to the actual age distribution  $\alpha$ , and the blue dotted line denoting the fit to the SFR-corrected age distribution  $\beta$ . The dashed vertical lines indicate the moments of first and second pericentre passage, and the shaded area marks the period over which the final coalescence occurs.

the concentrated star forming volume and the surrounding regions, which hardly contain any gas. In the meanwhile, the ongoing interaction ejects the clusters into the gas-poor stellar halo. The result is visible in Fig. 8.14, in which the slope of the age distribution evolves to shallower slopes during the starbursts. The extreme slopes in between the starbursts are typically  $-2.5$  to  $-3$ , which is steeper than found in isolated discs. The reason is illustrated below, in the discussion of Fig. 8.15.

Another interesting feature of Fig. 8.14 is the difference between the actual slope  $\alpha$  and the SFR-corrected slope  $\beta$ . Because for  $\beta$  the variation of the SFR is divided out, one would expect it to have a more stable evolution than  $\alpha$ . However, this is not the case in Fig. 8.14, where the variation of the SFR-corrected slope is larger than that of the actual slope. This is the result of the mechanism identified in Kruijssen et al. (2011b), who find that the gas

density in starbursts is so high that the young clusters formed in the starburst are disrupted on much shorter timescales than in isolated galaxies, even to the extent that the total number of star clusters decreases during a starburst. This counterintuitive result is mainly due to the lowest mass clusters, which are the most numerous for a power law initial mass function with a negative slope<sup>17</sup>. This large number of low mass clusters is susceptible to disruption by the strong tidal shocks in a starburst region. The surprising consequence is that after a certain time interval, the age distribution of all clusters lacks clusters in the age range corresponding to the starburst. After the starburst, the peak in the cluster age distribution shifts to ages just *before* the maximum of the starburst (also see Sect. 8.5.3 and Fig. 8.18), when the clusters are still formed in a less violent setting than at the height of the burst, and can be ejected from their primordial regions before the starburst reaches its maximum (like the halo cluster of Fig. 8.12).

The evolution of the age distribution is compared to the star formation history in Fig. 8.15, which shows the evolution of the age distribution at several times after the major starburst in simulation 1m14. It illustrates several of the points from the previous paragraphs. The first age distribution (at  $t = 2.02$  Gyr) shows the cause of the steep slope of about  $-3$  just before the second starburst. The fitted slope is steepened relative to isolated galaxies (compare Fig. 8.11) due to a deficit of clusters at ages close to  $\tau = 1$  Gyr, which corresponds to the first starburst, when the high densities triggered enhanced cluster disruption. The same mechanism causes an age-offset between the moment of the second starburst and the peak in the age distribution, which first emerges when the clusters formed in the starburst have had the time to be disrupted by their environment. This disruption is evident from the minimum in the age distribution at ages slightly younger than the starburst. The exact moment when the offset between the peaks becomes visible depends on the duration and strength of the starburst, but it typically appears 100 Myr after the starburst. The offset grows from  $\Delta\tau = 14.5$  Myr at  $t = 2.07$  Gyr to  $\Delta\tau = 132$  Myr at  $t = 2.41$  Gyr. As shown in Fig. 8.15, it is best seen about 150 Myr after the burst. When considering only the massive clusters ( $M \gtrsim 10^4 M_{\odot}$ ), which are much less numerous than the low-mass clusters, the deficit of clusters is less prominent. In the extreme case, the offset of the peak in the cluster age distribution with respect to the moment of maximum star formation corresponds to the time interval between the onset and the peak of the starburst.

The age-offset between the starburst and the peak in the cluster age distribution has an interesting consequence in relation to Fig. 8.14. When dividing the cluster age distribution by the star formation history for a galaxy merger with a recent starburst, the age range corresponding to the starburst will contain even fewer clusters than without the correction for the SFR. As a result, the variation of the age distribution is enhanced with respect to the actual age distribution. This causes the larger variation of  $\beta$  than that of  $\alpha$  in Fig. 8.14. The offset between the peaks in the age distributions of the clusters and stars is also seen when considering the formation history of the clusters that survive the merger (see Sect. 8.5.3 and Fig. 8.18), which shows that these clusters are typically formed before instead of during the starburst maximum. It depends on the accuracy of the age determinations of real clusters whether the offset can be distinguished observationally, especially because it is less pronounced for the

---

<sup>17</sup>The index  $-2$  of the cluster initial mass function adopted in this study implies that every decade in cluster mass initially has ten times more clusters than the next decade.

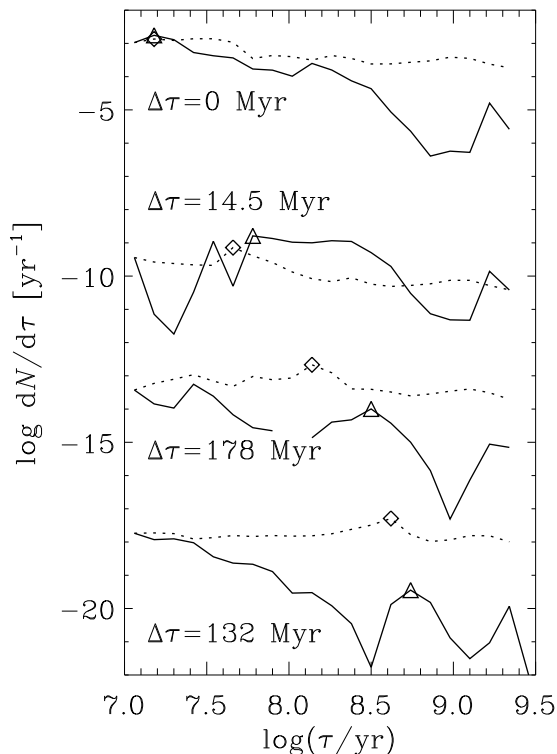


**Figure 8.15:** Time-evolution of the cluster age distribution (solid lines) and star formation history (dotted lines) shortly after the second passage of merger simulation 1m14 (at  $t \approx 2$  Gyr). From top to bottom, the distributions are shown at times  $t = \{2.02, 2.07, 2.18, 2.41\}$  Gyr, corresponding to about  $\{0, 50, 150, 400\}$  Myr after the starburst. For each line, the moment of the starburst is marked with a diamond, while the peak in the cluster age distribution is indicated with a triangle. Each age distribution is shifted down by 5 dex with respect to the distribution above it. The star formation histories are normalised to match the corresponding age distribution at the left end of the lines. For each pair of distributions, the age-offset between the peaks  $\Delta\tau$  is indicated.

high cluster masses to which observations are naturally limited.

In order to consider the relation between the slope of the age distribution and the star formation rate density, we have used the same approach as in Sect. 8.4.4 to determine a measure of the star formation rate density in galaxy mergers. For both galaxies, we determine the half-mass radius of the gas distribution and add the enclosed volumes, leaving out any overlap between both spheres. To avoid artificially low star formation rate densities, the tidal arms are omitted when calculating the half-mass radius by neglecting all material beyond 100 kpc from the centre of mass of the simulation. The plane of the fitted age distribution slope ver-

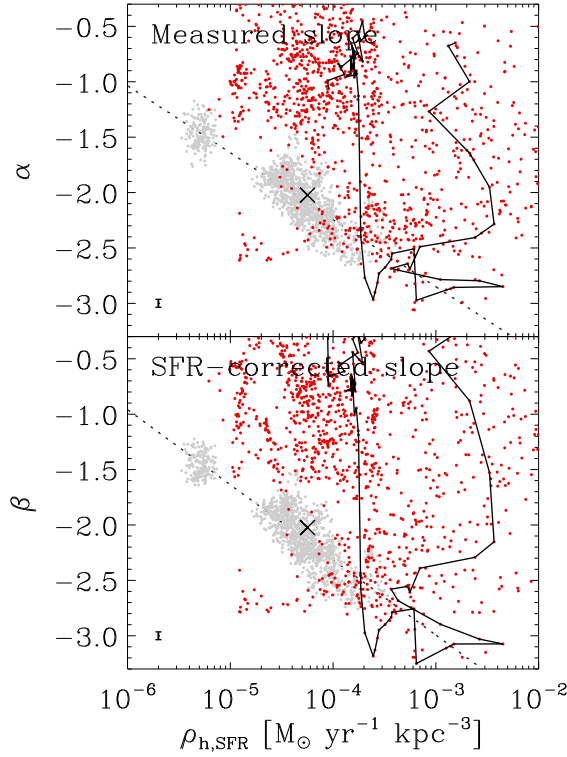


**Figure 8.16:** Relation between the fitted logarithmic slope of the cluster age distribution in the age range  $\log(\tau/\text{yr}) = 7.7\text{--}9$  and the mean star formation rate density  $\rho_{h,\text{SFR}}$ . Each point represents one galaxy snapshot. The isolated disc galaxies are shown as light grey points, and the galaxy mergers are shown as red points. As in Fig. 8.11, the fit to the isolated disc galaxies is represented by a dotted line, while the typical error on each data point is indicated in the bottom left corner. *Top:* the measured (unaltered) slopes of the cluster age distributions. *Bottom:* slopes that are corrected for the variation of the star formation rate (SFR). The solid line in both panels indicates the evolutionary track of simulation 1m14, of which the evolution of the slope is shown in Fig. 8.14. The mean slope and  $\rho_{h,\text{SFR}}$  of the progenitor galaxies (1dB) is indicated with a cross.

star formation rate density is shown in Fig. 8.16 for all galaxy merger simulations, also including the data from the galaxy disc simulations (see Fig. 8.11). As explained above in the discussion of Fig. 8.14, the galaxy mergers do not follow the relation between slope and star formation rate density that holds for isolated disc galaxies. Instead, during starbursts they typically move to shallower slopes and higher star formation rate densities, i.e. up and to the right in Fig. 8.16. The large scatter on the points of the galaxy merger simulations arises because of the wide range of possible age distribution slopes over the course of a single merger,

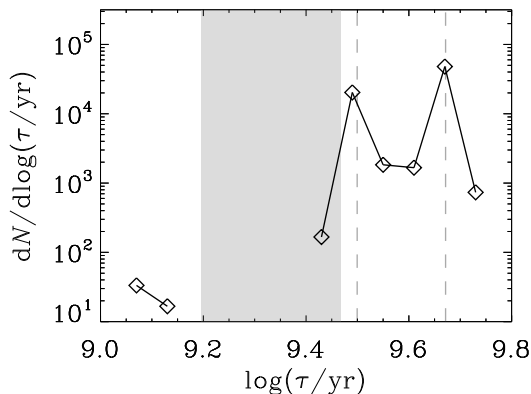


**Figure 8.17:** Logarithmic age distribution  $dN/d\log(\tau/\text{yr})$  of the clusters with ages  $\tau \geq 1$  Gyr in the merger remnant of simulation 1m14, shown for the snapshot at  $t = 4.9$  Gyr. The vertical dashed lines indicate the moments of first (right) and second (left) pericentre passage, while the shaded area marks the period over which the final coalescence occurs.

which is also present in Fig. 8.14. The scatter is also increased by our method of estimating a measure for the star formation rate density, which only allows for an order-of-magnitude analysis because it is sensitive to the global dynamical changes during the merger.

The typical evolution of a galaxy merger in the diagram of Fig. 8.16 is illustrated by the evolutionary track of simulation 1m14, which goes through three phases. Initially, both galaxies reside on the relation for isolated disc galaxies (dotted line and cross). For simulation 1m14, this is not shown in Fig. 8.16, because it occurs too early on in the simulation and insufficient clusters exist in the fitted age range. The evolutionary track starts at the top middle of the diagram, during the first pericentre passage, when the star formation rate density is still intermediate ( $\rho_{\text{h,SFR}} \sim 10^{-4} M_{\odot} \text{ kpc}^{-3}$ ) and cluster migration and natural selection are important, resulting in a shallow age distribution. In between both pericentre passages, it returns to the relation for isolated discs because the discs evolve back to a quasi-isolated state as in Fig. 8.11, but with a slightly higher star formation rate density. This changes just before the final coalescence, when the density contrast between the starburst region and the surroundings becomes important again, moving the galaxy to the top right of Fig. 8.16.

### 8.5.3 The cluster population of merger remnants

After a galaxy merger is completed and both galaxies have transformed into a single elliptical or S0 galaxy, the formation of stars and clusters ceases or proceeds at a low rate ( $\text{SFR} < 0.5 M_{\odot} \text{ yr}^{-1}$ ). As a result, the vast majority of clusters in a merger remnant is old, with ages dating back to the first and second pericentre passages of the interaction. A first indication of when and where these clusters (the ‘survivors’) were formed is obtained from

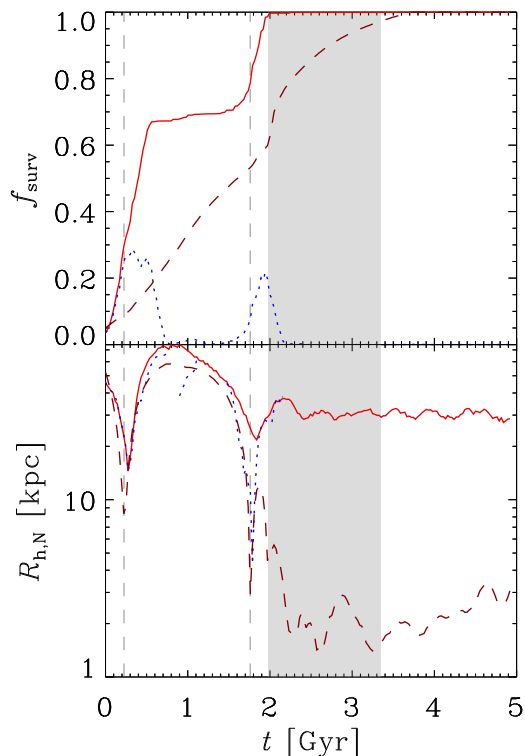


**Figure 8.18:** (Cumulative) formation history and radial evolution of the clusters that will survive the galaxy merger of simulation 1m14, i.e. those that are still present at  $t = 4.9$  Gyr. *Top:* For each time  $t$ , the figure shows the fraction of the surviving cluster population that has been formed since the start of the simulation (red solid line) and the fraction that was formed during the 200 Myr preceding  $t$  (blue dotted line). The dark red dashed line shows the cumulative fraction of star particles that have been formed since the start of the simulation. *Bottom:* Half-number radius of all present survivors (red solid line), of the survivors that were formed during the 200 Myr interval before time  $t$  (blue dotted line), and of the star particles that have been formed since the start of the simulation (dark red dashed line). Stars and clusters formed in the range  $t = 4\text{--}5$  Gyr are ignored.

their age distribution, which is shown in Fig. 8.17 for the cluster population older than 1 Gyr of simulation 1m14. The age distribution shows that most of the survivors are formed approximately at the times of the first and second pericentre passages, just before the corresponding starbursts. During the last part of the coalescence, some more clusters are formed that survive the merger. Interestingly, no clusters with ages corresponding to the onset of the coalescence exist in the merger remnant, because the violent gas influx and the resulting high gas density shortens the lifetimes of the clusters that are formed under these conditions.



A more precise picture of the origin of the cluster population in the merger remnant is obtained by considering their cumulative formation history and the radial evolution of their population. This is shown in Fig. 8.18, which follows the time evolution of the (cumulative) relative formation history and the half-number radius for three groups of objects: all survivors formed since the start of the simulation (giving a cumulative fraction), the survivors formed during the last 200 Myr, and all star particles formed since the start of the simulation (also giving a cumulative fraction). Contrary to the half-mass radius of the gas in Sects. 8.4.4 and 8.5.2, the half-number radius considered here is not defined with respect to the centre of the appropriate galaxy, but with respect to the centre of mass of the entire simulation.

The cumulative formation history of the survivors shows that each of both pericentre passages contributes about 30–60% of the old cluster population in the merger remnant. The precise distribution of percentages depends on the orbital geometry of the merger and on the properties of the progenitor galaxies. In the case of simulation 1m14, which is shown in Fig. 8.18, the galaxies pass each other on near-polar orbits, yielding a weaker starburst than a head-on or co-planar encounter and leaving some gas for post-merger star formation. For more violent starbursts, all gas is consumed and no young clusters exist in the merger remnant.

The assembly history of the stellar mass is distributed over both pericentre passages in a way that is similar to that of the clusters, even though the first passage gives rise to a much smaller starburst than the second passage. The stellar mass formed in both passages is comparable because the duration of the first starburst exceeds that of the second. The most remarkable difference between the formation history of the star particles and the surviving clusters is that they are offset with respect to each other. The surviving clusters are typically formed at earlier times than the star particles, which was also mentioned in Sect. 8.5.2 and the discussion of Fig. 8.17. Most of these survivors were ejected into the stellar halo during the pericentre passages and survived because halo clusters experience a lower disruption rate than clusters residing in the discs of both galaxies. These ejected clusters were formed before the starburst, because the onset of ejection into the halo precedes the moment of peak starburst intensity by  $\sim 200$  Myr. The combination of an already enhanced star formation rate before the ejection and the increased survival chances of halo clusters implies that the ejected clusters constitute a large part of the post-merger population of survivors.

The ejection of clusters can also be seen by considering the half-number radii of the system of (recently formed) surviving clusters and of the stars in Fig. 8.18. The pericentre passages of the two galaxies are visible as minima in the evolution of the half-number radius of the star particles. Already during the first passage, the half-number radius of the clusters exceeds that of the star particles, because the clusters that are ejected from the discs of both galaxies have higher survival chances than the clusters that stay confined to the discs. This effect becomes even more important during the second passage and final coalescence of the galaxies, during which the half-number radius of the clusters hardly changes, but the star particles end up in a much smaller volume. While this could suggest that almost no survivors are formed at small radii, the half-number radius of the recently formed surviving clusters proves the contrary. During and shortly ( $\sim 50$  Myr) after the second pericentre passage, the spatial distribution of the recently formed survivors (blue dotted line in Fig. 8.18) is as confined as the spatial distribution of star particles. This illustrates that the clusters may be

formed in the galactic discs, but are subsequently ejected due to the dynamical interaction of the galaxies, increasing their chances for survival. At later times ( $> 50$  Myr after the pericentre passage), the survivors are formed at different locations than the stars, because the clusters that are formed in the centre of the starburst are disrupted. These two examples of natural selection imply that the spatial distribution of the star cluster population in merger remnants does not follow the distribution of the stars, but is spatially more extended.

## 8.6 Discussion

In this section, we provide a summary and a discussion of the possible improvements and potential applications of our method.

### 8.6.1 Summary

We have presented numerical simulations of isolated and merging disc galaxies, in which a sub-grid model for the formation and evolution of the entire star cluster population is included. The description for the star clusters is semi-analytic and includes a model for their internal dynamical evolution and the resulting changes of the stellar mass function within the clusters. The prescription for cluster disruption has been validated by comparing to  $N$ -body simulations of dissolving star clusters, giving good agreement. When considering individual clusters within our simulations, the tidal field strength and tidal shocks are found to have a clear effect on the mass loss histories of the clusters. This provides a verification of the presented method.

One of the key advantages of the model is that it shows how the disruption rate of clusters varies in time and space. We have used our disc galaxy simulations to assess the implications of this for characteristic properties of the cluster populations. We find that the mean age of the cluster population increases with galactocentric radius, because the disruption rate and the cluster formation rate are highest near the galactic centre. This is also found in observations of the clusters in M51 (Gieles et al. 2005) and the Milky Way (van den Bergh & McClure 1980, Froebrich et al. 2010). The relative contribution of tidal shocks to the disruption of star clusters is found to be  $\sim 80\%$ , which weakly increases with increasing gas fraction of the galactic disc. A similar value was found by Lamers & Gieles (2006) from an analysis of clusters in the solar neighbourhood.

The combination of disruption due to two-body relaxation, tidal shocks, and their variation in time and space affects the slope of the cluster age distribution through two main mechanisms that lead to the same result. ‘Cluster migration’, i.e. the motion of clusters away from their formation sites, and ‘natural selection’, i.e. the higher survival probability of clusters in quiescent environments, both imply that the mean disruption rate decreases with age. In the extreme case, this can cause an age distribution with a single logarithmic slope of  $-1$  over the majority of the age range, instead of the classical flat distribution at young ages combined with a steep decline at old ages. For isolated disc galaxies, the effects of cluster migration and natural selection are largest in low gas density galaxies, because these have higher gas density contrasts between star forming regions and their surroundings. Combin-

ing this with the relation between gas density and star formation rate density (Schmidt 1959, Kennicutt 1998b), we obtain a clear correlation between the star formation rate density and the slope of the disruptive (old) end of the age distribution, which is steeper for higher star formation rate densities.

Our simulations of galaxy mergers show that the disruption rates of clusters vary widely and depend on their orbital histories during the merger. The clusters that reside in the central regions of the galaxies are disrupted on short timescales, while clusters that are ejected into the stellar halo can survive for several gigayears. The mechanisms of cluster migration and natural selection are prevalent in galaxy mergers, because the environment of clusters strongly varies in time and space. As a result, the fitted slope of the cluster age distribution (in the range  $\log(\tau/\text{yr}) = 7.7\text{--}9$ ) evolves from  $-0.5$  or  $-1$  during the starbursts, when the contrast between the concentrated star forming volume and its surroundings is largest, to  $-2.5$  or  $-3$  in between the pericentre passages, when the discs evolve back to a quasi-isolated state. This is a fundamental physical difference compared to isolated galaxies, in which the density contrast between star forming regions and their surroundings is largest for galaxies with low star formation rate densities.

The star clusters that survive the merger and populate the merger remnant are typically formed at the moments of the pericentre passages, i.e. slightly before the starbursts that occur during a galaxy merger. These clusters constitute a large fraction (30–60% per pericentre passage) of the survivors for two reasons. Firstly, they are formed in large numbers, because the star formation rate already increases before the peak of the starburst. Secondly, during the pericentre passage, the formed clusters are ejected into the stellar halo, where the disruption rate is low and the survival chance is high. The clusters that are produced in the central region during the peak of the starburst are short-lived and disrupt before they can migrate to the halo. As a result, a peak in the star formation rate does not necessarily correspond to a peak in the cluster age distribution. Depending on the properties of the starburst and the time that elapsed since it occurred, both peaks will be offset with respect to each other.

This chapter shows that the variability of the disruption rate in time and space has a pronounced impact on the properties of cluster populations in a range of galactic environments. It affects the spatial distribution of clusters, their age distribution, and the evolutionary histories of the clusters that survive until the present day. As discussed in Sect. 8.1, it has been common practice in literature to adopt a single, “mean” disruption rate for the entire cluster population of a galaxy. While this approach holds many advantages due to its simplicity, we now see that the resulting cluster populations have very different properties than those ensuing from a more realistic setting, in which the effects of the formation, disruption, and orbital histories of the clusters are intertwined.

## 8.6.2 Improvements

While the presented model gives a more detailed description of the formation and evolution of star cluster populations than before, there are several points at which it could be improved. We discuss five key improvements.

- (1) The current treatment for star formation uses one gas particle per spawned star particle.

This implies that the particle mass limits the maximum cluster mass, because it is not possible to form clusters that are more massive than the star particle which they are part of (see Sect. 8.2.2). As a result, it is not beneficial to increase the resolution of the simulation, because it will decrease the maximum cluster mass below the current value of  $\sim 10^{5.8} M_{\odot}$ . Especially when considering galaxy mergers, in which clusters with masses around  $10^7 M_{\odot}$  should be produced, improving this would be very relevant. We intend to include a group-finding algorithm in the near future, which will evaluate the Jeans criterion for groups of gas particles. This would enable the formation of a single star particle out of multiple gas particles, and will also allow us to increase the resolution of the simulations without compromising the mass range of the cluster population. In addition to giving a more realistic description of the star formation process, this would also enable us to resolve the ISM down to smaller scales, and improve the description of cluster disruption due to tidal shocks.

- (2) Supermassive black holes (SMBHs) and the possible feedback from SMBHs are presently not included. The vast majority of star clusters resides in the range where the tidal field due to the SMBH can be neglected, so the disruption rate of star clusters is not directly affected by the omission of SMBHs. An indirect effect of the presence of SMBHs could be important in galaxy mergers, during which feedback from SMBHs may be responsible for the expulsion of all gas from the galaxy (Di Matteo et al. 2005). This would disrupt any gas discs that may reform in the merger remnant and would halt further formation of star and clusters. Because it is a second order effect for the problem we are addressing, and because there are currently no definitive models for SMBH feedback (Pelupessy 2007, Sijacki et al. 2010), we have chosen to omit SMBHs in the present model. Whenever a more conclusive model for SMBH feedback becomes available, it will be included in our model.
- (3) We have approximated the evolution of the half-mass radius of star clusters with a simple power law dependence on the cluster mass, fixing the normalisation and power law index by means of a comparison to  $N$ -body simulations of dissolving clusters on eccentric orbits. This is important, because the disruption timescale due to tidal shocks depends on the half-mass density. Using the adopted relation, we reproduce the disruption times found in the  $N$ -body simulations. Even though the relation is consistent with the theoretically expected relation in the ‘mass loss-dominated’ regime from Gieles et al. (2011), a better approach would be to adopt a prescription for the half-mass radius that has a more extensive physical foundation. Unfortunately, current mass-radius relations in literature are based on the evolution of clusters in a smooth galactic potential, and depend on the galactocentric radius (Gieles et al. 2011). While this is accurate for globular clusters on orbits with a low eccentricity, it does not work for clusters orbiting within a galactic disc or in galaxy mergers, where the tidal field is erratic due to the non-uniform distribution of the gas. An appropriate model for the evolution of the half-mass radius in such an environment could be obtained by feeding an erratic tidal field into  $N$ -body simulations of star clusters and monitoring their structural evolution. Such an analysis is well beyond the scope of the present work, and we will update the mass-radius relation whenever a better description becomes available.

- (4) At present, the model does not include a description for chemical enrichment, and consequently all clusters have the same metallicity. While this has a negligible effect on the mass evolution of the clusters, their photometry is affected (see Kruijssen & Lamers 2008 for a quantitative analysis). Moreover, including a prescription for the chemical evolution of the star cluster population would enable a better comparison with (spectroscopic) observations, in which chemical abundances can be established with a generally higher accuracy than other properties such as cluster ages. It would also allow us to investigate the relation between metallicity and other characteristics of the cluster population, and to improve the model for star formation, which depends on the chemical composition of the gas. We aim to include a model for chemical enrichment in a future work.
- (5) The cluster formation efficiency (CFE), i.e. the fraction of stars that is formed in a clustered form, is assumed to be constant. This implies that the exact value acts as a normalisation of the total number of clusters, leaving it as a free parameter. It is set to 90% to obtain better statistics for the simulated cluster populations (see Sect. 8.2.2). However, there have been suggestions that the CFE depends on the local environment, particularly on quantities like the star formation rate density (Goddard et al. 2010). The exact dependence of the CFE is still far from certain, but if there exists an environmental dependence, this would affect the cluster population by favouring the formation of clusters in certain parts of a galaxy. This could also have a secondary effect on the cluster population, because cluster disruption may also proceed differently in parts with an enhanced CFE. Again, an environmental dependence of the CFE will be included when it is better constrained, either from models or observations.

Apart from these main areas for improvement, we will keep updating the models as  $N$ -body simulations and observations of clusters in a broader range of environments become available.

### 8.6.3 Applications

In order to trace the formation and evolution of galaxies using star cluster populations, it is necessary to investigate how different galactic environments affect the cluster population. Our model is a very suitable tool to gain more insight into this question, because it relates the evolution of each cluster to its (time-dependent) local environment. This implies a certain flexibility that allows us to apply the model to a broad range of galaxies. While a first analysis of the interplay between galaxies and their star cluster populations is already given in this chapter, there are many more observables of the cluster population that should be investigated under different galactic conditions.

It would be particularly useful to understand the impact of galaxy mergers on cluster populations, because such an understanding enables the use of cluster populations to probe merger histories and the hierarchical assembly of galaxies. Mergers are recognized as important drivers of starbursts and corresponding cluster formation, which are fuelled by high gas densities. However, as is shown in this chapter, a high gas density also implies a large disruption rate. It is not trivial to determine whether formation or destruction dominates. We

have considered this question in Kruijssen et al. (2011b) as a first application of the model, and find that the total number of clusters decreases during a merger, because the large gas densities result in more destruction than formation. Destruction is most prominent for the numerous clusters with low masses, whereas for the fewer massive clusters formation does dominate during certain episodes of the galaxy interaction. The corresponding change of the cluster mass function could be used as a tracer of the merger type.

By modeling specific, real galaxies, it is possible to explain observed properties of the cluster population and to predict its features that presently fall below the detection limit. Such case studies will also verify the model, and possibly provide constraints on aspects of the model that are currently uncertain (see Sect. 8.6.2). For instance, by comparing the observed and modeled star formation rates and the number of clusters within a certain mass and age range, it will be possible to infer the cluster formation efficiency in a particular galaxy<sup>18</sup>.

As is indicated in Sect. 8.1, the disruption rate of star clusters is commonly assumed to be constant when deriving the star formation history (SFH) of a galaxy from its star cluster population. Although this approximation is convenient, the thus obtained SFH will differ from the actual one. The impact of the disruption time on the inferred SFH was recently illustrated by Maschberger & Kroupa (2011, Fig. 4), who show that it depends on the adopted disruption rate to what extent the gap in the age distribution of clusters in the Large Magellanic Cloud is reflected in the inferred SFH. For their choice of disruption rates, the SFR in the age range corresponding to the age gap varies by about 1.5 dex, resulting in cases in which the SFR does and does not contain the age gap of the cluster age distribution. Because the conditions within an evolving galaxy vary widely, the impact of the time- and space-variation of the disruption rate are likely of the same order of magnitude. It is therefore essential to resolve how this variation may affect SFHs that are inferred from the star cluster population.

The formation and evolution of star cluster populations are the result of several mechanisms that act simultaneously, such as starbursts, feedback, tidal shocks, two-body relaxation, cluster migration, natural selection, and many other processes. While certain parts may still be uncertain, the current understanding of these mechanisms enables the modeling of the cluster population in a way that reflects the variability and complex nature of real galactic environments. Future applications of the model should therefore provide new clues to the (co-)evolution of galaxies and their star cluster populations.

**Acknowledgements** We would like to thank the anonymous referee for inspiring and stimulating suggestions. We are indebted to Oleg Gnedin for sending us his routines for tidal shock heating. Mark Gieles is thanked for interesting discussions and for providing some characteristic numbers for  $N$ -body King models. Holger Baumgardt kindly provided the evolution of the half-mass radius from his  $N$ -body simulations. We thank Nate Bastian, Søren Larsen and Esteban Silva Villa for helpful discussions. The calculations reported here were performed at the computing facilities of Leiden Observatory. This research is supported by the Netherlands Advanced School for Astronomy (NOVA),

---

<sup>18</sup>Before being able to combine different observational studies to look at trends of the properties of the cluster population with galactic environment, the current dichotomy in literature between groups drawing different conclusions from the exact same observational data (e.g. Chandar et al. 2006, Gieles et al. 2007b) should be settled. No model can bridge such differences.

the Leids Kerkhoven-Bosscha Fonds (LKBF) and the Netherlands Organisation for Scientific Research (NWO), grants 021.001.038, 639.073.803, and 643.200.503. JMDK acknowledges the kind hospitality of the Institute of Astronomy in Cambridge, where a large part of this work took place.





# Chapter 9

---

## Formation versus destruction: the evolution of the star cluster population in galaxy mergers

J. M. Diederik Kruijssen, F. Inti Pelupessy, Henny J. G. L. M. Lamers,  
Simon F. Portegies Zwart, Nate Bastian and Vincent Icke  
in preparation (2011)

**Abstract** We address the evolution of the star cluster population in galaxy mergers. While interacting galaxies are well-known for their high star formation rate and rich star cluster populations, it is also recognized that the rapidly changing tidal field can efficiently destroy clusters. We use numerical simulations of merging disc galaxies to investigate which mechanism dominates. Our study shows that the tidal forces during the merger are strong enough to destroy the majority of stellar clusters on short timescales. This implies that the wealth of star clusters observed in nearby merging galaxies is in fact extremely short-lived. While the merger can cause the formation of clusters with masses much higher than in normal non-interacting galaxies due to the increased star formation rate, it destroys an additional 95% of all stellar clusters compared to isolated galaxies, preferentially annihilating the lowest mass clusters. The mass distribution of the surviving star clusters in the merger remnant develops a peak at a mass of about  $10^{2.5} M_{\odot}$ , which subsequently evolves to higher masses. These results imply that globular cluster systems are the natural consequence of hierarchical cosmology and the large starbursts occurring in the early universe.

### 9.1 Introduction

Merging and interacting galaxies host huge starbursts and large populations of young massive stellar clusters (Holtzman et al. 1992, Schweizer et al. 1996, Whitmore et al. 1999). A galaxy interaction triggers inflows of interstellar gas towards the galaxy centres, where it fuels a burst of star formation (Hernquist 1989, Mihos & Hernquist 1996). The starbursts that are triggered in mergers of massive spiral galaxies play a central role in the assembly of the stellar mass in the universe, as galaxies are thought to have formed through hierarchical merging (White & Rees 1978), indicating that a large fraction of all stars were formed in starbursts (e.g.

Reddy & Steidel 2009). Some fraction of this star formation takes place in compact stellar clusters (Elmegreen 1983, Whitmore et al. 1999, Bastian 2008) with masses in the range  $10^2$ – $10^7 M_{\odot}$  (Portegies Zwart et al. 2010). The clusters that remain after the merger are often used as fossils to trace the formation history of the galaxy (Larsen et al. 2001).

Over the past two decades, observations with the Hubble Space Telescope have revealed that many nearby ongoing galaxy mergers host exceptionally rich star cluster populations with cluster masses exceeding  $10^7 M_{\odot}$  (Schweizer 1982, Holtzman et al. 1992, Bastian et al. 2006), which are formed due to the perturbation of the interstellar medium (ISM) (Schweizer 1987, Ashman & Zepf 1992). The multitude of star clusters suggests that they are useful tracers of past galaxy mergers, especially because they are easily observed up to distances of several tens of megaparsecs. The observed massive clusters ( $> 10^4 M_{\odot}$ ) are distributed according to a power law with index  $-2$  down to the detection limit (Zhang & Fall 1999). These clusters are just the ‘tip of the iceberg’, since the mass distribution appears to continue beyond the detection limit and down to the physical lower mass limit (see e.g. Portegies Zwart et al. 2010).

However, high gas densities and tidal shocks, both of which are prevalent in coalescing galaxies, are known to have a disruptive effect on star clusters (Spitzer 1958, Weinberg 1994b, Gieles et al. 2006b). The destruction rate of star clusters decreases with increasing cluster mass and density (Spitzer 1987, Lamers et al. 2005a). This indicates that star cluster disruption could be masked by observational selection effects and go unnoticed in observations, i.e. the brightest and therefore most massive clusters are easiest to detect and least affected by disruption. The important role of star cluster disruption is supported by the old (‘globular’) star cluster systems that are observed in nearby spiral and giant elliptical galaxies, which are strongly lacking low-mass clusters with respect to the young populations in presently merging galaxies (Vesperini 2001, Fall & Zhang 2001, Kruijssen & Portegies Zwart 2009, Elmegreen 2010). Whether or not the disruption of star clusters dominates over their formation is not easily determined on analytical grounds. Either way, a galaxy collision will affect the star cluster population.

To resolve whether cluster formation or destruction dominates in interacting galaxies, we have conducted numerical simulations of merging galaxies, which include a model for the formation and evolution of star clusters. This allows us to quantify the net effect of a galaxy merger on its star cluster population. In Sect. 9.2 we briefly summarize our model, while the evolution of the star cluster population is assessed in Sect. 9.3. We conclude this chapter by discussing the implications of the results.

## 9.2 Summary of the model

We model the formation and evolution of star clusters coupled to a numerical simulation code for galaxy evolution (Pelupessy 2005). Here we provide a summary of the model, which was presented and validated by Kruijssen et al. (2011c).

We use the code to calculate self gravity of gas, stars, and dark matter as well as the hydrodynamics of the gas. It includes a model for the ISM geared towards a faithful representation of the warm neutral medium and cold neutral medium phases, including metal

cooling, cosmic ray ionization, and UV heating. Stellar wind and supernova feedback are taken into account by using pressure particles (Pelupessy et al. 2004, Pelupessy 2005). Star cluster formation and evolution is included as a sub-grid model component of the star particles (Kruijssen & Lamers 2008, Kruijssen 2009). Sites of star and cluster formation are selected based on a Jeans mass criterion and the initial masses of the star clusters are drawn from a power law distribution with index  $-2$  in the range  $10^2$ – $10^7 M_\odot$ , with an exponential truncation at high masses (Schechter 1976). This reflects the observed mass distribution of young star clusters (Zhang & Fall 1999, Lada & Lada 2003, Larsen 2009). The cluster formation rate is proportional to the star formation rate (SFR), because we adopt a constant cluster formation efficiency (Bastian 2008). We do not include clusters more massive than about  $10^{5.9} M_\odot$  because they would exceed the particle mass.

The mass evolution of individual clusters is governed by mass loss due to stellar evolution and dynamical disruption:

$$\left(\frac{dM}{dt}\right) = \left(\frac{dM}{dt}\right)_{\text{se}} + \left(\frac{dM}{dt}\right)_{\text{dis}}, \quad (9.1)$$

with  $M$  the cluster mass and the subscripts ‘se’ and ‘dis’ denoting stellar evolution and disruption, respectively. The mass loss due to stellar evolution is taken from the Padova models (Marigo et al. 2008). The dynamical mass loss is caused by two simultaneous mechanisms. Firstly, the stars in the cluster are driven over the tidal boundary due to two-body relaxation (Spitzer 1987). Secondly, stars can gain energy from tidal shocks, i.e. fluctuations of the tidal field caused by passages through dense regions such as giant molecular clouds (GMCs) or spiral arms (Gieles et al. 2006b, 2007a). We parametrize the mass loss due to disruption as

$$\left(\frac{dM}{dt}\right)_{\text{dis}} = \left(\frac{dM}{dt}\right)_{\text{dis}}^{\text{rlx}} + \left(\frac{dM}{dt}\right)_{\text{dis}}^{\text{sh}} = -\frac{M}{t_{\text{dis}}^{\text{rlx}}} - \frac{M}{t_{\text{dis}}^{\text{sh}}}, \quad (9.2)$$

where  $t_{\text{dis}}^{\text{rlx}}$  represents the timescale for disruption by two-body relaxation and  $t_{\text{dis}}^{\text{sh}}$  the timescale for disruption by tidal shocks. Both timescales are related to the tidal field. The derivation is given in Kruijssen et al. (2011c), but here we give the final expressions. For  $t_{\text{dis}}^{\text{rlx}}$  the expression is:

$$t_{\text{dis}}^{\text{rlx}} = 1.7 \text{ Gyr } M_4^\gamma \left(\frac{T}{10^4 \text{ Gyr}^{-2}}\right)^{-1/2}, \quad (9.3)$$

where  $M_4$  is the cluster mass in units of  $10^4 M_\odot$ ,  $\gamma = 0.62$  is the mass dependence of the disruption timescale (Lamers et al. 2005a), and  $T$  is the tidal field strength.

For the disruption timescale due to tidal shocks, the approaches of Gieles et al. (2007a) and Prieto & Gnedin (2008) can be combined to obtain (Kruijssen et al. 2011c):

$$t_{\text{dis}}^{\text{sh}} = 3.1 \text{ Gyr } M_4 \left(\frac{r_h}{\text{pc}}\right)^{-3} \left(\frac{I_{\text{tid}}}{10^4 \text{ Gyr}^{-2}}\right)^{-1} \left(\frac{\Delta t}{\text{Myr}}\right), \quad (9.4)$$

where  $r_h$  is the half-mass radius,  $I_{\text{tid}}$  is the tidal heating parameter (see Prieto & Gnedin 2008), and  $\Delta t$  the time since the last shock, reflecting the timescale on which the cluster is

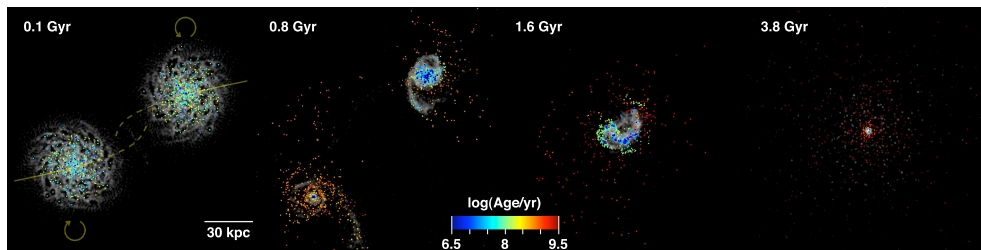


**Figure 9.1:** Evolution of the star cluster population during a galaxy merger. Sequence of snapshots from one of our galaxy merger simulations at four different times. The surface density of the gas is displayed in greyscale, while the particles that contain star clusters are shown in colours denoting the ages of the clusters as indicated by the legend. The subsequent images show the collision at four characteristic moments:  $t = 0.1$  Gyr, just before the first passage;  $t = 0.8$  Gyr, in between the first and second passage;  $t = 1.6$  Gyr, which is just after the second passage, but just before the final merger;  $t = 3.4$  Gyr, when only the merger remnant is left.

heated. We assume  $r_h = 4.35 \text{ pc} (M/10^4 M_\odot)^{0.225}$ , consistent with the  $N$ -body simulations by Baumgardt & Makino (2003) (see Kruijssen et al. 2011c). Both Eq. 9.3 and 9.4 are calibrated for clusters with King parameter  $W_0 = 5$ . For other density profiles, the constants in the equations change, but the lifetimes of the clusters are similar.

The above relations between the mass loss rate and the tidal field have been compared and calibrated to the  $N$ -body simulations of star cluster disruption by Baumgardt & Makino (2003) to ensure their accuracy. In isolated disc galaxies with 15–30% of their baryonic mass in gas, typically 85% of the cluster disruption is accounted for by tidal shocks (Eq. 9.4) (Kruijssen et al. 2011c), while the remainder is covered by two-body relaxation (Eq. 9.3), in excellent agreement with a study of the solar neighbourhood by Lamers & Gieles (2006). For a given amount of mass loss, we also compute the corresponding change of the stellar mass function within the cluster (Kruijssen 2009). The described model enables us to follow the formation and evolution of the entire star cluster population for different galactic histories.

### 9.3 Evolution of the star cluster population

We apply our model to the evolution of the star cluster population in galaxy mergers. For clarity, we first discuss one representative example here. Figure 9.1 shows a classical sequence of the evolution of a galaxy merger simulation together with the results from our cluster evolution model. Both galaxies are Milky Way-like, each having a total mass of  $M_{\text{gal}} = 10^{12} M_\odot$ . The gas fraction is 30%, and the galaxies contain a stellar bulge and dark matter halo (see Springel & Hernquist 2005 for details). The concentration index of the dark matter density profile corresponds to a formation epoch of  $z = 2$  (Bullock et al. 2001), such that the model is representative of precursors to current galaxies. Each galaxy is initially constituted by 45,875 star particles, 15,375 gas particles and 1,000,000 dark matter particles, giving particles masses of  $8 \times 10^5 M_\odot$  for the baryons and  $10^6 M_\odot$  for the dark matter. This is sufficient

to model cluster disruption, which occurs due to more massive structures (Kruijssen et al. 2011c). The galaxies follow a prograde-retrograde parabolic orbit (see the arrows and lines in Fig. 9.1), with a projected apocentre of 6 kpc and rotation axes perpendicular to the orbital plane. The panels in Fig. 9.1 show the distributions of gas and star clusters at different times during the interaction. The first image displays the galaxies as they approach each other for their first passage (at  $t = 0.1$  Gyr), when the tidal interaction between the galaxies is still relatively weak and the SFR is at an intermediate level ( $\sim 6 M_{\odot} \text{ yr}^{-1}$ ). The spatial distribution of star clusters is restricted to both galaxy discs, where the gas resides from which they are formed, and their destruction rate is low since it is dominated by the internal galactic tidal field and encounters between clusters and GMCs.

In the second image of Fig. 9.1 ( $t = 0.8$  Gyr), the galaxies are shown between their first and second passage. By this time, the gravitational interaction has produced long tidal tails. Most star clusters still follow the morphology of the gas because they have just been formed in a large starburst (about  $50 M_{\odot} \text{ yr}^{-1}$ ) that was triggered by the angular momentum loss and consequent inflow of the gas during the first pericentre passage. Some intermediate age clusters have been ejected from the discs by the interaction. They represent the first star cluster constituents of a stellar halo forming around the two galaxies. The total number of clusters has decreased since the previous snapshot, despite the large starburst (see below). This is due to the tidal perturbation of the star clusters by the large central gas density (that also drove the starburst), prompting a stronger increase of the cluster destruction rate than of the cluster formation rate.

As the galaxies proceed to merge, the effects of the interaction intensify. The third panel of Fig. 9.1 displays the galaxies during the short interval between the second passage and their final coalescence ( $t = 1.6$  Gyr), in a configuration that is similar to the ‘‘Antennae’’ galaxies (NGC 4038/4039, see Karl et al. 2010). During this phase, the remaining gas is strongly shocked and rapidly loses angular momentum, being funneled towards the centres of the galaxies where it cools to form large numbers of stars and star clusters (Mihos & Hernquist 1996). This second starburst is accompanied by an even stronger increase of the cluster destruction rate, this time decimating the cluster population. Many of the surviving clusters are ejected from the central region into the stellar halo that surrounds the galaxies. The population of surviving clusters develops a characteristic mass due to the destruction of low-mass clusters, which are more easily disrupted by tidal shocks. As a result, the number of clusters decreases more strongly than the total mass in clusters.

When the merger is completed, as is shown in the last image of Fig. 9.1 ( $t = 3.4$  Gyr), the system has transformed into a giant elliptical galaxy, in which the star cluster system has dispersed into the stellar halo. The SFR drops to a minimum after the merger, due to the depletion of the gas during the starbursts. The surviving population of clusters that were formed before and during the merger is reminiscent of currently observed globular cluster systems in many respects. First of all, the spatial configuration of these clusters is comparable to that of the globular cluster population of the Milky Way (Harris 1996), giant elliptical galaxies (Harris 2009) and young merger remnants (Schweizer et al. 1996), following a power law density profile with index  $-3.2$  in the outer parts, which is the approximate behaviour of a de Vaucouleurs profile (de Vaucouleurs 1948). Secondly, the mass distribution of the surviving clusters is developing a peak at a mass of  $10^{2.5} M_{\odot}$ , caused by the tidal disruption of

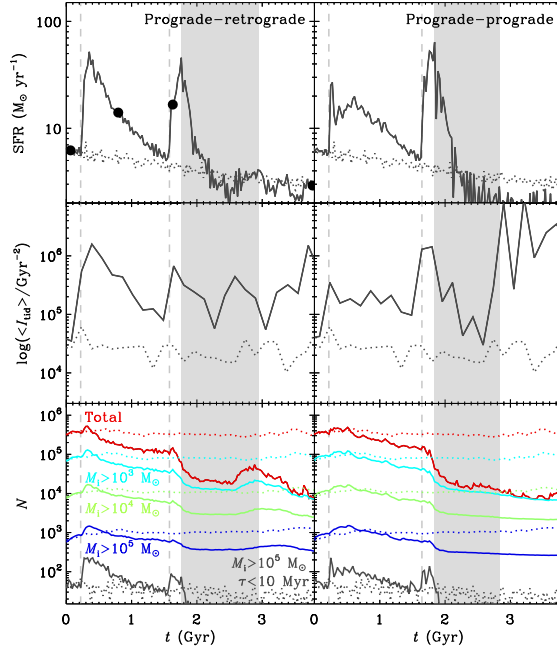


**Figure 9.2:** Evolution of the star formation rate (SFR, top), mean tidal heating ( $\langle I_{\text{tid}} \rangle$ , middle) and the number of star clusters ( $N$ , bottom) for two different galaxy merger simulations. The left-hand panels show the results for the prograde-retrograde encounter from Fig. 9.1, while the right-hand panels represent a similar encounter with both galaxies rotating in the prograde direction (anticlockwise in the configuration of Fig. 9.1). The thick dots mark the moments that are displayed in Fig. 9.1. The number of star clusters in the bottom panels is shown for different cuts in initial mass ( $\log(M_i/M_\odot) > \{2, 3, 4, 5\}$ ) and/or age ( $\tau < 10$  Myr, bottom lines only). The dotted curves denote the results for the two disc galaxies evolving in isolation. The vertical dashed lines indicate the times of first and second pericentre passage and the shaded areas specify the time interval over which the final coalescence occurs.

the low-mass clusters, which is also observed in recent merger remnants (e.g. Goudfrooij et al. 2007). This peak mass is still smaller than the characteristic mass of globular cluster systems ( $10^5 M_\odot$ , Harris 1996), which can be attained after the several billions of years of star cluster disruption following the merger until the present day (Vesperini 2001, Fall & Zhang 2001, Kruijssen & Portegies Zwart 2009), possibly also due to subsequent collisions with other galaxies. Lastly, due to the high peak SFR, the merger produces a population of clusters that extends to higher masses than for isolated galaxies, in agreement with observations (Bastian 2008).

In order to test the generality of these results, we have carried out a set of 24 major merger simulations, which are described in detail in Kruijssen et al. (2011c). We adjusted the galaxy mass ratio (1:1–1:2), virial mass ( $10^{11}$ – $10^{12} M_\odot$ ), halo formation redshift ( $z = 0$ –

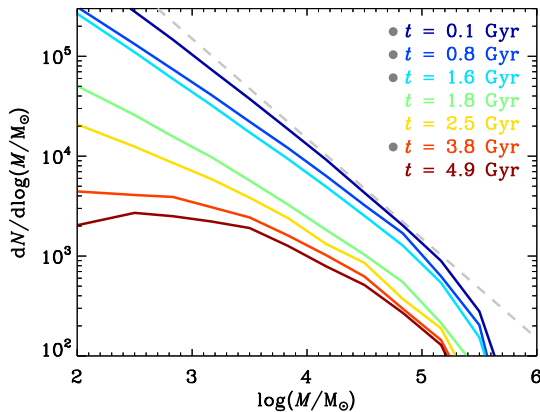


**Figure 9.3:** Evolution of the mass distribution of star clusters during the merger. Shown are the distributions at different times  $t$ . As time progresses, the distribution shifts downwards due to the net destruction of clusters. The dots in the legend mark the moments of Fig. 9.1. The slope of the initial mass distribution is shown as a dashed line, which would have closely resembled the mass distribution at all times had the two galaxies evolved in isolation.

5) , disc scale length (via the spin parameter  $\lambda = 0.05\text{--}0.10$ ), gas fraction (0.2–0.5), bulge presence, and the orbital geometry of the collision. The results of two simulations are shown in Fig. 9.2, where the star formation history as well as the time-evolution of the tidal shock heating and the number of star clusters for different initial mass cuts are shown. The figure also includes a comparison with the two disc galaxies evolving in isolation. Just after the pericentre passages, the galaxies exhibit a pronounced increase of the SFR (0.5–1 dex), but an even stronger increase of the mean tidal shock heating (1–1.5 dex), implying that the total number of clusters decreases. Both effects are driven by the strong tidal interaction between the galaxies and the subsequent growth of the central (gas) density. If tidal disruption were neglected, the number of clusters would have doubled during the merger compared to the two discs evolving in isolation. For both galaxy mergers, disruption is most prominent after the pericentre passage that triggers the strongest starburst. The resulting decrease of the number of clusters is largest for the lowest cluster masses, which is clearly seen in the number evolution for different initial mass cuts in Fig. 9.2. During the starbursts, the number of clusters temporarily increases only for the subset of young and massive clusters that are easily detected in observations. The preferential destruction of the low-mass clusters causes the initially scale-free (except for the Schechter-type truncation) cluster mass distribution to develop a characteristic mass, which is shown in Fig. 9.3. This would not occur for mass-radius relations  $r_h \propto M^\delta$  with  $\delta \geq 1/3$ , but such a strong correlation is not supported by any observational evidence. After the merger is completed, most of the gas has been exhausted and the SFR becomes much lower than would have been the case had the galaxies evolved in isolation.

For all simulations, the results are in accordance with those shown in Fig. 9.2, as they exhibit a very similar decrease of the number of clusters during the merger. The number of clusters after the merger is always 2–20% of the amount that the two discs would have contained in isolation. Much of the variation is caused by the different orbital geometries. Retrograde, co-planar encounters lead to enhanced angular momentum loss of the gas and correspondingly stronger starbursts and greater destruction of clusters, decreasing their number by a factor 20–50. Galaxies on inclined orbits such that they follow near-polar trajectories prompt a weaker effect due to a less pronounced gas inflow, yielding a decrease of about a factor 5. We find that the total number of surviving clusters strongly decreases with increasing peak SFR.

## 9.4 Discussion

We show that galaxy mergers efficiently disrupt star clusters, in apparent contradiction with the large star cluster populations that are observed in colliding galaxies. However, these two notions are in fact compatible. The observations are naturally constrained to massive ( $\gtrsim 10^4$ – $10^5 M_\odot$ ) and young ( $\lesssim 10$  Myr) clusters (Zhang & Fall 1999, e.g.), for which Fig. 9.2 shows that their number typically increases by more than a factor 3 during starbursts. Nonetheless, in terms of numbers, a star cluster population is dominated by the unseen low-mass star clusters that are effectively destroyed during the merger before they reach ages much older than a few tens of Myr. We predict that young to intermediate-age ( $\sim 2$  Gyr old) merger remnants should display a peak in the star cluster mass distribution at about  $10^3 M_\odot$  due to the destruction of low-mass clusters (see Fig. 9.3). Future observations will be able to detect this peak and thereby further constrain the assembly history of individual galaxies.

It is tempting to interpret the existence of a peak in the mass distribution of the surviving star clusters as the early formation of a globular cluster system (Ashman & Zepf 1992). If this were the case, the orbits of the clusters should be randomized during the galaxy interaction, such that there exists no radial trend of the characteristic mass (Vesperini et al. 2003). The violent relaxation occurring during galaxy mergers is efficient at ejecting clusters from their original environment (Prieto & Gnedin 2008, Bastian et al. 2009, Kruijssen et al. 2011c), which is also shown by the assembly of the stellar halo in the second and third images of Fig. 9.1. As a result, the mass distribution of the surviving clusters in our simulations is not correlated with galactocentric radius. Shortly after the completion of the merger, secular cluster disruption increases the characteristic mass by 0.2–0.3 dex per Gyr for the next two gigayears. If the merger took place in the early universe ( $\gtrsim 9$  Gyr ago), the characteristic mass would thus have the time to evolve to that of observed globular cluster systems. This would not be accomplished without the gas depletion, the migration of clusters into the halo, and the enhanced disruption occurring during the merger.

The increased cluster disruption rate in galaxy mergers is driven by the high gas densities that also cause the burst of star formation. This indicates that the mechanism of enhanced disruption is not necessarily constrained to major mergers, and can be generalized to any environment with a high gas density and a correspondingly high SFR. While major mergers provide a very efficient formation channel for globular cluster populations, they are not a



prerequisite. A generalisation to all dense environments is supported by dwarf galaxies like Fornax, which has not undergone a major merger and yet holds a handful of globular clusters (Shapley 1939, Hodge 1961). This generalization suggests that globular cluster populations may be the inevitable outcomes of the large starbursts occurring in the early universe.

**Acknowledgements** Our calculations were performed at the computing facilities of Leiden Observatory. This research is supported by the Netherlands Advanced School for Astronomy (NOVA), the Leids Kerkhoven-Bosscha Fonds (LKBF) and the Netherlands Organisation for Scientific Research (NWO), grants 021.001.038, 639.073.803, and 643.200.503. JMDK gratefully acknowledges the hospitality of the Institute of Astronomy in Cambridge, where a large part of this work took place.



---

# Chapter 10

## **Epilogue: Probing the co-evolution of star clusters and galaxies in the Antennae system – why the grand total is more than just the sum of its parts**

based on

J. M. Diederik Kruijssen and Nate Bastian  
in preparation (2011)

**Abstract** The Antennae galaxies (NGC 4038/9) are a prime example of a system with a well-studied star cluster population, of which the galactic environment has changed fundamentally over the past hundreds of Myrs. We model the Antennae system by using numerical simulations of interacting galaxies that include a description for the formation and evolution of the star cluster population. The age and mass distributions of star clusters, as well as the correlation with the spatial distribution of clusters is assessed. The modelled and observed distributions are found to be in good agreement. The slope of the cluster age distribution suggests that the time-evolution of the disruption rate due to cluster migration and natural selection (see Chapter 8) is important for ages below  $\tau \sim 150$  Myr. This hypothesis is confirmed by the age dependence of the mean ambient gas density of the clusters, which steeply decreases with age until  $\tau \sim 150$  Myr. The variability of the environment leads to the preferential disruption of young clusters, which illustrates that the implications of the cruel cradle effect (see Chapter 2) is observable on galactic scales. We conclude by pointing out that the properties of the cluster population are not a simple result of the adopted cluster disruption law, but instead arise due to the complex properties of the galactic environment, which underlines the necessity of accounting for the evolution of the environment when interpreting observed cluster populations.

### **10.1 Introduction**

The populations of young star clusters in interacting galaxies have received increasing attention over the past two decades (Holtzman et al. 1992, Whitmore & Schweizer 1995, Schweizer et al. 1996, Whitmore et al. 1999, Bastian et al. 2005), which has been primarily

driven by the launch of the Hubble Space Telescope and the potential of the latest generations of large-scale ground based facilities. The Antennae galaxies (NGC 4038/9) have emerged as the hallmark of cluster-forming systems (e.g. Whitmore et al. 1999), due their relatively close proximity of less than 22.5 Mpc (Schweizer et al. 2008) and the interaction-induced starburst of  $10\text{--}20 M_{\odot} \text{ yr}^{-1}$  (Zhang et al. 2001, Karl et al. 2010), which produces a large population of young star clusters. It is the nearest approximately equal-mass major merger of two gas-rich galaxies, which has enabled a detailed study of the system across all wavelengths, in X-ray (Fabbiano et al. 2004), UV (Hibbard et al. 2005), optical (Whitmore et al. 1999), IR (Gilbert & Graham 2007), and radio (Hibbard et al. 2001). With the large amounts of data on the Antennae system, it also raises a large number of questions. A property of the cluster population in the Antennae system that pushes known limits is the maximum cluster mass. Masses well over  $10^6 M_{\odot}$  (Zhang & Fall 1999) or even over  $10^7 M_{\odot}$  have been reported. Whether or not there is a fundamental upper mass limit for star clusters could thus potentially be tested in this particular merger.

Galaxy mergers are famous for their large nuclear starbursts, which are driven by the inflow of the gas due to the tidal torques that are exerted on the gas discs by the interaction (Hernquist 1989, Mihos & Hernquist 1996). In the Antennae, the region in which both galaxies touch (the ‘overlap region’) contains a plethora of young star clusters, indicating a recent starburst outside the galaxy centres (Whitmore et al. 1999). Explaining this extra-nuclear starburst has been one of the main challenges for numerical work on the Antennae (e.g. Mihos et al. 1993). In a recent paper, Karl et al. (2010) have presented the first numerical model that reproduces the spatial distribution of star formation, including the starburst in the overlap region. Out of a larger parameter search, they have isolated the orbital history that best fits the current properties of the system, thus enabling new studies that assess the properties of the Antennae in more detail.

Perhaps the most puzzling aspect of the cluster population of the Antennae galaxies is the suggestion that the cluster age distribution ( $dN/dt$ ) follows a power law with index  $-1$  up to ages of a few 100 Myr, independent of cluster mass (Fall et al. 2005, Whitmore et al. 2007). This would imply that 90% of all clusters is disrupted every age dex, a process which has been interpreted by these studies as being due to (long-duration) infant mortality – the disruptive effect of the expulsion of the primordial gas, which is traditionally thought to take place on much shorter time scales, of about 10 Myr (Lada & Lada 2003, Goodwin & Bastian 2006). However, our recent analysis of simulations of star formation (Kruijssen et al. 2011a) suggests that infant mortality may not be as ubiquitous as previously thought, due to the gas-poor state of stellar subclusters in star-forming regions. This would imply that other cluster disruption mechanisms are responsible for the long-duration infant mortality that is potentially observed in the Antennae, such as tidal shock heating and two-body relaxation. However, these mechanisms depend on the cluster mass and typically take place on longer time scales than gas expulsion itself. Either way, the observed age distribution requires a particularly high disruption rate for young clusters.

Classically, cluster age distributions have been modelled for constant disruption rates due to tidal shocks and two-body relaxation (e.g. Lamers et al. 2005a, Lamers & Gieles 2006), giving rise to a disruption time that increases with cluster mass. At young ages, the resulting age distribution is flat, because it takes a finite time for the clusters of the lowest masses to

be disrupted. At an age related to the disruption time scale of the lowest cluster mass, the age distribution bends down, to a slope that is determined by the slope of the cluster initial mass function and the mass dependence of the disruption time scale. This part of the age distribution is steeper than the slope of  $-1$  that is found in the Antennae.

The time dependence of the disruption rate has recently been addressed by Elmegreen & Hunter (2010) and Kruijssen et al. (2011c), who have shown that it decreases with cluster age. In Kruijssen et al. (2011c), we have attributed this to two processes.

- (1) Cluster migration, i.e. the motion of young star clusters away from star-forming regions, where the number density of giant molecular clouds (GMCs) and the disruption rate are high. Because older clusters are spatially less associated with star-forming regions than young clusters, this leads to a disruption rate that decreases with age.
- (2) Natural selection, i.e. the preferential destruction of clusters that reside in ‘disruptive’ environments. As a cluster population ages, the mean disruption rate is lower for those clusters that have survived longer, leading to a disruption rate that decreases with age.

These two mechanisms are important in environments with large changes in the environment of clusters during their lifetimes. A galaxy merger like the Antennae galaxies is therefore a prime location where cluster migration and natural selection could play a role. The imprint of a spectrum of disruption rates on the cluster age distribution is twofold. At young ages, the flat distribution steepens up to a slope of about  $-1$  due to the disruption of clusters with high disruption rates. At older ages, the classically disruptive slope becomes shallower, because not all clusters are being disrupted (yet). The end result could well be an age distribution with a slope close to  $-1$  over a long age range. If the disruptiveness of star-forming regions would be so high that clusters of all masses could be disrupted in a single encounter with a GMC, this age distribution would also be independent of mass.

In this chapter, we apply the numerical models of Kruijssen et al. (2011c) to simulate the Antennae system and its star cluster population. These models self-consistently combine  $N$ -body/SPH simulations of galaxies and galaxy mergers with a description for the formation and evolution of star clusters, allowing us to track the properties of the cluster population throughout the evolutionary history the Antennae. Next to being a suitable test for the models, the present chapter will also allow us to test the hypothesis that the recent evolution of the galactic environment shapes the cluster population of the Antennae galaxies, and that the processes of cluster migration and natural selection are important.

We begin with a summary of the modelling method and an overview of the adopted initial conditions in Sect. 10.2. The cluster population is discussed in Sect. 10.3, where the age-, mass- and spatial distributions are presented and explained. The chapter is concluded with a discussion of the results, and it is illustrated how the other chapters of this work have been combined in our effort to understand the Antennae galaxies.

## 10.2 A model for the Antennae system

In this section, we describe the way in which we model the Antennae system and which parameters we use for the simulation.

### 10.2.1 Summary of the model

We follow the formation and evolution of star clusters using a semi-analytic model that is coupled to a numerical simulation code for galaxy evolution (Pelupessy 2005). Here we provide a summary of the model, which has been described in more detail by Kruijssen et al. (2011c).

We use the numerical galaxy evolution code to calculate self gravity of gas, stars, and dark matter as well as the hydrodynamics of the gas. The model for the interstellar medium (ISM) is aimed at a reliably describing the warm neutral medium and cold neutral medium phases, and includes metal cooling, cosmic ray ionization, and UV heating. Stellar wind and supernova feedback are taken into account by using pressure particles (Pelupessy et al. 2004, Pelupessy 2005). Star cluster formation and evolution is included as a sub-grid model component of the star particles (expanding on the methods of Lamers et al. 2005a, Kruijssen & Lamers 2008, Kruijssen 2009). Sites of star and cluster formation are selected based on a Jeans mass criterion and the initial masses of the star clusters are drawn from a power law distribution with index  $-2$  in the range  $10^2$ – $10^7 M_\odot$ , with an exponential truncation at high masses (Schechter 1976). This is in accordance with the observed mass distribution of young star clusters (Zhang & Fall 1999, Lada & Lada 2003, Larsen 2009, Portegies Zwart et al. 2010). We adopt a constant cluster formation efficiency (Bastian 2008), implying that the cluster formation rate is proportional to the star formation rate (SFR). Clusters that are initially more massive than about  $10^{5.9} M_\odot$  are excluded because they would exceed the particle mass.

After their formation, the individual clusters lose mass due to stellar evolution and dynamical disruption:

$$\left(\frac{dM}{dt}\right) = \left(\frac{dM}{dt}\right)_{\text{se}} + \left(\frac{dM}{dt}\right)_{\text{dis}}, \quad (10.1)$$

with  $M$  the cluster mass and the subscripts ‘se’ and ‘dis’ denoting stellar evolution and disruption, respectively. The mass loss due to stellar evolution is taken from the Padova models (Marigo et al. 2008). The dynamical mass loss arises from two mechanisms. The stars in a cluster are driven over the tidal boundary due to two-body relaxation (Spitzer 1987), but they can also gain energy from tidal shocks, i.e. fluctuations of the tidal field caused by passages through dense regions such as GMCs or spiral arms (Gieles et al. 2006b, 2007a). The mass loss due to disruption written as

$$\left(\frac{dM}{dt}\right)_{\text{dis}} = \left(\frac{dM}{dt}\right)_{\text{dis}}^{\text{rlx}} + \left(\frac{dM}{dt}\right)_{\text{dis}}^{\text{sh}} = -\frac{M}{t_{\text{dis}}^{\text{rlx}}} - \frac{M}{t_{\text{dis}}^{\text{sh}}}, \quad (10.2)$$

where  $t_{\text{dis}}^{\text{rlx}}$  represents the timescale for disruption by two-body relaxation and  $t_{\text{dis}}^{\text{sh}}$  the timescale for disruption by tidal shocks. Both timescales are related to the tidal field, and their derivation is given in Kruijssen et al. (2011c). For  $t_{\text{dis}}^{\text{rlx}}$  the expression is:

$$t_{\text{dis}}^{\text{rlx}} = 1.7 \text{ Gyr } M_4^\gamma \left(\frac{T}{10^4 \text{ Gyr}^{-2}}\right)^{-1/2}, \quad (10.3)$$

where  $M_4$  is the cluster mass in units of  $10^4 M_\odot$ ,  $\gamma = 0.62$  is the mass dependence of the disruption timescale (Lamers et al. 2005a), and  $T$  is the tidal field strength, which is equal to the largest eigenvalue of the tidal tensor.

For the disruption timescale due to tidal shocks, the approaches of Gieles et al. (2007a) and Prieto & Gnedin (2008) can be combined to obtain (Kruijssen et al. 2011c):

$$t_{\text{dis}}^{\text{sh}} = 3.1 \text{ Gyr } M_4 \left( \frac{r_h}{\text{pc}} \right)^{-3} \left( \frac{I_{\text{tid}}}{10^4 \text{ Gyr}^{-2}} \right)^{-1} \left( \frac{\Delta t}{\text{Myr}} \right), \quad (10.4)$$

where  $r_h$  is the half-mass radius,  $I_{\text{tid}}$  is the tidal heating parameter (see Prieto & Gnedin 2008), and  $\Delta t$  the time since the last shock, reflecting the timescale on which the cluster is heated. We assume  $r_h = 4.35 \text{ pc } (M/10^4 M_\odot)^{0.225}$ , consistent with the  $N$ -body simulations by Baumgardt & Makino (2003) (see Kruijssen et al. 2011c). Both Eq. 10.3 and 10.4 are calibrated for clusters with King parameter  $W_0 = 5$ . For other density profiles, the constants in the equations change, but the lifetimes of the clusters are similar.

The above relations between the mass loss rate and the tidal field give results that accurately reproduce the  $N$ -body simulations of star cluster disruption by Baumgardt & Makino (2003). In isolated disc galaxies with 15–30% of their baryonic mass in gas, typically 85% of the cluster disruption is accounted for by tidal shocks (Eq. 10.4) (Kruijssen et al. 2011c), while the remainder is covered by two-body relaxation (Eq. 10.3), in excellent agreement with a study of the solar neighbourhood by Lamers & Gieles (2006). In the changing environments of galaxy mergers, the disruption due to tidal shocks is enhanced by more than an order of magnitude (1–1.5 dex) due to the high gas densities (see Kruijssen et al. 2011b). For a given amount of mass loss, we also compute the corresponding change of the stellar mass function within the cluster (Kruijssen 2009). The described model enables us to follow the formation and evolution of the entire star cluster population in the Antennae galaxies.

## 10.2.2 Simulation parameters and orbital history

A solution for the orbital history of the Antennae has recently been provided by Karl et al. (2010), who matched the observed spatial distributions of stars and star formation with a numerical galaxy merger model. The input snapshot used in our simulations was generated by S. Karl (priv. comm.) from the exact same initial conditions except for the numbers of particles, which were chosen to suit the modelling of the star cluster population with the method of Kruijssen et al. (2011c). Here, we briefly summarise the key parameters of the input model, most of which can also be found in Karl et al. (2010).

The progenitor discs of the two galaxies have been generated such that they can be related to the outcomes of  $\Lambda$ CDM cosmology (Mo et al. 1998, Springel & Hernquist 2005). Each galaxy contains a Hernquist (1990) dark matter halo, an exponential disc, and a stellar bulge. The total virial mass of each galaxy is  $5.52 \times 10^{11} M_\odot$ , with a disc mass fraction of  $m_d = 0.075$  and a bulge mass fraction of  $m_b = 0.025$ , yielding a bulge-to-disc ratio of 1:3. The gas fraction of the discs is  $f_g = 0.2$ , with the remainder of the disc as well as the bulge being constituted by stars. The halo spin parameter  $\lambda_1 = 0.10$  for NGC 4038, and  $\lambda_2 = 0.07$  for NGC 4039, implying discs with radial scale lengths of  $r_{d,1} = 6.28 \text{ kpc}$  and  $r_{d,1} = 4.12 \text{ kpc}$ , respectively (Mo et al. 1998). The bulge scale lengths and vertical scale lengths of the discs

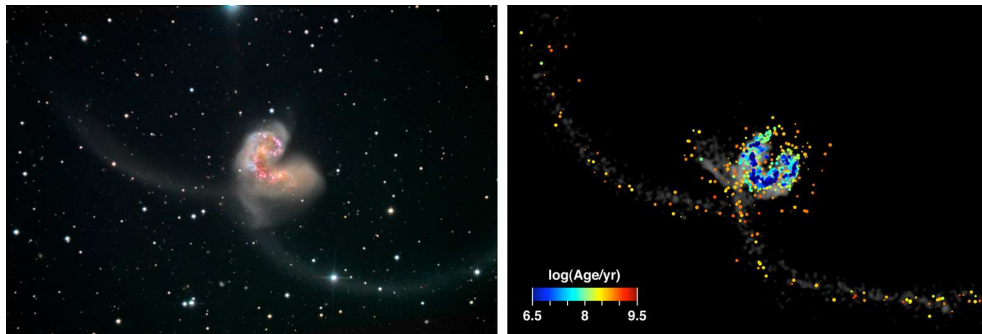


**Figure 10.1:** Morphology of the Antennae system and its star cluster population. *Left:* Composite optical image taken with the 20-inch telescope at Kitt Peak National Observatory (credit: Twardy & Twardy/Block/NOAO/AURA/NSF). *Right:* Best matching snapshot from our simulation, at  $t = 1.22$  Gyr. The surface density of the gas is displayed in greyscale, while the particles that contain star clusters are shown in colours denoting the ages of the clusters as indicated by the legend.

are  $r_{b,1} = z_{d,1} = 1.26$  kpc and  $r_{b,2} = z_{d,2} = 0.82$  kpc. The adopted particle numbers for each progenitor galaxy are 400,000 dark matter halo particles, 20,000 bulge particles, 48,000 stellar disc particles, and 12,000 gas disc particles, resulting in baryonic particle masses of  $6.9 \times 10^5 M_{\odot}$  and dark matter halo particle masses of  $1.2 \times 10^6 M_{\odot}$ .

The evolution of the system is computed using a gravitational softening length of 0.14 kpc, which ensures that the disruption of star clusters is not notably artificially enhanced by single-particle encounters (see Kruijssen et al. 2011c). The adopted orbit is prograde and near-parabolic, with a projected pericentre distance of 10.4 kpc and an initial separation of 168 kpc. The initial orientation of both discs can be characterised by rotation around the  $x$ -axis by an angle  $\theta$ , around the  $y$ -axis by an angle  $\psi$  and around the  $z$ -axis by an angle  $\phi$ . For NGC 4038, Karl et al. (2010) find  $\theta_1 = 60^\circ$  and  $\phi_1 = 60^\circ$ , while for NGC 4039 they obtain  $\theta_2 = 60^\circ$  and  $\phi_2 = 30^\circ$ . In order to consider the system from the same point of view as the Antennae, the entire simulation needs to be rotated. For subsequent rotations around the  $x$ -,  $y$ -, and  $z$ -axes, the required rotation angles are  $\{\theta, \psi, \phi\} = \{93^\circ, 69^\circ, 253.5^\circ\}$ . This setup produces a spatial configuration for the Antennae galaxies which best matches the observed system at  $t = 1.22$  Gyr, some  $\sim 20$  Myr after the second pericentre passage. This exact moment is slightly earlier than the best match at  $t = 1.24$  Gyr that was reported in Karl et al. (2010), which is due to the different particle numbers and smoothing length. Nonetheless, the  $\sim 20$  Myr time difference between the best match and the second pericentre passage is consistent with their analysis.

### 10.3 Properties of the cluster population

The observed and simulated spatial characteristics of the Antennae galaxies and their star cluster population are compared in Fig. 10.1. Both images are consistent in terms of the



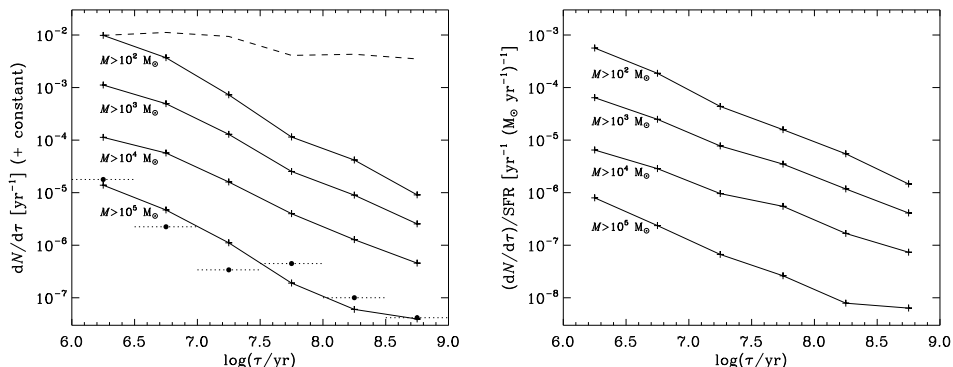


**Figure 10.2:** Age distributions of star clusters in the Antennae system. *Left:* Solid lines represent the mass-limited, simulated age distributions for (from top to bottom) lower mass limits of  $\{10^2, 10^3, 10^4, 10^5\} M_{\odot}$ . The dashed line gives the star formation history in the simulation, while the thick points and dotted lines denote the observed age distribution of clusters with masses above  $10^5 M_{\odot}$  from Whitmore et al. (2007). *Right:* Star formation rate-corrected, mass-limited, simulated age distributions for (from top to bottom) lower mass limits of  $\{10^2, 10^3, 10^4, 10^5\} M_{\odot}$ . For ages  $\tau < 150$  Myr, they are well-approximated with a power law with index  $-1$ .

global morphology, since the tidal arms and configuration of both galaxy discs are well-reproduced. The largest difference is the gas plume to the left of the main galaxies in the simulated image, which does not appear in the optical observations and is not visible in radio images either. The observed and simulated spatial distributions of star and cluster formation are well-matched, with several starburst regions – two in the central discs of both galaxies, one in the ‘western loop’ (top of the left-hand galaxy) and one in the ‘overlap’ region quoted by Whitmore et al. (1999, also see Sect. 10.1). The top sides of both galaxies in the simulated image host several intermediate-age clusters ( $\tau \sim 100$  Myr) which are currently escaping the discs. Similar examples have been observed in the actual Antennae by Bastian et al. (2009). They also identified a cluster projected onto southern tidal arm with an age of  $\sim 200$  Myr, which coincides with the ages of the clusters residing in the tidal tails of our simulation.

To address the ages of the clusters in some more detail, Fig. 10.2 shows the mass-limited age distributions of the observed and simulated cluster populations, as well as the star formation history (SFH) and the SFH-corrected age distributions. For the same lower mass limit  $M > 10^5 M_{\odot}$ , the observed and simulated age distributions are in good agreement, with mean slopes that differ by less than 5%. Regardless of the lower mass limit, the simulated age distributions have a logarithmic slope of about  $-1$  up to an age of about  $\tau \sim 150$  Myr, after which their slope becomes mass-dependent. This is particularly well visible in the SFH-corrected panel of Fig. 10.2, which shows that clusters more massive than  $10^5 M_{\odot}$  are less efficiently destroyed than those with masses  $10^2 M_{\odot}$ . This behaviour at old ages ( $\tau > 150$  Myr) is the ‘classical’ result that is expected from predictions that do not account for variations of the disruption rate (e.g. Lamers et al. 2005a). It is clear that while the interaction-induced

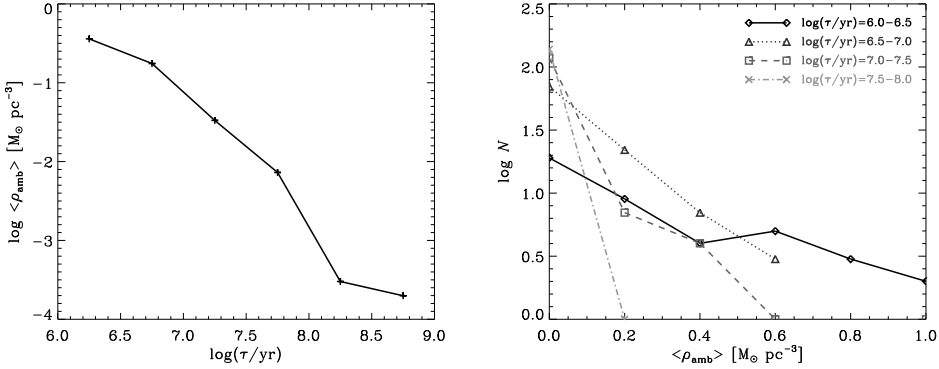


**Figure 10.3:** Simulated age-evolution of the ambient gas densities of star clusters in the Antennae system. *Left:* Mean ambient gas density as a function of cluster age. *Right:* Distribution of ambient gas densities for different cluster age ranges.

starburst influences the simulated age distribution at ages  $\tau < 50$  Myr, the fluctuation of the SFH is much smaller than the overall decline of the number of clusters with age.

It was shown by Elmegreen & Hunter (2010) and Kruijssen et al. (2011c) that an age distribution with a logarithmic slope of  $-1$  indicates an age-decrease of the mean disruption rate, which is caused by ‘cluster migration’ and ‘natural selection’ (see Sect. 10.1 and Kruijssen et al. 2011c). The disruption of clusters in a galaxy merger is mainly caused by tidal shocks due to encounters with GMCs and other high-density regions (Kruijssen et al. 2011b,c). Provided that these tidal shocks are initially strong enough to disrupt massive clusters in a single encounter, the imprint of disruption on the cluster age distribution will be independent of cluster mass.

We test whether the slope of the age distribution is indeed due to the age-evolution of the disruption rate by considering the mean ambient gas density of clusters as a function of their age. The ambient gas density is estimated by summing the gas particle masses within one smoothing length of the parent star particle of each cluster and dividing by the enclosed smoothing volume. The age-evolution of the mean ambient gas density and of the distribution of ambient gas densities is shown in Fig. 10.3. As expected from the slope of the age distribution, the mean ambient gas density decreases by more than three orders of magnitude before  $\tau \sim 150$  Myr. At older ages, it flattens to a constant value at which tidal shocks are unable to disrupt clusters in a single encounter. As a result, for ages  $\tau > 150$  Myr the imprint of cluster disruption on the age distribution returns to the ‘classical’, mass-dependent form (Lamers et al. 2005a). Not surprisingly, the age scale at which this occurs corresponds to the ages of the clusters escaping the main discs of the Antennae in Fig. 10.1 and Bastian et al. (2009).

The mass-independence of cluster disruption and the transition to a more mass-dependent form at ages  $\tau > 150$  Myr are also visible in the cluster mass function, which is shown for different age intervals in Fig. 10.4. The logarithmic slope of the mass distribution is close to

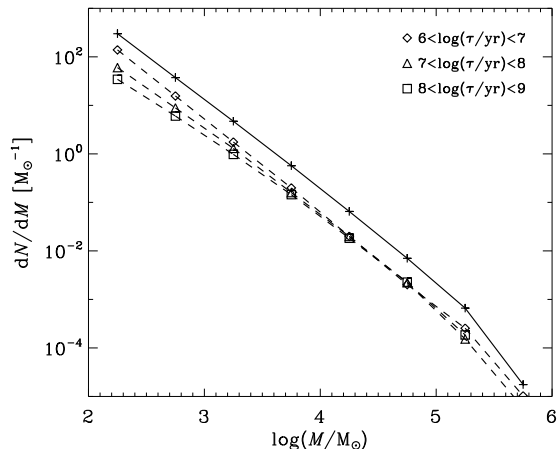


**Figure 10.4:** Simulated mass distribution of star clusters in the Antennae system. The solid line represents the total cluster mass function, while the dashed lines denote the mass function for different age intervals (see legend).

$-2$  for all age intervals, but it does become flatter for the oldest age interval (see the squares in Fig. 10.4, i.e.  $8 < \log(\tau/\text{yr}) < 9$ ). This is illustrated by the best fitting logarithmic slopes for the subsequent age intervals, which (from young to old) are  $-1.92$ ,  $-1.84$  and  $-1.74$  for the mass function below<sup>1</sup>  $\log(M/M_{\odot}) < 5.5$ . However, this flattening typically occurs in the part of the mass function at  $M < 10^4 M_{\odot}$ , which (especially at these old ages) is below the detection limit. Current observations of the cluster mass function in the Antennae should therefore yield the same slope for all age intervals, which is indeed the case (Zhang & Fall 1999). The mass functions for different age intervals in Fig. 10.4 are also nearly identical in terms of their absolute value, which is a result of the fact that the logarithmic slope of the age distribution is close to  $-1$ . This yields equal numbers of clusters in logarithmically spaced age intervals.

## 10.4 Emergent effects in galactic environments

It should be emphasised that the apparent cluster mass-independence of disruption that we find for the cluster population of the Antennae system does not apply to the mass evolution of individual clusters. The cluster disruption model that we used is based on a mass-dependent disruption time (Lamers et al. 2005a, Kruijssen et al. 2011c), which for a fixed disruption rate would produce a two-component age distribution that is flat at young ages, and has a logarithmic slope steeper of about  $-1.5$  at old ages (Lamers et al. 2005a, Lamers & Gieles

<sup>1</sup>At higher masses, the steepening of the mass functions is artificial due to the maximum cluster mass in our simulations.

2006). However, the variation of the galactic environment in time (or age) and space gives rise to a cluster population in which the disruption rate decreases with age, and specifically so that young clusters of all masses can be disrupted by a single, strong tidal shock due to the disruptive nature of their galactic environment. As a result, the observed and simulated age distributions of the cluster population in the Antennae system reflect the mechanisms of cluster migration and natural selection. Older clusters have migrated to less disruptive environments and are the remaining survivors after those clusters in disruptive environments were destroyed at younger ages. The combination of these effects yields an age distribution that is well-approximated by a single power law with a logarithmic slope of  $-1$  for ages  $\tau < 150$  Myr, independently of the cluster mass. At older ages, the disruption rate has decreased to a constant, low value, for which the imprint of disruption on the cluster age and mass distributions resembles the ‘classical’ model by Lamers et al. (2005a).

The properties of the star cluster population in the Antennae galaxies are consistent with the picture of mass-dependent disruption (Lamers et al. 2005a), in which more massive clusters are less easily disrupted, and also with the concept of ‘emergent’ mass-independent disruption (Elmegreen & Hunter 2010, Kruijssen et al. 2011c), in which the variation of the galactic environment influence the properties of the cluster population. However, our results are not consistent with the fundamentally mass-independent parameterisation of Whitmore et al. (2007), which is independent of the environment.

In summary, the Antennae system is an excellent example of how the properties of the star cluster population are the result of the interplay between the fundamental aspects of cluster evolution and the galactic environment. The dramatic metamorphosis of the two galaxies is leaving a clear imprint on the properties of the star cluster population, even to the extent that it mimics other known mechanisms – the rapid decline of the age distribution at young ages, in which 90% of all clusters are disrupted during each factor of ten in age, is similar to ‘infant mortality’ (Lada & Lada 2003, Bastian et al. 2006, Goodwin & Bastian 2006), which refers to the early disruption of clusters due to gas expulsion. This parallel was also drawn by Whitmore et al. (2007), who referred to the destruction of clusters in the Antennae as infant mortality. However, gas expulsion should be expected to occur on a time scale of  $\sim 10$  Myr, rather than the  $\sim 150$  Myr that spans the rapid, mass-independent disruption of clusters in the Antennae. It is now clear that it is not infant mortality which efficiently disrupts the clusters independently of their mass, but the tidal interaction of the young clusters with their primordial environment. We named this mechanism the ‘cruel cradle effect’ in Kruijssen et al. (2011a, Chapter 2 of this work), where we analysed hydrodynamical simulations of star formation and found that the stellar substructure can evolve to a gas-poor state before the onset of feedback, potentially implying that disruptive effect of gas expulsion could be much weaker than anticipated. Whether or not the cruel cradle effect plays an observable role compared to infant mortality (and on which time scale it acts) will depend on the global dynamics of a galactic system and on its gas content.

In order to understand the star cluster population of the Antennae galaxies, it is required to follow the formation and evolution of the individual clusters within their galactic context. We have connected the dynamics of stellar (sub)clusters in star-forming regions (Chapter 2) with the dynamical evolution of star clusters (Chapters 3–7), and with the dynamical evolution of galaxies and galaxy mergers (Chapters 8 & 9). While it is clear that these steps have

led to new insights, and have improved our understanding of the co-evolution of star clusters and galaxies, it is also evident that some questions have been left unanswered, and new questions have arisen. How do the chemical properties of the star cluster population evolve in a dynamically changing galactic environment? How does the dark matter halo of a galaxy influence its star cluster population? And given the relation between star clusters and their host galaxies, is it possible to use globular cluster systems to trace the hierarchical assembly of galaxies back to the early universe?

The field of astrophysics is not progressing in a linear way, but it is continuously developing into a plethora of directions, which cannot be covered by the mere three dimensions we have at hand. Some of them will prove to be fruitful, others will turn out to be dead ends. In this work we set out to understand the dynamics of the star clusters in a seemingly immobile sky. Setting these systems in motion revealed more than just their histories – it opened up a direction through which we can grasp the influence that a complex cosmic environment has on their characteristics. This interplay of the different physical processes gives rise to certain emergent properties, and illustrates that an evolving star cluster population is more than just the sum of its parts.

We have not only made the stranger move. He has also spoken.

**Acknowledgements** Simon Karl and Thorsten Naab are thanked for sharing their initial conditions for the Antennae galaxies. Our calculations were performed at the computing facilities of Leiden Observatory. This research is supported by the Netherlands Organisation for Scientific Research (NWO), grant 021.001.038.



# Bibliography

- Aarseth, S. J. 1999, *Publ. Astron. Soc. Pac.*, 111, 1333 (cited on page 142)
- Aarseth, S. J. & Heggie, D. C. 1998, *MNRAS*, 297, 794 (cited on page 145)
- Adams, F. C. 2000, *Astrophys. J.*, 542, 964 (cited on page 16)
- Aguilar, L., Hut, P., & Ostriker, J. P. 1988, *Astrophys. J.*, 335, 720 (cited on pages 122 and 165)
- Albrow, M. D., De Marchi, G., & Sahu, K. C. 2002, *Astrophys. J.*, 579, 660 (cited on pages 45 and 83)
- Allen, C., Moreno, E., & Pichardo, B. 2006, *Astrophys. J.*, 652, 1150 (cited on pages 91 and 117)
- Allen, C., Moreno, E., & Pichardo, B. 2008, *Astrophys. J.*, 674, 237 (cited on pages 91 and 117)
- Allen, C. & Santillan, A. 1991, *Revista Mexicana de Astronomia y Astrofisica*, 22, 255 (cited on page 91)
- Allison, R. J., Goodwin, S. P., Parker, R. J., et al. 2009a, *Astrophys. J. Lett.*, 700, L99 (cited on pages 16, 18, and 157)
- Allison, R. J., Goodwin, S. P., Parker, R. J., et al. 2009b, *MNRAS*, 395, 1449 (cited on page 18)
- Anders, P. & Fritze-v. Alvensleben, U. 2003, *Astron. Astrophys.*, 401, 1063 (cited on pages 44, 47, 57, 82, and 85)
- Anders, P., Lamers, H. J. G. L. M., & Baumgardt, H. 2009, *Astron. Astrophys.*, 502, 817 (cited on pages 76, 130, and 157)
- Anderson, J. & King, I. R. 1996, in *Astronomical Society of the Pacific Conference Series*, Vol. 92, *Formation of the Galactic Halo...Inside and Out*, ed. H. L. Morrison & A. Sarajedini, 257+ (cited on pages 45 and 109)
- Arzoumanian, Z., Chernoff, D. F., & Cordes, J. M. 2002, *Astrophys. J.*, 568, 289 (cited on page 133)
- Ashman, K. M. & Zepf, S. E. 1992, *Astrophys. J.*, 384, 50 (cited on pages 9, 164, 216, and 222)
- Baraffe, I., Chabrier, G., Allard, F., & Hauschildt, P. H. 1997, *Astron. Astrophys.*, 327, 1054 (cited on page 112)

- Barnes, J. & Hut, P. 1986, *Nature*, 324, 446 (cited on page 167)
- Barnes, J. E. 1988, *Astrophys. J.*, 331, 699 (cited on page 184)
- Bastian, N. 2008, *MNRAS*, 390, 759 (cited on pages 2, 216, 217, 220, and 228)
- Bastian, N., Covey, K. R., & Meyer, M. R. 2010, *Annu. Rev. Astron. Astrophys.*, 48, 339 (cited on pages 4 and 16)
- Bastian, N., Ercolano, B., Gieles, M., et al. 2007, *MNRAS*, 379, 1302 (cited on page 18)
- Bastian, N., Gieles, M., Lamers, H. J. G. L. M., Scheepmaker, R. A., & De Grijs, R. 2005, *Astron. Astrophys.*, 431, 905 (cited on pages 164, 170, and 225)
- Bastian, N. & Goodwin, S. P. 2006, *MNRAS*, 369, L9 (cited on pages 16, 33, and 34)
- Bastian, N., Saglia, R. P., Goudfrooij, P., et al. 2006, *Astron. Astrophys.*, 448, 881 (cited on pages 216 and 234)
- Bastian, N., Trancho, G., Konstantopoulos, I. S., & Miller, B. W. 2009, *Astrophys. J.*, 701, 607 (cited on pages 188, 222, 231, and 232)
- Bate, M. R., Bonnell, I. A., & Bromm, V. 2003, *MNRAS*, 339, 577 (cited on pages 2 and 16)
- Baumgardt, H. 2001, *MNRAS*, 325, 1323 (cited on pages 120, 131, and 136)
- Baumgardt, H., De Marchi, G., & Kroupa, P. 2008, *Astrophys. J.*, 685, 247 (cited on pages 91, 109, 110, 157, 158, 159, and 160)
- Baumgardt, H., Hut, P., Makino, J., McMillan, S., & Portegies Zwart, S. 2003a, *Astrophys. J. Lett.*, 582, L21 (cited on page 45)
- Baumgardt, H. & Kroupa, P. 2007, *MNRAS*, 380, 1589 (cited on pages 16, 34, and 128)
- Baumgardt, H. & Makino, J. 2003, *MNRAS*, 340, 227 (cited on pages 5, 44, 45, 51, 52, 58, 72, 73, 74, 75, 76, 78, 82, 83, 84, 90, 95, 96, 100, 108, 109, 111, 114, 120, 123, 130, 131, 135, 136, 137, 139, 142, 143, 144, 148, 153, 156, 157, 158, 159, 160, 164, 166, 167, 170, 171, 174, 175, 176, 177, 218, and 229)
- Baumgardt, H., Makino, J., Hut, P., McMillan, S., & Portegies Zwart, S. 2003b, *Astrophys. J. Lett.*, 589, L25 (cited on page 45)
- Baumgardt, H. & Mieske, S. 2008, *ArXiv e-prints* (cited on page 90)
- Beasley, M. A., Bridges, T., Peng, E., et al. 2008, *MNRAS*, 386, 1443 (cited on page 87)
- Bedin, L. R., Piotto, G., Anderson, J., et al. 2004, *Astrophys. J. Lett.*, 605, L125 (cited on page 92)
- Bekki, K., Forbes, D. A., Beasley, M. A., & Couch, W. J. 2002, *MNRAS*, 335, 1176 (cited on page 164)
- Bekki, K., Yahagi, H., & Forbes, D. A. 2007, *MNRAS*, 377, 215 (cited on page 82)
- Bell, E. F., Papovich, C., Wolf, C., et al. 2005, *Astrophys. J.*, 625, 23 (cited on pages 7 and 164)
- Bell, E. F., Zucker, D. B., Belokurov, V., et al. 2008, *Astrophys. J.*, 680, 295 (cited on page 125)
- Bertelli, G., Bressan, A., Chiosi, C., Fagotto, F., & Nasi, E. 1994, *A&A Suppl.*, 106, 275 (cited on pages 57, 82, 94, and 131)



- Boily, C. M., Fleck, J.-J., Lançon, A., & Renaud, F. 2009, *Astrophys. Space Sci.*, 110 (cited on page 157)
- Boily, C. M. & Kroupa, P. 2003a, *MNRAS*, 338, 665 (cited on pages 2, 16, and 34)
- Boily, C. M. & Kroupa, P. 2003b, *MNRAS*, 338, 673 (cited on pages 2, 16, and 34)
- Bonnell, I. A., Bate, M. R., & Vine, S. G. 2003, *MNRAS*, 343, 413 (cited on pages 17, 35, and 157)
- Bonnell, I. A., Bate, M. R., & Zinnecker, H. 1998, *MNRAS*, 298, 93 (cited on pages 2, 16, and 26)
- Bonnell, I. A., Clark, P., & Bate, M. R. 2008, *MNRAS*, 389, 1556 (cited on pages 2, 16, 17, 21, 34, 35, and 37)
- Bonnell, I. A., Clarke, C. J., & Bate, M. R. 2006, *MNRAS*, 368, 1296 (cited on page 4)
- Borch, A., Spurzem, R., & Hurley, J. 2007, ArXiv e-prints, 0704.3915 (cited on page 44)
- Bournaud, F., Duc, P., & Emsellem, E. 2008, *MNRAS*, 389, L8 (cited on page 164)
- Boutloukos, S. G. & Lamers, H. J. G. L. M. 2003, *MNRAS*, 338, 717 (cited on pages 6, 50, 83, 95, 165, 189, 192, and 196)
- Bressert, E., Bastian, N., Gutermuth, R., et al. 2010, *MNRAS*, 409, L54 (cited on pages 2, 3, 16, 20, 33, 34, and 35)
- Bromm, V. & Larson, R. B. 2004, *Annu. Rev. Astron. Astrophys.*, 42, 79 (cited on page 4)
- Bruzual, G. & Charlot, S. 2003, *MNRAS*, 344, 1000 (cited on pages 44, 66, 82, 85, 93, 115, and 168)
- Bullock, J. S., Kolatt, T. S., Sigad, Y., et al. 2001, *MNRAS*, 321, 559 (cited on pages 181 and 218)
- Burkert, A. & Smith, G. H. 2000, *Astrophys. J. Lett.*, 542, L95 (cited on page 120)
- Camilo, F., Lorimer, D. R., Freire, P., Lyne, A. G., & Manchester, R. N. 2000, *Astrophys. J.*, 535, 975 (cited on page 72)
- Carretta, E. & Gratton, R. G. 1997, *A&A Suppl.*, 121, 95 (cited on page 91)
- Cartwright, A. & Whitworth, A. P. 2004, *MNRAS*, 348, 589 (cited on page 18)
- Casares, J. 2007, in *IAU Symposium, Vol. 238, Black Holes from Stars to Galaxies – Across the Range of Masses*, ed. V. Karas & G. Matt, 3–12 (cited on pages 49, 71, and 94)
- Casertano, S. & Hut, P. 1985, *Astrophys. J.*, 298, 80 (cited on page 18)
- Chabrier, G. 2003, *Publ. Astron. Soc. Pac.*, 115, 763 (cited on page 93)
- Chandar, R., Fall, S. M., & Whitmore, B. C. 2006, *Astrophys. J. Lett.*, 650, L111 (cited on pages 191 and 212)
- Chandar, R., Fall, S. M., & Whitmore, B. C. 2010, *Astrophys. J.*, 711, 1263 (cited on page 196)
- Chernoff, D. F., Kochanek, C. S., & Shapiro, S. L. 1986, *Astrophys. J.*, 309, 183 (cited on pages 5, 99, 123, and 164)
- Chernoff, D. F. & Weinberg, M. D. 1990, *Astrophys. J.*, 351, 121 (cited on pages 108, 130, and 165)

- Chilingarian, I. V., Cayatte, V., & Bergond, G. 2008, *MNRAS*, 390, 906 (cited on page 90)
- Cole, S., Lacey, C. G., Baugh, C. M., & Frenk, C. S. 2000, *MNRAS*, 319, 168 (cited on page 164)
- Conselice, C. J., Bershad, M. A., Dickinson, M., & Papovich, C. 2003, *Astron. J.*, 126, 1183 (cited on pages 7 and 164)
- Dabringhausen, J., Hilker, M., & Kroupa, P. 2008, *MNRAS*, 386, 864 (cited on pages 82 and 90)
- Dale, J. E. & Bonnell, I. A. 2008, *MNRAS*, 391, 2 (cited on page 36)
- Davis, D. S., Richer, H. B., King, I. R., et al. 2008, *MNRAS*, 383, L20 (cited on page 133)
- de la Fuente Marcos, R. 2000, in *Astronomical Society of the Pacific Conference Series*, Vol. 198, *Stellar Clusters and Associations: Convection, Rotation, and Dynamos*, ed. R. Pallavicini, G. Micela, & S. Sciortino, 151–+ (cited on page 44)
- De Marchi, G., Paresce, F., & Pulone, L. 2000, *Astrophys. J.*, 530, 342 (cited on page 157)
- De Marchi, G., Paresce, F., & Pulone, L. 2007, *Astrophys. J. Lett.*, 656, L65 (cited on pages 69, 91, 108, 109, 110, 111, 112, 113, 114, 117, 125, 130, 148, 158, and 159)
- De Marchi, G. & Pulone, L. 2007, *Astron. Astrophys.*, 467, 107 (cited on pages 111, 130, and 148)
- de Vaucouleurs, G. 1948, *Annales d'Astrophysique*, 11, 247 (cited on page 219)
- D'Ercole, A., Vesperini, E., D'Antona, F., McMillan, S. L. W., & Recchi, S. 2008, *MNRAS*, 1228 (cited on page 4)
- Di Matteo, T., Springel, V., & Hernquist, L. 2005, *Nature*, 433, 604 (cited on page 210)
- Dinescu, D. I., Girard, T. M., & van Altena, W. F. 1999, *Astron. J.*, 117, 1792 (cited on pages 5, 91, 92, 99, 100, 101, 115, and 117)
- Drukier, G. A. 1996, *MNRAS*, 280, 498 (cited on page 133)
- Dubath, P. & Grillmair, C. J. 1997, *Astron. Astrophys.*, 321, 379 (cited on page 87)
- Eddington, A. S. 1915, *MNRAS*, 75, 366 (cited on page 122)
- Elmegreen, B. G. 1983, *MNRAS*, 203, 1011 (cited on pages 2 and 216)
- Elmegreen, B. G. 2000, *Astrophys. J.*, 530, 277 (cited on page 157)
- Elmegreen, B. G. 2010, *Astrophys. J. Lett.*, 712, L184 (cited on page 216)
- Elmegreen, B. G. & Efremov, Y. N. 1997, *Astrophys. J.*, 480, 235 (cited on pages 6, 7, 120, 164, and 165)
- Elmegreen, B. G. & Elmegreen, D. M. 2005, *Astrophys. J.*, 627, 632 (cited on page 8)
- Elmegreen, B. G. & Hunter, D. A. 2010, *Astrophys. J.*, 712, 604 (cited on pages 34, 36, 186, 193, 227, 232, and 234)
- Evstigneeva, E. A., Gregg, M. D., Drinkwater, M. J., & Hilker, M. 2007, *Astron. J.*, 133, 1722 (cited on pages 45 and 90)
- Fabbiano, G., Baldi, A., King, A. R., et al. 2004, *Astrophys. J. Lett.*, 605, L21 (cited on page 226)

- Fagiolini, M., Raimondo, G., & Degl'Innocenti, S. 2007, *Astron. Astrophys.*, 462, 107 (cited on page 44)
- Fall, S. M., Chandar, R., & Whitmore, B. C. 2005, *Astrophys. J. Lett.*, 631, L133 (cited on pages 188 and 226)
- Fall, S. M. & Zhang, Q. 2001, *Astrophys. J.*, 561, 751 (cited on pages 7, 119, 120, 121, 122, 126, 127, 164, 165, 216, and 220)
- Forbes, D. A., Lasky, P., Graham, A. W., & Spitler, L. 2008, *MNRAS*, 389, 1924 (cited on page 90)
- Fregeau, J. M., Richer, H. B., Rasio, F. A., & Hurley, J. R. 2009, *Astrophys. J. Lett.*, 695, L20 (cited on pages 109, 128, and 133)
- Froebrich, D., Schmeja, S., Samuel, D., & Lucas, P. W. 2010, *MNRAS*, 408, 1546 (cited on pages 189 and 208)
- Fryer, C. L. & Kalogera, V. 2001, *Astrophys. J.*, 554, 548 (cited on page 132)
- Fukushige, T. & Heggie, D. C. 1995, *MNRAS*, 276, 206 (cited on page 171)
- Fukushige, T. & Heggie, D. C. 2000, *MNRAS*, 318, 753 (cited on pages 5, 120, 135, 136, and 164)
- Gaburov, E., Lombardi, Jr., J. C., & Portegies Zwart, S. 2010, *MNRAS*, 402, 105 (cited on page 2)
- Gebhardt, K., Rich, R. M., & Ho, L. C. 2005, *Astrophys. J.*, 634, 1093 (cited on page 45)
- Geyer, M. P. & Burkert, A. 2001, *MNRAS*, 323, 988 (cited on page 16)
- Gieles, M. 2009, *MNRAS*, 277 (cited on page 120)
- Gieles, M., Athanassoula, E., & Portegies Zwart, S. F. 2007a, *MNRAS*, 376, 809 (cited on pages 5, 44, 171, 172, 173, 217, 228, and 229)
- Gieles, M. & Bastian, N. 2008, *Astron. Astrophys.*, 482, 165 (cited on pages 120 and 188)
- Gieles, M., Bastian, N., Lamers, H. J. G. L. M., & Mout, J. N. 2005, *Astron. Astrophys.*, 441, 949 (cited on pages 83, 95, 165, 170, 188, 189, 191, and 208)
- Gieles, M. & Baumgardt, H. 2008, *MNRAS*, 389, L28 (cited on pages 75, 120, 131, 139, and 170)
- Gieles, M., Baumgardt, H., Bastian, N., & Lamers, H. J. G. L. M. 2004, in *Astronomical Society of the Pacific Conference Series*, Vol. 322, *The Formation and Evolution of Massive Young Star Clusters*, ed. H. J. G. L. M. Lamers, L. J. Smith, & A. Nota, 481–+ (cited on page 51)
- Gieles, M., Heggie, D. C., & Zhao, H. 2011, *MNRAS* accepted, *ArXiv:1101.1821* (cited on pages 174, 176, and 210)
- Gieles, M., Lamers, H. J. G. L. M., & Portegies Zwart, S. F. 2007b, *Astrophys. J.*, 668, 268 (cited on page 212)
- Gieles, M., Larsen, S. S., Scheepmaker, R. A., et al. 2006a, *Astron. Astrophys.*, 446, L9 (cited on page 120)
- Gieles, M. & Portegies Zwart, S. F. 2011, *MNRAS*, 410, L6 (cited on pages 3, 16, and 33)

- Gieles, M., Portegies Zwart, S. F., Baumgardt, H., et al. 2006b, *MNRAS*, 371, 793 (cited on pages 5, 44, 115, 164, 165, 172, 173, 186, 216, 217, and 228)
- Gilbert, A. M. & Graham, J. R. 2007, *Astrophys. J.*, 668, 168 (cited on page 226)
- Girardi, L., Bressan, A., Bertelli, G., & Chiosi, C. 2000, *A&A Suppl.*, 141, 371 (cited on pages 57, 65, 82, 94, and 131)
- Gnedin, O. Y., Hernquist, L., & Ostriker, J. P. 1999, *Astrophys. J.*, 514, 109 (cited on page 172)
- Gnedin, O. Y. & Ostriker, J. P. 1997, *Astrophys. J.*, 474, 223 (cited on pages 5, 91, 123, 124, 165, 171, and 173)
- Gnedin, O. Y. & Ostriker, J. P. 1999, *Astrophys. J.*, 513, 626 (cited on page 173)
- Goddard, Q. E., Bastian, N., & Kennicutt, R. C. 2010, *MNRAS*, 405, 857 (cited on pages 33 and 211)
- Goodwin, S. P. 2009, *Astrophys. Space Sci.*, 324, 259 (cited on page 22)
- Goodwin, S. P. & Bastian, N. 2006, *MNRAS*, 373, 752 (cited on pages 2, 16, 22, 34, 169, 226, and 234)
- Goudfrooij, P., Schweizer, F., Gilmore, D., & Whitmore, B. C. 2007, *Astron. J.*, 133, 2737 (cited on page 220)
- Gratton, R. G., Sneden, C., Carretta, E., & Bragaglia, A. 2000, *Astron. Astrophys.*, 354, 169 (cited on page 125)
- Gürkan, M. A., Freitag, M., & Rasio, F. A. 2004, *Astrophys. J.*, 604, 632 (cited on page 45)
- Haşegan, M., Jordán, A., Côté, P., et al. 2005, *Astrophys. J.*, 627, 203 (cited on pages 45 and 90)
- Harris, W. E. 1996, *Astron. J.*, 112, 1487 (cited on pages 7, 67, 87, 92, 113, 121, 122, 123, 133, 219, and 220)
- Harris, W. E. 2009, *Astrophys. J.*, 703, 939 (cited on page 219)
- Harris, W. E., Kavelaars, J. J., Hanes, D. A., Pritchet, C. J., & Baum, W. A. 2009, *Astron. J.*, 137, 3314 (cited on page 123)
- Harris, W. E. & Pudritz, R. E. 1994, *Astrophys. J.*, 429, 177 (cited on pages 7, 120, and 164)
- Harris, W. E., Whitmore, B. C., Karakla, D., et al. 2006, *Astrophys. J.*, 636, 90 (cited on pages 82 and 159)
- Heggie, D. & Hut, P. 2003, *The Gravitational Million-Body Problem: A Multidisciplinary Approach to Star Cluster Dynamics* (Cambridge University Press, 2003, 372 pp.) (cited on pages 5, 30, 78, 133, 135, 136, and 138)
- Heggie, D. C. & Mathieu, R. D. 1986, in *Lecture Notes in Physics*, Berlin Springer Verlag, Vol. 267, *The Use of Supercomputers in Stellar Dynamics*, ed. P. Hut & S. L. W. McMillan, 233–+ (cited on page 173)
- Hénon, M. 1960, *Annales d’Astrophysique*, 23, 668 (cited on page 134)
- Hénon, M. 1969, *Astron. Astrophys.*, 2, 151 (cited on pages 5, 97, 130, 133, 134, 135, 136, 138, and 175)

- Hernquist, L. 1989, *Nature*, 340, 687 (cited on pages 9, 165, 215, and 226)
- Hernquist, L. 1990, *Astrophys. J.*, 356, 359 (cited on pages 181 and 229)
- Hibbard, J. E., Bianchi, L., Thilker, D. A., et al. 2005, *Astrophys. J. Lett.*, 619, L87 (cited on page 226)
- Hibbard, J. E., van der Hulst, J. M., Barnes, J. E., & Rich, R. M. 2001, *Astron. J.*, 122, 2969 (cited on page 226)
- Hilker, M., Baumgardt, H., Infante, L., et al. 2007, *Astron. Astrophys.*, 463, 119 (cited on pages 70, 85, and 90)
- Hillenbrand, L. A. & Hartmann, L. W. 1998, *Astrophys. J.*, 492, 540 (cited on pages 20, 45, and 83)
- Hills, J. G. 1980, *Astrophys. J.*, 235, 986 (cited on pages 2 and 29)
- Hodge, P. W. 1961, *Astron. J.*, 66, 83 (cited on page 223)
- Holtzman, J. A., Faber, S. M., Shaya, E. J., et al. 1992, *Astron. J.*, 103, 691 (cited on pages 9, 165, 215, 216, and 225)
- Hopkins, P. F., Bundy, K., Croton, D., et al. 2010, *Astrophys. J.*, 715, 202 (cited on page 164)
- Hopkins, P. F., Cox, T. J., Younger, J. D., & Hernquist, L. 2009, *Astrophys. J.*, 691, 1168 (cited on page 184)
- Hopkins, P. F., Hernquist, L., Cox, T. J., et al. 2006, *Astrophys. J. Suppl.*, 163, 1 (cited on page 165)
- Hunter, D. A., Elmegreen, B. G., Dupuy, T. J., & Mortonson, M. 2003, *Astron. J.*, 126, 1836 (cited on pages 6, 165, and 191)
- Hurley, J. R. 2007, *MNRAS*, 379, 93 (cited on page 45)
- Hurley, J. R., Pols, O. R., Aarseth, S. J., & Tout, C. A. 2005, *MNRAS*, 363, 293 (cited on page 44)
- Hurley, J. R., Pols, O. R., & Tout, C. A. 2000, *MNRAS*, 315, 543 (cited on pages 65, 71, and 73)
- Hurley, J. R., Tout, C. A., Aarseth, S. J., & Pols, O. R. 2004, *MNRAS*, 355, 1207 (cited on pages 65 and 77)
- Ideta, M. & Makino, J. 2004, *Astrophys. J. Lett.*, 616, L107 (cited on page 68)
- Jeans, J. H. 1902, *Royal Society of London Philosophical Transactions Series A*, 199, 1 (cited on page 2)
- Johnston, K. V., Spergel, D. N., & Hernquist, L. 1995, *Astrophys. J.*, 451, 598 (cited on pages 91, 100, and 123)
- Jordán, A., McLaughlin, D. E., Côté, P., et al. 2007, *Astrophys. J. Suppl.*, 171, 101 (cited on pages 119 and 123)
- Kalirai, J. S., Hansen, B. M. S., Kelson, D. D., et al. 2008, *Astrophys. J.*, 676, 594 (cited on pages 49, 71, 94, and 132)
- Kalirai, J. S., Richer, H. B., Reitzel, D., et al. 2005, *Astrophys. J. Lett.*, 618, L123 (cited on page 71)

- Karl, S. J., Naab, T., Johansson, P. H., et al. 2010, *Astrophys. J. Lett.*, 715, L88 (cited on pages 219, 226, 229, and 230)
- Kauffmann, G., Heckman, T. M., White, S. D. M., et al. 2003, *MNRAS*, 341, 54 (cited on page 164)
- Kauffmann, G., White, S. D. M., & Guiderdoni, B. 1993, *MNRAS*, 264, 201 (cited on pages 7 and 164)
- Kennicutt, Jr., R. C. 1989, *Astrophys. J.*, 344, 685 (cited on page 190)
- Kennicutt, Jr., R. C. 1998a, *Annu. Rev. Astron. Astrophys.*, 36, 189 (cited on page 164)
- Kennicutt, Jr., R. C. 1998b, *Astrophys. J.*, 498, 541 (cited on pages 8, 33, 194, and 209)
- Khochfar, S. & Burkert, A. 2006, *Astron. Astrophys.*, 445, 403 (cited on page 181)
- King, I. R. 1966, *Astron. J.*, 71, 64 (cited on pages 44, 78, 137, and 175)
- Kirk, H. & Myers, P. C. 2011, *Astrophys. J.*, 727, 64 (cited on page 17)
- Klessen, R. S. & Burkert, A. 2000, *Astrophys. J. Suppl.*, 128, 287 (cited on page 16)
- Koch, A., Grebel, E. K., Odenkirchen, M., Martínez-Delgado, D., & Caldwell, J. A. R. 2004, *Astron. J.*, 128, 2274 (cited on page 45)
- Kopp, J. 2008, *International Journal of Modern Physics C*, 19, 523 (cited on page 171)
- Kouwenhoven, M. B. N., Brown, A. G. A., Goodwin, S. P., Portegies Zwart, S. F., & Kaper, L. 2009, *Astron. Astrophys.*, 493, 979 (cited on page 156)
- Kroupa, P. 2001, *MNRAS*, 322, 231 (cited on pages 4, 45, 82, 90, 94, 109, 116, 122, 130, 132, 169, and 175)
- Kruijssen, J. M. D. 2008, *Astron. Astrophys.*, 486, L21 (cited on pages 67, 69, 76, 77, 90, 91, 94, 95, 98, 101, 106, 114, 120, 124, 130, 148, and 175)
- Kruijssen, J. M. D. 2009, *Astron. Astrophys.*, 507, 1409 (cited on pages 166, 169, 170, 175, 217, 218, 228, and 229)
- Kruijssen, J. M. D. & Bastian, N. 2011, in prep. (cited on page 34)
- Kruijssen, J. M. D. & Lamers, H. J. G. L. M. 2008, *Astron. Astrophys.*, 490, 151 (cited on pages 82, 90, 114, 121, 130, 131, 132, 143, 148, 166, 169, 170, 211, 217, and 228)
- Kruijssen, J. M. D., Maschberger, T., Moeckel, N., et al. 2011a, *MNRAS* submitted (cited on pages 226 and 234)
- Kruijssen, J. M. D. & Mieske, S. 2009, *Astron. Astrophys.*, 500, 785 (cited on pages 76, 124, 125, 128, 130, 139, 154, 158, 170, and 171)
- Kruijssen, J. M. D., Pelupessy, F. I., Lamers, H. J. G. L. M., et al. 2011b, in prep. (cited on pages 166, 184, 196, 201, 212, 229, and 232)
- Kruijssen, J. M. D., Pelupessy, F. I., Lamers, H. J. G. L. M., Portegies Zwart, S. F., & Icke, V. 2011c, *MNRAS* accepted, *ArXiv:1102.1013* (cited on pages 33, 34, 36, 216, 217, 218, 219, 220, 222, 227, 228, 229, 230, 232, 233, and 234)
- Kruijssen, J. M. D. & Portegies Zwart, S. F. 2009, *Astrophys. J. Lett.*, 698, L158 (cited on pages 109, 130, 158, 164, 168, 216, and 220)

- Kundic, T. & Ostriker, J. P. 1995, *Astrophys. J.*, 438, 702 (cited on pages 165, 171, 172, and 173)
- Küpper, A. H. W., Kroupa, P., & Baumgardt, H. 2008, *MNRAS*, 389, 889 (cited on pages 156, 175, and 176)
- Kurucz, R. L. 1992, in *IAU Symp. 149: The Stellar Populations of Galaxies*, ed. B. Barbuy & A. Renzini, 225–+ (cited on page 57)
- Lada, C. J. & Lada, E. A. 2003, *Annu. Rev. Astron. Astrophys.*, 41, 57 (cited on pages 2, 6, 16, 33, 169, 217, 226, 228, and 234)
- Lamers, H. J. G. L. M., Anders, P., & De Grijs, R. 2006, *Astron. Astrophys.*, 452, 131 (cited on pages 5, 44, 52, 58, 59, 61, 82, 95, 130, and 132)
- Lamers, H. J. G. L. M., Baumgardt, H., & Gieles, M. 2010, *MNRAS*, 409, 305 (cited on pages 4, 95, 122, 170, and 171)
- Lamers, H. J. G. L. M. & Gieles, M. 2006, *Astron. Astrophys.*, 455, L17 (cited on pages 100, 170, 190, 208, 218, 226, 229, and 233)
- Lamers, H. J. G. L. M., Gieles, M., Bastian, N., et al. 2005a, *Astron. Astrophys.*, 441, 117 (cited on pages 4, 6, 47, 50, 67, 76, 83, 94, 100, 120, 121, 122, 127, 131, 135, 143, 165, 169, 170, 175, 192, 216, 217, 226, 228, 229, 231, 232, 233, and 234)
- Lamers, H. J. G. L. M., Gieles, M., & Portegies Zwart, S. F. 2005b, *Astron. Astrophys.*, 429, 173 (cited on pages 33, 58, 83, 86, 95, 100, 164, 170, and 189)
- Larsen, S. S. 2004, *Astron. Astrophys.*, 416, 537 (cited on pages 33, 59, 124, 133, 145, and 174)
- Larsen, S. S. 2009, *Astron. Astrophys.*, 494, 539 (cited on pages 6, 120, 165, 188, 217, and 228)
- Larsen, S. S., Brodie, J. P., Huchra, J. P., Forbes, D. A., & Grillmair, C. J. 2001, *Astron. J.*, 121, 2974 (cited on pages 159, 164, and 216)
- Larsen, S. S. & Richtler, T. 2000, *Astron. Astrophys.*, 354, 836 (cited on page 33)
- Larson, R. B. 2005, *MNRAS*, 359, 211 (cited on page 17)
- Leitherer, C., Schaerer, D., Goldader, J. D., et al. 1999, *Astrophys. J. Suppl.*, 123, 3 (cited on page 44)
- Leon, S., Meylan, G., & Combes, F. 2000, *Astron. Astrophys.*, 359, 907 (cited on page 44)
- Li, Y., Mac Low, M., & Klessen, R. S. 2004, *Astrophys. J. Lett.*, 614, L29 (cited on page 164)
- Lyne, A. G. & Lorimer, D. R. 1994, *Nature*, 369, 127 (cited on pages 72, 133, and 169)
- Mackey, A. D. & Broby Nielsen, P. 2007, *MNRAS*, 379, 151 (cited on page 4)
- Mackey, A. D., Broby Nielsen, P., Ferguson, A. M. N., & Richardson, J. C. 2008, *Astrophys. J. Lett.*, 681, L17 (cited on page 4)
- Mackey, A. D. & Gilmore, G. F. 2004, *MNRAS*, 355, 504 (cited on page 87)
- Mandushev, G., Staneva, A., & Spasova, N. 1991, *Astron. Astrophys.*, 252, 94 (cited on pages 69, 82, 90, 98, 104, 105, and 120)

- Maraston, C. 2005, *MNRAS*, 362, 799 (cited on pages 44 and 65)
- Marigo, P., Girardi, L., Bressan, A., et al. 2008, *Astron. Astrophys.*, 482, 883 (cited on pages 132, 169, 217, and 228)
- Marino, A. F., Villanova, S., Piotto, G., et al. 2008, *Astron. Astrophys.*, 490, 625 (cited on page 116)
- Maschberger, T. & Clarke, C. 2011, *MNRAS*, submitted (cited on pages 17 and 18)
- Maschberger, T., Clarke, C. J., Bonnell, I. A., & Kroupa, P. 2010, *MNRAS*, 404, 1061 (cited on pages 16, 17, 18, 21, 22, and 35)
- Maschberger, T. & Kroupa, P. 2011, *MNRAS*, 411, 1495 (cited on page 212)
- McConnachie, A. W., Irwin, M. J., Ibata, R. A., et al. 2009, *Nature*, 461, 66 (cited on pages 7 and 164)
- McKee, C. F. & Ostriker, E. C. 2007, *Annu. Rev. Astron. Astrophys.*, 45, 565 (cited on pages 2, 16, 36, and 37)
- McLaughlin, D. E. 2000, *Astrophys. J.*, 539, 618 (cited on pages 45, 67, and 82)
- McLaughlin, D. E. & Fall, S. M. 2008, *Astrophys. J.*, 679, 1272 (cited on page 119)
- McLaughlin, D. E. & Pudritz, R. E. 1996, *Astrophys. J.*, 457, 578 (cited on page 120)
- McLaughlin, D. E. & van der Marel, R. P. 2005, *Astrophys. J. Suppl.*, 161, 304 (cited on pages 72, 81, 90, 91, 92, 100, 107, 108, 114, 115, 116, 125, 126, and 171)
- McMillan, S. L. W., Vesperini, E., & Portegies Zwart, S. F. 2007, *Astrophys. J. Lett.*, 655, L45 (cited on pages 16 and 157)
- Meng, X., Chen, X., & Han, Z. 2008, *Astron. Astrophys.*, 487, 625 (cited on page 71)
- Meylan, G. & Heggie, D. C. 1997, *A&AR*, 8, 1 (cited on page 120)
- Mieske, S. & Baumgardt, H. 2007, *Astron. Astrophys.*, 475, 851 (cited on page 46)
- Mieske, S., Hilker, M., Jordán, A., et al. 2008, *Astron. Astrophys.*, 487, 921 (cited on pages 70, 82, 85, 88, and 90)
- Mieske, S. & Kroupa, P. 2008, *Astrophys. J.*, 677, 276 (cited on pages 45, 70, and 81)
- Mihos, J. C., Bothun, G. D., & Richstone, D. O. 1993, *Astrophys. J.*, 418, 82 (cited on page 226)
- Mihos, J. C. & Hernquist, L. 1996, *Astrophys. J.*, 464, 641 (cited on pages 9, 165, 215, 219, and 226)
- Mo, H. J., Mao, S., & White, S. D. M. 1998, *MNRAS*, 295, 319 (cited on pages 181 and 229)
- Moeckel, N. & Bate, M. R. 2010, *MNRAS*, 404, 721 (cited on pages 16, 26, and 34)
- Moeckel, N. & Bonnell, I. A. 2009, *MNRAS*, 400, 657 (cited on pages 16 and 18)
- Moeckel, N. & Clarke, C. J. 2010, *MNRAS*, 1774 (cited on pages 16 and 26)
- Monaghan, J. J. 1992, *Annu. Rev. Astron. Astrophys.*, 30, 543 (cited on page 167)
- Moody, K. & Sigurdsson, S. 2009, *Astrophys. J.*, 690, 1370 (cited on page 133)
- Mora, M. D., Larsen, S. S., & Kissler-Patig, M. 2007, *Astron. Astrophys.*, 464, 495 (cited on page 82)



- Navarro, J. F., Frenk, C. S., & White, S. D. M. 1996, *Astrophys. J.*, 462, 563 (cited on page 181)
- Navarro, J. F., Frenk, C. S., & White, S. D. M. 1997, *Astrophys. J.*, 490, 493 (cited on page 181)
- Nomoto, K., Shigeyama, T., & Hashimoto, M. 1988, in *Supernovae, Remnants, Active Galaxies, Cosmology*, ed. G. Boerner, 34–56 (cited on pages 49, 71, 94, and 132)
- Noyola, E., Gebhardt, K., & Bergmann, M. 2006, in *Astronomical Society of the Pacific Conference Series*, Vol. 352, *New Horizons in Astronomy: Frank N. Bash Symposium*, ed. S. J. Kannappan, S. Redfield, J. E. Kessler-Silacci, M. Landriau, & N. Drory, 269–+ (cited on page 45)
- Offner, S. S. R., Hansen, C. E., & Krumholz, M. R. 2009, *Astrophys. J. Lett.*, 704, L124 (cited on pages 16 and 33)
- Ostriker, J. P., Spitzer, L. J., & Chevalier, R. A. 1972, *Astrophys. J. Lett.*, 176, L51+ (cited on pages 5, 164, and 171)
- Paczynski, B. 1990, *Astrophys. J.*, 348, 485 (cited on pages 91, 99, 100, and 101)
- Parker, R. J., Bouvier, J., Goodwin, S. P., et al. 2011, *MNRAS*, 412, 2489 (cited on page 18)
- Parker, R. J. & Goodwin, S. P. 2007, *MNRAS*, 380, 1271 (cited on page 16)
- Parmentier, G. & Gilmore, G. 2007, *MNRAS*, 377, 352 (cited on page 7)
- Parmentier, G., Goodwin, S. P., Kroupa, P., & Baumgardt, H. 2008, *Astrophys. J.*, 678, 347 (cited on pages 16 and 34)
- Pasquali, A., De Marchi, G., Pulone, L., & Brigas, M. S. 2004, *Astron. Astrophys.*, 428, 469 (cited on page 45)
- Pelupessy, F. I. 2005, PhD thesis, Leiden Observatory, Leiden University, P.O. Box 9513, 2300 RA Leiden, The Netherlands (cited on pages 166, 168, 178, 216, 217, and 228)
- Pelupessy, F. I., van der Werf, P. P., & Icke, V. 2004, *Astron. Astrophys.*, 422, 55 (cited on pages 166, 168, 178, 190, 217, and 228)
- Pelupessy, I. 2007, *New Ast. Rev.*, 51, 179 (cited on page 210)
- Pfahl, E., Rappaport, S., Podsiadlowski, P., & Spruit, H. 2002, *Astrophys. J.*, 574, 364 (cited on pages 72 and 133)
- Pflamm-Altenburg, J., Weidner, C., & Kroupa, P. 2007, *Astrophys. J.*, 671, 1550 (cited on page 16)
- Pichardo, B., Martos, M., & Moreno, E. 2004, *Astrophys. J.*, 609, 144 (cited on page 91)
- Piotto, G., Bedin, L. R., Anderson, J., et al. 2007, *Astrophys. J. Lett.*, 661, L53 (cited on page 4)
- Plummer, H. C. 1911, *MNRAS*, 71, 460 (cited on pages 30, 133, 134, 136, and 137)
- Portegies Zwart, S. F., Kouwenhoven, M. L. A., & Reynolds, A. P. 1997, *Astron. Astrophys.*, 328, L33 (cited on page 72)
- Portegies Zwart, S. F., Makino, J., McMillan, S. L. W., & Hut, P. 1999, *Astron. Astrophys.*, 348, 117 (cited on page 2)

- Portegies Zwart, S. F. & McMillan, S. L. W. 2002, *Astrophys. J.*, 576, 899 (cited on page 45)
- Portegies Zwart, S. F., McMillan, S. L. W., & Gieles, M. 2010, *Annu. Rev. Astron. Astrophys.*, 48, 431 (cited on pages 2, 5, 6, 7, 16, 166, 171, 216, and 228)
- Portegies Zwart, S. F., McMillan, S. L. W., Hut, P., & Makino, J. 2001, *MNRAS*, 321, 199 (cited on pages 44, 45, 130, and 164)
- Praagman, A., Hurley, J., & Power, C. 2010, *New Ast.*, 15, 46 (cited on page 166)
- Prieto, J. L. & Gnedin, O. Y. 2008, *Astrophys. J.*, 689, 919 (cited on pages 127, 165, 166, 167, 171, 172, 175, 217, 222, and 229)
- Pryor, C. & Meylan, G. 1993, in *Astronomical Society of the Pacific Conference Series*, Vol. 50, *Structure and Dynamics of Globular Clusters*, ed. S. G. Djorgovski & G. Meylan, 357–+ (cited on page 108)
- Reddy, N. A. & Steidel, C. C. 2009, *Astrophys. J.*, 692, 778 (cited on pages 166 and 216)
- Rejkuba, M., Dubath, P., Minniti, D., & Meylan, G. 2007, *Astron. Astrophys.*, 469, 147 (cited on pages 45, 69, 70, 77, 81, 82, 85, 88, 90, 105, 120, and 125)
- Renaud, F., Boily, C. M., Fleck, J., Naab, T., & Theis, C. 2008, *MNRAS*, 391, L98 (cited on pages 164 and 171)
- Richer, H. B., Fahlman, G. G., Brewer, J., et al. 2004, *Astron. J.*, 127, 2771 (cited on pages 45 and 156)
- Richer, H. B., Fahlman, G. G., Buonanno, R., et al. 1991, *Astrophys. J.*, 381, 147 (cited on pages 96, 111, 130, and 148)
- Salpeter, E. E. 1955, *Astrophys. J.*, 121, 161 (cited on page 130)
- Sanders, D. B. & Mirabel, I. F. 1996, *Annu. Rev. Astron. Astrophys.*, 34, 749 (cited on pages 7 and 164)
- Schaye, J. 2004, *Astrophys. J.*, 609, 667 (cited on page 190)
- Schechter, P. 1976, *Astrophys. J.*, 203, 297 (cited on pages 119, 123, 168, 184, 217, and 228)
- Schmeja, S., Kumar, M. S. N., & Ferreira, B. 2008, *MNRAS*, 389, 1209 (cited on page 18)
- Schmidt, M. 1959, *Astrophys. J.*, 129, 243 (cited on pages 8, 33, 194, and 209)
- Schulz, J., Fritze-v. Alvensleben, U., Möller, C. S., & Fricke, K. J. 2002, *Astron. Astrophys.*, 392, 1 (cited on page 47)
- Schweizer, F. 1982, *Astrophys. J.*, 252, 455 (cited on page 216)
- Schweizer, F. 1987, in *Nearly Normal Galaxies. From the Planck Time to the Present*, New York, Springer-Verlag, ed. S. M. Faber, 18–25 (cited on pages 164 and 216)
- Schweizer, F., Burns, C. R., Madore, B. F., et al. 2008, *Astron. J.*, 136, 1482 (cited on page 226)
- Schweizer, F., Miller, B. W., Whitmore, B. C., & Fall, S. M. 1996, *Astron. J.*, 112, 1839 (cited on pages 9, 165, 215, 219, and 225)
- Schweizer, F. & Seitzer, P. 1998, *Astron. J.*, 116, 2206 (cited on page 164)
- Searle, L. 1971, *Astrophys. J.*, 168, 327 (cited on page 86)

- Shapiro, K. L., Genzel, R., & Förster Schreiber, N. M. 2010, *MNRAS*, 403, L36 (cited on pages 8 and 164)
- Shapley, H. 1939, *Proceedings of the National Academy of Science*, 25, 565 (cited on page 223)
- Sijacki, D., Springel, V., & Haehnelt, M. 2010, *ArXiv:1008.3313* (cited on page 210)
- Smith, L. J., Bastian, N., Konstantopoulos, I. S., et al. 2007, *Astrophys. J. Lett.*, 667, L145 (cited on pages 6, 69, 70, 77, 165, and 191)
- Somerville, R. S. & Primack, J. R. 1999, *MNRAS*, 310, 1087 (cited on pages 7 and 164)
- Spergel, D. N., Bean, R., Doré, O., et al. 2007, *Astrophys. J. Suppl.*, 170, 377 (cited on page 167)
- Spitzer, L. 1987, *Dynamical evolution of globular clusters* (Princeton, NJ, Princeton University Press, 1987, 191 p.) (cited on pages 5, 78, 135, 164, 171, 172, 216, 217, and 228)
- Spitzer, Jr., L. 1958, *Astrophys. J.*, 127, 17 (cited on pages 5, 164, 171, and 216)
- Springel, V., Di Matteo, T., & Hernquist, L. 2005, *MNRAS*, 361, 776 (cited on page 181)
- Springel, V. & Hernquist, L. 2002, *MNRAS*, 333, 649 (cited on page 167)
- Springel, V. & Hernquist, L. 2005, *Astrophys. J. Lett.*, 622, L9 (cited on pages 218 and 229)
- Strader, J., Smith, G. H., Larsen, S., Brodie, J. P., & Huchra, J. P. 2009, *Astron. J.*, 138, 547 (cited on page 159)
- Takahashi, K. & Portegies Zwart, S. F. 2000, *Astrophys. J.*, 535, 759 (cited on pages 108, 130, and 175)
- Tutukov, A. V. 1978, *Astron. Astrophys.*, 70, 57 (cited on page 16)
- van de Ven, G., van den Bosch, R. C. E., Verolme, E. K., & de Zeeuw, P. T. 2006, *Astron. Astrophys.*, 445, 513 (cited on pages 45 and 68)
- van den Bergh, S. & McClure, R. D. 1980, *Astron. Astrophys.*, 88, 360 (cited on pages 188 and 208)
- van den Bosch, R., de Zeeuw, T., Gebhardt, K., Noyola, E., & van de Ven, G. 2006, *Astrophys. J.*, 641, 852 (cited on page 45)
- van Dokkum, P. G. 2005, *Astron. J.*, 130, 2647 (cited on page 164)
- VanDalsen, M. L. & Harris, W. E. 2004, *Astron. J.*, 127, 368 (cited on page 67)
- Vandenberg, D. A., Bolte, M., & Stetson, P. B. 1990, *Astron. J.*, 100, 445 (cited on pages 84 and 97)
- Verschueren, W. 1990, *Astron. Astrophys.*, 234, 156 (cited on page 22)
- Vesperini, E. 1997, *MNRAS*, 287, 915 (cited on page 175)
- Vesperini, E. 1998, *MNRAS*, 299, 1019 (cited on pages 7 and 164)
- Vesperini, E. 2001, *MNRAS*, 322, 247 (cited on pages 6, 119, 164, 165, 216, and 220)
- Vesperini, E. & Heggie, D. C. 1997, *MNRAS*, 289, 898 (cited on pages 90, 130, 139, and 166)
- Vesperini, E., McMillan, S. L. W., & Portegies Zwart, S. 2009, *Astrophys. J.*, 698, 615 (cited on pages 128, 148, 157, 158, and 159)

- Vesperini, E. & Zepf, S. E. 2003, *Astrophys. J. Lett.*, 587, L97 (cited on pages 7 and 128)
- Vesperini, E., Zepf, S. E., Kundu, A., & Ashman, K. M. 2003, *Astrophys. J.*, 593, 760 (cited on pages 119, 127, and 222)
- Vitvitska, M., Klypin, A. A., Kravtsov, A. V., et al. 2002, *Astrophys. J.*, 581, 799 (cited on page 181)
- von Hippel, T., Jefferys, W. H., Scott, J., et al. 2006, *Astrophys. J.*, 645, 1436 (cited on page 44)
- Wehner, E. M. H. & Harris, W. E. 2007, *Astrophys. J. Lett.*, 668, L35 (cited on page 70)
- Weidner, C., Kroupa, P., & Larsen, S. S. 2004, *MNRAS*, 350, 1503 (cited on page 4)
- Weinberg, M. D. 1994a, *Astron. J.*, 108, 1398 (cited on pages 124 and 172)
- Weinberg, M. D. 1994b, *Astron. J.*, 108, 1403 (cited on pages 124, 172, and 216)
- Weinberg, M. D. 1994c, *Astron. J.*, 108, 1414 (cited on pages 124 and 172)
- White, S. D. M. & Rees, M. J. 1978, *MNRAS*, 183, 341 (cited on pages 7, 164, and 215)
- Whitmore, B. C., Chandar, R., & Fall, S. M. 2007, *Astron. J.*, 133, 1067 (cited on pages 188, 196, 226, 231, and 234)
- Whitmore, B. C. & Schweizer, F. 1995, *Astron. J.*, 109, 960 (cited on pages 165 and 225)
- Whitmore, B. C., Zhang, Q., Leitherer, C., et al. 1999, *Astron. J.*, 118, 1551 (cited on pages 9, 165, 215, 216, 225, 226, and 231)
- Wielen, R. 1971, *Astron. Astrophys.*, 13, 309 (cited on page 134)
- Zahn, C. T. 1971, *IEEE Transactions on Computers*, 20, 68 (cited on page 18)
- Zepf, S. E., Ashman, K. M., English, J., Freeman, K. C., & Sharples, R. M. 1999, *Astron. J.*, 118, 752 (cited on page 33)
- Zhang, Q. & Fall, S. M. 1999, *Astrophys. J. Lett.*, 527, L81 (cited on pages 216, 217, 222, 226, 228, and 233)
- Zhang, Q., Fall, S. M., & Whitmore, B. C. 2001, *Astrophys. J.*, 561, 727 (cited on page 226)
- Zoccali, M., Piotto, G., Zaggia, S. R., & Capaccioli, M. 1998, *Astron. Astrophys.*, 331, 541 (cited on page 45)

# Nederlandse samenvatting

Het heelal is oud. Heel oud. Volgens de huidige schattingen is het universum waarin wij ons bevinden ongeveer 13,7 miljard jaar geleden ontstaan. Dat is gelijk aan tweehonderd miljoen mensenlevens, zeven miljoen keer de tijd die verstreken is sinds Caesar de Rubicon overstak, zeventigduizend keer de leeftijd van de diersoort *Homo Sapiens*, of zestig keer de ouderdom van de oudste dinosauriërfossielen. De aarde zelf bestaat eveneens al erg lang: het heelal is slechts drie keer ouder.

Eén blik op een heldere sterrenhemel is genoeg om de aarde om ons heen te zien vervagen, en roept talloze vragen op over onze plek in de kosmos. De vele<sup>1</sup> sterren en nevels lijken misschien stil te staan, maar in werkelijkheid is het heelal een en al dynamiek. Door de gigantische afstanden waarover kosmische processen zich afspelen, duren ze vaak te lang om met het blote oog te onderscheiden tijdens een mensenleven. Niet alleen is het zo dat het heelal onvoorstelbaar groot is, het heeft ook een substantiële ontwikkeling doorgemaakt. Het is een van de belangrijkste doelstellingen van de moderne astrofysica om te achterhalen hoe deze ontwikkeling zich precies heeft afgespeeld.

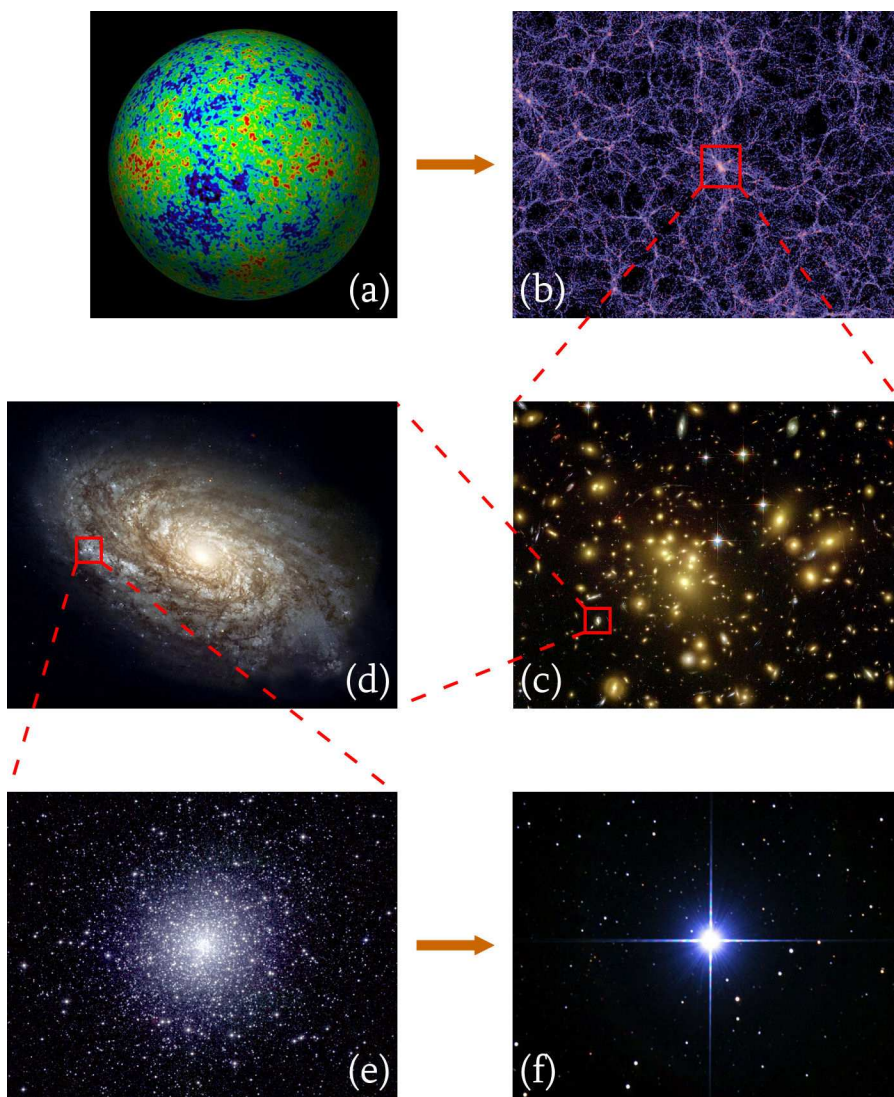
## Sterrenhopen en sterrenstelsels in het heelal

In dit proefschrift wordt de vorming en ontwikkeling van sterrenhopen en sterrenstelsels behandeld. Hoe deze vorming en ontwikkeling precies verlopen hangt af van de ontwikkeling van het heelal als geheel. Het is daarom belangrijk kort de structuur van heelal te bespreken.

In figuur A.1 wordt de hiërarchische opbouw van het heelal getoond. Op de grootst zichtbare afstand van de aarde is er een gloed zichtbaar, die een beeld geeft van de meest omvangrijke bekende structuur – de verdeling van licht in het vroege heelal. Deze *kosmische achtergrondstraling* kan worden gezien als het nagloeien van de oerknal en is min of meer homogeen. De afwijkingen van het gemiddelde zijn van de orde van een duizendste procent. Naarmate deze minieme fluctuaties van de materieverdeling in het vroege heelal groeiden onder invloed van de zwaartekracht, ontstonden er grotere dichtheidscontrasten, wat het heelal op grote schaal een sponsachtige structuur heeft gegeven. In de knooppunten en filamenten

---

<sup>1</sup>Zoals wel vaker in de astrofysica is dit begrip relatief. Op een heldere nacht kan het menselijk oog enkele duizenden sterren onderscheiden, maar alleen al in de Melkweg bevinden zich honderden miljoenen exemplaren.



**Figuur A.1:** Versimpelde weergave van de hiërarchische opbouw van het heelal. Paneel (a) toont de verdeling van licht in het (gehele) vroege heelal, kort na de oerknal (afkomstig van de WMAP satelliet/NASA). Het helderheidsverschil tussen rood en blauw is van de orde van slechts een duizendste procent. Paneel (b) toont een computersimulatie van de sponsachtige materieverdeling in het heelal (uit de *Millennium Simulatie*, V. Springel), die zichtbaar wordt na enkele miljarden jaren ontwikkeling en enige vergroting. Paneel (c) toont een cluster van sterrenstelsels (van de Hubble Space Telescope/NASA), die zich in de knooppunten van het kosmisch web bevinden. Paneel (d) bevat een enkel (spiraal)sterrenstelsel (van de Hubble Space Telescope/NASA). Paneel (e) geeft een voorbeeld van een (bolvormige) sterrenhoop (47 Tucanae, opname van 2MASS/Caltech). De ster Sirius (na de zon de helderste ster aan de hemel, opname van Yuuji Katahira) is afgebeeld in paneel (f).

van dit *kosmisch web* bevinden zich clusters van sterrenstelsels, de grootste structuren in het heelal die gebonden zijn door de zwaartekracht. Een enkel sterrenstelsel herbergt tientallen miljoenen tot honderd biljoen sterren, en een cluster van sterrenstelsels bevat typisch vijftig tot duizend sterrenstelsels. Wij bevinden ons in een buitenwijk van het Virgo cluster van sterrenstelsels, in een spiraalsterrenstelsel dat de Melkweg genoemd wordt en een paar honderd miljoen sterren bevat. Deze sterren zijn meestal geïsoleerd, maar soms bevinden ze zich in sterrenhopen, groepen van honderd tot een miljoen sterren die door hun onderlinge aantreking bij elkaar blijven. Een enkel sterrenstelsel zoals de Melkweg kan vele tienduizenden sterrenhopen bevatten.

De eigenschappen van de verschillende structuren in het heelal zijn verre van onveranderlijk. Gedurende de afgelopen 13,7 miljard jaar hebben sterren, sterrenhopen, sterrenstelsels en clusters van sterrenstelsels een enorme ontwikkeling doorgemaakt. Onder invloed van de zwaartekracht hebben de meeste sterrenstelsels interacties, botsingen en samensmeltingen met andere sterrenstelsels ondergaan. De gebeurtenissen op deze schaal zijn het gevolg van de eigenschappen van het heelal als geheel, en laten op hun beurt het gas, de sterren en de sterrenhopen in de sterrenstelsels ook niet ongemoeid. In botsende sterrenstelsels blijven individuele sterren weliswaar ongeschonden<sup>2</sup>, maar de gigantische moleculaire gaswolken in de sterrenstelsels komen vaak wel met elkaar in botsing. Hierdoor trekken de gaswolken samen en worden nieuwe sterren en sterrenhopen gevormd. Het aangezicht van sterrenstelsels wordt getransformeerd tijdens een botsing, maar in de vorm van oude en nieuwgevormde sterrenhopen dragen ze nog steeds de overblijfselen van hun historie met zich mee. Sommige sterrenhopen in een sterrenstelsel zijn bijna net zo oud als het heelal zelf, en mits juist geïnterpreteerd kunnen deze structuren inzicht verschaffen in de ontwikkeling van het sterrenstelsel waarin ze zich bevinden. Daarvoor is het noodzakelijk om de vorming en ontwikkeling van sterrenhopen en hun moederstelsels van begin tot einde te begrijpen.

## Stervorming

Het bestaan van sterrenhopen is te danken aan de manier waarop de vorming van sterren verloopt. De gaswolken in een sterrenstelsel bevinden zich in een zekere mate van evenwicht tussen de naar buiten gerichte gasdruk en de naar binnen gerichte zwaartekracht. Wanneer een gaswolk verstoord wordt, zij het door een passerende spiraalarm of door een gravitationele interactie met een andere gaswolk, dan kan het zijn dat de zwaartekracht het wint van de druk – de gaswolk krimpt ineen onder zijn eigen massa. Het ineenkrimpen verloopt lokaal sneller dan op grote schaal, waardoor de gaswolk fragmenteert. De fragmenten veranderen in sterren wanneer hun dichtheid zo hoog wordt dat er in hun binnenste kernfusie optreedt. Deze sterren zijn op dat moment nog aan het zicht onttrokken door de omringende gaswolk.

De fragmentatie van een ineenstortende gaswolk zorgt ervoor dat sterren nooit alleen worden geboren. In de nabije omgeving van jonge sterren bevinden zich altijd andere exemplaren. Het hangt vervolgens af van de onderlinge afstanden of deze sterren ook gravitationeel gebonden blijven. Wanneer de dichtheid hoog genoeg is en de sterren op voldoende korte af-

---

<sup>2</sup>Dit komt doordat binnen een sterrenstelsel de onderlinge afstanden tussen sterren veel groter zijn dan hun omvang. Een botsing tussen twee sterren is daardoor zeer onwaarschijnlijk, terwijl botsingen tussen sterrenstelsels haast onafwendbaar zijn doordat de verhouding tussen hun onderlinge afstand en omvang veel kleiner is.

stand van elkaar staan, is de onderlinge aantrekkingskracht sterk genoeg om de groep sterren bij elkaar te houden. Al deze sterren draaien dan hun banen binnen de groep. De groep jonge sterren is een sterrenhoop geworden.

Het gas dat zich in en rond een jonge sterrenhoop bevindt, wordt uitgedreven door de energie die de sterren leveren in de vorm van sterwinden en supernova-explosies. De uitdrijving van het gas veroorzaakt een afname van de totale zwaartekrachtspotential in de sterrenhoop, waardoor (een deel van) de sterrenhoop ongebonden kan worden en uiteendrijft. Omdat dit proces plaatsvindt in sterrenhopen met een zeer jonge leeftijd, wordt dit *infant mortality* genoemd. Het is echter de vraag in hoeverre infant mortality in staat is sterrenhopen te vernietigen. Ooit werd gedacht dat alle sterren in sterrenhopen werden geboren, waardoor de ratio van het aantal sterren in sterrenhopen en het aantal losse sterren (de *cluster formation efficiency*, CFE) kon worden gebruikt om de sterkte van infant mortality te bepalen. Dit gaf aan dat ongeveer 90% van alle sterrenhopen door infant mortality vernietigd zou moeten worden. Tegenwoordig weten we echter dat niet alle jonge groepen sterren gravitationeel gebonden zijn, ondanks de fragmentatie in stervormingsgebieden. Daardoor is de CFE niet voldoende om inzicht te krijgen in de rol die gasuitdrijving speelt in de vernietiging van jonge sterrenhopen. Naast infant mortality en de vorming van ongebonden groepen sterren, wordt er in Hoofdstuk 2 nog een ander mechanisme besproken dat leidt tot een lagere efficiëntie van de vorming van gebonden sterrenhopen (zie onder).

Ongeacht de precieze fractie van de stervorming die resulteert in gebonden sterrenhopen, is het zo dat de sterrenhopen die gevormd worden bepaalde eigenschappen hebben door de manier waarop het stervormingsproces verloopt. De fragmentatie van een ineenstortende gaswolk leidt tot een groep sterren die niet alleen bij benadering dezelfde leeftijd hebben, maar ook min of meer dezelfde chemische samenstelling. Daarnaast verloopt de fragmentatie en accretie van gas zodanig dat de massaverdeling van jonge sterren altijd dezelfde vorm volgt. Zware sterren zijn veel zeldzamer dan lichte sterren: de *initiële massafunctie* (IMF) van sterren kan goed worden beschreven met een stuksgewijze machtswet, die voor sterren met massa's groter dan een halve zonsmassa geschreven wordt als  $dn/dm \propto m^{-2.3}$ . De universaliteit van de IMF wordt alleen geschonden door de verdere dynamische ontwikkeling van sterrenhopen (zie onder), waarbij sterren met lage massa's over het algemeen een grotere ontsnappingskans hebben dan zware sterren. Door al deze eigenschappen van de sterren in een jonge sterrenhoop is de helderheid en het spectrum van een sterrenhoop op ieder moment van zijn bestaan goed te voorspellen, op voorwaarde dat de verdere ontwikkeling eveneens bekend is.

## De ontwikkeling van sterrenhopen

Nadat een sterrenhoop gevormd is, neemt het aantal sterren in de sterrenhoop (en dus ook zijn massa) alleen maar af. Dit wordt veroorzaakt door een aantal interne en externe processen. Het eerste interne proces dat tot een afname van de massa leidt, is de beperkte levensduur van sterren. Hoe zwaarder een ster is, des te korter deze leeft, en al blijft er van een gestorven ster bijna altijd een witte dwerg, neutronenster of zwart gat achter, het merendeel van de massa gaat verloren in de vorm van uitgestoten gas. Daarnaast resulteren de onderlinge zwaartekrachtsinteracties tussen de sterren in een afname van het aantal sterren in een sterrenhoop,



doordat de banen van de sterren worden gewijzigd. Tijdens de sterkste interacties worden sterren uit de sterrenhoop geslingerd. Het resulterende massaverlies van een sterrenhoop wordt bepaald door zijn interne eigenschappen en door de omgeving. Zware sterrenhopen verliezen per tijdseenheid een lagere fractie van hun massa dan lichte sterrenhopen, en in een sterk getijdeveld verloopt het massaverlies sneller dan in een zwak getijdeveld. Het laatste proces dat bijdraagt aan het massaverlies van sterrenhopen is extern – getijdeschokken versnellen de sterren in een sterrenhoop wanneer deze een zware structuur passeert. Zo zijn niet alleen een spiraalarm in een sterrenstelsel of een zware gaswolk in staat om een sterrenhoop behoorlijk te verstoren, maar ook wanneer de baan van een sterrenhoop de schijf van een sterrenstelsel of het centrum ervan doorkruist, kan dit tot een verlies van sterren leiden. Van de genoemde processen dragen getijdeschokken het sterkst bij aan het massaverlies van sterrenhopen.

De interacties tussen de sterren in een sterrenhoop beïnvloeden tevens de interne structuur van een sterrenhoop. De zware sterren verplaatsen zich richting het centrum van de sterrenhoop, terwijl de lichte sterren zich naar de buitenste regionen bewegen. Deze *massasegregatie* zorgt ervoor dat lichte sterren gemakkelijker ontsnappen uit een sterrenhoop dan zware sterren. De massafunctie van sterren in een sterrenhoop mag dan in eerste instantie universeel zijn, op de langere termijn zorgt de dynamische ontwikkeling van een sterrenhoop voor afwijkingen. Het verlies van sterren met lage massa's uit een sterrenhoop betekent ook dat de verhouding tussen massa en helderheid van een sterrenhoop verandert. Dit mechanisme wordt besproken in Hoofdstukken 3–7.

Doordat het massaverlies van sterrenhopen in hoge mate bepaald wordt door omgevingsfactoren, bevat een populatie sterrenhopen een schat aan informatie over zijn omgeving. Net als bij de sterren in een sterrenhoop is de initiële massaverdeling van sterrenhopen min of meer universeel. Deze volgt een machtwet met index  $-2$ , wat inhoudt dat zware sterrenhopen veel minder vaak voorkomen dan lichte sterrenhopen. Sterrenhopen hebben aanvankelijk massa's tussen de vijftig en tien miljoen zonsmassa's, maar na verloop van tijd wordt de massaverdeling beïnvloed door het uiteenvallen van de sterrenhopen. Ook de leeftjidsverdelingen van de sterrenhopen veranderen door disruptie. Als sterrenhopen nooit vernietigd zouden worden, dan zou de leeftjidsverdeling van sterrenhopen een directe weerspiegeling zijn van de stervormingsgeschiedenis – een periode van veel stervorming zou leiden tot een groot aantal sterrenhopen met een corresponderende leeftijd. Het uiteenvallen van sterrenhopen zorgt er echter voor dat er bijna altijd minder oude dan jonge sterrenhopen zijn. De leeftjidsverdeling van sterrenhopen wordt dus zowel bepaald door hun vormingsgeschiedenis als door hun disruptiegeschiedenis, die beide het directe gevolg zijn van de (ontwikkeling van de) eigenschappen van het sterrenstelsel waarin de sterrenhooppopulatie zich bevindt.

Onze eigen Melkweg geeft een schoolvoorbeeld van hoe de omgeving bepaalt wat de eigenschappen van een sterrenhooppopulatie zijn, en hoe deze benadering kan worden omgekeerd om uit de sterrenhopen af te leiden wat de geschiedenis van een sterrenstelsel is. In de Melkweg bevinden zich op het eerste gezicht twee soorten sterrenhopen: open en bolvormige (zie figuur A.2). Open sterrenhopen bevinden zich in de schijf van de Melkweg, zijn minder dan een miljard jaar oud, hebben massa's lager dan tienduizend zonsmassa's, en zijn metaalrijk. Bolvormige sterrenhopen bevinden zich in een soort halo rond de Melkweg, zijn met twaalf miljard jaar bijna net zo oud als het heelal zelf, hebben massa's van rond



**Figuur A.2:** *Links:* de Pleiaden, een open sterrenhoop met een leeftijd van ongeveer honderd miljoen jaar (afkomstig van de Palomar 48-inch Schmidt telescoop, NASA/ESA/AURA/Caltech). *Rechts:* M80, een bolvormige sterrenhoop met een leeftijd van ongeveer twaalf miljard jaar (afkomstig van de Hubble Space Telescope/WFPC2, Hubble Heritage Team/AURA/STScI/NASA).

de honderdduizend zonsmassa's, en zijn metaalarm. De massaverdeling van open sterrenhopen komt overeen met de eerder genoemde archetypische machtswet met index  $-2$ , maar de massaverdeling van bolvormige sterrenhopen heeft een tekort aan lichte sterrenhopen. De verschillen tussen open en bolvormige sterrenhopen tonen onder meer aan dat de lokale omgeving in de schijf van de Melkweg sterk disruptief is in vergelijking met de halo, waardoor er nauwelijks open sterrenhopen zijn met leeftijden ouder dan een miljard jaar, en dat bolvormige sterrenhopen desondanks een sterk massaverlies hebben ondergaan, aangezien de massaverdeling zo sterk verschilt van die van jonge sterrenhopen. Dit is weinig verrassend – aangezien bolvormige sterrenhopen bijna net zo oud zijn als het heelal, valt het te verwachten dat hun omgeving sterke veranderingen heeft ondergaan. In Hoofdstukken 8–10 wordt gepoogd te achterhalen hoe dergelijke veranderingen de eigenschappen van de sterrenhoop-populatie beïnvloeden.

## De ontwikkeling van sterrenstelsels

De galactische omgeving van sterrenhooppopulaties is sinds de vorming van de eerste sterrenstelsels sterk veranderd. Dwerfsterrenstelsels bevolkten het vroege heelal, terwijl de zwaarste sterrenstelsels later ontstonden door het samensmelten van kleinere stelsels. Dit model van *hiërarchische kosmologie* staat centraal in ons huidige begrip van de ontwikkeling van sterrenstelsels, en botsingen tussen sterrenstelsels zijn daarin het belangrijkste proces. In het vroege heelal waren botsingen weliswaar frequenter, maar ook tegenwoordig komen ze nog voor. In onze nabije omgeving zijn de Antennestelsels en de Draaikolknevel (zie figuur A.3) goede voorbeelden, en het Andromedastelsel nadert onze eigen Melkweg met een snelheid van meer dan honderd kilometer per seconde. Ook het Sagittarius dwerfsterrenstelsel wordt



**Figuur A.3:** De Draaikolknevel (M51), een interactie tussen een spiraalsterrenstelsel en een stelsel dat ongeveer drie keer minder zwaar is (afkomstig van de Hubble Space Telescope/ACS, Hubble Heritage Team/Beckwith/NASA/ESA/STScI). Uiteindelijk zullen de beide sterrenstelsels samensmelten tot een enkel elliptisch reuzenstelsel.

momenteel door de Melkweg opgeslokt.

Een botsing tussen twee sterrenstelsels leidt tot een sterke stijging van de stervormingsactiviteit. Gaswolken botsen op elkaar, worden door de getijde-interactie ineengedrukt, of worden naar het centrum van de sterrenstelsels gedreven. Deze piek in de stervorming betekent dat in botsingen tussen sterrenstelsels grote aantallen sterren en sterrenhopen geproduceerd worden. Als de sterrenstelsels in een botsing een vergelijkbare massa hebben, ondergaan ze een metamorfose. Wanneer spiraalsterrenstelsels zoals de Melkweg of het Andromedastelsel botsen, vervormen ze tot een enkel elliptisch reuzenstelsel, dat de vorm heeft van een uitgerekte bol en (bijna) geen gas meer bevat, zo efficiënt is de stervorming tijdens de voorafgaande botsing geweest. Wanneer een dwergsterrenstelsel wordt opgeslokt door een groter spiraal- of elliptisch sterrenstelsel<sup>3</sup> is de morfologische verandering minder sterk. Hoogstens wordt de schijf van een spiraalstelsel dikker, of wordt de halo van het sterrenstelsel bevolkt met sterren die uit het dwergsterrenstelsel getrokken zijn.

De interacties tussen sterrenstelsels hebben een sterke invloed op hun sterrenhooppopu-

---

<sup>3</sup>In populaire literatuur wordt dit vaak *kannibalisme* genoemd.

laties. In geïsoleerde sterrenstelsels bepalen interne eigenschappen zoals de structuur van de spiraalarmen en de gasdichtheid de vormings- en disruptiegeschiedenis van sterrenhoop-populaties. In botsende sterrenstelsels zorgen de globale processen die ook het aangezicht van de sterrenstelsels beïnvloeden voor een continu veranderende galactische omgeving. Tijdens de piek in de stervorming worden grote aantallen sterrenhopen geboren, waarvan de zwaarste exemplaren statistisch veel zwaarder kunnen worden dan gewoonlijk is voor de jonge sterrenhopen in een statischer galactische omgeving zoals de Melkweg. Er wordt in de literatuur vaak geopperd dat deze zware, jonge sterrenhopen de voorlopers van bolvormige sterrenhopen zouden kunnen zijn. Naast de verhoogde vormingsactiviteit is het echter ook zo dat de hoge gas dichtheid en de sterke veranderingen in het getijdenveld voor een efficiëntere vernietiging van sterrenhopen kan zorgen. In Hoofdstukken 8–10 wordt bekeken welk van beide effecten domineert in botsende sterrenstelsels, welke sterrenhopen botsingen tussen sterrenstelsels kunnen overleven, en wat de invloed van botsingen is op de eigenschappen van sterrenhooppopulaties.

## Dit proefschrift

In dit proefschrift worden theoretische berekeningen en numerieke simulaties gecombineerd en vergeleken met waarnemingen uit de literatuur, met als doel inzicht te krijgen in de vorming en ontwikkeling van (populaties van) sterrenhopen in de context van hun galactische omgeving. Het is daarvoor essentieel om de interne dynamica van sterrenhopen te begrijpen en om hun vorming en ontwikkeling te koppelen aan de gebeurtenissen die hun moederstelsel ondergaat. Alleen met een dergelijk begrip is het mogelijk om de grootschalige ontwikkeling van het heelal af te kunnen leiden uit sterrenhooppopulaties.

**Hoofdstuk 2** Sterrenhopen worden gevormd in fragmenterende gaswolken, waarvan de restanten op een zeker moment worden weggeblazen door sterwinden en supernova-explosies. In dit hoofdstuk wordt de dynamica van proto-sterrenhopen onderzocht, met als doel te achterhalen in hoeverre de uitdrijving van het gas kan zorgen voor het uiteendrijven van proto-sterrenhopen. Uit een analyse van numerieke simulaties van stervormingsgebieden blijkt dat de proto-sterrenhopen zich in een hoge mate van dynamisch evenwicht bevinden, zelfs wanneer de zwaartekrachtsaanrekening van het gas wordt genegeerd. Dit komt doordat de proto-sterrenhopen gasarm zijn – de inval van gas op de sterren verloopt minstens even snel als de globale instroom van het gas. Het gevolg is dat de uitdrijving van het gas slechts een kleine invloed heeft op de overlevingskansen van een proto-sterrenhoop. Op basis van de resultaten uit Hoofdstuk 8 en 10 wordt voorgesteld dat in plaats van een intern effect (*infant mortality*) een extern proces verantwoordelijk is voor de vroege ontbinding van sterrenhopen. De hoge gasdichtheid in stervormingsgebieden kan getijdeschokken veroorzaken die mogelijk in staat zijn jonge sterrenhopen te ontbinden. Dit *cruel cradle effect* moet het belangrijkste zijn in gebieden met een hoge concentratie van stervorming.

**Hoofdstuk 3** De massa's van sterren in een sterrenhoop zijn in eerste instantie verdeeld volgens de IMF (zie boven). Naarmate een sterrenhoop ouder wordt, verdwijnen de zware sterren doordat ze aan het eind van hun leven komen en een compacte, dode ster achterlaten

in de vorm van een witte dwerg, neutronenster of zwart gat. Daarnaast verliest een sterrenhoop sterren door hun onderlinge zwaartekrachtsinteracties en door getijdeschokken. Bij deze processen ontsnappen vooral lichte sterren. In dit hoofdstuk wordt een simpel model voor de ontwikkeling van sterrenhopen gepresenteerd en wordt onderzocht hoe de helderheid en kleur van sterrenhopen worden beïnvloed door de verandering van de massaverdeling van sterren in een sterrenhoop, het behoud van compacte objecten, de vorm van IMF en de chemische samenstelling van de sterren. Deze afhankelijkheden kunnen worden gebruikt om de eigenschappen van sterrenhopen af te leiden uit hun kleur en helderheid. De kleur van de sterrenhopen blijkt het meest stabiel te zijn, en wordt overwegend bepaald door de leeftijd en chemische samenstelling van de sterrenhoop. De helderheid is veel gevoeliger voor wijzigingen in de getoetste parameters en mechanismen. Doordat lichte sterren relatief lichtzwak zijn in vergelijking met hun massa, en zware sterren relatief helder, zorgt de ontsnapping van lichte sterren voor een verandering van de hoeveelheid licht die een sterrenhoop uitzendt per massa-eenheid. Deze *massa-lichtkracht verhouding* daalt naarmate een sterrenhoop meer sterren verliest: met de ontsnapping van de lichte sterren verliest de sterrenhoop meer massa dan helderheid. Daardoor lijken oude sterrenhopen op basis van hun helderheid vaak zwaarder dan ze zijn. Aangezien zware sterrenhopen over het algemeen minder sterren verloren hebben dan lichte sterrenhopen, is deze daling van de massa-lichtkracht verhouding het sterkst voor lichte sterrenhopen, wat leidt tot de voorspelling dat de massa-lichtkracht verhouding toeneemt met de massa en helderheid van een sterrenhoop. Daarnaast zorgt het behoud van compacte objecten voor een toename van de massa-lichtkracht verhouding, en deze grootte is eveneens sterk afhankelijk van de IMF en de chemische samenstelling van een sterrenhoop. De voorspelde massa-lichtkracht verhoudingen komen goed overeen met de waargenomen waarden voor bolvormige sterrenhopen in de Melkweg.

**Hoofdstuk 4** De massa-lichtkracht verhoudingen van bolvormige sterrenhopen in de Melkweg zijn systematisch lager dan verwacht mag worden op basis van modellen waarin geen rekening wordt gehouden dynamische effecten. Daarnaast is er een trend van lagere massa-lichtkracht verhoudingen voor sterrenhopen met lagere massa's. In dit hoofdstuk wordt het model uit Hoofdstuk 3 gebruikt om na te gaan of deze karakteristieken te wijten zijn aan het verlies van lichte sterren uit de sterrenhopen. Daarbij wordt rekening gehouden met de verschillen in chemische samenstelling tussen de sterrenhopen. De modellen worden toegepast op de bolvormige sterrenhopen in de Melkweg, het elliptische reuzenstelsel Centaurus A, het Andromedastelsel en het dwergsterrenstelsel de Grote Magelhaense Wolk. De typische efficiëntie van het verlies van sterren die nodig is om de waargenomen massa-lichtkracht verhoudingen te verklaren door het ontsnappen van lichte sterren komt goed overeen met de verwachte waarden. Het percentage bolvormige sterrenhopen waarvan de massa-lichtkracht verhouding verklaard kan worden stijgt van 39% tot 92% wanneer de modellen uit Hoofdstuk 3 worden gebruikt.

**Hoofdstuk 5** Van 24 bolvormige sterrenhopen in de Melkweg zijn de baan en massa-lichtkracht verhouding bekend. In dit hoofdstuk wordt die informatie gebruikt om te berekenen hoeveel sterren deze sterrenhopen sinds hun vorming hebben verloren, en wat op

basis daarvan volgens het model uit Hoofdstuk 3 de verwachte massa-lichtkracht verhouding van deze individuele sterrenhopen is. Voor de helft van de sterrenhopen komen waarneming en theorie overeen. De discrepantie voor de overige sterrenhopen komt vermoedelijk doordat de waargenomen massa-lichtkracht verhoudingen bepaald zijn in het centrum van de sterrenhoop, terwijl de modellen globale massa-lichtkracht verhoudingen voorspellen. Dat is relevant voor deze sterrenhopen, omdat ze eigenschappen hebben die leiden tot verschillen tussen de massa-lichtkracht verhoudingen in hun centra en hun buitenste regionen. Wanneer slechts de sterrenhopen worden bekeken waarbij geen ruimtelijke variatie van de massa-lichtkracht verhouding wordt verwacht, zijn de waarnemingen en theorie in overeenstemming. Beide geven een massa-lichtkracht verhouding die gemiddeld 20% lager is dan in modellen zonder dynamische effecten. Het belang van het verlies van lichte sterren wordt bevestigd door een verband tussen de helling van de waargenomen massaverdeling van sterren in de sterrenhopen en hun waargenomen en voorspelde afname in massa-lichtkracht verhouding. Aan het eind van het hoofdstuk wordt een inschatting gemaakt van de haalbaarheid van waarnemingen die erop gericht zijn het verlies van lichte sterren af te leiden uit de massaverdeling van sterren in bolvormige sterrenhopen, en zo de bevindingen uit dit hoofdstuk te verifiëren.

**Hoofdstuk 6** De massaverdeling van bolvormige sterrenhopen kan gebruikt worden om te bepalen hoe het verlies van sterren afhangt van de sterrenhoop-massa. Hiervoor moeten de helderheden van bolvormige sterrenhopen echter eerst worden omgezet in massa's. Voorheen gebeurde dit altijd door een constante massa-lichtkracht verhouding aan te nemen, waarmee werd geconcludeerd dat het aantal sterren dat per tijdseenheid ontsnapt uit sterrenhopen niet afhangt van de sterrenhoop-massa. In dit hoofdstuk wordt het model uit Hoofdstuk 3 gebruikt waarin de massa-lichtkracht verhouding toeneemt met massa en helderheid. Het gebruik van deze modellen leidt tot een massaverdeling van bolvormige sterrenhopen in de Melkweg met een andere helling dan voorheen - er zijn relatief meer lichte bolvormige sterrenhopen, waarvan de massa wordt overschat wanneer een constante massa-lichtkracht verhouding wordt gebruikt. Hieruit kan worden afgeleid dat de snelheid waarmee sterrenhopen sterren verliezen niet onafhankelijk is van de sterrenhoop-massa, maar iets hoger is voor zware sterrenhopen. De fractie van de totale sterrenhoop-massa die verloren wordt per tijdseenheid blijft echter het grootst voor lichte sterrenhopen, die zodoende ook in deze nieuwe analyse korter leven dan zware sterrenhopen.

**Hoofdstuk 7** De ontwikkeling van de massaverdeling van sterren in een sterrenhoop wordt over het algemeen onderzocht middels computersimulaties, waarin de beweging en zwaartekracht van alle individuele sterren wordt gevolgd. Deze simulaties kosten erg veel rekentijd en daardoor is het niet mogelijk om alle mogelijke omstandigheden waaronder sterrenhopen zich ontwikkelen te simuleren. In dit hoofdstuk wordt een simpel fysisch model afgeleid voor de ontwikkeling van de massaverdeling van sterren in sterrenhopen, waarmee het mogelijk wordt om de stellaire massaverdelingen van hele populaties van sterrenhopen te modelleren. Daarnaast biedt een dergelijk model inzicht in de processen die verantwoordelijk zijn voor het verlies van sterren uit sterrenhopen. De basis wordt gevormd door een model van

Hénon uit 1969, waarin wordt aangenomen dat de sterrenhoop zich in isolatie ontwikkelt<sup>4</sup> en de invloed van massasegregatie (zie boven) wordt verwaarloosd. Omdat echte sterrenhopen zich in een extern getijdeveld bevinden en massasegregatie ondergaan, worden deze aannames niet gemaakt in dit hoofdstuk. Het model van Hénon wordt aangevuld met correcties voor de (massa-afhankelijke) tijdschalen waarop massasegregatie wordt bereikt en de massa-afhankelijkheid van de ontsnapingsenergie in een massa-gesegregeerde sterrenhoop. De resulterende ontwikkeling van de stellaire massaverdeling verandert sterk door deze toevoegingen, en komt uitstekend overeen met de resultaten van computersimulaties van sterrenhopen. Tijdens de eerste 400 miljoen jaar is de ontsnapping van sterren het meest efficiënt voor sterren met massa's van ongeveer 20% van de zwaarste ster in de sterrenhoop. Op latere momenten hebben sterren met de laagste massa's de grootste kans op ontsnapping. Door dit verschil hangt de ontwikkeling van de stellaire massaverdeling af van het moment waarop de sterren ontsnappen uit de sterrenhoop. Het model bevestigt dat de massa-lichtkracht verhouding van sterrenhopen afneemt door het verlies van lichte sterren. De mate waarin dit gebeurt wordt bepaald door de fractie van compacte objecten die behouden wordt wanneer sterren aan het eind van hun leven komen. Tot slot wordt het model gebruikt om de helling van de massaverdeling bij lage stermassa's te voorspellen voor bolvormige sterrenhopen in de Melkweg. De resultaten hiervan zijn in overeenstemming met de waargenomen hellingen, in tegenstelling tot de computersimulaties, die slechts een deel beslaan van het vereiste scala aan omstandigheden waaronder de sterrenhopen zich hebben ontwikkeld.

**Hoofdstuk 8** De vorming en ontwikkeling van sterrenhopen wordt bepaald door de galactische omgeving waarin ze zich bevinden. Niet alleen variëren de omstandigheden binnen een enkel sterrenstelsel sterk tussen het centrum en de buitenste regionen, maar in het huidige kosmologische model vormen en groeien sterrenstelsels door samen te smelten met andere stelsels. Dit betekent dat de invloed van de galactische omgeving op sterrenhopen afhangt van de plaats waar ze zich bevinden en het moment waarop ze bestaan, en dat deze tevens verandert gedurende hun baan en naarmate ze ouder worden. Om de gezamenlijke invloed van al deze processen op de vorming en ontwikkeling van sterrenhooppopulaties te kunnen begrijpen, wordt in dit hoofdstuk een nieuw soort model gepresenteerd, gevalideerd en toegepast. In dit model wordt de ontwikkeling van (botsende en geïsoleerde) sterrenstelsels gesimuleerd en aangevuld met het sterrenhoopmodel uit Hoofdstukken 3 en 7. De berekende ontwikkeling van individuele sterrenhopen op geïdealiseerde banen komt goed overeen met de resultaten uit computersimulaties van sterrenhopen op dezelfde banen. De eigenschappen van de sterrenhooppopulatie worden onderzocht met behulp van negen simulaties van geïsoleerde spiraalsterrenstelsels en 24 simulaties van botsingen. In geïsoleerde sterrenstelsels neemt de gemiddelde leeftijd van de sterrenhopen toe naarmate ze zich verder uit het galactisch centrum bevinden, doordat de vernietiging van sterrenhopen het meest efficiënt is in het centrum. Deze vernietiging wordt voor 80–90% veroorzaakt door getijdeschokken. Wanneer de hele sterrenhooppopulatie wordt beschouwd, neemt de vernietiging van sterrenhopen af met de leeftijd. Dit wordt veroorzaakt door twee mechanismen. Ten eerste worden

---

<sup>4</sup>Hierdoor kunnen sterren slechts ontsnappen door een enkele sterke zwaartekrachtsinteractie met een andere ster, in plaats van meerdere zwakke interacties gedurende een langere tijdsspanne.

sterrenhopen geboren in gebieden met een hoge gasdichtheid, die daardoor erg disruptief zijn. Naarmate ze ouder worden, ontsnappen de sterrenhopen uit deze gebieden – dit proces van *sterrenhoop-migratie* vermindert de efficiëntie van sterrenhoop-vernietiging voor oudere sterrenhopen. Daarnaast bevinden de sterrenhopen in een populatie zich in een breed scala aan omgevingen die in verschillende mate disruptief zijn. Voor een dergelijke spreiding worden de sterrenhopen in de meest disruptieve omgevingen het eerst vernietigd – deze *natuurlijke selectie* zorgt eveneens voor een afname van de gemiddelde sterrenhoop-vernietiging met de leeftijd. De combinatie van beide effecten beïnvloedt de vorm van de leeftijdsverdeling van sterrenhopen. In botsende sterrenstelsels is het contrast tussen de omgevingen waar bepaalde sterrenhopen zich in bevinden groter dan in geïsoleerde stelsels, wat ervoor zorgt dat de leeftijdsverdeling van sterrenhopen op bepaalde momenten tijdens de botsing volledig bepaald wordt door sterrenhoop-migratie en natuurlijke selectie. De vernietiging van sterrenhopen is door de verhoogde dichtheid het sterkst in de gebieden waar veel sterren geboren worden, waardoor na de botsing de piek in de leeftijdsverdelingen van sterren en sterrenhopen verschilt. Met name in de centrale gebieden is de vernietiging efficiënt, wat er voor zorgt dat de ruimtelijke verdelingen van sterrenhopen en sterren na een botsing eveneens van elkaar afwijken.

**Hoofdstuk 9** De hoge (gas)dichtheden die bereikt worden in botsende sterrenstelsels hebben een tweevoudige invloed op de sterrenhooppopulatie. Enerzijds worden er veel meer sterren en sterrenhopen geboren dan in geïsoleerde stelsels, maar anderzijds neemt ook de vernietiging door getijdeschokken toe. In dit hoofdstuk worden de simulaties uit Hoofdstuk 8 gebruikt om te kijken welk van beide effecten domineert. Uit de simulaties blijkt dat de toename van de vernietiging groter is dan de toename van de vorming van sterrenhopen, wat leidt tot een afname van het totale aantal sterrenhopen tijdens een botsing. Dit lijkt in tegenspraak te zijn met de waarnemingen van grote aantallen sterrenhopen in nabije botsingen. Deze waarnemingen worden echter beperkt door een magnitudelimiet, waardoor voornamelijk jonge, zware sterrenhopen worden gedetecteerd, die relatief ongevoelig zijn voor de getijdeschokken. Wanneer eenzelfde limiet wordt toegepast op de simulaties, *lijkt* het aantal sterrenhopen inderdaad toe te nemen, net zoals in de waarnemingen. Doordat lichte sterrenhopen het makkelijkst worden vernietigd, blijven na een botsing met name de zware sterrenhopen over. Hun ruimtelijke verdeling lijkt sterk op die van bolvormige sterrenhopen, en er wordt dan ook voorgesteld dat bolvormige sterrenhopen gevormd zijn in botsingen tussen sterrenstelsels (of andere dichte stervormingsgebieden) in het vroege heelal.

**Hoofdstuk 10** De Antennestelsels zijn een klassiek voorbeeld van een nabije botsing tussen twee spiraalsterrenstelsels, waarin grote aantallen sterrenhopen worden gevormd (en vernietigd). Daarnaast is het een systeem waarin de leeftijdsverdeling van sterrenhopen afwijkt van de theoretisch voorspelde vorm. Naar aanleiding hiervan is er in de literatuur voorgesteld dat de theorie van sterrenhoopdisruptie gewijzigd dient te worden. In dit hoofdstuk wordt het model uit Hoofdstuk 8 gebruikt om de Antennestelsels te simuleren, teneinde het model te verifiëren en mogelijk de waarnemingen te verklaren. De gesimuleerde leeftijds- en massaverdelingen van de sterrenhopen in de Antennestelsels blijken in uitstekende overeen-



stemming te zijn met het waargenomen systeem, en ook de correlatie van de leeftijden van de sterrenhopen met hun ruimtelijke verdeling is consistent met de waarnemingen. Dit komt op het eerste gezicht niet overeen met de verwachting op basis van de gebruikte theorie voor sterrenhoopdisruptie. De variatie van de omgeving zorgt er echter voor dat de vernietiging van sterrenhopen zwakker wordt naarmate de populatie ouder wordt, waardoor de leeftijdsverdeling een gedaanteverwisseling ondergaat – de combinatie van het *cruel cradle effect* (zie Hoofdstuk 2), sterrenhoop-migratie en natuurlijke selectie verandert de leeftijdsverdeling zodanig dat de simpele theoretische verwachting niet overeenkomt met het uiteindelijke resultaat. Dit betekent echter niet dat de theorie onjuist is. De complexiteit van de galactische omgeving bepaalt wat de eigenschappen van de sterrenhopen in de Antennestelsels zijn, en biedt een specifiek raamwerk waarbinnen de theorie toegepast moet worden. Deze invloed van de omgeving toont aan dat sterrenhopen inderdaad gebruikt kunnen worden om de vormingsgeschiedenis af te leiden van de sterrenstelsels waarin ze zich bevinden.



# List of publications

## Published in refereed journals

1. Kruijssen, Pelupessy, Lamers, Portegies Zwart & Icke 2011, MNRAS, in press *Modelling the formation and evolution of star cluster populations in galaxy simulations* (Chapter 8)
2. Kruijssen 2009, A&A, 507, 1409 *The evolution of the stellar mass function in star clusters* (Chapter 7)
3. Kruijssen & Portegies Zwart 2009, ApJ, 698, L158 *On the Interpretation of the Globular Cluster Luminosity Function* (Chapter 6)
4. Kruijssen & Mieske 2009, A&A, 500, 785 *Dissolution is the solution: on the reduced mass-to-light ratios of Galactic globular clusters* (Chapter 5)
5. Kruijssen & Lamers 2008, A&A, 490, 151 *The photometric evolution of star clusters and the preferential loss of low-mass bodies – with an application to globular clusters* (Chapter 3)
6. Kruijssen 2008, A&A, 486, L21 *Explaining the mass-to-light ratios of globular clusters* (Chapter 4)

## Submitted to refereed journals or in preparation

1. Kruijssen, Maschberger, Clarke, Bastian, Moeckel & Bonnell 2011, MNRAS submitted *The dynamical state of stellar substructure in star-forming regions* (Chapter 2)
2. Kruijssen, Pelupessy, Lamers, Portegies Zwart, Bastian & Icke 2011, in preparation *Formation versus destruction: the evolution of the star cluster population in galaxy mergers* (Chapter 9)
3. Kruijssen & Bastian 2011, in preparation *The star cluster population of the Antennae galaxies* (Chapter 10)

## Published data sets

1. Kruijssen 2009, VizieR Online Data Catalog, 507, 1409 *Models for dynamically dissolving star clusters*
2. Kruijssen & Lamers 2008, VizieR Online Data Catalog, 490, 151 *Photometric evolution of star clusters: models*

## Published in conference proceedings

1. Kruijssen, Pelupessy, Lamers, Portegies Zwart & Icke 2010, in ASP Conf. Ser. 423, *Galaxy Wars: Stellar Populations and Star Formation in Interacting Galaxies*, ed. Beverly Smith, Nate Bastian, Sarah J. U. Higdon, & James L. Higdon, pp. 203 *Simulations of Interacting Galaxies Covering More Than Ten Orders of Magnitude*
2. Kruijssen & Portegies Zwart 2010, in ASP Conf. Ser. 423, *Galaxy Wars: Stellar Populations and Star Formation in Interacting Galaxies*, ed. Beverly Smith, Nate Bastian, Sarah J. U. Higdon, & James L. Higdon, pp. 151 *The Relation Between the Globular Cluster Mass and Luminosity Functions*
3. Kruijssen & Mieske 2010, in ASP Conf. Ser. 423, *Galaxy Wars: Stellar Populations and Star Formation in Interacting Galaxies*, ed. Beverly Smith, Nate Bastian, Sarah J. U. Higdon, & James L. Higdon, pp. 146 *The Mass-to-Light Ratios of Galactic Globular Clusters*
4. Kruijssen & Lamers 2008, in ASP Conf. Ser. 396, *Formation and Evolution of Galaxy Disks*, ed. José G. Funes, S. J., & Enrico Maria Corsini, pp. 149 *The Age Distributions of Clusters and Field Stars in the Small Magellanic Cloud – Implications for Star Formation Histories*

# Dankwoord

Dit proefschrift is het resultaat van vier jaar steun, wijsheid en vriendschap die velen mij geboden hebben. Mijn familie, vrienden en collega's hebben allen een onmisbare rol gespeeld in de totstandkoming van dit werk. Hoewel ik niet in staat zal zijn om allen voldoende eer te geven, laat staan iedereen te noemen, wil ik toch mijn dank betuigen aan een aantal mensen.

Ik heb de eer en het genoegen gehad om van mijn drie promotoren alles te mogen leren wat ik had kunnen hopen – en nog veel meer. Henny, je bent de afgelopen negen jaar zoveel meer geweest dan docent, afstudeerbegeleider en promotor. Als mentor en wetenschappelijke vader heb je me niet alleen laten zien hoe wetenschap werkt, maar ik begrijp nu ook hoe je wetenschap kunt beleven op een manier waardoor het vak over decennia nog steeds uitdagingen zal bieden – jouw nieuwsgierigheid en vastberadenheid zijn bijzonder aanstekelijk, en je brede kennis en interesse zijn bewonderenswaardig. Daarnaast waren de conferenties waar we samen naartoe zijn gegaan en de uitstapjes met de onderzoeksgroep altijd heel ontspannend. Je bent het grote voorbeeld voor ieder die ooit in staat wil zijn om zijn studenten te stimuleren en zich op hun gemak te laten voelen. De vrijheid en mogelijkheden die je me de afgelopen jaren hebt geboden waren fantastisch, en ik ben er heel erg trots op dat ik jouw promovendus heb mogen zijn. Simon, je hebt me geleerd hoe ieder woord van een artikel telt, hoe je daar rekening mee moet houden, en hoe je een wetenschappelijk betoog objectief houdt. Hoe diplomatie in de wetenschap werkt, waarom het belangrijk is, en wat de (on)geschreven regels van de wetenschap zijn. Maar bovenal wil ik je bedanken voor de openheid waarmee je mij geadopteerd hebt in de Castle-groep, en hoe je altijd tijd maakte om me van advies te voorzien, soms zelfs vanaf de andere kant van de wereld. Vincent, ik ben heel dankbaar voor je tijd en raad. De deur was altijd open, en menigmaal heb je me eraan herinnerd dat tijd, ruimte en een gezonde mate van individualisme tot de mooiste resultaten kunnen leiden. Je kritische positiviteit heeft me vaak het gevoel gegeven dat de *sky* ook daadwerkelijk de *limit* is.

Natuurlijk waren jullie het niet altijd eens in de raad die jullie mij gaven (over details zelfs zelden), maar ik heb dat altijd enorm waardevol gevonden, omdat de resulterende discussies bijzonder stimulerend waren. Temidden van zulke wetenschappelijke reuzen krijgt zelfs de kleinste kabouter moed, en jullie steun heeft mij de afgelopen jaren een onontbeerlijke zekerheid geboden. Dat zal ik nooit vergeten.

Apart from my formal promotors, I have learned a lot from others as well. My time in Cambridge was an unrivalled experience in many ways. I am very grateful to Cathie Clarke for the many interesting discussions we had, for the hospitality, and for always making me

wonder *why I didn't think of that before*. Nate, you have been an amazing colleague and friend. Thank you for all the exciting projects we have worked and will work on, and for the fun that makes everything easy (I should especially mention the *scientific peer review from 1945*, but also karting, footie, and the famous quote 'such is life'). I would like to thank Gerry Gilmore and Rob Kennicutt for many interesting and stimulating discussions and for adopting me into their research groups during my stay. Thomas, next to being a very kind and helpful office mate, you have taught me a new perspective on Bach, antique musical instruments, statistics, and much more. Thanks also to Barbara, Jorge (your booze pulled us through the Peak District), Matt, and the football squad – Dom and Alex (Wembley was fantastic), Becky, James M., James O. and all the others.

Inti, vier jaar geleden begonnen we samen aan een bijzonder spannend project, waarvan het duidelijk was dat het zonder goede samenwerking onbegonnen werk zou worden. Terugkijkend is het niet alleen zo dat we onze doelstellingen hebben gehaald, maar ook dat deze samenwerking heel erg plezierig is geweest. Jouw hulp bij deel C van dit proefschrift was ongeëvenaard, en ik ben je daar heel erg dankbaar voor.

I am grateful to many colleagues and collaborators for co-authoring papers and/or for the many interesting discussions that contributed to this work. In no particular order, Mark Gieles (we should really write a paper together!), Steffen Mieske, Bruce Elmegeen, Holger Baumgardt, Pavel Kroupa, Ian Bonnell, Nick Moeckel, Douglas Heggie, Sverre Aarseth, Simon Goodwin, Guido de Marchi, Thorsten Naab, Simon Karl, Dean McLaughlin, Scott Chapman, Markus Kissler-Patig, Alex de Koter, Koen Kuijken and Frank Verbunt have helped me greatly over the past years.

The star cluster group at Utrecht has been a great environment to work in. Søren, Ana, Elizabeth, Peter, Remco, Angela, thank you for the interesting discussions, and the valuable advice. Also thanks to the students in our group, Nick, Steven, Gregal and Jorien. The same holds for the courses I have taught and have assisted in teaching – thanks to Peter, John and Bram for very pleasant times.

Esteban, of course we have had great discussions in the context of the star cluster group, but I think the vast majority of our discussions was in our office, addressing *slightly* different topics. Thank you for brilliant assists and unlimited energy during football, for sharing joy, frustration and infinite laughs, and for making me realise that it isn't nice to be *alone in the office*. I think we made up for that last bit by teaming up during some long nights while finishing our theses. Maria, cheers to 'world domination and everlasting glory'! Thank you for the music, for the enjoyable dinners, for allowing me a 'desk' in your office from time to time, and all our lengthy discussions on the things that really matter. I am very grateful to both of you for doing the impossible and showing me that such friendships are perfectly possible in science.

The weekly football was always a very entertaining event, and particularly the 'balance' snacks and drinks afterwards provided a welcome break. Thank you Sjors (also for our discussions on 'Museic'), Carlo, Alex, Joke, Tim, João, Laurens and Stefano. Also to Marijke, Marcel, Ernst, Selma, Matteo, Hector, Jurjen, Sander and Eveline, thank you for all kinds of fun and the discussions on astrophysics, life, job markets, music, sociology, theses and everything else. I am very grateful to Christoph, Marion and Sake for all their efforts in streamlining the organisation of the institute, to Jan Lub and Erik Deul for their hospitality

and for helping me out in Leiden, and to Peter van der Wilt and Robert Kerst for their endless support and belief in our exciting popularisation projects.

Het is mij een groot genoegen mijn beide paranimfen te bedanken. Reinier, je bent de afgelopen jaren onmisbaar geweest in vele opzichten. Natuurlijk als vriend, maar ook door me scherp te houden en door altijd de juiste vragen te stellen, zowel binnen als buiten de wetenschap. Geen enkel idee was ooit te gek (wat overigens ook in de keuken gold) en zelfs diep in de nacht waren onze discussies nog leerzaam. We hebben veel meegemaakt, en ik ben je oprecht dankbaar voor ieder moment. Leanne, al meer dan een decennium (we worden oud) kan ik op je rekenen en verbreed je mijn horizon. Kunst, muziek, festivals, (uit) eten, al deze momenten hebben me de ontspanning gegeven die nodig was om dit proefschrift te voltooien. Van (lang geleden) het Domus Aurea tot (recenter) de kluiten van Pinkpop, van het Concertgebouw tot de betere restaurants in Utrecht, het was altijd weer een geweldig rustpunt.

Ik ben mijn ouders heel dankbaar voor een leven lang steun, wijsheid, en bovenal verdraagzaamheid. Jullie waarden en principes gelden met een wonderlijke universaliteit, en hebben me een kompas gegeven waarmee ik de woeligste zeeën durf te bedwingen. Ik prijs mij daar heel gelukkig mee. Machteld, je laat me telkens weer zien hoe kracht, vastberadenheid en aanpassingsvermogen iemand tot grote hoogten kunnen drijven. Ik heb daar veel van geleerd – je bent een voorbeeld voor ons allen. Mijn beide grootvaders hebben me de wijsheid en het positivisme gegeven waarop dit proefschrift is gebouwd.

Sophie, ik heb je nooit gekend zonder te werken aan mijn promotieonderzoek, en mijn hele onderzoek lang heb ik geen dag hoeven doen zonder jouw steun. Als ik iemand dankbaar ben voor onvoorwaardelijke verdraagzaamheid ben jij het wel. Jouw toewijding is bewonderenswaardig en wordt weerspiegeld in iedere vezel van dit proefschrift. Dankjewel.





# Curriculum vitae

Diederik Kruijssen was born on May 4, 1985 in Nieuwegein, The Netherlands. He obtained his Gymnasium degree in 2002 at the Gemeentelijk Gymnasium in Apeldoorn. In 2005, he received his B.Sc. degree in Physics and Astronomy ‘cum laude’ at Utrecht University after working under the supervision of dr. Frank M. C. Witte on gravitational dynamics in Space-time Algebra. In April 2007, he obtained his M.Sc. degree in Astrophysics ‘cum laude’ at Utrecht University, after working under the supervision of prof. dr. Henny J. G. L. M. Lamers on semi-analytic models for the evolution of the star cluster and field star populations in nearby galaxies. He was awarded a Toptalent Fellowship from the Netherlands Organisation for Scientific Research (NWO) to carry out the PhD research on which this book is based, with prof. Lamers at the Astronomical Institute of Utrecht University, and prof. dr. Simon F. Portegies Zwart and prof. dr. Vincent Icke at Leiden Observatory, Leiden University. He visited the Institute of Astronomy, University of Cambridge (United Kingdom) for three months to work with prof. dr. Cathie J. Clarke and dr. Nate Bastian, the results of which are treated in Chapters 2, 7, 8 and 9 of this work. Outside The Netherlands, he presented his work at conferences, workshops and meetings in Cambridge, Bonn, Bern, Rome, Sheffield, Santa Barbara, Johnson City, Barcelona, Puebla, Santiago, Ringberg and Granada. Starting summer 2011, he will continue his astrophysical research as a Research Fellow at the Max-Planck Institute for Astrophysics, Garching bei München (Germany).

